The Key Laboratory of Weak Light Nonlinear Photonics,
Ministry of Education

Annual Report 2010

南开大学弱光非线性光子学

教育部重点实验室

Annual Report 2010

The Key Laboratory of Weak Light Nonlinear Photonics,
Ministry of Education

南开大学弱光非线性光子学

教育部重点实验室

▼ 德国 Osnabrück 大学博士研究生 Kay 和硕士生 Anikka 来实验室进行交流研究。

（2010.1.19-3.21）

▼ 德国 Osnabrück 大学的 Peter Hertel 教授讲授线性响应理论及计算物理。

（2010.3.15-4.24; 9.7-10.30）

▼ 第二届国际先进光子学讲习班在泰达应用物理学院举办。（2010.6.30-7.1）

▼ 马里兰大学史砚华教授来实验室进行学术交流。　　（2010.8.10）

▼ 北爱尔兰 Ulster 大学的博士 Nason 来我院进行合作交流。（2010.9.19-11.20）

▼ 辛辛那提大学王小生博士来访并作了关于离散光学的报告。　　（2010.10.12）

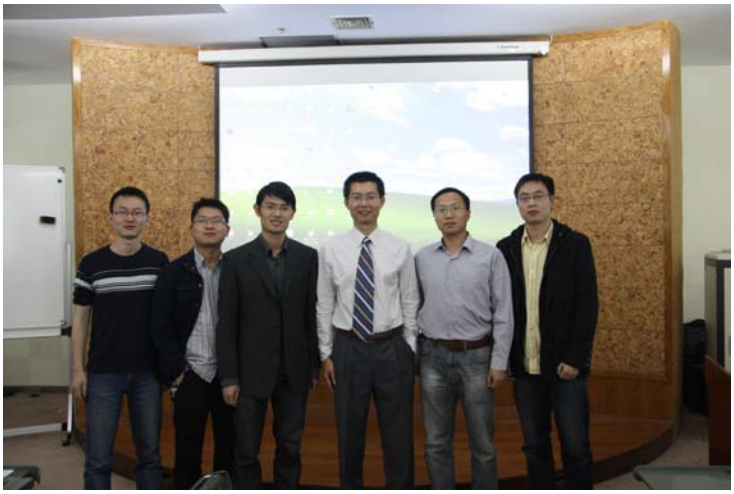

▼柏林洪堡大学 Nikolaus Ernsting 教授来访并作了超快光学和分子动力学方向的报告。（2010.10.17-28）

▼ 南安普顿大学 Nikolay I. Zheludev 教授来访。（2010.11.5-11.7）

▼2010 年中俄激光物理研讨会专家来实验室参观访问。（2010.12.2）

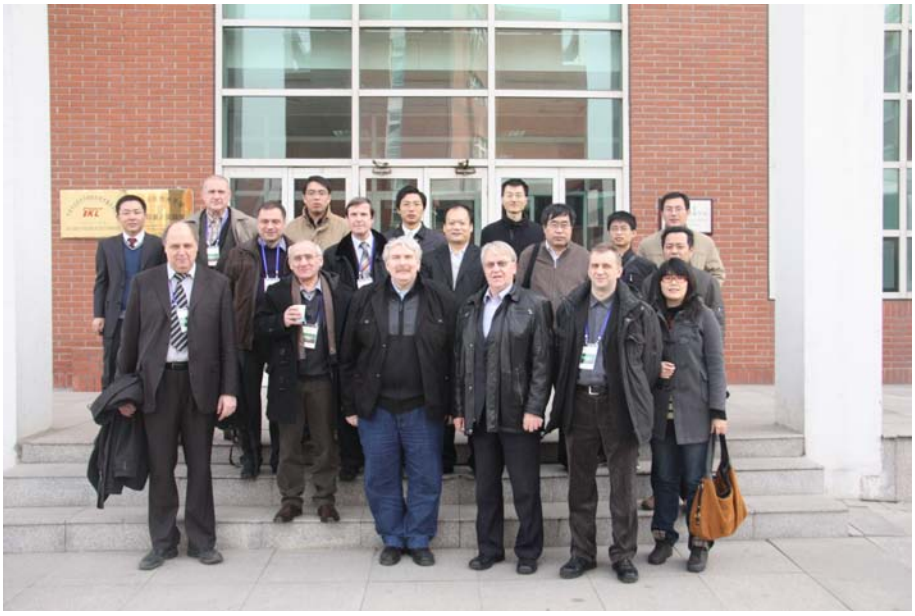

前　言/Preface

In 2010, the work at our lab was mainly focused on optical nonlinearities of organic materials, functional optical crystals, micro-crystal glass ceramics, nano-particulate films, up-conversion-luminescent materials, rare-earth doped glasses and their microstructures, also nonlinear optical manipulation of light in photonics structures. Especially achieved some fruitful results in the slow-light nonlinear optics and addressable optical buffer memory by EIT, the graphene hybrid material covalently functionalized with Porphyrin and optical limiting, optical trapping and manipulation of metallic micro-particles, generation of propagating plasmons by electron beams. In addition our newly startup researches are going along well, such as the silicon based MOS light emitting devices, weak-light nonlinear bio-optical effects, et al. In this report, we present a short summary of the results achieved in each line of activity of 2010.

All the activities summarised here have been done in the frame of international projects, cooperation agreements, and contracts with NSFC, MOE, MOST and Tianjin Municipal government. We also benefit a lot from our colleagues from other units all over world, who provide us advices and supports. Many thanks for their kind supports. In addition, our staff and students worked hard in order to make our research better and faster. Thanks a lot for their indispensible contributions and wonderful research works.

Hereby I would also like to stress that Prof. Hutian Wang joined our lab last year and started the research works on topics of manipulation of optical fields and its application.

Prof. Dr. Jingjun Xu

Director,

The Key laboratory of Weak-Light Nonlinear Photonics

目　录/Contents

人员结构/Organization

实验室主任/Director

许京军　教　授

实验室副主任/Deputy Directors

张国权　教　授

孙　骞　教　授

学术秘书/Academical Secretary

禹宣伊　副教授

研究方向负责人/Research Group Leaders

弱光非线性及量子相干光学	许京军　教　授
非线性物理与光子技术	田建国　教　授
光子学材料及先进制备技术	孔勇发　教　授
光谱表征及传感技术	臧维平　教　授
半导体生长技术和半导体器件	舒永春　教　授

学术委员会/Academic Committee

主　任/Chairman

王占国　院　士　（中国科学院半导体研究所）

委　员/ Committee Members

沈德忠　院　士	（清华大学化学系功能晶体与薄膜研究所）
薛其坤　院　士	（清华大学物理系）
姚建年　院　士	（中国科学院化学研究所）
许宁生　院　士	（中山大学理学院）
陈志刚　教　授	（南开大学物理科学学院）
龚旗煌　教　授	（北京大学物理学院）
陆　卫　研究员	（中国科学院上海技术物理研究所）
田建国　教　授	（南开大学物理科学学院）
王慧田　教　授	（南开大学物理科学学院）
徐现刚　教　授	（山东大学晶体材料国家重点实验室）
许京军　教　授	（南开大学物理科学学院）
资　剑　教　授	（上海市复旦大学表面物理国家重点实验室）

外籍学术顾问委员

D. Kip	教　授	德国 Cauthburge 大学
L. Hessenlink	教　授	美国斯坦福大学物理系
R. A. Rupp	教　授	奥地利维也纳大学实验物理所
T. Volk	教　授	俄罗斯国家晶体研究所
Y. Tomita	教　授	日本电气通信大学
K. A. Nelson	教　授	美国麻省理工学院

杰出人才/Intelligent Staff

教育部“长江奖励计划”特聘教授

许京军（1999）　王慧田（1999）　陈志刚（2006）

国家杰出青年基金获得者

许京军（1998）　田建国（2001）　王慧田（2003）　李宝会（2009）

教育部“优秀青年教师资助计划”入选者

张国权（2002）　宋　峰（2003）

教育部“跨世纪优秀人才培养计划”入选者

许京军（1998）　田建国（2000）　孙　骞（2001）　孔勇发（2002）

教育部“新世纪优秀人才支持计划”入选者

张国权（2004）　宋　峰（2004）　臧维平（2005）　李宝会（2005）
徐章程（2006）　孙甲明（2007）　张心正（2008）　刘智波（2009）
陈　璟（2009）　顾　兵（2010）

首批新世纪百千万人才工程国家级人选

田建国（2004）

国家海外青年学者合作研究基金获得者

陈志刚（2005）

“天津市授衔专家”称号获得者

许京军（2005）　田建国（2005）

教育部“长江学者和创新团队发展计划”创新团队基金资助

弱光非线性光子学重点实验室人员名录/Name List

研究人员/Scientific Staff（50 人）

王占国　许京军　王慧田　田建国　Romano A. Rupp　陈志刚　张国权　孔勇发　孙　骞
宋　峰　臧维平　李宝会　舒永春　徐章程　姚江宏　赵丽娟　曹亚安　孙甲明　张天浩
李玉栋　徐晓轩　张心正　周文远　乔海军　邢晓东　禹宣伊　余　华　吴　强　孙同庆
武　莉　楼慈波　高　峰　刘智波　李祖斌　薄　方　齐继伟　叶　青　潘雷霆　蔡　卫
陈树琪　宋道红　孙　军　张　玲（兼）　刘士国（兼）　唐柏权（兼）　李　威（兼）
王振华（兼）　陈　璟　顾　兵　李勇男

技术人员/Technical Staff（6 人）

黄自恒　陈绍林　马玉祥　张　玲　刘士国　王振华

行政人员/ administrative Staff（3 人）

梁　建　李　威　唐柏权

博士生/Ph.D Students（80 人）

王丕东　王　垒　陈宗强　谢　楠　徐　雷　张文定　李　俊　杨程亮　张学智　任梦昕
石　凡　谭信辉　吴　限　向吟啸　梁　毅　刘鹏闵　孔凡磊　郝志强　孙立萍　胡　毅
叶卓艺　刘建彬　祁轶舲　窦宜领　翟召辉　辛非非　洪佩龙　胡　毅　叶卓艺　郭　贺
孔凡磊　孙立萍　郝志强　刘建彬　祁轶舲　陈旭东　赵　欣　孔翔天　李志莉　赵子宇
杨　阳　王　槿　杨　熹　鄢小卿　张校亮　程　化　应翠凤　闫卫国　刘　欣　栗建兴
刘　悦　于彦龙　陈小东　刘　敏　王文杰　刘富才　裴子栋　师丽红　葛新宇　田　甜
董江舟　李燕丽　冯页新　周凯迪　张新星　张　鹏　叶志诚　龚　亮　李俊梅　刘海旭
袁志翔　程　辉　刘艳玲　于　音　赵红艳　明成国　王青茹　刘家东　李　伟　韦　晨

硕士生/M.S. Students（135 人）

张　斌　马寅星　云志强　易三铭　王　萌　王午登　马志刚　孙　哲　马腾飞　殷　毅
张永哲　郭尚雨　陈战东　杨　明　徐　燕　胡　皓　陈子坚　孟　涛　李海燕　李　祥
潘　登　李　健　杨　冉　王莲莲　刘　泽　孙海峰　李　斌　赵　飞　郜向阳　周玉波
李　毅　门双仁　马　跃　王秋明　高　原　彭秋明　张　阳　史　硕　阚颖慧　李亚东
徐　建　刘世松　代　林　范小龙　栾艳彩　刘博洋　李　艳　石伟科　张光子　尹鹏飞
杨晓玲　杨　涛　郭燕磊　辛建康　李西峰　孟翔峰　何　嵩　李　莉　马　强　赵明铎
周　开　丁芳媛　闫　铮　寇大勇　高洪利　张洪术　韩　榕　马海梅　刘张赛　郑守君
黄　明　甄彦赞　谢桂娟　刘　艳　罗师强　张　华　赵丹丹　李　芳　张芳馨　杨金凤
曾　浩　刘文波　张建峰　杨晓丹　王海涛　郑先明　郭丽梅　陈金金　樊文博　孟　楠
胡　男　满　荣　张　铭　王亚洲　张　盼　韩文卿　王　俊　董印锋　赵建彬　陈　猛
陈　鸿　张　宇　田　澍　王景声　王肖珩　候琼琼　靳亚粉　卢旭岑　吴玉娥　刘　畅
曹　雪　康　培　胡永能　王静密　程　辉　姚惠梓　李　洁　卢志璐　王红亚　孟繁杰
颜艳花　王云峰　栾　星　李广平　邢　飞　张　俊　王凤潇　王津津　张　超　张　弓
王　芳　朴文益　郭　宁　杜　鹏　蔡莹莹

承担课题/Projects under Researching

序号	项 目 名 称	项 目 来 源	起止时间	负责人
1	纳/微结构非线性光学、光调控与器件应用研究	973 项目	2007.5-2012.8	许京军
2	光诱导人工光学结构及光传播特性研究	973 项目	2007.7-2011.12	陈志刚
3	硅基发光材料与光互联的基础研究（南开部分）	973 项目	2007.7-2012.12	孙甲明
4	氧化物介观薄膜原子尺度可控制备与超快紫外器件研究（南开部分）	973 项目	2007.5-2011.4	孔勇发
5	表面等离子体共振定向辐射机理及超高方向性辐射特性研究（南开部分）	973 项目	2006.7-2010.6	宋 峰
6	基于亚波长尺度光纤的复合波导结构与新器件（南开部分）	973 项目	2008.1-2010.12	孙 骞
7	超快激光与硅表面相互作用机理研究	973 项目	2010.1-2011.12	姚江宏
8	光子束超衍射纳米加工基本原理基础研究	973 项目	2010.1-2014.12	张心正
9	纳米器件制备工艺创新与应用基础研究（南开部分）	973 项目子课题	2010.1-2011.12	王振华
10	特种材料及构件的高压烧结致密化机理与技术（南开部分）	973 项目子课题	2010.01-2013.12	陈 璟 李勇男

11	四价掺杂铌酸锂晶体	863 新材料技术	2007.12-2010.11	孔勇发
12	关联光子学微结构阵列的光传输与调控研究	国家重大科学研究计划	2007.1-2011.12	田建国
13	关联光子学微结构的非线性光学特性与调控机理研究	国家重大科学研究计划	2010.1-2014.12	田建国
14	铌酸锂晶体的紫外带边缺陷结构和非线性光学性质研究	国家自然科学基金重大研究计划培育项目	2010.1-2012.12	张国权
15	稀土掺杂光学材料中金属纳米微结构的制造及其对发光的影响	国家自然科学基金重大研究计划培育项目	2010.1-2012.12	宋　峰
16	国家自然科学基金重大研究计划《功能导向晶态材料的结构设计和可控制备》专家管理工作计划	国家自然科学基金	2010.1-2010.12	许京军
17	矢量光场的动态调控：新方法、新效应和应用	国家自然科学基金 重点项目	2010.01-2013.12	王慧田
18	弱光非线性光子学科学与技术创新引智基地	111 计划	2007.1-2011.12	许京军
19	基于一维光自带隙结构的光限制效应研究	国家自然科学基金	2007.1-2009.12	臧维平
20	弱关联光子晶格体系中飞秒光传播特性及其导致的非线性光学效应	国家自然科学基金	2007.1-2009.12	吴　强
21	光学相干周期微结构系综的光学性质	国家自然科学基金	2007.1-2009.12	张国权
22	光折变非线性表面光波导及其应用研究	国家自然科学基金	2007.1-2009.12	张天浩

23	电场调制下纳米硅微晶和 Er 离子耦合系统的发光特性和高效率场致发光	国家自然科学基金	2008.1-2010.12	孙甲明
24	掺铒磷酸盐玻璃陶瓷的发光和激光特性	国家自然科学基金	2008.1-2010.12	宋　峰
25	聚合物/无机量子点红外复合材料的非线性和超快光谱研究	国家自然科学基金	2008.1-2010.12	徐章程
26	Er^{3+}离子掺杂钨酸镧钾晶体的生长和性质研究	国家自然科学基金	2008.1-2010.12	孙同庆
27	有机超分子材料的光学非线性调控及其应用研究	国家自然科学基金	2008.1-2010.12	刘智波
28	光诱导铌酸锂表面金属微纳结构及其与光的相互作用	国家自然科学基金	2009.1-2011.12	张心正
29	超声调制复合周期性折射率结构与光群速调控的研究	国家自然科学基金	2009.1-2011.12	高　峰
30	基于光流体的荧光光源及其光子学性质的研究	国家自然科学基金	2009.1-2011.12	禹宣伊
31	高效率纳米 TiO2 基复合固溶体新型可见光催化剂的制备	国家自然科学基金	2009.1-2011.12	曹亚安
32	光折变离散表面孤子研究	国家自然科学基金	2009.1-2011.12	张天浩
33	级联光子晶体光纤喇曼放大器中飞秒脉冲光速减慢的研究	国家自然科学基金	2009.1-2011.12	李勇男
34	碳结构及其杂化材料的光学非线性与超快特性研究	国家自然科学基金	2010.1-2012.12	田建国
35	三维磁光光子晶体飞秒激光直写技术研究	国家自然科学基金	2010.1-2012.12	李玉栋

36	缺陷光子晶格中的光动力学研究	国家自然科学基金	2010.1-2012.12	楼慈波
37	稀土离子掺杂的硅基紫外纳米层状结构发光器件	国家自然科学基金	2010.1-2012.12	孙甲明
38	高灵敏度快响应 InP 和 InN 胶体量子点近红外光探测器	国家自然科学基金	2010.1-2012.12	徐章程
39	新型碱金属碱土金属硼酸盐材料结构与荧光性质研究	国家自然科学基金	2010.1-2012.12	武　莉
40	利用法珀腔共振效应提高有机材料中慢光的相对延迟	国家自然科学基金	2010.1-2012.12	薄　方
41	各向异性介质亚波长结构的光学异常透射及其应用研究	国家自然科学基金	2010.1-2012.12	陈　璟
42	复合微纳阵列结构的光调控及其应用研究	教育部科技创新工程重大项目培育资金项目	2009.1-2011.12	张国权
43	高效率的硅 MOS 电致发光器件	教育部新世纪优秀人才支持计划	2008.1-2010.12	孙甲明
44	光子局域化中的相干背散射研究	教育部新世纪优秀人才支持计划	2009.1-2011.12	张心正
45	有机杂化结构光学非线性及其应用研究	教育部新世纪优秀人才支持计划	2010.1-2012.12	刘智波
46	Peter Hertel	教育部“海外名师”项目	2010.1-2010.12	许京军
47	石墨烯材料光学非线性及其机制研究	教育部科学技术研究重点项目	2009.1-2011.12	刘智波
48	新型激光自倍频晶体基质材料五磷酸镧二钾的生长与性质研究	教育部高等学校博士点新教师基金	2008.1-2010.12	孙同庆

49	Er 掺杂的富硅 SiO_2 MOS 结构的高效率场效应电致发光	教育部高等学校博士点新教师基金	2008.1-2010.12	孙甲明
50	新型硼酸盐发光材料结构与性能研究	教育部高等学校博士点新教师基金	2008.1-2010.12	武　莉
51	有机超分子材料光学非线性研究	教育部高等学校博士点新教师基金	2008.1-2010.12	刘智波
52	亚波长结构光传播性质的研究	教育部高等学校博士点新教师基金	2008.1-2010.12	李祖斌
53	表面等离子体共振及共振条件下的拉曼光谱研究	教育部高等学校博士点新教师基金	2008.1-2010.12	王　斌
54	动态和静态光栅中光脉冲形变的抑制	教育部高等学校博士点新教师基金	2009.1-2011.12	薄　方
55	掺锆铌酸锂晶体的缺陷模型和畴反转研究	教育部高等学校博士点新教师基金	2009.1-2011.12	刘宏德
56	稀土掺杂的硅基 MOS 结构电致发光	教育部留学回国人员基金	2009.1-2010.12	孙甲明
57	用于可调谐光子学器件的光敏纳米复合材料的研究	中国与斯洛文尼亚政府间科技合作项目	2009.6-2011.6	张心正
58	新型无机液体激光介质-掺稀土氟化物纳米晶溶胶	天津市自然科学基金重点基金	2009.4-2012.3	赵丽娟
59	矿石检测小型化激光拉曼光谱仪	天津市科技支撑计划重点项目	2007.4-2009.10	徐晓轩
60	若干新型弱光非线性效应及其应用的研究	天津市国际科技合作项目	2006.4-2009.3	张国权
61	弱光非线性光学新效应和机制	天津市科技创新能力与环境建设平台项目	2006.7-2009.6	孙　骞

62	用相位编码方法在铌酸锂表面构造亚微米金属微结构	天津市自然科学基金	2007.4-2009.9	张心正
63	电磁波与微结构的瞬态相互作用	天津市自然科学基金	2009.4-2012.3	吴　强
64	碳基材料复合物光学非线性及其应用研究	天津市自然科学基金	2009.4-2012.3	刘智波
65	碱金属碱土金属硼酸盐基发光材料结构与性能研究	天津市自然科学基金	2009.4-2012.3	武　莉
66	亚波长微结构异常光学性质及其应用的研究	天津市自然科学基金	2009.4-2012.3	李祖斌
67	长江学者启动基金	985	2006.3-2009.2	陈志刚
68	离散体系对瞬态量子相干的影响	教育部留学回国人员科研启动基金	2008.8-2009.08	张心正
69	聚合物/无机量子点红外复合材料中的载流子动力学	中科院上海技物所红外物理国家重点实验室开放课题	2007.6-2009.6	徐章程
70	拉曼表面增强传感器	精密测试技术及仪器国家重点实验室开放基金	2009.9-2012.9	徐晓轩
71	光学异常透射效应的电磁调控机理及应用的研究	微系统所开放课题	2009.06-2011.05	陈　璟
72	若干掺杂铌酸锂晶体的研制	横向课题	2008.8-2010.7	张　玲
73	太阳能电池增透膜技术开发	横向课题	2009.12-2010.12	曹亚安
74	XXXXXX	军品配套项目		张　玲

75	小型自动光纤拉丝机的研制	横向课题	2009.1-2009.6	宋峰
76	ITO 靶材用 SnO_2 纳米粉末的工艺技术开发	横向课题	2010.12-2011.12	舒永春
77	铌酸锂晶体电光调 Q 开关研制	横向课题	2010.2-2010.4	张　玲
78	近红外多光子诱导丙烯酸基树脂光聚合的微观动力学研究	中央高校基本科研业务费专项基金	2010.6-2012.5	王振华
79	电子显微镜高分辨成像表面等离激元的理论研究	中央高校基本科研业务费专项基金	2010.6-2012.5	蔡卫
80	紫外光折变材料及器件研究	中央高校基本科研业务费专项基金	2010.6-2012.5	李威
81	利用快速显微荧光成像法对嗜中性粒细胞免疫信号转导过程中耗散现象的研究	中央高校基本科研业务费专项基金	2010.6-2012.5	潘雷霆
82	有序与无序金属亚波长微纳结构的表面增强非线性	中央高校基本科研业务费专项基金	2010.6-2012.5	李祖斌
83	微结构光纤表面等离子体谐振和局域场增强及其应用研究	中央高校基本科研业务费专项基金	2010.6-2012.5	陈树琪
84	粗糙表面效应对组织光学参数测定的影响及相关问题研究	中央高校基本科研业务费专项基金	2010.6-2012.5	叶青
85	表面等离子激光磁光非线性效应的研究	中央高校基本科研业务费专项基金	2010.6-2012.5	齐继伟
86	非线性介质纳米波导阵列光学性质的研究	中央高校基本科研业务费专项基金	2010.6-2012.5	陈靖

仪器设备平台/Facilities

仪器设备名称	规格型号	购置时间
激光器工作站	899-29	2005.09
飞秒激光器	VF-T2S	2000.08
皮秒激光器	PY61	2003.11
纳秒激光器	Panther OPO	2003.11
光纤激光器	PLY-20-M	2003.11
可调频再生放大器	Spitfire F-1K	2000.04
时间分辨光谱及瞬态吸收光谱系统	Spectrapro.300i	2000.04
光谱分析仪	AQ6315A	2005.09
显微拉曼光谱仪	MKI2000	1998.09
分子速外延生长炉	Riber Compact 21T	2003.09
提拉法晶体生长炉	研制	2002.04
晶体切割研磨抛光系统	Logitech 系列	2001.06
扫描探针显微镜	Nanoscope Ⅲa	2006.08

注：除开放基金外，所有仪器设备均为有偿使用

研究工作报告/Scientific Report

非线性物理与光子技术/ Nonlinear Physics and Photonics Techniques

负责人：田建国

本方向涉及有机材料光学非线性、光在介质中的传播、光子带隙材料、亚波长微结构、以及非线性表面波等方面。本年度发表论文 22 篇；申请或授权专利 2 项。在研课题经费 667 万元。2010 年度“非线性物理与光子技术”方向主要在以下方面取得了进展:

In this field, we mainly focused on optical nonlinearities of organic materials, beam propagation, one dimensional photon crystal, sub-wavelength microstructures, and nonlinear surface waves. There were 22 scientific papers published in international academic journals, and 2 patents applied in this year. The total researching funds are 6.67 millions. This year, we obtained some important results as following:

在碳结构纳米材料的光学非线性方面，我们报道了羟基修饰的多壁碳纳米管的光学非线性，我们发现羟基修饰的多壁碳纳米管在水和N,N-二甲基甲酰胺(DMF)中比在氯仿中具有更好的分散性，同时保留了较强的非线性散射特性。另外，在紧聚焦、厚样品条件下，发现氧化石墨烯的DMF悬浮液在纳秒下表现出负的非线性折射特性，而在 皮秒脉冲下，随着氧化石墨烯浓度的增加，悬浮液表现出从正到负的非线性折射的演变，我们认为纳秒脉冲下其非线性折射来源于溶液的瞬态热效应，而皮秒脉冲下则来源于溶剂DMF和氧化石墨烯自身。

In the aspect of the nonlinear optical properties of carbon-based nanomaterials, we reported that the hydroxyl groups modified multi-walled carbon nanotubes can be dispersed both in water and N, N-dimethylformamide (DMF) much better than in chloroform, strong nonlinear scattering properties from these suspensions were also observed. We also studied the nonlinear refraction properties of graphene oxide suspension in DMF in nanosecond and picosecond pulse regime under tight focusing geometry and thick sample cell conditions. The suspension shows negative nonlinear refraction due to transient thermal effect in nanosecond regime, while exhibits a changeover from positive to negative nonlinear refraction as the graphene oxide concentration increases due to the opposite sign between nonlinear refraction of DMF and graphene oxide itself in picosecond regime.

在各向同性介质中，我研究了飞秒脉冲下非线性光学的偏振特性，我们发现非线性折射，非线性吸收和非线性散射的强度是随入射激光偏振态而变化的。在非线性散射的研究中，我们设计实验验证了二硫化碳在800nm附件开孔Z扫描的信号主要来源于非线性散射，而不是双光子或者三光子吸收。

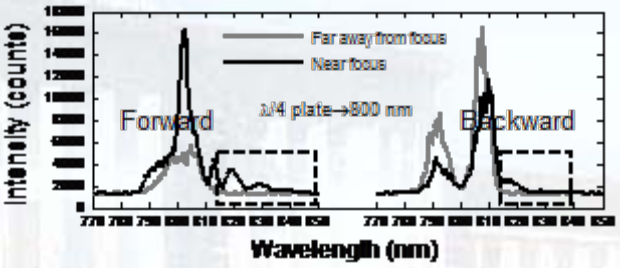

图 1 样品在不同位置时的光谱比较

Fig. 1. Comparison of spectra at different sample position. Left side: FTL, Right side: BSL

The polarization characteristic of ultrafast nonlinearity was systematically studied in isotropic medium, we found that nonlinear refraction, nonlinear absorption and nonlinear scattering changed greatly with the polarization states (linearly, elliptically and circularly) of incident beam. During the nonlinear scattering, we have designed

experiments to analyze the signal of femtosecond open-aperture Z-scan of carbon disulfide around 800 nm. The signal is verified to arise mainly from nonlinear scattering, not two- or three- photon absorption.

在计算加速电子的理论分析方面，我们分析了艾利光束加速电子的能量增益问题。我们发现光束的横向加速和无衍射特性可以导致沿光束传播轴形成一个不对称的加速通道，从而将电子加速到更高的能量；同时电子注入参数在加速过程中也扮演重要的角色。通过详细的数值分析，我们得到进入加速通道后电子被捕获和加速到更高能量的条件，同时也分析了衰减参数、电子初始入射能量在电子加速中的作用。

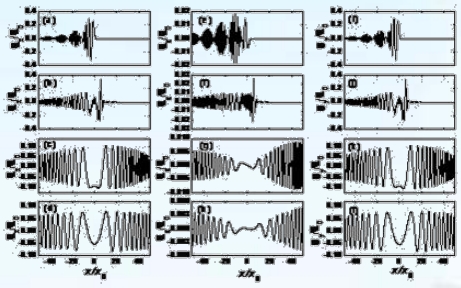

图 2 电场和磁场沿传播方向在不同 z 位置处的截面分布图。

Fig. 2. (a)-(d) Cross sections of E_x at zr, 10zr, 30zr, and 50zr, respectively. (e)-(h) Cross sections of E_z at zr, 10zr, 30zr, and 50zr, respectively. And, (i)-(l) cross sections of B_y at zr, 10zr, 30zr, and 50zr, respectively.

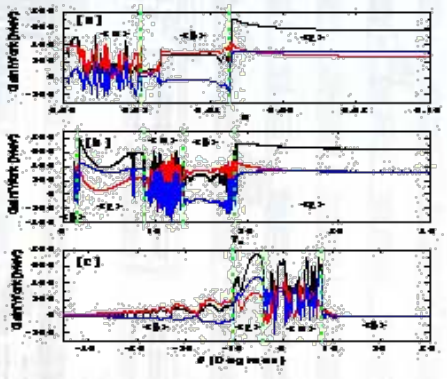

图 3 电场 E_x 和 E_z 做的总功、能量增益和衰减参数 a，入射角 θ 和初始电子能量 γ_0 的关系曲线。

Fig. 3. (a)-(c) Variation of the energy gain with a, γ_0, and θ. The black curves, red curves, and blue curves present the energy gains, the total work done by E_x, and E_z, respectively.

In theory analysis of accelerating electron using laser beam，we analyze the energy gain in vacuum electron acceleration by Airy beam. We find the characteristics of transverse acceleration and non-diffraction of Airy beam can lead to the formation of a long “asymmetric field channel” along the propagation axis, where the intense asymmetric field can accelerate the injected electron to higher energy. Meanwhile, the injection energy of electron plays an important role in determining the final energy gain. Through numerical simulation, we have studied detailedly vacuum electron acceleration induced by an Airy beam. Results show that an electron entering into asymmetric field channel may be captured and gain high energy and decaying parameter, the injection energy and inject angle of electron, play important roles in the electron energy gain.

在光对微粒操控方面，我们详细分析了一维艾利光束对瑞利粒子的辐射力和粒子的运动轨迹。分析结果表明艾利光束牵曳粒子到最强场，导引粒子沿抛物轨迹运动。捕获的稳定性可以通过增加输入光强或粒子半径来获得。

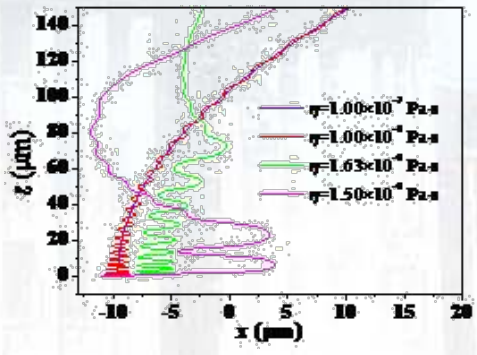

图 4 一个直径 50nm 融硅小球在不同粘滞介质中，在 Airy 光束作用下的动力学轨迹。

Fig. 4. The trajectories of a 50 nm (radius) fused silica nanoparticle at the initial position of x = -11 μm (z = 0) with different viscosity of surrounding medium.

In theory analysis of microparticles

manipulation by light, the radiation forces and trajectories of Rayleigh dielectric particles induced by one-dimensional Airy beam were numerically analyzed. Results show that the Airy beam drags particles into the optical intensity peaks, and guides particles vertically along parabolic trajectories. The trapping stability could be improved by increasing either the input peak intensity or the particles radius.

在非线性表面波研究中，我们提出了光折变表面光孤子。利用局域非线性实现亮孤子和暗孤子，利用非局域非线性可以使孤子束缚在介质近表面传播，将两者结合即可以实现表面孤子。在 SBN 晶体实现了表面亮孤子的激发，在 LN 晶体实现了表面暗孤子的激发。由于表面波孤子的能量的局域，更因为沿表面传播实现的相位匹配，利用表面波孤子还可以实现二次谐波巨增强，我们在 SBN 晶体实现了 80.3%/W 的高二次谐波转化效率。

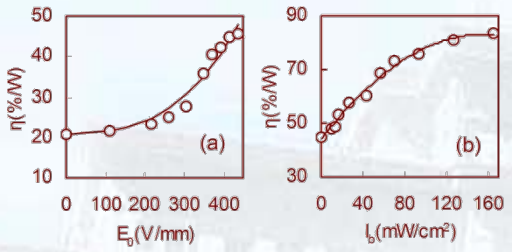

图 5 利用表面波孤子在 SBN 晶体实现二次谐波巨增强. （a）外电场对转换效率的影响;（b）背景光对转换效率的影响

Fig. 5. Conversion efficiency η of SHG vs. (*a*) applied external electric field E_0 and (*b*) background illumination I_b

We introduced a new type of solitons, Photorefeactive surfaces solitons Local nonlinearities can lead to the concentration of light energy, consequently bright solitons and dark solitons can be excited; nonlocal nonlinearities can lead to the confining of a light beam near a boundary and propagating along the surface of medium. In virtue of the cooperation of nonlocal and local nonlinearities, Surface solitons can be implemented. We successfully excited bright surface solitons and dark surface solitons in SBN crystal and LN crystal, respectively. For one hand, take advantage of surface wave solitons light energy can be concentrated; for another hand, take advantage of the natural linepath of surface the phase matching can be satisfied successfully. As a result, the giant enhancement of SHG can realized and we have obtained high of 80.3%/W efficiency in SBN crystal.

在非线性光子带隙材料及其应用方面，我们研究了一种由一维光子带隙材料和厚金属膜构成的光学通道异质结构的透射和反射 Z 扫描特性。结果表明即使入射光强度非常低，在光学通道附近也会出现明显的 Z 扫描信号；并且从左侧入射的透射和反射 Z 扫描信号远大于从右侧入射的 Z 扫描信号，证明光学异质结构从两个方向入射的非对易性；随着入射光波长的增加，反射 Z 扫描曲线的形状变化同透射 Z 扫描曲线的形状变化恰好相反；在光学通道附近，从左侧入射的反射 Z 扫描信号将会出现一个非常尖锐的峰。应用光学异质结构这些特性，由一维光子带隙材料和厚金属膜构成的光学通道异质结构可以在激光腔、光学二极管和全光开关等方面得到应用。

The transmitted and reflected Z-scan characteristics for light-tunneling heterostructures composed of one-dimensional photonic bandgap material and metallic film are theoretically investigated. An apparent Z-scan signal will appear around the light-tunneling even if the incident peak intensity is very low. Both of the transmitted and reflected Z-scan signals from left incidence are much larger than those from right incidence, demonstrating the nonreciprocal for two incident directions. The variation of the reflected Z-scan curve shape is opposite to that of transmitted Z-scan curve shape as light wavelength increases. Moreover, the reflected Z-scan signals from left

incidence will appear a very sharp peak around the light-tunneling. Applying our results enable to optimize the PBG-metal heterostructure designs and operation wavelengths for particular applications such as laser cavity, optical diode and optical switching.

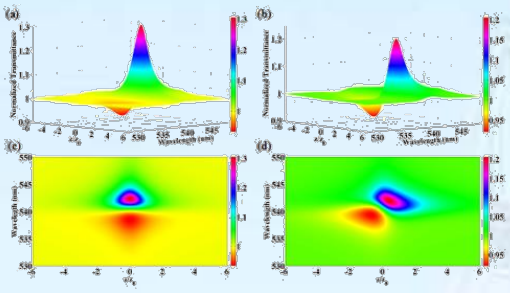

图 6 不同入射光波长下（从 530 nm 到 550 nm）从左侧入射的透射 Z 扫描曲线。(a)和(c) 开孔 Z 扫描曲线；(b)和(d)闭孔 Z 扫描曲线。

Fig. 6. The transmitted Z-scan curves from left incidence for different wavelengths from 530.0 nm to 550.0 nm. (a), (c) Open-aperture Z-scan; (b), (d) close-aperture Z-scan.

在亚波长微结构方向，我们设计了一种带有特殊结构的亚波长小孔，通过小孔内的两个缺口结构，实现了小孔的近场增强效应。与脊状孔不同，缺口孔的增强需要入射偏振垂直于缺口的连线，这是因为缺口对局域表面等离激元的激发方式不同导致的。我们尝试了两种其他形状的缺口结构来验证局域表面等离激元的作用。我们给出了缺口小孔的偏振依赖性质，并且设计了四缺口小孔结构获得了不依赖入射偏振的增强效应。最后，我们将缺口孔和脊形孔组合在一起，这种组合小孔可以结合两种小孔的优点，同时实现了更强的增强效果和超分辨能力。

We design another kind of the structured subwavelength aperture with two gaps inside, which can lead to strong near-field enhancement. Different from the ridged-aperture, the gap-aperture require an incident polarization perpendicular to the connecting line of the gaps. It is due to the different way of the localized surface plasmon excitation. We try two other gap-apertures with triangle gaps and trapezoid gaps to confirm the effect of the localized surface plasmon. We present the polarization properties of the gap-aperture and design a four-gap-aperture to obtain polarization independence enhancement. In addition, we present a combined aperture original from both the gap-aperture and the tooth-aperture, which can combine the advantages of the two original apertures and achieve strong enhancement and super resolution simultaneously.

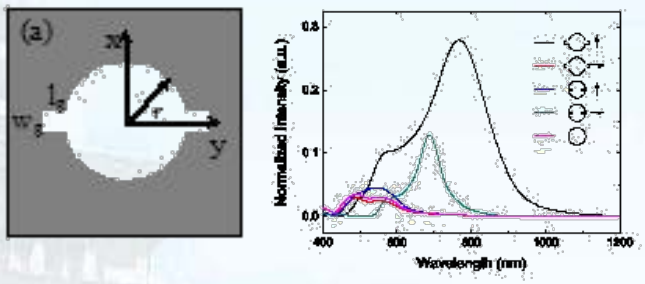

图 7（a）带有缺口结构的亚波长小孔示意图；(b) 缺口小孔、脊形小孔、参考圆孔在 x、y 偏振入射下的归一化强度谱。

Fig. 7. (a) A subwavelength aperture in silver film with two gaps. (b) Normalized intensity spectra of the gap-aperture for x- and y-polarizations as well as spectra of the tooth-aperture and a bare circleh ole for comparison.

光子学材料及先进制备技术/ Photonics Materials and Advanced Fabrication Techniques

负责人：孔勇发

本方向涉及功能光学晶体、微晶玻璃陶瓷、光子学微结构、纳米光子学、低维功能材料等方面。本年度发表论文21篇，申请发明专利2项，获得授权专利2项，在研课题经费400余万元。取得的代表性成果如下：

In this field, we mainly focused on the functional optical crystals, micro-crystal glass ceramics, photonic microstructure, nano-photonics, and nano-particulate films. 21 papers were published in international academic journals, 2 invention patents applied, and 2 patents issued. The total researching founds are more than 4 millions. This year, we obtained some important results, they are mainly shown as following:

发现掺锆铌酸锂晶体的抗紫外光折变效应，掺锆铌酸锂晶体不但对于篮、绿光具有超强的抗光折变能力，即使是紫外光区，其抗光折变能力也在 10^5 W/cm^2 以上，如图 1 所示；在 351 nm、1.8 W/cm^2 激光写入下，光致折射率的变化仅为 1.1×10^{-6}，为同成分晶体的 1/8、掺镁铌酸锂晶体的 1/20。该发现将铌酸锂晶体的高光强非线性光学应用拓展到紫外光区，其中紫外抗光损伤的照片被 Optics Letters 选为当期的封面图，并且该结果被 Nature Photonics（4, 128-129 (2010)）选作 Research Highlights。掺锆铌酸锂将铌酸锂晶体在高光强下的非线性光学应用拓展为紫外—可见—红外的透光波段，有望成为一种常用的非线性光学晶体。

The ultraviolet (UV) photorefraction of Zr doped lithium niobate (LN:Zr) was investigated. The experimental results show LN:Zr crystals have high resistance against photorefraction in UV region as well as in visible range, which can withstand UV light intensity of above 10^5 W/cm^2. According to the fitting results of erasing curves with UV and green lights, a two-center $O^{2-/-}$-defect model was suggested. Our results indicate LN:Zr is an excellent candidate for optical damage resistance from UV to visible spectrum.

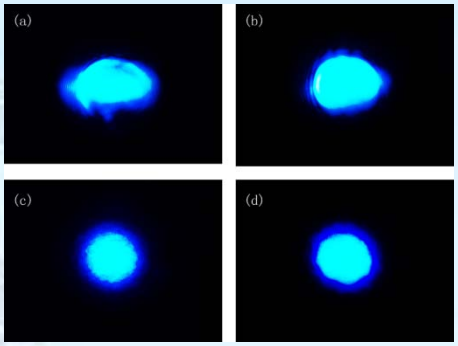

Fig. 1. Beam distortion of the transmitted UV lights (wavelength 351 nm, intensity 1.6×10^5 W/cm^2) after passing through LN crystals. (a) PLN; (b) LN:Zr$_1$; (c) LN:Zr$_2$; (d) LN:Zr$_5$

发明了掺锡铌酸锂晶体，发现其抗光损伤阈值 2.5 mol%，阈值附近分凝系数 0.98，抗光损伤阈值光强 3×10^5 W/cm^2，如图 2 所示，饱和光致折射率改变量约为 6×10^{-6}，是另一种性能优异的四价掺杂铌酸锂晶体。该结果发表于 Opt. Lett. 35, 883 (2010)，其中抗光损伤的照片被选为该期的封面图。

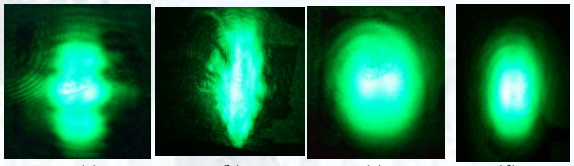

Fig. 2. Distortion of transmitted argon laser beam spots after 5 min of irradiation.

(a)-(d) for Sn1:LN, Sn2:LN, Sn2.5:LN, and Sn5:LN, respectively. The light intensities are (a) 2.5×10^2 W/cm^2, (b) 4.7×10^3 W/cm^2, (c) 4.8×10^5 W/cm^2, and (d) 5.4×10^5 W/cm^2.

Applications of lithium niobate in nonlinear optics at high light intensities are seriously hampered by optical damage. Recent investigations have shown that Hf^{4+} and Zr^{4+} ions have some advantages in suppressing optical damage of $LiNbO_3$ with respect to Mg^{2+}. Here we present Sn doped $LiNbO_3$ (Sn:LN). Experimental results indicate that

Sn:LN has similar optical damage resistance as Mg doped $LiNbO_3$, but the doping threshold of Sn is only 2.5 mol%, where its distribution coefficient is 0.98. Hence Sn^{4+} ion turns out to be another good choice for increasing optical damage resistance of $LiNbO_3$.

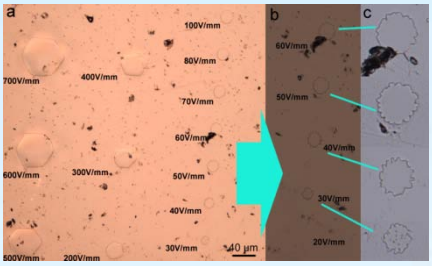

Fig. 3. Microscopic images of inverted domains with different applied electric fields at the same reverse time of 100 s and light intensity of 6.4×10^4 W/cm^2.
(a) Electric field varies from 700 to 30 V/mm; (b) amplified images for electric fields from 60 to 20 V/mm; (c) amplified images of the inverted domains of (b).

研究了近化学计量比掺镁铌酸锂晶体的光致畴反转，发现在聚焦 532 nm 激光照射下，晶体的畴反转电场可以下降 80 倍，达到 30 V/mm，如图 3 所示。该超低的畴反转电场对于实际操作既安全又方便。在该超低电场下，畴壁的钉扎作用非常明显，以至于在高电场下反转呈六角形的畴变成了齿轮状。我们进一步制作了畴直径为 4 μm 的二维畴结构。

Light-induced domain reversal of near-stoichiometric Mg-doped $LiNbO_3$ crystal was investigated with a focused 532 nm continuous laser beam. The lowest electric field applied to accomplish domain nucleation is only 30 V/mm and 1/80 of the coercive field, which is safe and convenient for us to fabricate domain structures. Under this super low applied field the pinning effect of domain wall is so obvious that the inverted domain reveals a gear shape contrary to the hexagon in a higher applied field. Then two-dimensional domain patterns with the smallest domain size of 4 μm have been fabricated.

光致畴反转是目前热门的畴反转工艺，但畴反转的深度通常仅有几十微米，限制了其在体器件方面的应用。我们利用聚焦的 532 nm 激光首先在近化学计量比掺镁铌酸锂晶体的–z 表面制作了二维畴结构，然后通过关闭激光施加合适的外场，成功地将该二维结构转录到+z 面。+z 面的畴结构可以基本贯穿晶片的厚度，并且反复转录 100 次以上畴结构没有明显的形变，但通过加光转录一个周期可将该畴结构擦除。我们进一步建立了光致畴结构的转录机理模型。

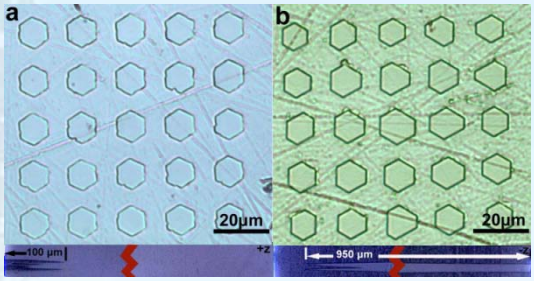

Fig. 4. Comparison between light-induced –z patterns and transcribed +z patterns. (a) Two dimensional domain patterns on –z face fabricated by a focal laser beam and electric field of 600 V/mm and a duration time of 10 s. (b) The corresponding transcribed domain patterns on +z face. The imagines beneath are etched y face profiles of domain spots.

Recently light-induced domain reversal has been developed to a promising method for domain engineering, but the depth of reversed domain is only of several tens microns, which greatly limits its practical applications. In this letter, we fabricated domain patterns on the –z face of 1.0 mol% Mg doped near-stoichiometric lithium niobate with the assistance of a focal 532 nm laser, and then succeeded to transcribe these domain patterns from the –z to the +z face by applying external field without laser illumination. The transcribed domains have much larger depths, can sustain more than 100 times of the transcription cycles without large deformation, and can be erased by one transcription cycle with illumination of 532 nm laser. Finally, a light-induced ferroelectric domain transcription model was proposed.

我们采用Pechini法研究了Er^{3+}和Yb^{3+}掺杂的$KLa(WO_4)_2$纳米晶的制备，并使用XRD和TEM对样品进行了相和形貌分析。$KLa(WO_4)_2$纳米晶的大小随着热处理温度的升高而增大。Rietved精修结果表明，双掺纳米晶的晶胞尺寸随着掺杂浓度的增大而变小。采用980nm LD泵浦，研究了$KLa(WO_4)_2$纳米晶的发光性质，实验发现其下转换1.5μm发光很弱，而上转换发光较强。Er^{3+}和Yb^{3+}双掺样品的上转换发光强度明显强于Er^{3+}单掺样品，这与Yb^{3+}在980nm处大的吸收截面和Yb^{3+}对Er^{3+}的敏化有关。在$KLa(WO_4)_2$纳米晶中，Er^{3+}的上转换发光的三个波段的强度不等，两个波段的绿光辐射明显强于红光，这与$KLa(WO_4)_2$晶格的声子能量大小有关。不同功率下的上转换发光强度对比表明，所有的上转换发光均为双光子过程。

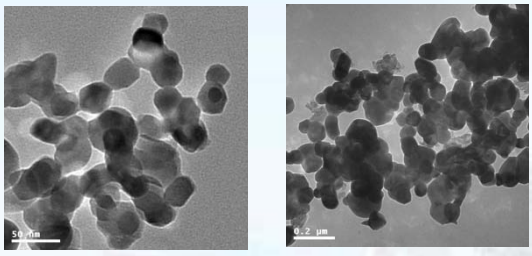

Fig. 5. TEM photographs of KLW nanocrystalline powders annealed at 500 °C (left) and 600 °C (right) for 2 h..

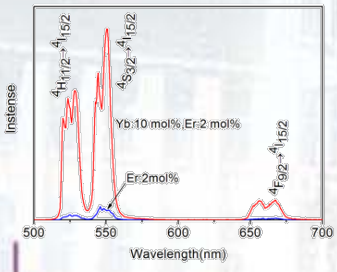

Fig. 6. UC emission spectra of 10 mol% Yb^{3+} - 2 mol% Er^{3+} codoped KLW nanoparticles (red line) and the 2 mol% Er^{3+} single doped KLW nanoparticles (blue line).

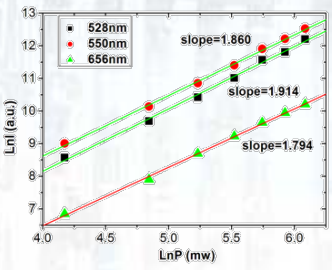

Fig. 7. Pump power dependence of all the three bands of UC emission spectra of KLW codoped with 10 mol% Yb^{3+} and 2 mol% Er^{3+}.

The luminescent nanocrystalline Yb^{3+} and Er^{3+} codoped $KLa(WO_4)_2$ has been prepared by Pechini method. X-ray diffraction and transmission electron microscope were used to study the structure of the obtained samples. The average grain size of these samples depended on the annealing temperature, increasing with the increase of the temperature. The cell parameters and the crystallite size of $KYb_xEr_{0.02}La_{0.98-x}(WO_4)_2$ nanocrystalline decreased with the increase of x value. Luminescence studies showed that the intensity of upconversion emission of the Yb^{3+} and Er^{3+} codoped samples was much stronger than that of the Er^{3+} single doped samples (pumped by 980 nm LD). The upconversion emission mechanisms suggested that all the three bands of upconversion emissions were two-photon process.

对硼酸盐化合物$NaSrB_5O_9$和$Na_3SrB_5O_{10}$进行Dy^{3+}离子掺杂，研究其光致发光性质。并通过Rietveld精修分析其掺杂后的结构变化。研究中发现，两个五硼酸盐掺镝样品可获得有效的黄光发射，Dy^{3+}占据Sr^{2+}的晶格位置。对以$KSr_4(BO_3)_3$为基质的多种稀土离子掺杂样品的光致发光性质进行了研究，获得了色纯度和饱和度较好的红色和蓝色荧光粉。通过对比多种晶体结构发现，K^+在晶体结构由有心向无心的转变过程中起重要作用。在双折射晶体$NaMgBO_3$的基础上，设计合成了非线性旋光晶体$KMgBO_3$。该化合物具有包括深紫外在内的较宽透光范围；粉末样品的圆二色谱显示了可重复的康顿效应，该信号尚有待证明为取材不均或非对称合成导致。

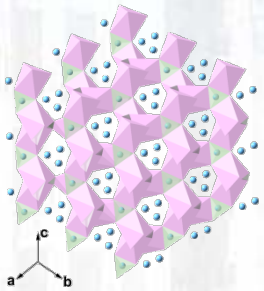

Fig. 8. Structure projection of $KMgBO_3$ viewed along [111]

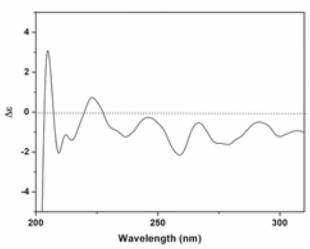

Fig. 9. Circular dichroism spectrum of polycrystalline $KMgBO_3$

The work continued with the work of last year, concentrated on the investigation of new borate luminescence materials and structural study. Photoluminescence of Dy^{3+} doped

$NaSrB_5O_9$ and $Na_3SrB_5O_{10}$ were investigated, and the structures of the doped samples were refined by Rietveld method. It was found that the Dy^{3+} doped pentaborates had effective yellow emission, and Dy^{3+} occupied the Sr^{2+} positions. The photoluminescence of various rare earth ionic doped $KSr_4(BO_3)_3$ were investigated, and effective red and blue emissions with good color purity and saturation were detected. After the structural comparison of many crystals, it was found that K^+ plays a key role in the structure transformation from centrosymmetry to non-centrosymmetry. Then a nonlinear chiral borate $KMgBO_3$ was synthesized based on the structure of birefringent crystal $NaMgBO_3$. The new compound was found to have a wide transparency, including the vacuum ultraviolet region. The circular dichroism spectrum collected from a polycrystalline sample showed several weak peaks of Cotton effects, which can be easily repeated. It may come from the random inequality of enantiomers in the polycrystalline sample or occasionally asymmetric synthesis, which confirm the optical activity of $KMgBO_3$.

采用溶胶-凝胶法，制备出Sn/N双相掺杂TiO_2催化剂；并通过X射线衍射，X射线光电谱，紫外可见吸收谱，荧光谱等多种表征手段对其进行分析；Sn元素通过取代形式掺入TiO_2晶格，而N元素则作为表面物种存在。Sn的掺杂能级与N的表面态能级均在TiO_2带隙内分别靠近导带和价带。与纯TiO_2和单掺N的TiO_2催化剂相比，Sn/N双掺可以增加TiO_2的可见光吸收，抑制光生载流子的复合，从而使双掺的TiO_2催化剂的紫外和可见光活性有效提高。实验证明两种离子同时掺杂是提高TiO_2光催化活性的有效方法。

Tin and nitrogen co-doped titania has been prepared by hydrolysis precipitation method, which has been studied by X-ray diffraction, X-ray photoelectron spectroscopy, diffuse reflectance UV-vis absorption spectra, and photoluminescence. The surface area has been determined by using the BET method. Tin is incorporated into TiO_2 crystal lattice in substitutional mode, while nitrogen is present as surface species. The resultant energy levels of tin doping and nitrogen surface states are located inside the bandgap, which are close to the conduction and valence bands, respectively. Hence, co-doping of tin and nitrogen can greatly enhance the absorption in visible light region and inhibit the recombination of photogenerated charge carries, leading to a higher photocatalytic activity for the co-doped catalyst than pure TiO_2 and solely doped TiO_2 with nitrogen or tin for 15 degradation of 4-chlorophenol under both visible and UV-light irradiation. This indicates that codoping simultaneously with two foreign elements is a feasible way to improve the photocatalytic activity of TiO_2.

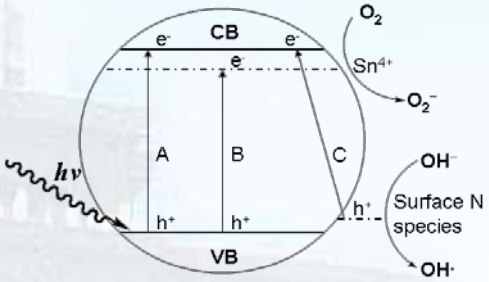

Fig. 10. Scheme of photocatalytic mechanism of nitrogen and tin doubly doped TiO_2

采用溶胶凝胶法，将Sn掺杂的金红石TiO_2(R-TiO_2-Sn)与N掺杂的锐钛矿TiO_2(A-TiO_2-N)复合，制备出具有良好光电性能的新型结构复合膜催化剂。该催化剂的可见、紫外光催化活性远高于R-TiO_2-Sn或A-TiO_2-N单一薄膜，其原因在于该催化剂异质结的形成、光生载流子的增加和掺杂能级的引入。该研究成果为开发太阳能电池，光催化剂，光合成等光电功能材料提供了很好的范例。

A new type of composite film (heterostructure) with optoelectronic properties have been prepared by coupling

Sn-doped rutile TiO_2 (R-TiO_2-Sn) and N-doped anatase TiO_2 (A-TiO_2-N) with use of a sol-gel method. Under visible and UV light irradiation, it exhibits a higher photocatalytic activity than both R-TiO_2-Sn and A-TiO_2-N films due to the formation of a heterojunction at the interface, as well as the increase of total amount of photogenerated charge carriers and introduction of doping states. Our results offer a paradigm for developing optoelectronic functional materials that can be used in many fields, such as solar cells, photocatalysis, and photosynthesis.

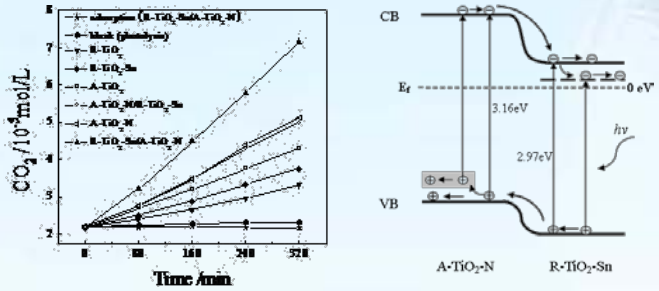

Fig 11. The heterostructure and photocatalytic activity of R-TiO_2-Sn/A-TiO_2-N sample.

采用离子束溅射技术制备出TiO_2/ITO、Zn^{2+} 掺杂的 TiO_2(TiO_2-Zn)/ITO 和 TiO_2/ZnO/ITO 薄膜，采用表面敏化技术和旋转涂膜法，制备出(1,10-邻菲咯啉)$_2$-2-(2-吡啶基)苯咪唑钌混配配合物(Rup_2P)表面敏化 TiO_2 基复合薄膜 Rup_2P/TiO_2/ITO 、Rup_2P/TiO_2-Zn/ITO和Rup_2P/TiO_2/ZnO/ITO。表面光电压谱(SPS)结果发现：敏化后的TiO_2基薄膜在可见区(400-600 nm)产生SPS响应；TiO_2基薄膜的能带结构不同，其在400-600nm和350nm处的SPS响应的峰高比不同.利用电场诱导表面光电压谱(EFISPS)，测定TiO_2基薄膜和表面敏化TiO_2基复合薄膜各种物理参数,并确定其能带结构。分析可知，表面敏化TiO_2基复合薄膜在400-600 nm的SPS响应峰主要源于Rup_2P分子的中心离子Ru4*d*能级到配体1,10-邻菲咯啉π^*_1和2-(2-吡啶基)苯咪唑π^*_2能级的跃迁；TiO_2中Zn^{2+}掺杂能级有利于Ru4*d*能级到配体π^*_1和π^*_2跃迁的光生电子向TiO_2-Zn导带的注入；TiO_2/ZnO异质结构有利于光生电子向ITO表面的转移，从而导致可见光(400-600nm)SPS响应增强以及光电转换效率的提高。

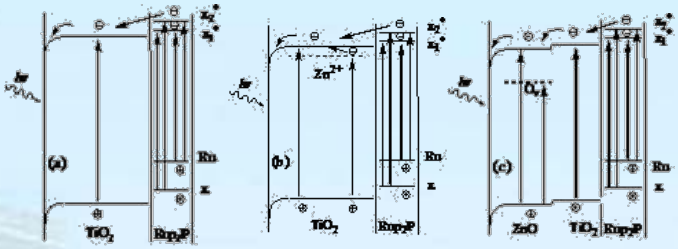

Fig. 12. Schematic representation for energy band levels of Rup_2P/TiO_2/ITO(a), Rup_2P/TiO_2-Zn/ITO(b) and Rup_2P/TiO_2/ZnO/ITO(c) film.

TiO_2/ITO, TiO_2-Zn/ITO and TiO_2/ZnO/ITO films were prepared by ion-beam sputtering, and then furthersurface-sensitized with the $Ru(phen)_2$(PIBH) complex (Rup_2P) of Rup_2P/TiO_2/ITO, Rup_2P/TiO_2-Zn/ITO, and Rup_2P/TiO_2/ZnO/ITO by the spin-coating method. Surface photovoltage spectra (SPS) of the films revealed that SPS responses were present at 400-600nm after surface-sensitization and the SPS intensity ratios between the peaks at 400-600 nm and 350nm were different because of the different energy band structures in the TiO_2-based films. The physical parameters and energy band structures of TiO_2-based and Rup_2P modified TiO_2-based films were determined by electric field induced surface photovoltage spectroscopy (EFISPS). We found that the 400-600 nm SPS peaks of the Rup_2P modified films came from the Ru 4*d* to phenπ^*_1 and PIBHπ^*_2 electron transitions. The Zn^{2+} doping level in TiO_2-Zn benefits the injection of photogenerated electrons from the ligand levels to the conduction band. The TiO_2/ZnO heterostructure favors electron transfer to the surface of ITO, which can enhance the SPS response in the visible light region (400-600 nm) as well as the photoelectron transformation efficiency.

以ZnO纳米柱阵列为模板,采用溶胶-凝

胶法，制备出 TiO_2/ZnO 和 N 掺杂 TiO_2/ZnO 复合纳米管阵列。SEM、UV-Vis、and XPS 表征结果表明, 两种阵列的纳米管均为六角形结构(直径约为 100nm, 壁厚约为 20nm)。在 N-TiO_2/ZnO 样品中, 掺入的 N 离子主要是以 N-Ox、N-C 和 N-N 物种的形式化学吸附在纳米管表面，仅有少量的 N 离子以取代式掺杂的方式占据 TiO_2 晶格 O 的位置。N 物种的取代式掺杂导致带隙的窄化，增强了纳米管阵列光的吸收效率, 促进了光生载流子的分离，因此，与 TiO_2/ZnO 复合纳米管阵列相比，N-TiO_2/ZnO 复合纳米管阵列光催化活性得到了提高。

TiO_2/ZnO and N-doped TiO_2/ZnO composite nanotube arrays were synthesized by sol-gel method using ZnO nanorod arrays as template. SEM, UV-Vis, and XPS were used to characterize the samples. The nanotubes showed a uniform hexagonal shape. The diameter and wall thickness of the nanotubes were about 100 nm and 20 nm, respectively. Some N dopants were substitutionally doped into the TiO_2/ZnO lattice, while the majorities, such as N-O_x, N-C and N-N species were chemically absorbed on the surface of TiO_2/ZnO composite nanotubes. The dopant-induced narrow of the band gap is due to the doping of N ions in the TiO_2 lattices，which enhance the visible-light response and promote the separation of photogenerated carriers. Compared with the TiO_2/ZnO composite nanotube arrays, N-TiO_2/ZnO composite nanotube arrays exhibited a higher photocatalytic activity.

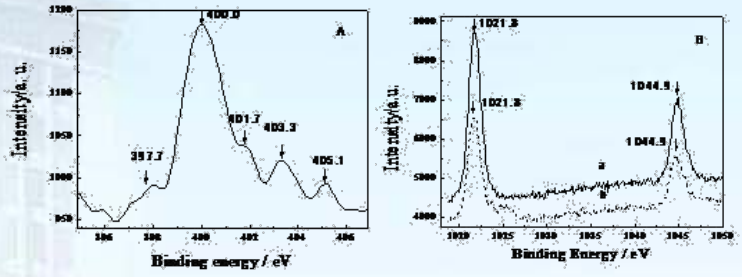

Fig. 13. N 1s XPS spectra of N-TiO_2/ZnO (b) composite nanotube arrays(A). Zn_{2p} XPS spectra of the TiO_2/ZnO(a) and N-TiO_2/ZnO (b) composite nanotube arrays (B).

弱光非线性及量子相干光学/ Weak Light Nonlinear Optics and Quantum Coherent Optics

负责人：许京军

本方向主要开展纳微结构制备及其光学性质、非线性光调控与应用、量子非线性光学、飞秒超快探测技术以及光折变材料与新效应等方面的研究。2010 年度本方向共发表论文 33 篇，主要取得如下进展：

The main research topics in this group are fabrication and optic properties of nano/micro-structure, nonlinear optical manipulation and its applications, quantum nonlinear optics, ultrafast detection and analysis by using fs technology and photorefractive materials and nonlinear optics. We published 33 papers in various academic journals. The main research progresses in 2010 are as follows.

我们研究了两维脊背型光子学晶格中的线性离散衍射性质，结果表明，随着晶格折射率调制度的增大，高阶带隙依次打开，并且传输带变得越来越平坦（如图 1(a)）。因此，无论是格点激发还是非格点激发，光束在晶格中传输时其衍射效应将受到抑制。尤其是当折射率调制度足够大时（如正方型晶格为 0.01），光束在晶格中传输时出现线性横向局域现象（如图 1(b)、(c)）。此时，光束在晶格中传输时只能激发若干个具有平坦线形的传输带模式，这些传输模式的横向扩展速度接近于 0。该线性横向局域效应在光控光传输和光学信息处理方面有潜在的应用。

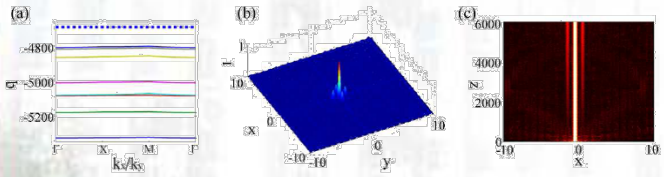

图 1. 折射率调制度为 0.0224 的正方型光子学晶格的带隙图(a)，格点激发条件下光波传输 6.6cm 后在出射面上的光强分布(b)和光波在晶格中的传输轨迹(c)。/Fig. 1 The band structure diagram of a square lattice with a refractive index modulation depth of 0.0224 (a), the output intensity distribution after a 6.6-cm propagation length with on-site excitation (b), and the propagation dynamics of light in the lattice (c).

We study the linear discrete diffraction characteristics of light in two dimensional backbone lattices. It is found that, as the refractive index modulation depth of the backbone lattice increases, high-order band gaps become open and broad in sequence, and the allowed band curves of the Floquet-Bloch modes become flat gradually (see Fig. 1(a)). As a result, the diffraction pattern at the exit face converges gradually for both the on-site and off-site excitation cases. Particularly, when the refractive index modulation depth of the backbone lattice is high enough, for example, on the order of 0.01 for a square lattice, the light wave propagating in the backbone lattice will be localized in transverse dimension for both the on-site and off-site excitation cases (Fig. 1(b), (c)). This is because only the first several allowed bands with nearly flat band curves are excited in the lattice, and the transverse expansion velocities of the Floquet-Bloch modes in these flat allowed bands approach to zero. Such a linear transverse localization of light may have potential applications in navigating light propagation dynamics and optical signal processing.

在光子晶格中的缺陷带隙导光方面，我们实验上观察到了高阶的偶极缺陷模式和涡旋缺陷模式（如图 2）。在此项工作中我们成功的制备了缺陷深度可调的二维光子晶格，该光子晶格是由两个周期完全一样的晶格光叠加而成，其中一个为完整的晶格光，另一个是有单格点的光强为零的晶格光，只要合理的调节这两个晶格的光强比就可以使得负缺陷深度在 0 与 1 之间变化。然后研究了一阶涡旋光在这种缺陷深度可调的负缺陷光子晶格中的线性传播行为，发现只有当负缺陷的深度为一定值的时候，涡旋缺陷模式才能够被传导，并且该涡旋缺陷模式的

拖尾也具有由各向异性导致的多涡旋的结构，这种高阶涡旋缺陷模式可以看出是由偶极缺陷模式叠加而成。

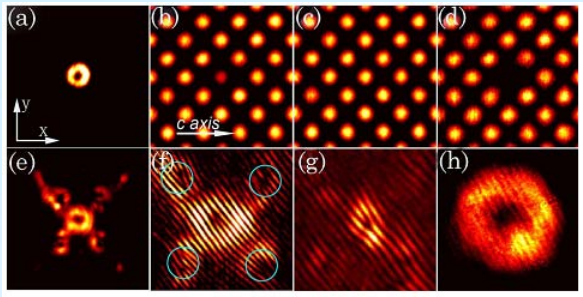

图 2　一阶涡旋光在缺陷光子晶格中传播的实验结果(a)入射涡旋光 （b-d）分别为具有非零光强缺陷，没有缺陷和具有零光强缺陷的晶格光 （e-f）线性出射涡旋光及其干涉图 （g）在完整光子晶格中的出射干涉图 （h）无光子晶格的出射图。/Fig.2. Experimental results of bandgap guidance of a vortex beam in a tunable negative defect.(a)vortex at input.(b)-(d)induced lattices with non-zero intensity defect, no defect and zero-intensity defect,(e)(f)vortex output from the defect in (b) and its interferogram.the circles in (f)mark the location of the vortex pairs.(g)interferogram when the vortex is excited at non defect site.(h)vortex diffraction output when lattice is absent.

In this work, we experimentally observed band gap guidance of higher order dipole defect modes(DMs) and vortex defect modes in photonic lattices with a negative defect (see Fig. 2). Firstly, we succeeded in fabricating 2D photonic lattices with a tunable negative defect, such lattices are obtained by superposition of two lattices with the same period, one is a uniform periodic intensity pattern and the other has a zero-intensity defect site on otherwise uniform periodic pattern. By fine tuning the ratio of the two lattices, the defect strength can be varying from zero to one, and then we send a singly charged vortex beam to the defect site to study the linear propagation behavior. We find that the donut-shaped vortex beams can be guided in the lower-index defect, provided that the defect strength is set at an appropriate level. Such vortex DMs have fine features in the “tails” associated with the lattice anisotropy and can be considered as superposition of dipole DMs.

我们研究了简单一维晶格和超晶格的界面处（由图 3（a）的虚线标记）的光传播的非线性动力学过程。通过理论计算，利用自聚焦非线性我们从数值上得到了三种不同的界面孤子，它们同时受到简单晶格和超晶格的调制影响，因此可能同时位于两种晶格的半无限带（如图 3（b）中的 C 类孤子），也有可能位于两种晶格不同的禁带中（如图 3（b）中的 D 和 E 类孤子），正是由于这些丰富的物理特性，它们在相位结构和空间分布上表现出巨大的差异（如图 3（c-e）），特别的是，我们发现了以前从没有注意到的类偶极界面带隙孤子（如图 3（e））。实验上通过在 i，j，k 位置（如图 3（a））采取合适的入射光作为激发条件，经过自聚焦非线性演化之后，我们成功实现了相应的界面孤子。

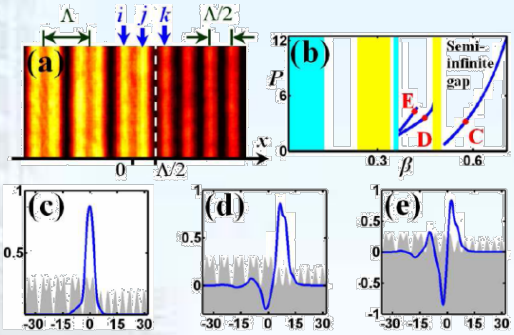

图 3：（a）普通晶格（虚线右侧）和超晶格（虚线左侧）形成的界面；（b）普通晶格（蓝色）和超晶格（黄色）的带隙结构以及三种不同界面孤子的存在曲线；（c-e）三种不同的界面孤子。/Fig. 3: (a) the interface between a simple (right) and super lattice(left); (b) the band gap structures of simple (blue) and super lattice (yellow) and the existence curve of the three types of the interface solitons; (c-e) the typical profiles of the three interface solitons.

We investigated the nonlinear beam dynamics at the interface (marked by the dashed line in Fig. 3(a)) between a simple and a super lattice light-induced in photorefractive crystal. Three different types of interface solitons are obtained numerically with self-focusing nonlinearity, including the dipole-like interface gap soliton [Fig. 3(e)] which has never been reported before to our knowledge. They either localize in the semi-infinite band gaps of both lattices [like

the solitons of “C” family in Fig. 3(b)], or in different band gaps of the lattices [like the solitons of “D” or “E” type in Fig. 3(b)], due to the simultaneous influence of both the lattices, so these solitons at this interface have very big difference in the profiles and phase structures [Figs. 3(c-e)]. Depending on the excitation conditions at the positions i, j and k near the interface [Fig. 3(a)], we observed experimentally the three types of solitons under a self-focusing nonlinearity.

我们研究了一阶涡旋光在二维光子晶格与连续介质界面处的非线性自陷传播特性，结果表明：在适当的自聚焦非线性下，在四格点激发时，一阶涡旋光能够自陷形成稳定的表面离散涡旋孤子，而在单格点激发下，能在第一个布拉格反射禁带中形成表面涡旋带隙孤子，我们的理论分析表明这种带隙表面涡旋孤子是不稳定的（如图 4）。

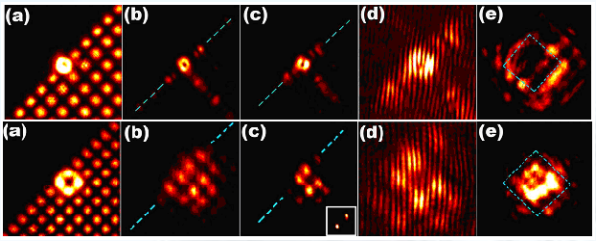

图 4. 单格点激发（第一排）与四格点激发（第二排）的表面涡旋孤子实验结果。(a）入射涡旋光与晶格光，(b）线性出射，(c）非线性出射，(d）非线性出射干涉图，(e）非线性频谱图。 /Fig. 4 Experimental results of vortex self-trapping under single site(top) and four-site (bottom) surface excitation (a)lattice beam superimposed with the vortex beam,(b)linear and (c)nonlinear output of the vortex beam, where the blue dashed line indicates the surface location,(d)zoom-in interferogram of (c) with an inclined plane wave and (e)k-space spectrum of (c).

We demonstrate self-trapping of singly-charged vortices at the surface of an optically induced two-dimensional photonic lattice. Under appropriate conditions of self-focusing nonlinearity, a singly-charged vortex beam can self-trap into a stable semi-infinite gap surface vortex soliton through a four-site excitation. However, a single-site excitation leads to a quasi-localized state in the first photonic gap, and our theoretical analysis illustrates that such a bandgap surface vortex soliton is always unstable (see Fig. 4).

离子型光子晶格具有交错的正与负的晶格势，与固体物理中的离子晶体类似。我们在离子型的光子晶格中研究了不完整的布里渊区谱与可调控的布拉格反射（如图 5）。利用改进的几何结构因子来描述非布拉菲格子的光子晶格中布拉格反射，我们发现晶格重构导致的非完整的布里渊区谱是由于选择性的带隙结构的闭合造成的。并且我们实验上在离子型的光子晶格中观察到了这种非完整的布里渊区谱与布拉格反射的抑制。

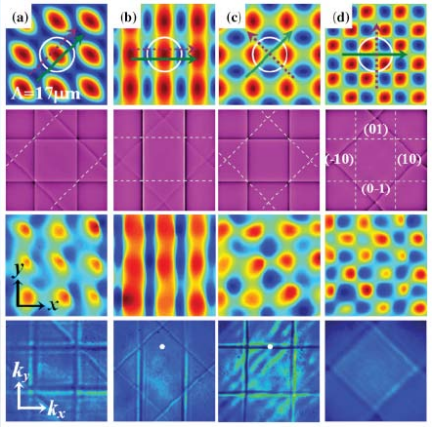

图 5: 光子晶格结构与对应的布里渊区谱的数值模拟（上两排）与实验结果（下两排）；第一排与第三排是折射率分布，第二排与第四排是对应的布里渊区谱图。外加电场为（a）-(d) 分别是 2.4, 3.4, 3.2, and 8.0 kV/cm。/Fig.5 Numerical (upper two rows) and experimental (bottom two rows) results of optically induced lattice structures and corresponding Brillouin zone spectra. The first and third rows show the refractive index distributions, and second and fourth rows are the corresponding BZ spectra. Solid and dashed arrows in first row represent the directions of c axis and bias field, and the white circle corresponds to an intensity spot of the lattice-inducing beam. The bias field for (a)–(d) is 2.4, 3.4, 3.2, and 8.0 kV/cm, respectively. Dashed lines in the second row indicate the missing Bragg-reflection lines in the BZs of induced lattices.

We demonstrate ionic-type photonic lattices consisting of alternating positive and negative lattice potentials akin to those of ionic crystals in solids. A modified geometrical structure factor is developed for

describing Bragg scattering in these non-Bravais photonic lattices. We show that lattice reconfiguration leads to incomplete Brillouin zone spectra due to selective band-gap closures. Experimentally, incomplete Brillouin zone spectra and associated Bragg-reflection suppression are observed in such ionic-type lattices optically induced in a bulk nonlinear crystal (see Fig. 5).

我们在二维的离子型光子晶格中实现了，不同高对称点之间的布洛波模式的转变，正常衍射与反常衍射的控制，以及正常折射与反常折射的控制（如图 6），所有的这些调控都是在相同的激发条件下，仅仅是通过改变外加偏压条件使得晶格结构的重构来实现的。

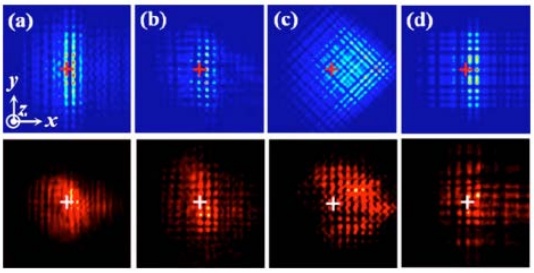

图 6 由晶格重构导致的正常衍射与反常衍射的转变。（a）-（d）在相同的激发条件下由于不同的晶格结构导致的出射衍射输出的数值模拟（第一排）与实验结果（第二排）。十字叉表示入射光的中心。/Fig .6 Demonstration of 2D normal and anomalous diffraction by lattice reconfiguration. (a)–(d) Numerical (top) and experimental (bottom) results of output diffraction patterns of the same probe beam. The crosses indicate the center of the input beam.

We demonstrate controlled excitation of Bloch modes and manipulation of diffraction and refraction in optically induced two-dimensional photonic lattices. Solely by adjusting the bias condition, the lattice structures can be reconfigured at ease, enabling the observation of transition between Bloch modes associated with different high-symmetry points of a photonic band, and interplay between normal and anomalous diffraction as well as positive and negative refraction under identical excitation condition (see Fig. 6).

我们研究了三维光子晶格中的线性波动力学过程。通过数值模拟和实验我们发现三维光子晶格的纵向折射率调制度对光束的能量流动有很大的影响。在某些纵向折射率调制度的三维光子晶格中，光束在演化时不会发生衍射（图7（a2）和（b2）以及（a4）），称之为相干破坏隧穿，而其它调制情况下衍射仍然存在（图7（a1），（b1），（a3）和（b3））。利用相干破坏隧穿效应，我们成功地实现了三维光子晶格中的图像无衍射传输（图7（c）和（d））。另外通过控制纵向折射率调制度，我们很容易将三维光子晶格中的耦合常数改变为负，进而实现了探测光束的反常衍射（图7（a）和（b））和反常折射（图7（c）和（d）），实验结果和数值模拟取得了一致的结果。

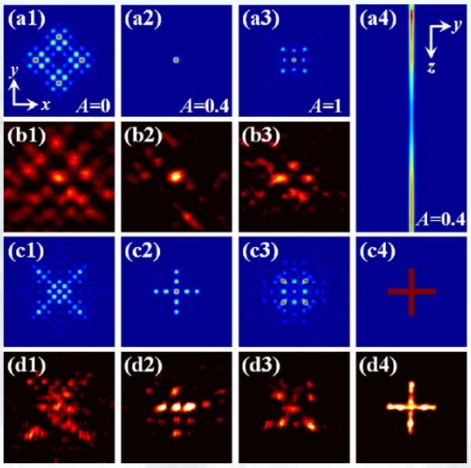

图7：（a）数值模拟和（b）实验结果给出了不同纵向折射率调制度下的光束演化；（c）数值模拟和（d）实验结果给出了三维光子晶格中的图像传输，1到3分别对于A=0, 0.4和1的出射情况，4对应入射的图像。/ Fig. 7: (a), (c) Numerical and (b), (d) experimental demonstrations of (a), (b) CDT and (c), (d) image transmission. (a1)–(a3) and (b1)–(b3) show output transverse patterns of a focused Gaussian probe beam at different modulations, and (a4) shows a side view of the probe beam propagating along z under the CDT condition A=0.4. (c1)–(c3) and (d1)–(d3) show corresponding output patterns of a “+” shape [input shown in (c4) and (d4)] after propagating through the 3D lattice.

We investigate the linear beam dynamics in three dimensional (3D) optical lattices. We

find both numerically and experimentally that the longitudinal index modulation of the 3D lattices play an important part in the energy flow of a probe beam. With some special longitudinal index modulations, the probe beam doesn't diffract during propagation [Figs. 7(a2), (b2) and (a4)], which is called coherent destruction of tunneling (CDT); while with other index modulations, diffraction of the probe beam in the lattices also exist [Figs. 7(a1), (b1), (a3) and (b3)]. Image transmission based on CDT has been proposed and successfully demonstrated [Figs. 7(c) and (d)]. Additionally, the couple constant of the lattice can be easily switched to negative by tuning the longitudinal index modulations, and then anomalous diffraction [Figs. 7(a) and (b)] and negative refraction [Figs. 7(c) and (d)] of the probe beam have been observed. Our experimental results agree well with the numerical simulations.

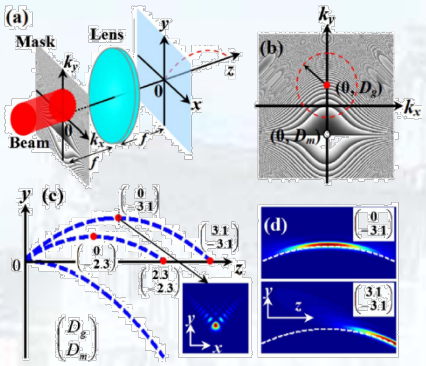

图 8：（a）实验配置；（b）相位模板和高斯光的平移示意，平移量为 D_g 和 D_m；（c，d）数值模拟实现不同 D_g 和 D_m 对应的光束轨迹及光强最强位置。/ Fig. 8: (a) experimental setup; (b) schematical shifting of the phase mask and the Gaussian beam, whose distance of translating are respectively D_m and D_g; (c, d) numerically optimal control of the trajectory and peak intensity of Airy beams with different D_m and D_g.

我们实现了二维Airy光束抛物线运动的优化控制，不仅能很容易地控制光束轨迹的射高和射程，而且能方便地将光强最强入射到预设的目标上。在如图8（a）的实验配置中，仅仅通过平移相位模板和高斯光（如图8（b）中的平移量Dg和Dm），我们理论上实现了图8（c）和（d）中轨迹和光强最强的优化控制。实验中如果只向下移动相位模板，Airy光束的轨迹会发生变化，伴随着光强最强出现在最高点，而且模板平移越大预示轨迹射程越远，如图9（b）和（d）；在此基础上，向上平移高斯光且保证|Dg|=|Dm|，这时 Airy光束的轨迹不会发生变化，但是光强最强会出现在轨迹落点位置，如图9（c）和（e）。如果让相位模板和高斯光在二维上平移，这种方法的潜在应用是能将偏离靶点的光束以最强的光强重新入射到靶点位置。

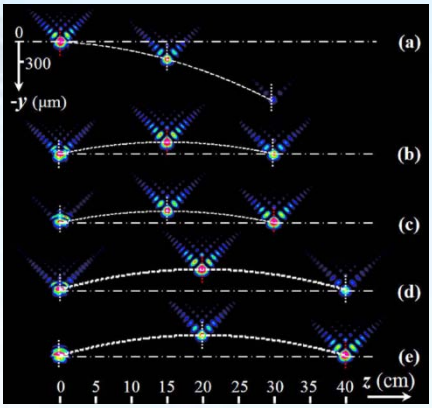

图 9：（a）正常 Airy 光束的传播；（b，d）向下平移相位模板后 Airy 光束的传播；（c，e）在（b，d）的操作基础上，向上平移高斯光后（平移量等于模板的平移量）Airy 光束的传播。/ Fig. 9: (a) propagation of normal Airy beams; (b, d) propagation of Airy beams generated by shifting only phase mask downwards; (c, e) propagation of Airy beams generated by further shifting the Gaussian beam upwards and keeping $|D_g|=|D_m|$.

We demonstrated the optimal control of the projective motion of two dimensional Airy beams. We have shown that the range and height of the beam trajectories can be controlled with ease, and the peak beam intensity can be easily delivered and repositioned to a given target. Fig. 8 shows that only shifting the phase mask and the Gaussian beam, whose distance of translating are respectively Dm and Dg in Fig. 8(b), can control optimally the trajectory as well as the position of the peak intensity numerically. In experiment, if only phase mask is shifted downwards, the trajectory of Airy beams will

be changed and the peak intensity always appears at the maximum height [Figs. 9(b) and (d)]. If we further shift Gaussian beam upwards and keep |Dg|=|Dm|, the trajectory will not be changed, but the peak intensity will appear at maximum range [Figs. 9(c) and (e)]. A potential application of this method through shifting the mask and the Gaussian two-dimensionally is that a beam deflected from a desired target can be repositioned with peak intensity.

我们研究了Airy光束从非线性介质（偏压下的光折变晶体）到线性介质（空气）中的演化过程。我们发现Airy光束在自散焦非线性下传播时会表现出反常衍射的特性，而且在接下来的线性传输过程中还能继续保持它的形态基本不变（图10（d1）和（d2）），通过严格的理论分析，我们发现Airy光束在自散焦非线性下表现出的异常的特性直接依赖于由它自身诱导形成的啁啾光子晶格的衍射调制，导致它的空间频谱不均匀地整形为四部分（图10（d3））。但是在自聚焦非线性下，Airy光束在传输过程中不仅不能保持它自身的形态不变（图10（c1）），而且在接下来的线性演化中其整体的横向加速度（图10（c2））和参考的Airy光束（图10（b2），未施加非线性）相比有所减小，这也可以从它的频谱得到反映，其大部分能量集中在了布里渊区的中心附近（图10（c3））。

We study the behavior of Airy beams propagating from a nonlinear medium (a biased photorefractive crystal) to a linear medium (air). We show that an Airy beam initially driven by a self-defocusing nonlinearity experiences anomalous diffraction and can maintain its shape in subsequent linear propagation [Figs. 10(d1) and (d2)], which can be numerically explained with the modulations (of the chirped lattice induced by the Airy beam itself) reshaping the spectra into four parts inhomogeneously [Fig. 10(d3)], but its intensity pattern and acceleration cannot persist when driven by a self-focusing nonlinearity [Fig. 10(c)], which can also be demonstrated by its spectrum that mostly localize in the area near the center of the Fourier space [Fig. 10(c3)].

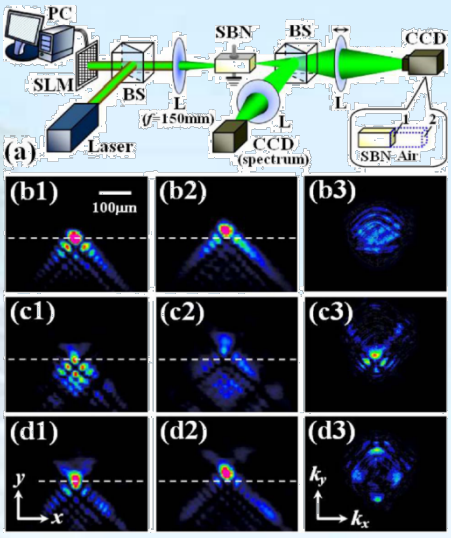

图10：（a）实验配置；（b-d）第一列到第三列分别为晶体中传播1cm和接下来在空气中传播1cm后的出射以及空间频谱分布；第一行到第三行分别为线性，自聚焦和自散焦非线性的情况。/Fig. 10: (a) Schematic of experimental setup. SLM, spatial light modulator; SBN, strontium–barium–niobate crystal; PC, personal computer; BS, beam splitter; L, Fourier transform lens. (b)–(d) Output intensity patterns of an Airy beam after 1 cm through crystal (first column) plus another 1 cm through air (second column) when (b) no nonlinearity, (c) self-focusing nonlinearity, and (d) self-defocusing nonlinearity are present. White dashed line marks the “head” position of the Airy beam at crystal output. The third column shows Fourier spectra of the Airy beam corresponding to the first column.

我们通过摩尔条纹技术在空间相位调制器上编码产生多个扇叶的旋转光束，并且利用光折变晶体中的自聚焦非线性实现这些旋转光束的自陷。实验上我们不仅可以方便地控制旋转光束扇叶的数量和旋转方向（如图 11 中顺时针旋转的两扇叶和三扇叶光束以及图 12（b）中逆时针旋转的单扇叶光束），而且能不依赖任何机械运动或相位相干控制光束的转速。尽管这种旋转光束线性传播时会发生衍射（图 12（c）），但是利用光折变晶体中的非瞬时自聚焦非线性，可以让它在演化过程中由于受到它时间上

的平均光场诱导产生的波导而发生自陷（图12（d）），并且保持其旋转特性不变。我们期望多扇叶旋转光束的产生和非线性控制能应用于光学和生物微型机械中。

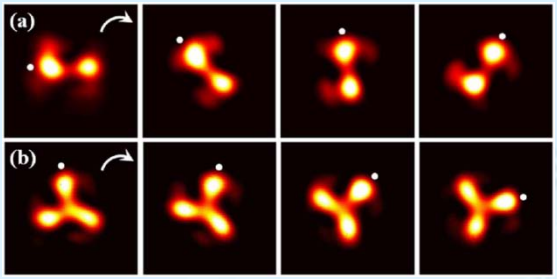

图 11：顺时针旋转的两扇叶（a）和三扇叶（b）光束。

Fig. 11: clockwise rotating two (a) and three (b) blades beams.

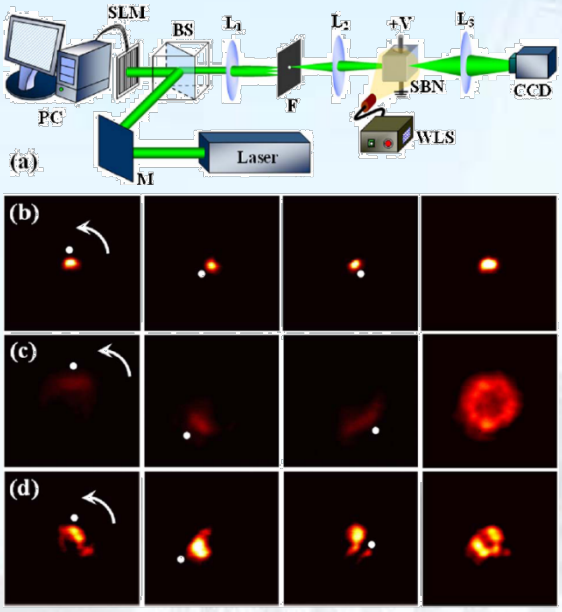

图 12：（a）实验配置；（b-d）分别给出了入射和衍射及自陷的旋转光束，其中最后一列是各自的时间平均光强分布。/Fig. 12: (a) Experimental setup. SLM, spatial light modulator; BS, beam splitter; F, spatial filter; WLS, white-light source. (b) Single-blade propeller generated in experiment. Four panels are snapshots of three instantaneous patterns plus the time-averaged intensity pattern at input; (c) and (d) depict output patterns after (c) linear diffra ction and (d) nonlinear self-trapping through the crystal.

We generate multiple-blades rotating beams by moiré technique with spatial light modulator (SLM), and demonstrate self-trapping of such rotating beams with noninstantaneous self-focusing nonlinearity in a photorefractive crystal. Experimentally the number and rotating direction of these rotating beams can be control at ease [clockwise rotating 2 and 3 blades beams in Fig. 11 and anti-clockwise rotating single blade beam in Fig. 12(b)], and the rotating speed can be controlled independent of any mechanic movement or phase-sensitive interference. During linear propagation, these beams will suffer diffraction [Fig. 12(c)], however, they can be self-trapped [Fig. 12(d)] due to the waveguide induced by the time-average light intensity with non-instantaneous self-focusing nonlinearity while keeping the rotating property. We expect that the generation and self-trapping of multiple-blades rotating beams may find applications in optical and biological micromachines.

飞秒激光脉冲在光折变波导阵列中的非线性光谱展宽 [Optics Express, **18**, 10112 (2010)]。我们从实验和理论上研究了光折变波导阵列（光子晶格）中，飞秒激光脉冲由于自位相调制作用产生的展宽过程和展宽程度（图 13、14）。光子晶格中的自位相调制的阈值比普通体材料中的阈值要高两倍左右。对应于材料的本身的自相位调制阈值（我们称其为第一阈值），我们定义这种由结构引起的阈值为第二阈值。它大大影响了飞秒激光脉冲的展宽过程和展宽量。光子晶格的耦合长度和第一阈值与入射峰值光强的比是两个主要影响这个过程的参量。这个工作为在光子晶格中用飞秒激光脉冲实现超快光开关提供了相应的参考。

Nonlinear spectrum broadening of femtosecond laser pulses in photorefractive waveguide arrays. In photorefractive waveguide arrays, the process and extent of spectral broadening of femtosecond laser pulse caused by self-phase modulation are studied theoretically and experimentally (see Figs. 13, 14). The threshold of self-phase modulation is more than two times larger than the common threshold in a bulk sample, which affects the extent of spectral broadening

dramatically. Comparing to the threshold in bulk material, we defined the threshold induced by the structure as the second threshold. The coupling length and the ratio between the common threshold and the input peak intensity of the femtosecond laser pulse are the two key parameters dominating these phenomena. This work is useful to achieve ultrafast switch in photonics lattice using femtosecond laser pulse.

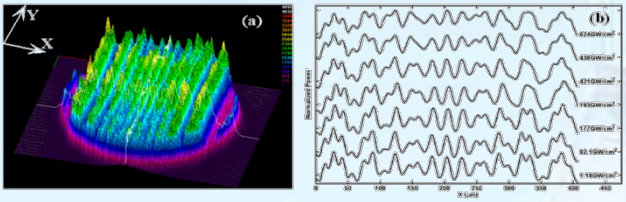

图 13. 飞秒激光脉冲在光子晶格中的离散衍射图样。（a）三维显示图样。（b）不同入射光强情况下离散衍射的能量分布。/Fig. 13. Discrete diffraction pattern of femtosecond laser pulse at output facet. (a): 3D image of discrete diffraction; (b): power distribution of discrete diffraction for different input peak intensities.

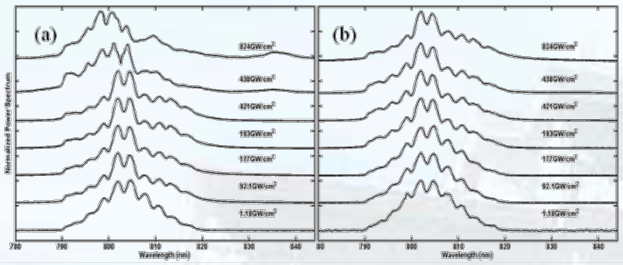

图 14. 不同入射光强下，体材料中（a）和光子晶格中（b）飞秒脉冲光谱的展宽对比。/Fig. 14. Contrast of spectrum broadening for bulk material (a) and photonics lattice (b) versus the input peak intensities.

我们研究分析了在吸收介质的纳米光纤中反向传播的两束光对纳米光纤附近的纳米粒子产生作用力的情况。结果表明由于两束光的散射力的引入，沿着光纤方向我们能得到稳定的俘获位置，并且梯度力使得俘获位置位于纳米光纤的横截面上。通过调节两束光的强度比和偏振方向，能分别实现在沿纳米光纤方向和纳米光纤横截面上对纳米粒子的操控（如图15）。数值模拟结果显示这是一种实现准三维操控的可行方案。

Optical forces on a nanoparticle around an absorptive dielectric nano-fiber illuminated by two linear polarized counter-propagating beams were investigated. The results show the scattering force of the two beams causes the steady trapping along the fiber and the gradient force makes the trapping in the transverse plane of the nano-fiber. By altering the intensity ratio between the two incident beams and the polarization direction of the beams, manipulation along the nano-fiber and in the transverse direction can be realized (see Fig. 15), respectively. The numerical results present a new promising method to realize quasi 3-dimensional optical manipulation.

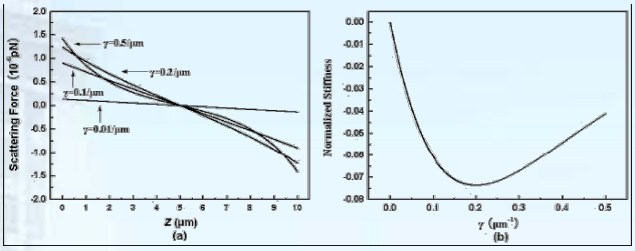

图.15. 20纳米直径颗粒的散射力（a）和归一化的刚度随吸收系数的变化关系（b）。这里L=10.0μm, r=0.21μm and φ=0. 图（a）中四条线分别代表γ=0.01/μm, 0.1/μm, 0.2/μm 和 0.5/μm的情形。图（b）中，z=5.0μm。/Fig. 15. The scattering forces versus z on a particle with diameter of 20nm (a) and the normalized stiffness versus the absorption coefficient γ (b). Here D=400nm, L=10.0μm, r=0.21μm and φ=0. In (a), the four lines present the cases that γ=0.01/μm, 0.1/μm, 0.2/μm and 0.5/μm, respectively. In (b), z=5.0μm.

我们用原子力显微镜、吸收光谱和荧光光谱等手段对比研究了掺金属纳米颗粒和不掺金属纳米颗粒的罗丹明6G填充到高有序排列多孔氧化铝中后的物理性质。实验结果表明掺金属纳米颗粒和不掺金属纳米颗粒的罗丹明6G填充到高有序排列多孔氧化铝中后，它们的光学性质都有明显变化，这种变化和多孔氧化铝的表面积-体积比有关。通过选取合适的表面积-体积比我们得到了最大的荧光增强。掺金属粒子越多，填充到AAO之后荧光增强的效果就比填充前越明显，这表明AAO的作用抑制了荧光猝灭效应。通过选择最佳的AAO尺寸和金属纳米颗粒浓度，我们得到了大于5.5倍的荧光增强信号（如图16）。

Highly ordered nanocomposite arrays formed by filling anodized aluminum oxide

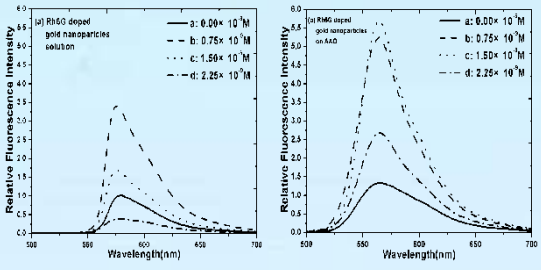

图. 16. 掺金属纳米粒子的Rh6G在溶液状态（a）和填充进AAO-III之后（b）的荧光光谱。Rh6G的浓度为：0.50×10^{-3}M。掺入的金属纳米颗粒的浓度分别为：a: 0.00×10^{-9}M, b: 0.75×10^{-9}M, c: 1.5×10^{-9}M and d: 2.25×10^{-9}M。结果以Rh6G的纯乙醇溶液的荧光峰强度为准进行归一化。/Fig. 16 The fluorescence spectra of samples of Rh6G doped with gold nanoparticles solution (a) and Rh6G doped with gold nanoparticles incorporated in AAO-III (b). The concentration of Rh6G solution in ethanol is 0.50×10^{-3}M. The concentrations of gold nanoparticles are a: 0.00×10^{-9}M, b: 0.75×10^{-9}M, c: 1.5×10^{-9}M and d: 2.25×10^{-9}M. The results are normalized basing on the fluorescence peak intensity of Rh6G in the pure ethanol solution。

(AAO) with Rhodamine 6G (Rh6G) which is doped with/without metal nanoparticles, are studied by visible absorptive, fluorescence spectra and atomic force microscopy (AFM). The results show that the optical properties of Rh6G dyes doped with and without metal nanoparticles are both influenced by the highly ordered porous AAO nanostructures, and the influence depends on the surface-to-volume ratio (SA/V) of the samples which decided by the size of nanopores (the diameter and spacing distance of nanopores) in the AAO. The optimized size of nanopores in this experiment is selected with the maximum SA/V and then the maximum fluorescence enhancement. The fluorescence spectra of Rh6G doped with gold nanoparticles incorporated in AAO yields a surprised enhancement and a ~12nm blue shift comparing with it in the solution environment, and the enhancement increases with the increasing doped concentration of the gold nanoparticles. It's contributed to the effective inhibition of the spatial confinement and large SA/V of AAO to the quenching effect induced by the metal nanoparticles. More than 5.5 times fluorescence enhancement is achieved in this work through optimizing the size of AAO and the concentration of gold nanoparticles (see Fig. 16).

安德森局域化最初是在固体物理中提出的，意识到安德森局域化是波动现象的一种体现后，对它的研究逐渐推广到声波、光波，以及物质波。相干背散射由于具有直观和易操作的特点，成为研究光子局域化的一种最重要手段。

通过研磨过滤，得到直径小于 220nm 的同成分铌酸锂微晶。然后将铌酸锂微晶分散到水中形成悬浊液，并实验研究了该悬浊液中的相干背散射。成功利用线偏振泵浦光，首次在悬浊液中实现了光控的光子局域化。无泵浦光时，探测光的光子局域化程度基本不变；探测光和泵浦光偏振一致时，光子局域化程度增强；探测光和泵浦光偏振正交时，光子局域化程度减弱（如图 17）。通过分析，我们认为在线偏光的辐照下微晶颗粒发生重新取向，宏观各向同性的悬浊液转变为各向异性。

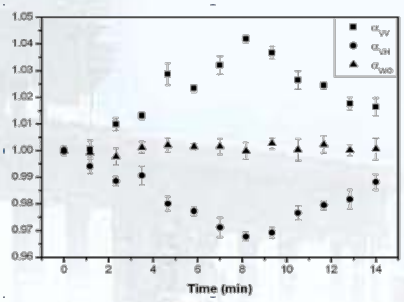

图17 不同泵浦光状态下悬浊液中光子传输平均自由程随时间的变化。/Fig. 17. Temporal evolution of the angular width of CBS cones. The vertical coordinate $\alpha = W_t/W_o$ is the ratio between the width W_t at the time t and the initial width W_o. The quantity α_{WO} is the ratio without pump light, and α_{VV} and α_{VH} are the ratios for VV and VH geometries, respectively.

We experimentally study coherent backscattering of light for a water suspension of lithium niobate microcrystalline particles. Light-controllable weak localization of photons in a suspension is demonstrated (see Fig. 17) for the first time to our knowledge. The effect is attributed to the reorientation of

microcrystalline particles in the field of a linearly polarized pump beam. Thus the isotropic suspension becomes partially anisotropic.

研究发现少量紫外线辐射有益于健康，这是人体产生维生素 D 所必需的。但是，过度暴露于紫外线辐射易导致多种疾病，如皮肤癌、灼伤、白内障及其他眼病。更有证据表明，紫外线辐射可降低免疫系统的有效性。红细胞是人体血液重要组成之一，通过血液循环系统，是紫外辐射的重要靶点之一。本研究工作中，我们利用 365/50 nm 波段的紫外光体外照射红细胞，监测其自体荧光动力学变化过程。实验结果显示，连续的的紫外光（9400 mW/cm^2）可明显导致红细胞内自体荧光增强，而非连续紫外光（0.25 Hz, 1.25% 占空比）在同样时间内没有导致类似现象（Fig. 18A）。当红细胞用双氧水孵育后，连续的紫外光更加快速的导致红细胞内自体荧光的增强，非连续的紫外光也可导致红细胞内荧光缓慢增强。而连续的绿光照射却不能引起红细胞自体荧光的增强。最终分析表明：紫外光是利用其高的单光子能量和产生超氧自由基的特性，使得红细胞内原本低荧光效率的血红素转变为高荧光效率的胆红素，从而引起红细胞内自体荧光的显著增强。同时，我们根据该结论，利用速率方程建模成功模拟出该自体荧光变化过程，并且给出各荧光分子数的变化过程（Fig. 18B）。本研究结果可为体外研究光动力疗法提供一定的实验支持和新的思考视角。

Ultraviolet (UV) light has a significant influence on human health. In this study, human erythrocytes were exposed to UV light to investigate the effects of UV irradiation (UVI) on autofluorescence. Our results showed that high-dose continuous UVI enhanced erythrocyte autofluorescence, whereas low-dose pulsed UVI alone did not have this effect. Further, we found that H_2O_2, one type of reactive oxygen species (ROS), accelerated autofluorescence enhancement under both continuous and pulsed UVI. In contrast, continuous and pulsed visible light did not result in erythrocyte autofluorescence enhancement in the presence or absence of H_2O_2. Moreover, NAD(P)H had little effect on UVI-induced autofluorescence enhancement. From these studies, we conclude that UVI-induced erythrocyte autofluorescence enhancement via both UVI-dependent ROS production and photodecomposition. Finally, we present a theoretical study of this autofluorescence enhancement using a rate equation model. Notably, the results of this theoretical simulation agree well with the experimental data further supporting our conclusion that UVI plays two roles in the autofluorescence enhancement process. See Fig. 18.

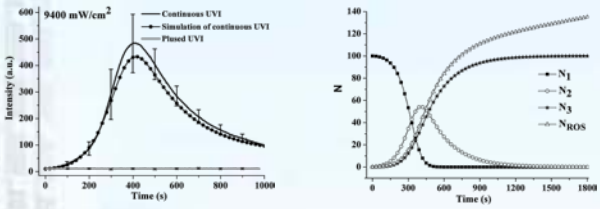

图 18. 紫外光（365/50 nm）照射诱导红细胞自体荧光增强。（A）连续紫外光（9400 mW/cm^2）诱导红细胞自体荧光变化曲线；非连续紫外光（9400 mW/cm^2, 0.25 Hz, 1.25% 占空比）引起红细胞自体荧光变化曲线；理论模拟连续紫外光照射导致的自体荧光增强曲线。(B) 速率方程模拟红细胞内三种荧光分子（N_1，N_2，N_3）及超氧自由基（N_{ROS}）数量密度随时间变化趋势。/Fig. 18. (A) Experimental (solid) and simulation (-d-) results of UVI-induced autofluorescence enhancement in erythrocytes. Experimental evolution of autofluorescence change induced by pulsed UVI at 9400 mW/cm^2 (pulsed UVI and continuous UVI). (B) Theoretical population density time evolutions of hemoglobin (N_1), bilirubin (N_2), photodegradation products of bilirubin (N_3), and ROS (NROS) at a UVI intensity of 9400 mW/cm^2 using a rate equation.

传播表面等离激元在未来的芯片通讯和信号处理等方面具有重要的潜在应用。然而，如何最优化其传播距离与光场局域的矛盾是现在研究的重点之一。在此基础上，许多金属结构波导被提出用于表面等离激元的传输和集成，包括金属纳米粒子链、金属凹槽、金属纳米线对和介质-金属混合结构等。其中，金属纳米线对中的间隙表面等离

激元模式（gap plasmons）拥有最小的临近波导耦合作用，因此可以实现高度的空间集成。然而，如何实现高度局域的间隙表面等离激元的定点高效的激发是实验中未解决的困难之一。在本文中，与利用复杂的光学方法如 Otto 耦合等方式不同，我们提出了利用快电子在银纳米线对中实现间隙表面等离激元的可控激发。在我们的研究中，利用边界元方法严格求解 Maxwell 方程组，分析频率和沿着纳米线方向的动量分辨的电子能量损失谱，从而得到电子所激发的表面等离激元的色散关系（Fig. 19）。同时，计算电磁场近场分布得到激发的等离激元模式在金属结构截面的电荷对称性。我们发现快电子横穿纳米线对会有效产生间隙表面等离激元、四种耦合的偶极模式和一种耦合四极模式。通过改变电子运动轨道与纳米线对的相对位置可以实现不同等离激元模式的选择激发，在完全对称的激发配置下间隙表面等离激元将被抑制。同时，间隙模式的激发效率一般约为 10^{-4} 量级。该研究提出了间隙等离激元的有效激发方式，为利用电子实现间隙等离激元模式的激发提供了完善的理论支持，在实验上很容易通过电子显微镜的阴极发光光谱证实。

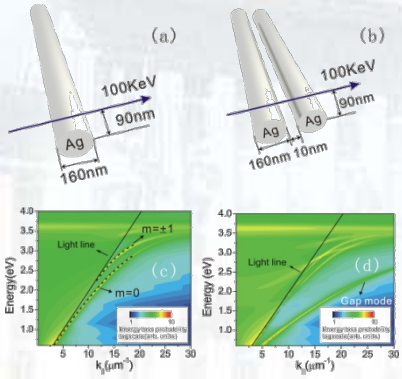

Fig. 19 电子束耦合纳米线表面等离激元。（a）和（b）分别对应快电子在单根纳米线和纳米线对中激发表面等离激元的示意图。通过分析动量-能量分辨的电子能量损失谱所得到的快电子在单根纳米线和纳米线对中激发的表面等离激元的模式的色散关系分别如（c）和（d）所示。/Fig. 19. Coupling of an electron beam to metallic wire plasmons. (a) and (b) show schematic views of electrons passing at a distance of 10 nm from the surface of an infinitely long free-standing silver wire of 160 nm in diameter and an infinitely long silver wire pair, respectively. (c) Electron energy-loss probability for the single wire considered in (a). (d) Energy-loss probability for the wire pair of (b).

We show that electron beams can efficiently excite gap-plasmon modes in metallic waveguides defined by nanowire pairs. These modes are characterized by monopole-monopole charge symmetry. Significant excitation yields of higher-order dipole-dipole and quadrupole-quadrupole modes are also predicted. Our results are based on rigorous numerical solution of Maxwell's equations in which the electron is described as a classical external current. In our analysis, we find it convenient to simulate electron energy-loss spectra, which are resolved in the frequency and parallel momentum transferred from the electron to the wires for various perpendicular electron trajectories. The charge symmetry of these modes is inferred from the distribution of the induced near fields. The emission yield for the gap modes is as high as 10^{-4} plasmons per incoming electron over the visible range of frequencies. Higher-order modes can be selectively excited by playing with the orientation of the electron trajectory whereas the gap plasmon is preferentially launched in nonsymmetric configurations and it is totally suppressed in symmetric arrangements. The effect of curvature along the direction of the wires is also explored by considering the excitation of plasmons defined in the gap between two circularly shaped wires. Our results provide full support for the excitation of gap plasmons with designated electron-beam sources in nanocircuits. See Fig. 19.

光学周期结构对荧光发射的调制在通信光学、微腔激光、平面发光器件等诸多领域有十分重要的意义。尤其是光子晶体的出现更为这个领域增添了新的活力。但对于传统全息材料在此领域的研究还很少。

我们研究了周期结构对荧光发射的调制作用。在实验上，观察到了在重铬酸盐明胶中的一维结构对荧光的增强的调制；在理

论上，借鉴光子晶体对荧光调制的态密度重新分布理论，首次引入态密度理论计算了传统的全息存储材料中周期结构对诺丹明 6G 荧光的调制进行了解释，如图 20 所示。和光子晶体相比，全息存储材料的周期结构更容易构建，且周期的精密性更高，缺陷更少。只是折射率调制振幅受材料本身的影响，要比光子晶体小的多。但在全息存储材料中的周期结构同样对嵌入其中的荧光染料的荧光发射进行了有效的调制，这种调制也同样遵从态密度重新分布理论计算得到的结果。从而为更进一步的开发光子学领域应用器件提供了强大的支持。

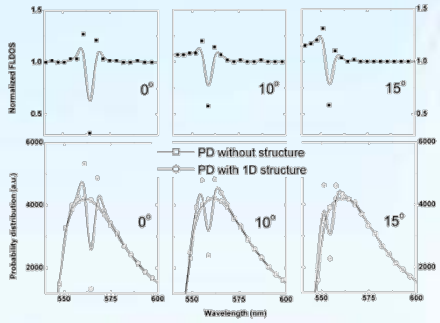

图 20 在与重铬酸盐明胶薄膜法向夹角 0°,10°,15°方向上的归一化的精细局域态密度、R6G 的光子发射概率分布函数（PD）和两者相乘得到的可能的调制光谱的发射分布。

Fig. 20. The normalized FLDOS distribution and the simulated PL in EHM and in structured sample at different detection angles.

The modulation of the spontaneous emission of Rhodamine 6G has been observed in one-dimensional periodic dielectric structure of dichromated gelatin film with refractive index contrast as low as 0.01. The spontaneous emission is enhanced at the band edges and inhibits in the band gap, which agree well with the theoretical analysis on the redistribution of the fractional local density of optical states. See Fig. 20.

在太赫兹声子极化激元的研究中，我们取得了一些阶段性的成果[Optics Express, **18**, 26351 (2010); J. Opt. Soc. Am. B, **27**, 2350 (2010); Optics Express **17**, 9219 (2009)]。我们用相衬法和自补偿偏振快门法在铌酸锂晶体中实现了太赫兹声子极化激元的定量时间分辨成像。我们还研究了亚波长、各向异性波导中太赫兹声子极化激元的模式、传输行为、能量分布等情况。太赫兹声子极化激元作为非常重要的一种元激发，无论是在理论研究还是实际应用中都有着非常重要的价值。我们的这些研究成果，解决了太赫兹声子极化激元的定量时间分辨成像的探测问题，解决了其主要的基质材料—亚波长厚度的铌酸锂晶体薄片中的激发和传输问题。为太赫兹声子激元的进一步研究，无论是相干调控还是其光学特性的研究等，奠定了坚实的基础。

For the research of Thz phonon polariton, we have gotten a series of achievements [Optics Express, **18**, 26351 (2010); J. Opt. Soc. Am. B, **27**, 2350 (2010); Optics Express **17**, 9219 (2009)]. Using a phase contrast and self-compensating polarization gating geometry, we brought out the quantitative time-resolved imaging of Thz phonon polariton in lithium niobate crystal. We also studied the modes, propagation, energy distribution of Thz phonon polariton in subwavelength, anisotropic slab waveguide. Thz phonon polariton is an important kind of elementary excitation, which has significant value for both theoretical research and practical application. Our achievements brought out the methods of quantitative time-resolved imaging for Thz phonon polariton, and show its properties in subwavelength anisotropic slab waveguide, which is the production and propagation material for Thz phonon polariton. We do believe that our results opened the door for the further research of Thz phonon polariton, such as coherent control, specific optical property of Thz phonon polariton.

亚波长各向异性平面波导中太赫兹声子极化激元的方向依赖的模式理论和实验研究 [Optics Express, **18**, 26351 (2010)]。不同的传输角度，声子极化激元波有着不同的模式。图 21 给出了不同角度下的声子极化

激元波的色散图。其中红线为实验结果。蓝线为 TE 模式的理论计算结果，绿线是 TM 模式的理论计算结果。

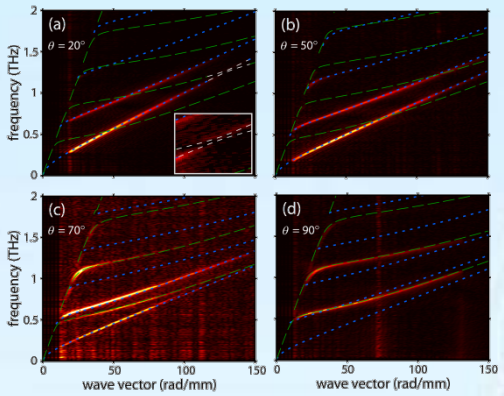

图 21. (a), (b), (c), (d)分别对应传输角度 θ = 20°50°, 70°, 90° 的色散曲线。 /Fig. 21 (a), (b), (c), and (d), Dispersion curves for θ = 20°, 50°, 70°, and 90°, respectively.

Experimental and theoretical analysis of THz-frequency, direction-dependent, phonon polariton modes in a subwavelength, anisotropic slab waveguide. For different propagation direction, phonon polariton waves have different modes. Fig. 21 shows the dispersion curves for different propagation directions, in which the red curves are the experimental results, the blue dot curves are the calculated TE mode, and the green dot curves are the calculated TM mode.

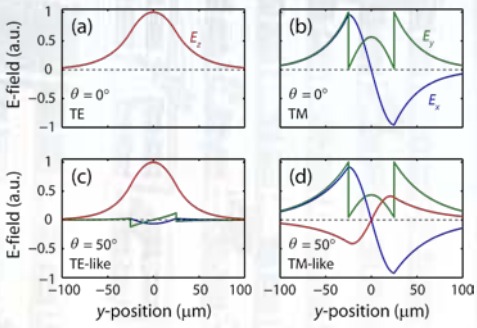

图 22. 0.5 THz 最低对称和反对称模式的电场分布。

Fig. 22. Electric field profiles for the lowest symmetric and antisymmetric modes at 0.5 THz.

因为太赫兹声子极化激元在晶体中的波长大约在百微米左右，而晶体的厚度只有 50 微米，所以很多的能量分布到晶体的表面。这种表面波可以与沉积在晶体表面的物质相互作用，使得声子极化激元波与其它光学或光电子学器件相互作用成为可能。图 22 是其电场的分布情况。

The wavelength of Thz phonon polariton waves in the sample is about 100 micrometer and while the thickness of the crystal is 50 micrometer. So a lot of energy distributes on the crystal surface (see Fig. 22). This kind of surface wave can interact with material deposited on the crystal surface. It opens the door for the interfacing of Thz phonon polariton waves with other optical or photoelectric devices.

为了研究 Thz 声子极化激元的非线性过程，我们也给出了它的有效折射率椭圆，结果如图23所示。其中开符号是实验结果，实线是我们的理论计算结果。

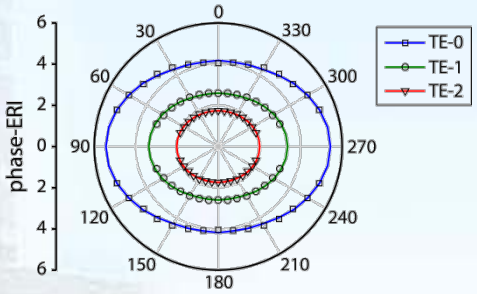

图 23. 波矢β = 50 rad/mm，三个 TE 模式的有效折射率椭圆。开符号是实验结果，实线是我们的理论计算结果。

Fig. 23. Effective refractive index (phase ERI) ellipse for three TE modes at a wave vector β = 50 rad/mm. The open symbols are experimental data and the solid lines are calculated results.

To do research of nonlinear process of Thz phonon polariton, we also show its effective refractive index ellipse in Fig. 23. The open symbols are experimental data and the solid lines are the calculated results.

安息香双甲醚光敏剂掺杂的紫色光敏有机玻璃在紫外光诱导下可以通过光致聚合效应得到折射率调制，这是光致折射率变化的一个重要方面，也正在得到越来越广泛的应用。但是由于在紫外波段光致变色效应的存在，在折射率栅建立的同时也会有以吸收栅为主的耗散栅的存在；更重要的是在以往的实验结果中发现以上两种机制建立起来的复合光栅具有非局域性特征，这与通常的光致聚合效应有所差异。本工作应用二波

耦合理论，对计算方法进行改进，测量了在紫外波段下复合光栅的相位移动数据，并对相移机理进行了分析。研究结果表明，光栅相移的存在是由于光致聚合的非局域性所致，主要来源于光致聚合过程中的热传导导致的进一步聚合反应和聚合导致的样品密度差引起的应变。与聚合过程密切相关，相移的稳定程度随聚合的进行逐渐趋于稳定。研究结果也表明，折射率光栅在复合光栅中占有绝对大的比例，在实际的可见光应用中可以忽略吸收栅的存在。光致聚合的后聚合效应可以在保证光栅写入深度的同时减少光栅的相移。合理利用后聚合效应是减小光栅相移，提高基本有机玻璃的光子学器件质量的可行手段。如图 24 所示。

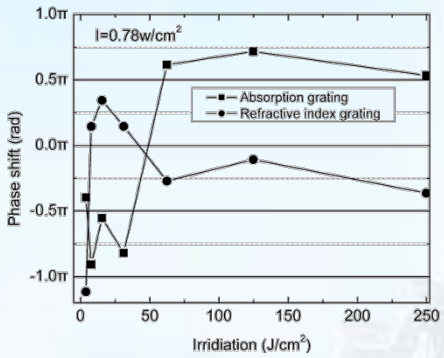

图 24 光栅记录过程中相位栅和振幅栅相对光场的相位移动。/Fig. 24. Phase shift of the absorption grating and the refractive index grating versus irradiation at I = 0.78 W/cm^2.

The phase shifts of the extinction and refractive index gratings to the illumination pattern are revealed in doped polymethyl methacrylate (PMMA). The dynamic process of these shifts is studied via two-wave coupling at 351 nm. It is shown that these shifts are from the strain and the shrinkage inside the sample and accompanied with the photo-repolymerization process during the building process of the holographic grating. Such shifts will cause obvious energy exchange between the two recording beams and enough attention should be paid to the nonlocal property of the holographic gratings of the material in the application. See Fig. 24.

我们研究了高掺 Mg, Zn, In 和 Hf 铌酸锂晶体在 325nm 紫外带边的光折变性能。结果表明，和名义纯铌酸锂晶体相比，上述掺杂铌酸锂晶体的紫外带边光折变性能大大增强，甚至要优于在 351nm 处的紫外光折变性能（见表 1）。例如，掺 9mol%Zn 铌酸锂晶体的两波耦合能量增益系数和光折变记录灵敏度可分别达到 38cm^{-1} 和 37.7cm/J@325nm；而掺 9m0l%Mg 的铌酸锂晶体在 614mW/cm^2@325nm 的总记录光强下，其响应速度达到 73ms。此外，在高掺 Mg, Zn, In 和 Hf 铌酸锂晶体的紫外带边光折变效应中，电子是主导光激发载流子，扩散是光激发载流子的主导迁移机制。这些结果对于研究铌酸锂晶体的紫外带边缺陷结构具有一定意义。

表 1 掺杂铌酸锂晶体的紫外带边 325nm 处的光折变性能。

Table 1 The photorefractive properties of doped lithium niobate crystals at 325 nm.

Samples	CLN	CMg1	CMg2	CMg4	CMg5	CMg7	CMg9	M22
α(cm^{-1})	7.79	5.81	5.32	2.47	5.75	1.72	2.07	17.75
η_{ex} (%)[a]	1.52	1.18	1.73	2.10	46.8	75.9	81.7	50.7
σ_{ph}/I_e (×10^{-12} cm/Ω W)	2.31	9.22	9.57	10.8	82.6	110	278	3.64
τ_r (s)[a]	4.38	2.85	2.33	1.90	0.35	0.43	0.073	3.08
Γ (cm^{-1}) [b]	4.75	4.53	5.41	1.69	23.5	20.6	25.3	29.2
Δn (×10^{-5})	2.39	1.50	1.82	0.33	2.75	1.97	3.35	4.03
S (cm/J)[a]	4.29	2.78	2.86	0.45	8.60	9.13	33.1	7.75
(M/#)/d (cm^{-1}) [a]	4.76	0.78	0.77	0.11	0.28	0.22	0.31	5.63
Samples	**CZn5**	**CZn7**	**CZn9**	**CIn1**	**CIn3**	**CIn5**	**CHf4**	**CHf6**
α(cm^{-1})	3.49	3.03	2.90	10.80	6.38	5.02	2.47	2.51
η_{ex} (%)[a]	13.6	61.4	67.7	9.76	15.4	49.5	1.23	2.77
σ_{ph}/I_e (×10^{-12} cm/Ω W)	52.7	237	255	1.42	33.7	98.8	105	120
τ_r (s)[a]	0.33	0.20	0.19	8.60	0.24	0.27	0.48	0.28
Γ (cm^{-1}) [b]	11.9	27.6	38.0	2.46	11.6	22.9	23.1	29.3
Δn (×10^{-5})	1.75	4.26	4.67	0.91	1.16	2.24	2.15	3.23
S (cm/J)[a]	10.9	24.5	37.7	1.44	7.35	25.5	5.30	28.5
(M/#)/d (cm^{-1}) [a]	0.54	0.28	0.39	2.62	0.57	0.69	0.13	0.38

We studied the photorefractive effect of lithium niobate $LiNbO_3$ doped with Mg, Zn, In, or Hf at an ultraviolet (UV) wavelength down to 325 nm. It is found that the UV photorefraction of $LiNbO_3$ doped with Mg, Zn, In, or Hf was enhanced significantly as compared to that of the nominally pure $LiNbO_3$. The UV photorefraction of these crystals at 325 nm is even better than that at 351 nm (see table 1). For example, the photorefractive two-wave coupling gain coefficient and the photorefractive recording sensitivity at 325 nm were measured to be 38 cm^{-1} and 37.7 cm/J, respectively, in a $LiNbO_3$ crystal doped with 9 mol % Zn. The

photorefractive response time of a Mg:$LiNbO_3$ with a 9 mol % Mg was measured to be 73 ms with a total recording intensity of 614 mW/cm^2 at 325 nm. In highly Mg, Zn, In, or Hf doped $LiNbO_3$ crystals, diffusion dominates over photovoltaic effect and electrons are the dominant charge carriers in UV photorefraction at 325 nm. The results are also of interest to the study on the defect structure of $LiNbO_3$ near to the absorption edge.

我们理论研究了横向直流偏压配置条件下GaAs-AlGaAs量子阱中基于位相耦合色散效应的慢光和超光速传输现象。结果表明，在横向配置条件下，基于GaAs-AlGaAs量子阱强的平方电光效应和快响应特性，可实现带宽为100kHz、群速 为cm/s量级的慢光，如图25所示。与其它光折变材料相比，基于GaAs-AlGaAs量子阱的慢光的时延带宽积得到了显著的提高。

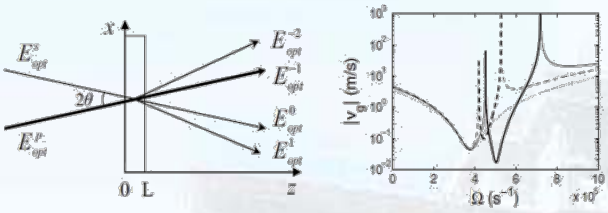

图 25 GaAs-AlGaAs 量子阱中的 Raman-Nath 多波耦合配置图和-2 阶（点线）、0 阶（实线）和 1 阶（虚线）衍射光的群速色散曲线。/Fig. 25 The multi-wave mixing configuration in the Raman-Nath region in GaAs-AlGaAs quantum well, and the dispersion curves of group velocity for the -2nd (dotted curve), zero-th (solid curve), and 1st (dashed curve) diffraction beams.

We show theoretically that, based on the dispersive phase coupling effect during the wave mixing process, both slow and fast light can be achieved in GaAs–AlGaAs photorefractive multiple quantum wells (PRMQWs) films applied with a transverse direct-current electric field. The simulation results in the transverse-geometry PRMQWs films show that the group velocity and bandwidth of slow light can be on the order of centimeter per second and 100 kHz (see Fig. 25), respectively. The extremely low group velocity and the relatively broad bandwidth are mainly originated from the strong quadratic electro-optic effect and the fast response rate of the PRMQWs films, respectively. Our results show that the delay-bandwidth product of slow light can be significantly improved in PRMQWs films as compared to the reported results in other photorefractive materials.

我们在改进的迈克尔逊干涉仪上，观测到了单模连续激光的二阶空间亚波长干涉，如图 26 所示。并基于费曼路径积分理论，统一解释了所有的二阶亚波长干涉现象。

The second-order spatial subwavelength interference pattern is observed in a modified Michelson interferometer with single-mode continuous-wave laser beams，as shown in Fig. 26. By analyzing our subwavelength interference experiment based on Feynman's path integral theory, a unified interpretation for all the second-order subwavelength interference is suggested.

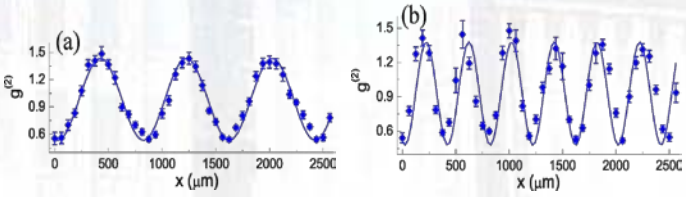

图 26 一般的空间二阶干涉图(a)和亚波长二阶干涉图(b)。

Fig.26 Normal spatial second-order interference (a) and subwavelength second-order interference.

光谱表征及传感技术/Spectral Charaterization and Sensing Techniques

负责人：臧维平

本方向涉及激光器，上转换发光材料，光纤器件，稀土掺杂发光材料，应用光谱学和光谱仪器等方面。取得的代表性成果如下：

In this field, we mainly focused on the laser, up conversion luminescent material, fiber optic, rare earth dope glass, applied spectroscopy and spectral instrument. This year, we obtained some important results, they are mainly shown as following:

玻璃陶瓷的研究

Research on glass ceramics

Er^{3+}/b^{3+}共掺磷酸盐玻璃具有储能大、能量传递效率高等优点，这对上转换和下转换发光都有很大的益处。但磷酸盐玻璃自身又具有一些缺点，比如机械强度较差、易潮解和发光效率底等，这使得在应用上受到了很大限制。但玻璃陶瓷能结合玻璃和晶体的优点，从而弥补玻璃材料的不足。目前对于掺铒的氟氧化物玻璃陶瓷的研究较多，但是对掺铒磷酸盐玻璃陶瓷的报道很少。尤其热处理温度和时间对析出的纳米晶类型的影响研究还很不深入。为此，我们制备了多种配比的玻璃样品，并最终通过热处理得到玻璃陶瓷，取得的具体成果有：

表1 不同Li浓度的磷酸盐玻璃陶瓷

Table1 Phosphate glass ceramics with different Li-doped concentration

玻璃组分	P_2O_5	Li_20	Er_2O_3	Yb_2O_3
摩尔比（mol％）	80	20	0.05	0.25
摩尔比（mol％）	75	25	0.05	0.25
摩尔比（mol％）	70	30	0.05	0.25
摩尔比（mol％）	65	35	0.05	0.25
原料	$NH_4H_2PO_4$	Li_2CO_3	Er_2O_3	Yb_2O_3

Er^{3+}/Yb^{3+} phosphate glass has advantages of large energy storage and high energy transfer efficiency, which has important applications in the upconversion. However, the glass itself has some weaknesses, such as the weak mechanical strength, easy to deliquescence and lower luminous efficiency, which make the applications of the materials limited. But glass ceramic combines the advantages of glass and ceramic. Now Er^{3+}-doped fluoride glass-ceramic have widely been studied. But the research on the phosphate glass ceramics (especially, the impacts of the annealing temperature, time on the type of nanocrystal) is less. Therefore, we prepared the Er^{3+}/Yb^{3+} phosphate glasses. And by annealing, the phosphate glass ceramics were obtained.

(1) 通过热处理前驱玻璃，我们成功得到了掺铒磷酸盐玻璃陶瓷.下图为配比$(80P_2O_5\text{-}20Li_2O)\text{-}0.05\ Er_2O_3\text{-}0.25Yb_2O_3$ (mol%)在不同热处理温度的 XRD 图。图中明显显示随热处理时间的增长，衍射峰的数目和纳米晶的种类也随着增加。

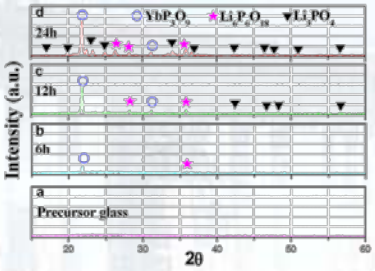

图 1 前驱玻璃和玻璃陶瓷（在 790K 热处理不同时间）的 XRD 谱

Fig.1 XRD patterns of the precursor glass and glass ceramics that were annealed at 790K for different heat treatment times

By annealing the precursor glasses, the phosphate glass ceramics were prepared. The next picture shows the XRD diagrams of the samples with the ratio of $(80P_2O_5\text{-}20Li_2O)\text{-}0.05\ Er_2O_3\text{-}0.25Yb_2O_3$ (mol%), which were heated at 790K for different times. From the figure, it is obvious that the numbers and kinds of diffraction peaks increase with the increasing of

annealing time.

(2) 为了进一步证实 XRD 的结果，我们对玻璃陶瓷样品做了透射电镜（TEM）测试。测试结果和通过 XRD 得到的结论很好吻合，见图 2。

For proving the results of XRD, the TEM diagrams of the glass ceramics were measured. And the results were in good agreement with the XRD measurements and calculations.

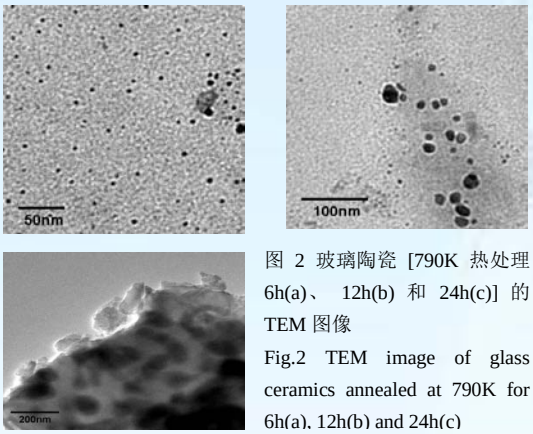

图 2 玻璃陶瓷 [790K 热处理 6h(a)、 12h(b) 和 24h(c)] 的 TEM 图像

Fig.2 TEM image of glass ceramics annealed at 790K for 6h(a), 12h(b) and 24h(c)

(3) 图 3 是前驱玻璃和玻璃陶瓷在 975nm 激光二极管泵浦下的发光光谱。如图可见，玻璃陶瓷样品的发光要明显强于玻璃的，而且谱线也出现了明显的劈裂，证明了 Er^{3+}周围的晶体场明显增强。

Fig.3 shows the luminescence spectra of the glass and glass ceramics at 975 nm laser diode pump. From Fig.3, the emission intensity of the glass ceramics are stronger compared to that of the glass. And the Stark split is very obvious, which shows that the crystal field intensity around Er^{3+} has increased.

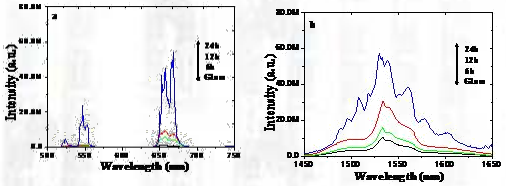

图 3 在 975nm 激光二极管泵浦下，前驱玻璃和玻璃陶瓷的上转换和红外光谱

Fig.3 UC emission and infrared luminescence spectra of the glass and glass ceramics at 975nm LD pump

(4) 图 4 是上转换发光强度与泵浦功率的关系图。如图可知玻璃和玻璃陶瓷的上转换红光和绿光的布居进程基本一样，都是两光子进程。

Fig.4 is the log-log plots for the dependence of the green emissions and the red emission intensities on pump power. The population processes of both the red emission and the green emissions are two-photon processes.

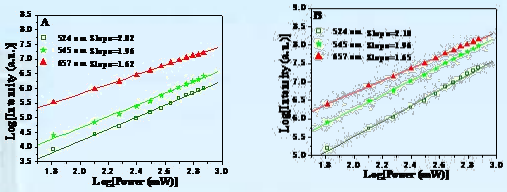

图 4 上转换红光和绿光的发光强度与泵浦功率的关系

Fig.4 log-log plots for the dependence of the green emissions and the red emission intensities of on pump power

(5) 荧光的增强

(5) Increasing of luminescence

表 2 不同掺 Ce 浓度的磷酸盐玻璃陶瓷

Table 2 Phosphate glass ceramics with different Ce-doped concentration

Samples	CeO_2(mol%)	Er_2O_3(mol%)	Yb_2O_3(mol%)
CYE0	0	0.2	7.0
CYE1	0.2	0.2	7.0
CYE2	0.4	0.2	7.0
CYE3	0.8	0.2	7.0
CYE4	1.2	0.2	7.0
CYE5	1.6	0.2	7.0

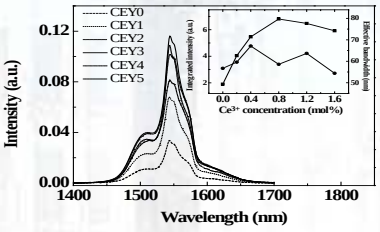

图 5 Ce^{3+}的敏化对于 1.54um 荧光的影响

Fig.5 Impact 1.54um luminescence on the sensitizing of Ce^{3+}

表 2 是样品中掺入了 Ce,Yb,Er 的比例，通过 Ce 的掺入，我们发现 $^4I_{11/2}$ 能级寿命明显降低，$^4I_{13/2}$ 能级寿命变化不大，1.54um 荧光强度有所增强，见图 5。

Table 2 is the rate of Ce,Yb,Er in the glass ceramics. Through doping Ce, we observed that

the lifetime of $^4I_{11/2}$ energy level obviously decreased, but the lifetime of $^4I_{13/2}$ energy level changed less. And the 1.54um luminescence intensity increased, seen in Fig.5.

表 3 不同掺 Tm、Tb、Mn 浓度的磷酸盐玻璃

Table3 Phosphate glasses doped with different Tm、Tb、Mn concentrations.

Samples	P_2O_5 (mol%)	Li_2O (mol%)	Sb_2O_3 (mol%)	Tm_2O_3 (mol%)	Tb_4O_7 (mol%)	MnO_2 (mol%)
Tm1	80	15	5	0.2		
Tb1	80	15	5		0.3	
Mn1	80	15	5			0.5
TBM1	80	15	5	0.2	0.3	0.5

表 3 是掺不同 Tm、Tb、Mn 浓度的磷酸盐玻璃。我们对玻璃样品 TBM1 在 720K 进行热处理 6h，并进一步研究了前驱玻璃和热处理后的玻璃陶瓷的发光特性。

Table 3 shows phosphate glasses doped with different Tm、Tb、Mn concentrations. The sampleTBM1 is annealed at 720K for 6h. The luminescence properties of the glass and glass ceramic are discussed.

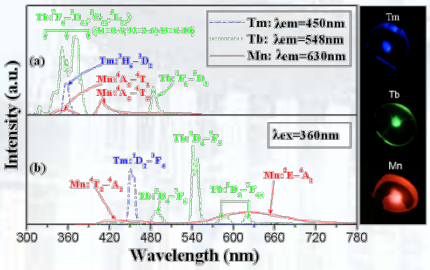

表 6(a) 样品 Tm1、Tb1 和 Mn1 的激发谱。(b) 在 360nm 激发下，样品 Tm1、Tb1 和 Mn1 的发射谱。插图是样品发光的照片。

Fig.6(a) Excitation spectra of the Tm^{3+}(λ_{em}=450nm), Tb^{3+}(λ_{em}=548nm), and Mn^{4+}(λ_{em}=630nm) doped phosphate glasses. (b) Emission spectra of the Tm^{3+}, Tb^{3+}, and Mn^{4+} doped phosphate glasses at 360nm light excitation. The inset is the photos of the samples at 360nm light excitation.

图 6 是样品 Tm1、Tb1 和 Mn1 的激发和发射谱。在 36nm 激发下，样品 Tm1、Tb1 和 Mn1 分别发射蓝光、绿光和红光。

Figure 6 is the excitation and emission spectra of the Tm1, Tb1 and Mn1 samples. At 360nm excitation, the Tm1, Tb1 and Mn1 samples emit blue, green and red emissions.

图 6 是在 360nm 激发下，$Tm^{3+}/Tb^{3+}/Mn^{4+}$三掺磷酸盐玻璃和玻璃陶瓷的发光光谱。插图是相应的玻璃和玻璃陶瓷的发光照片。玻璃和玻璃陶瓷都发射白色光，但是玻璃陶瓷的发光强度明显要强于玻璃的。

Figure 6 is $Tm^{3+}/Tb^{3+}/Mn^{4+}$ tri-doped phosphate glass and glass ceramic at 360 nm light excitation. The inset is the photos of the $Tm^{3+}/Tb^{3+}/Mn^{4+}$ tri-doped phosphate glass and glass ceramic. The emission spectrum of the glass ceramic has covered the whole visible light range. Of special note, a very dazzling white disc appears on the glass ceramic sample. The emission intensity of the glass ceramic is approximately 20 times stronger than that of the glass.

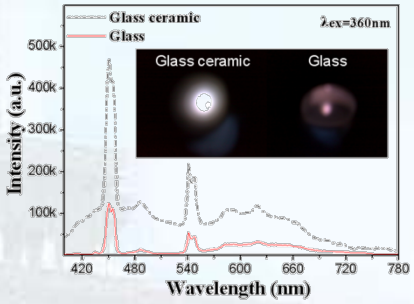

图 6 在 360nm 激发下，$Tm^{3+}/Tb^{3+}/Mn^{4+}$三掺磷酸盐玻璃和玻璃陶瓷的发光光谱。插图是相应的玻璃和玻璃陶瓷的发光照片。

Fig.6Emission spectra of the $Tm^{3+}/Tb^{3+}/Mn^{4+}$ tri-doped phosphate glass and glass ceramic at 360 nm light excitation. The inset is the photos of the $Tm^{3+}/Tb^{3+}/Mn^{4+}$ tri-doped phosphate glass and glass ceramic at 360nm light excitation.

结论：通过在 790K 热处理前驱玻璃我们得到了磷酸盐玻璃陶瓷，并且发现随热处理时间的增长，纳米晶的尺寸和类型都发生转变。在光谱的测试中发现，玻璃陶瓷样品的发光要明显强于玻璃的。

Results: By annealing the precursor glasses at 790K, we obtained the phosphate glass ceramics. And we observed that the type and size had changed with the increasing of

annealing time. By measuring the luminescence spectra, we also found that the emission intensity of the glass ceramics are stronger than that of glass.

氟氧化物玻璃陶瓷的相关研究

对于氟氧化物玻璃陶瓷中微晶的结构、对称性和稀土离子在其中的占位情况进行了研究。通过热诱导腐蚀法获得的微晶水溶解决了对于其成分分析中玻璃基质的干扰问题。通过X射线衍射和能量散射谱提出微晶的$PbREF_5$模型，在不同的热诱导情况下，微晶的结构会发生一定程度的畸变。通过理论模拟对微晶结构进行了分析，对于之前在氟氧化物玻璃材料中的不同微晶模型进行了澄清。此外，通过实验还对于微晶形成的热力学和热动力学过程进行了研究。

综述了稀土掺杂的上转换发光材料和电子俘获材料在近红外激光检测卡上的应用。稀土掺杂的上转换发光材料主要利用多光子吸收原理将近红外光子转换为可见光，电子俘获材料主要通过光激励发光原理实现频率转换，通过这两大类材料的综述，理论上实现了从800 nm到2000 nm区域内的近红外光的连续探测。

研究了在氟氧化物玻璃陶瓷和碲酸盐玻璃陶瓷中Er^{3+}离子的量子剪裁过程和能量传递过程。

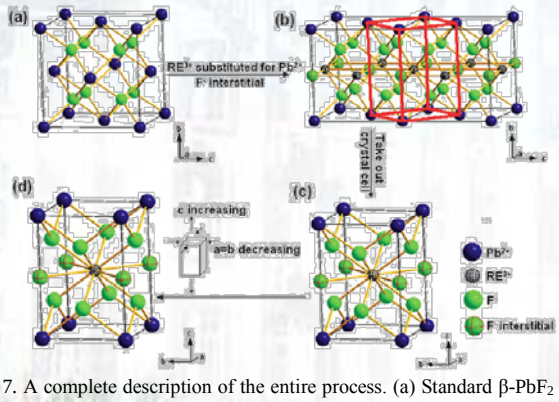

Fig. 7. A complete description of the entire process. (a) Standard β-PbF_2 crystal, which has a typical face-centered cubic structure. (b) The super ''pseudo-cubic'' cell (thin black frame) forms by RE^{3+} substitution for Pb^{2+} and F^- interstitial. (c) Crystal cell of low temperature group sample taken out from the pseudo-cubic cells as thick red frame. (d) Crystal cell of high temperature group sample by a (= b) decreasing and c increasing from the crystal cell of the low temperature group sample.

Rare-earth doped oxyfluoride glasses and nanocrystalline glass ceramics have been prepared and studied by energy dispersive X-ray spectroscopy (EDS) and X-ray diffraction (XRD) aiming at investigating the structure and the symmetry of the nanocrystal as well as the site of the rare-earth ion. To solve the problem encountered by previous researchers due to glass host interference, we etched off glass matrix and released the fluoride nanocrystal, which is more convenient for EDS measurement. A tetragonal phase model with the chemical formula as PbREF5 proved by quantitative EDS and XRD analyses has been proposed in this paper for the first time. Two specific crystalline phases with the same space group have been observed at 460 ℃–500 ℃ and 520 ℃–560 ℃, respectively. Moreover, a super ''pseudo-cubic'' cell based on our tetragonal model may give a good explanation to the probable previous cubic-symmetry misunderstanding by researchers. Additionally, the thermodynamic mechanism of phase transition and the thermal stability related to the structure of nanocrystals in glass ceramics have been studied and supported by *ab initio* calculations and experimental methods. The structure and thermal stability of the nanocrystal and clear environment of the rare-earth ion reported here have far-reaching significance with respect to the optical investigations and further applications of rare-earth doped oxyfluoride glass ceramics.

Near-infrared laser has been more widely in the areas of military and medical applications. However, near-infrared light is not visible, so applications and experiments need to detect card. Electron trapping material can convert near infrared laser to visible light by means of photostimulated luminescence. The up-conversion luminescent materials can also performance the process though the multi-photon absorption. The

detection card made by electron trapping materials or up-conversion luminescent materials is used to detect near infrared laser. From the review of two types of materials, the novel near-infrared laser detection card could be applied wavelength range from 800 nm to 2000 nm.

The quantum cutting and energy transfer processes of rare earth ions were researched in oxyfluoride and tellurate glass ceramics.

半导体生长技术和半导体器件/ Semiconductor Growth and Devices

负责人：舒永春

2010 年度本方向主要在以下方面取得了进展：

This year, we obtained some important results, they are mainly shown as following:

硅基发光器件的研究进展

（1）搭建了光致发光和电致发光测量系统利用 Laview 程序将锁相放大器、高压源表、光谱仪和数据采集系统结合起来，实现了光致发光光谱、激发光谱、电致发光光谱、光强－电流－电压特性、电致发光老化的自动化测量，如图 1 所示。程序方框图如图 2。系统可以测量红外－紫外波段的光谱，电流范围 10pA－1A， 电压 0-1100V，最低探测光强极限小于 1 纳瓦。

图 1.电致发光、光致发光、I-V，L－I－V 综合自动测量系统

Fig.1 the automatic EL and PL measurement system and the programs

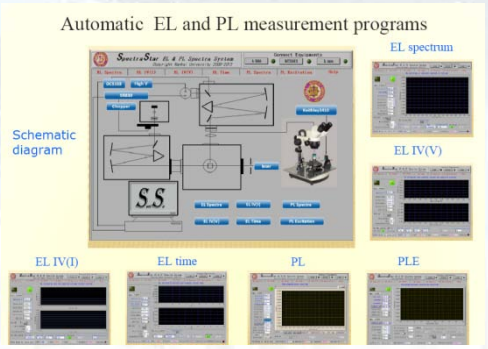

图 2.程序方框图

Fig.2 the automatic EL and PL measurement programs

PL, EL and optoelectrical system has been set up.We have set up a photoluminescence and electroluminescence study system with Labview program. Fig.1 and Fig.2 show the automatic EL and PL measurement system and the programs. With this system we can measure photoluminescence spectra from ultraviolet to near infrared (200-1700nm). Electroluminescence from silicon pn diodes and MOS light emitting devices at constant current from 10pA to 1A or constant voltage from 0-1100V. I-V-L characteristics in a current controlled or voltage controlled mode. The sensitivity of the system are very high, the lowest detectable light intensity <1nW.

建立起了一套硅基电致发光器件工艺线。包含硅片标准清洗柜原子层沉积系统，用来制备高质量稀土掺杂的 SiO_2 发光薄膜，HfO_2 high-K 薄膜等，超声波雾化热分解透明 ITO 薄膜沉积系统，真空热蒸发技术金属薄膜沉积系统，光刻系统和旋转涂敷系统。

A processing line for silicon based MOS light emitting devices has been installed including Silicon wafer cleaning. An atomic layer deposition system for deposition of rare-earth oxide, HfO_2 high-K dielectric layers, and SiO_2 layer doped with rare earths. Ultrasonic Spray Pyrolysis Method for deposition of transparent ITO electrode. Vacuum thermal evaporation system for Al Au and Ag metallic films. Photolithography system and spin coating system.

（2）确定了电致发光器件的标准 MOS 工艺流程，最终制备的硅基 MOS 电致发光器件 ITO/SiON/Si-rich$SiOB_{2B}$ /Si MOS 电致发光器件。

Er-doped silicon nanocluster based MOS light emitting devices have been processed with a structure of ITO/SiON/Si-rich$SiOB_{2B}$ /Si.

纳米硅的强烈敏化作用使 Er 离子的红外发光增强了 2 个数量级。在功率 20 mW、波长 405 nm 的 GaN 激光器激发下，可以观测到来自纳米硅和 Er 离子的强烈光致发光。图 3 为具有不同过量纳米硅浓度的富硅

$TSiOB_{2B}$ 薄膜的光致发光光谱。当纳米硅浓度大于 5% 时，来自纳米硅微晶法人发光峰随着纳米硅浓度的增大显著增强，随着富硅含量的增加，纳米硅的直径增大，相应的发光峰发生红移，符合低维半导体的量子尺寸效应。

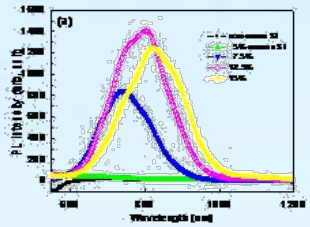

图 3. 具有不同过量纳米硅浓度的富硅 SiO_2 薄膜的光致发光光谱。

Fig.3 PL spectra from the Si-rich SiO2 films containing different excess Si concentrations of 0,5,7.5,12.5 and 15%.

图 4 为 1.5% Er掺杂的分别具有 0、5、7.5、12.5 过量纳米硅浓度的Si-rich SiO_2：Er薄膜的光致发光光谱，可以看出，当纳米硅浓度大于 5% 时，来自Er的红外发光峰值随着纳米硅浓度的增大显著增强，比不含纳米硅的样品增强两个数量级，这表明，在Er掺杂的富硅SiO_2 薄膜中，来自纳米硅的能量转移对于Er离子的光致发光具有很大的增强作用。

Efficient photoluminescence from the silicon nanoclusters in Si-rich SiO_2 has beeen observed, and strong energy transfer from silicon cluster to Er luminescent centers causes a strong increased of the luminescence efficiency of the infrared emission. Fig.3

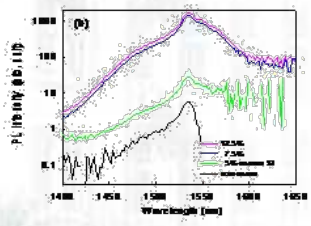

图 4. 1.5%Er 掺杂的分别具有不同过量纳米硅浓度的 Si-richSiO_2：Er 薄膜的光致发光光谱

Fig.4 PL spectra from the 1.5% Er doped Si-rich SiO2:Er films containing different excess Si concentrations of 0,5,7.5,12.5 and 15%.

shows the PL spectra from the Si-rich SiO_2 films containing different excess Si concentrations of 0, 5 ,7.5, 12.5 and 15%. Fig.4 shows the PL spectra from the 1.5% Er doped Si-rich SiO_2:Er films containing different excess Si concentrations of 0,5,7.5,12.5 and 15%.

（3）利用 SiON 缓冲层结构提高了电致发光器件的稳定性。通过采用 SiON 缓冲层符合薄膜结构，制备出 ITO/SiON/Si-rich SiO_2:Er/Si MOS 结构电致发光器件，图 5 是器件结构示意图。为了增加光耦合输出效率，表面电极采用 100 nm 的透明 ITO 导电层。图 6 为固定 SiO_2：Er 发光层厚度，MOS 结构的 I-V 特性随 SiON 缓冲层厚度的变化曲线。其中 SiON 缓冲层显著提高了电致发光器件的工作电压和电流范围， 提高了电致发光器件的稳定性和可靠性，器件的平均寿命提高了四个量级。

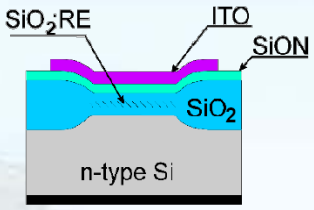

图 5. 复合栅层 MOS 结构电致发光结构简图。结构中 SiON 作为器件的防击穿缓冲层。

Fig.5 Scheme of the Double-gate layer MOS EL structure.

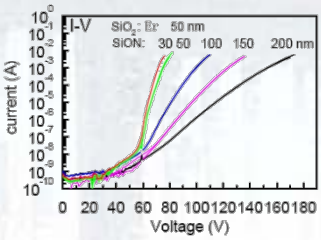

图 6 固定 SiO_2：Er 发光层厚度，MOS 结构的 I-V 特性随 SiON 缓冲层厚度的变化。

Fig.6 I-V characteristics of the MOS structure with different thickness of SiON buffer layer and fixed thickness of SiO2:Er light-emitting layer

The stability of the MOS light emitting devices was strongly improved with SiON buffer layers in the MOS devices.Fig.5 shows the scheme of the Double-gate layer MOS EL structure. Fig.6 is the I-V characteristics of the MOS structure with different thickness of

SiON buffer layer and fixed thickness of SiO_2:Er light-emitting layer.

（4）获得了较强的红外电致发光。系统研究了硅微晶密度的变化对于 MOS 结构的电致发光影响。主要结果如图 7、图 8 所示：与光致发光相反，随着纳米硅微晶的增多，电致发光效率有所降低。其原因为增加纳米硅微晶数量的同时也增加了 SiO_2 薄膜中的电子俘获陷阱，在电场作用下，纳米硅中的激子在空间上分离为电子和空穴，电子和空穴在纳米硅微晶之间的隧穿降低了过热电子的数量和平均能量，因而降低了碰撞激发 Er 离子产生的电致发光效率。

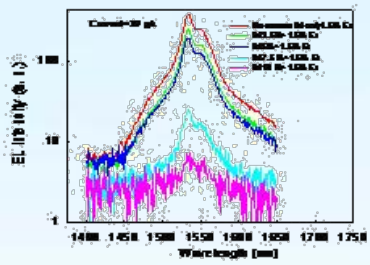

图 7. 1.5%Er 掺杂的分别具有不同过量纳米硅浓度的 Si-richSiO$_2$：Er 薄膜的电致发光光谱， 器件直径 0.5 mm，电流为 100 微安。

Fig.7 EL spectra from the 1.5% Er doped Si-rich SiO2:Er films containing different excess Si concentrations of 0,2.5, 5,7.5 and 10%

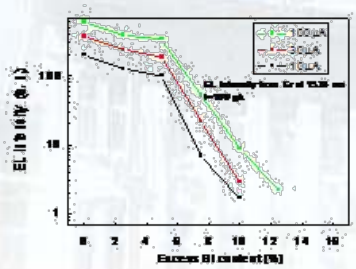

图 8. 1.5%Er掺杂的分别具有不同过量纳米硅浓度的Si-rich SiO$_2$：Er薄膜的电致发光强度随纳米硅含量的关系。

Fig.8 The relationship of EL intensity from the 1.5% Er doped Si-rich SiO2:Er films with the excess Si content.

Strong infrared electroluminescence from Er doped silicon rich SiO_2 MOS devices has been observed. Fig.7 EL spectra from the 1.5% Er doped Si-rich SiO_2:Er films containing different excess Si concentrations of 0,2.5, 5,7.5 and 10%.Fig.8 shows the relationship of EL intensity from the 1.5% Er doped Si-rich SiO_2:Er films with the different content of excess Si.

MBE 工作汇报

The MBE working report

利用变温光致发光（PL）研究了 $In_{0.182}Ga_{0.818}As/GaAs$ 应变及应变补偿三量子阱样品在 77 ~ 300 K 温度范围内的发光特性，如图 9 所示。通过理论分析和计算，研究了量子阱中的应力对变温光致发光谱变化规律的影响。在 Varshni 公式基础上，引入由应力导致的带隙能量变化 ΔE_g 项，ΔE_g 是温度和组分的函数。带隙能量计算结果与实验数据具有较好的吻合，如图 10 所示。

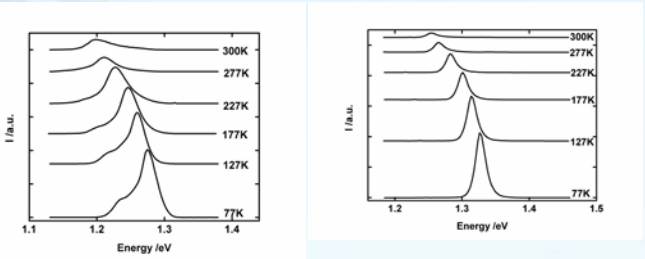

图 9 $In_{0.182}Ga_{0.818}As/GaAs$ 三量子阱变温光致发光谱：（a）应变 （b）应变补偿。

Fig.9 Photoluminescence spectra of $In_{0.182}Ga_{0.818}As/GaAs$ three quantum wells at various temperatures: (a) strained; (b) strain-compensation.

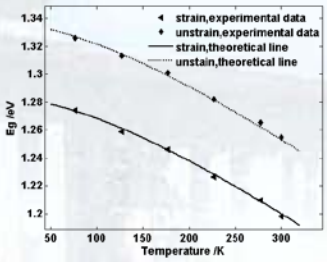

图 10 $In_{0.182}Ga_{0.818}As/GaAs$ 应变及应变补偿三量子阱带隙与温度的关系

Fig.10 Dependence of temperature on energy gap of $In_{0.182}Ga_{0.818}As/GaAs$ strained and strain-compensation three quantum wells

The variable-temperature photoluminescence (PL) spectra of $In_{0.182}Ga_{0.818}As/GaAs$ strained and strain-compensation three quantum wells (QWs) were experimentally determined in the temperature range 77～300 K, as shown in Fig.9. A theoretical calculation was presented

that takes into account the temperature-induced variations in band gap and biaxial strain to explain the PL spectra. Based on the Varshni relationship, the change of the band gap energy ΔE_g caused by the strain was introduced. ΔE_g is the function of the temperature and the alloy composition. The calculated results are in good agreement with the experimental results, as shown in Fig.10.

建立了 III-V 族三元化合物半导体材料的 MBE 生长热力学模型，与我们的实验材料 InGaP/GaAs, InGaAs/InP 及已发表的 GaAsP/GaAs, InAsP/InP 的数据具有很好的吻合。如图 11 和图 12 所示。首次将晶格应变能 ΔG 及脱附对温度敏感这两个因素同时纳入热力学模型之中。束流和生长温度直接影响合金组分，晶格应变能是合金组分的函数。热力学模型计算结果反映了束流和生长温度是生长过程中最主要的影响因素。

Thermodynamic models for molecular-beam epitaxy (MBE) growth of ternary III-V semiconductor materials are proposed, which are in agreement with our experimental materials InGaP/GaAs, InGaAs/InP and reported data about GaAsP/GaAs, InAsP/InP. As shown in Fig.11 and Fig.12. The lattice strain energy ΔG and thermal decomposition sensitized to growth temperature are demonstrated in the models simultaneously for the first time. ΔG is the function of the alloy composition, which affected by flux ratio and growth temperature directly. The calculation results reveal that flux ratio and growth temperature most strongly influence the growth processes.

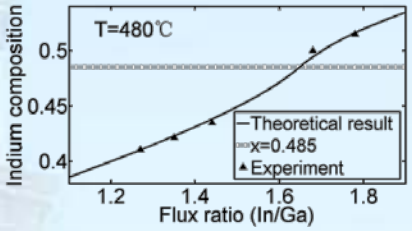

图 11. In/Ga 束流比对 $In_xGa_{1-x}P/GaAs$ 外延层 In 组分的影响

Fig. 11 Dependence of the In/Ga flux ratio on indium composition x of $In_xGa_{1-x}P/GaAs$ at 480 ℃.

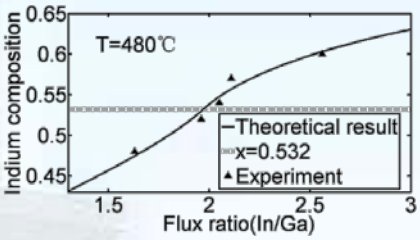

图 12. In/Ga 束流比对 $In_xGa_{1-x}As/InP$ 外延层 In 组分的影响

Fig. 12 Dependence of the In/Ga flux ratio on indium composition x of $In_xGa_{1-x}As/InP$ at 480 ℃

光场调控及其应用/Manipulation of Optical Fields and Its Application

负责人：王慧田

本方向主要开展连续光和飞秒脉冲矢量光场和光学涡旋等新型光场的调控生成、焦场工程、非线性光学效应、微加工和微操纵等方向的研究。取得的代表性成果如下：

In this field, we mainly focused on the generation of the new optical fields such as vector fields and optical vortex by continuous wave and femtosecond pulse; the focusing engineering, the nonlinear effect, the micro manipulation and fabrication by the new optical fields. This year, we obtained some respective results as following.

与均匀偏振标量光场相比，矢量光场有许多独特的性质由于空间非均匀偏振态的分布，引起了广泛关注。以往生成的矢量光场集中于局域线偏振分布，基于庞加莱球（如图 1 所示），我们打破这一局限，提出了一种生成具有局域线偏振、椭圆偏振和圆偏振分布的杂化偏振矢量光场的方法并实验验证。作为一个例子，图 2 示出了生成的杂化偏振矢量光场。其重要性在于：提出了一种灵活的、原理上可以生成任意偏振分布矢量光场的途径；生成的矢量光场与物质相互作用可以导致新奇的效应与应用。

In recent years, vector fields have attracted significant interest due to the unique feature compared with homogeneously polarized beams. Unlike the previous vector fields with local linear state of polarization (SoP), we present an idea based on the Poincaré sphere (as shown in Fig. 1) and demonstrate the creation of a new type of vector fields, which have hybrid states of polarization. Such a type of vector fields have completely different property from the reported scalar and vector fields. As an example, the generated vector fields with hybrid SoPs are shown in Fig. 2. It is important to propose a flexible technique to generate arbitrary vector fields in principle. The novel vector fields are anticipated to result in new effects, phenomena, and applications.

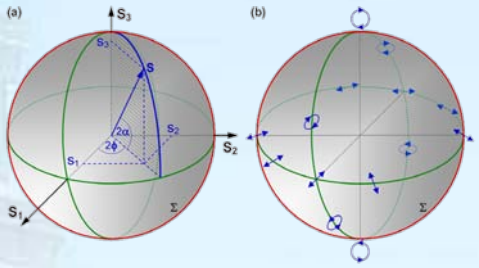

图 1 (a)庞加莱球和(b)不同偏振态在庞加莱球上的表示。

Fig. 1. (a) The Poincaré sphere and (b) different SoPs on the Poincaré sphere.

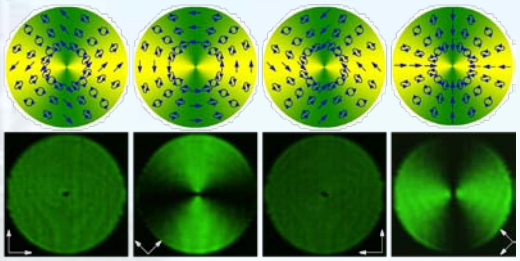

图 2. 四种不同杂化偏振态矢量光场。第一行为偏振态分布，第二行为通过水平偏振片的光强分布图。

Fig. 2. Created four different vector fields with hybrid SoPs, the SoPs (the first row) and the intensity patterns behind the horizontal polarizer (the second row).

杂化偏振矢量光场能够产生一类新的光学轨道角动量。众所周知，光场可以携带自旋角动量和轨道角动量，自旋角动量仅具有两个可能量子化值$\pm\hbar$，分别对应于右旋和左旋圆偏振光。已知的 光学轨道角动量仅由具有螺旋位相 $\exp(-j\ell\phi)$的光学涡旋携带且具有量值 $\ell\hbar$，其中ϕ为极坐标系中的方位角，而整数 ℓ 为螺旋位相的拓扑数。显然，这种轨道角动量源于角向变化位相的梯度。自然地提出一个问题，偏振作为光场的另一个重要属性，偏振态的空间分布是否也可以产生光学轨道角动量？我们从理论上预言偏振的旋度(而非梯度)可以产生轨道角动量。在实验上，设计并生成了沿径向变化的杂化

偏振矢量光场(如图 3 所示)，进而光镊实验(如图 4 所示)观测到被俘获的各向同性聚苯乙烯微球沿着聚焦环轨道移动(如图 5 所示)。实验结果证实了我们的理论预言，源于偏振旋度的光学轨道角动量存在。研究成果发表在 Physical Review Letters 上。其重要性在于：在光学轨道角动量与矢量光场两个重要领域建起了一座桥梁，打破了光偏振不能作用于各向同性材料的观念，激发了具有轨道角动量其它种类波的生成，有助于诸多光学系统功能的拓展和新奇的应用。

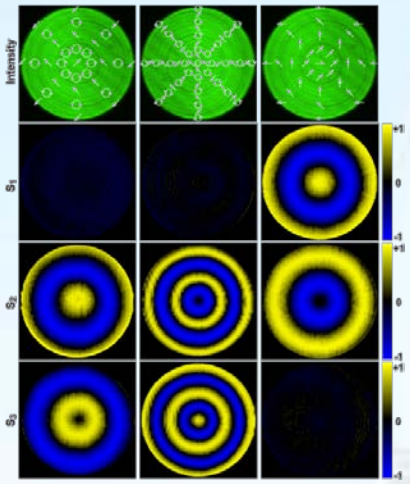

图 3. 沿径向变化杂化偏振矢量光场实验结果图。第一栏为光强和偏振态分布，第二、三、四栏为斯托克斯参量分布图。

Fig. 3. Experimental results for the vector fields with spatial-variant SoPs. Intensity patterns and the schematics of SoPs (the first row) and the measured Stokes parameters (the rest three rows).

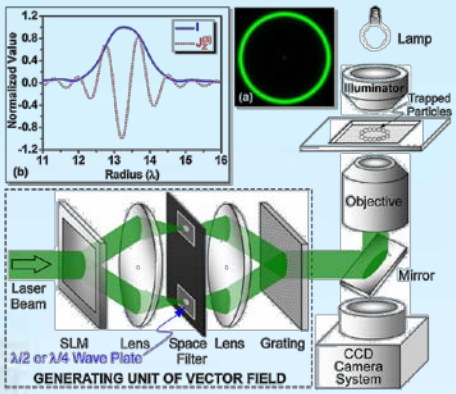

图 4. 利用光镊验证轨道角动量实验装置图。（a）理论计算聚焦环光强分布图，（b）沿径向光强（蓝色）和轨道角动量（红色）分布图。

Fig. 4. Experimental configuration to validate OAM associated with the curl of polarization. The dashed-line box shows the generating unit of radial-variant vector fields. Inset (a) shows an example of simulated ring focus. Inset (b) shows the properties of the ring focus for a radial-variant vector field with hybrid SoPs, where the blue and red lines are the radial dependences of intensity and OAM respectively.

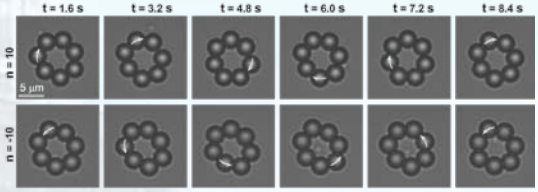

图 5. 光学轨道角动量旋转粒子实验结果图。

Fig. 5. Snapshots of the motion of trapped particles around the ring focus generated by radial-variant vector fields with hybrid SoPs, caused by polarization-curl-induced OAM.

Vector fields with hybrid SoPs could result in a new category of optical orbital angular momentum (OAM). As is well known, a light field can carry spin angular momentum (SAM) or OAM. As an intrinsic part of the nature of a light field, SAM is associated with circular polarization and has two possible quantized values of $\pm\hbar$. The previous OAM is carried by an optical vortex with helical phase $\exp(-j\ell\phi)$ and has a value of $\ell\hbar$, where ϕ is the azimuth angle in polar coordinate and the integer ℓ is the topological of the vortex phase. The present OAM is resulted from the azimuthal phase gradient. Evidently, the space-variant phase is a prerequisite for possibility of producing optical OAM caused by the phase. The question is whether the polarization as a fundamental nature of light can also be used to produce optical OAM. It is imaginable that the light fields with the space variant distribution of SoPs have the possibility of carrying OAM. We predict a new category of optical orbital angular momentum that is associated with the curl (not the gradient) of polarization in theory. In experiment, we design and generate vector fields with radial-variant SoPs as shown in Fig. 3, then the created vector fields are used in an

optical tweezers experiment as shown in Fig. 4. The orbital motions of the trapped optical isotropic particles are observed. The experiments agree well with our theoretical prediction and the OAM from the curl of polarization was validated. The work was published on the Physical Review Letters. Our results create a link between two important issues on optical OAM and vector field. As we predicted, the induction of the vector fields breaks the limitation that the polarization nature of light field can not influence optical isotropic materials. Our idea may spur further independent insights into the generation of natural waves carrying OAM and the expansion of the functionality of many optical systems, thereby facilitating the development of additional surprising applications.

发表论文/Publications in Journal

1. Fu-Cai Liu, Yong-Fa Kong, Wei Li, Hong-De Liu, Shi-Guo Liu, Shao-Lin Chen, Xin-Zheng Zhang, Romano Rupp and Jingjun Xu, “High resistance against ultraviolet photorefraction in zirconium-doped lithium niobate crystals”, *Opt. Lett.*, 35(1), 10-12 (2010). * (Research Highlights, *Nature Photonics*, Vol.4, March 2010)
2. Wang XiLin, Chen Jing, Li Yongnan, Ding Jianping, Guo Chengshan, and Wang Huitian, “Optical Orbital Angular Momentum from the Curl of Polarization”, *Phys. Rev. Lett.* 105, 253602 (2010). *
3. Hao Zeng, Yong-Fa Kong, Tian Tian, Shao-Lin Chen, Ling Zhang, Tong-Qing Sun, Romano Rupp and Jing-Jun Xu, “Transcription of domain patterns in near-stoichiometric magnesium-doped lithium niobate”, *Appl. Phys. Lett.* 97, 201901 (2010). *
4. Jianxing Li, Weiping Zang, and Jianguo Tian, “Electron acceleration in vacuum induced by a tightly focused chirped laser pulse,” *Appl. Phys. Lett.* 96, 031103 (2010). *
5. Fu-Cai Liu, T. Makino, H. Hiraga, T. Fukumura, Yong-Fa Kong and M. Kawasaki, “Ultrafast dynamics of excitons in delafossite $CuScO_2$ thin films”, *Appl. Phys. Lett.* 96, 211904 (2010).
6. Gu B, Ji W, Yang HZ, and Wang HT, “Theoretical and experimental studies of three-photon-induced excited-state absorption”, *Appl. Phys. Lett.* 96, 081104 (2010).
7. Xinzheng Zhang, Jun Li, Fan Shi, Yan Xu, Zhenhua Wang, Romano A. Rupp, and Jingjun Xu, “Light- controllable coherent backscattering from water suspension of lithium niobate microcrystalline particles”, *Opt. Lett.* 35(11), 1746-1748 (2010). *
8. Y. Hu, S. Huang, P. Zhang, C. Lou, J. Xu, and Z. Chen, "Persistence and breakdown of Airy beams driven by an initial nonlinearity," *Opt. Lett.* 35, 3952-3954 (2010). *
9. Jianxing Li, Weiping Zang, and Jianguo Tian, “Analysis of electron capture acceleration channel in an Airy beam,” *Opt. Lett*. 35, 3258-3260 (2010). *
10. H. Z. Kang, T. H. Zhang, H. H. Ma, C. B. Lou, S. M. Liu, J. G. Tian, and J. J. Xu, “Giant enhancement of surface second-harmonic generation using photorefractive surface waves with diffusion and drift nonlinearities,” *Opt. Lett.* 35, 1605-1607 (2010). *
11. Y. Hu, P. Zhang, C. Lou, S. Huang, J. Xu, and Z. Chen, "Optimal control of the ballistic motion of Airy beams," *Opt. Lett.* 35, 2260-2262 (2010).
12. D. Song, X. Wang, D. Shuldman, J. Wang, L. Tang, C. Lou, J. Xu, J. Yang, and Z. Chen, "Observation of bandgap guidance of optical vortices in a tunable negative defect," *Opt. Lett.* 35, 2106-2108 (2010).
13. Xinyuan Qi, Ivan L. Garanovich Andrey A. Sukhorukov, Wieslaw Krolikowski, Arnan Mitchell, Guoquan Zhang, Dragomir N. Neshev, and Yuri S. Kivshar, "Polychromatic solitons and symmetry breaking in periodically curved waveguide arrays", *Opt. Lett.* 35, 1371-1373 (2010).
14. P. Zhang, C. Lou, S. Liu, J. Zhao, J. Xu, and Z. Chen, "Tuning of Bloch modes, diffraction, and refraction by two-dimensional lattice reconfiguration," *Opt. Lett.* 35, 892-894 (2010).
15. P. Zhang, S. Huang, Y. Hu, D. Hernandez, and Z. Chen, "Generation and nonlinear self-trapping of optical propelling beams," *Opt. Lett.* 35, 3129-3131 (2010).

---

* 选录论文/Selected papers

16. P. Zhang, N. K. Efremidis, A. Miller, Y. Hu, and Z. Chen, "Observation of coherent destruction of tunneling and unusual beam dynamics due to negative coupling in three-dimensional photonic lattices," *Opt. Lett.* 35, 3252-3254 (2010).
17. Wen-Bo Yan, Li-Hong Shi, Hong-Jian Chen, Xin-Zheng Zhang and Yong-Fa Kong, "Investigations on the UV photorefractivity of $LiNbO_3$:Hf", *Opt. Lett.*, 35(4), 601-603 (2010).
18. Li-Zhong Wang, Shi-Guo Liu, Yong-Fa Kong, Shao-Lin Chen, Zi-Heng Huang, Li Wu, Romano Rupp and Jing-Jun Xu, "Increased optical damage resistance in Tin doped lithium niobate", *Opt. Lett.*, 35(6), 883-885 (2010).
19. Wen-Jie Wang, Yan Sheng, Yong-Fa Kong, Ady Arie and Wieslaw Krolikowski, "Multiple Čerenkov second-harmonic waves in a two-dimensional nonlinear photonic structure", *Opt. Lett.*, 35(22), 3790-3792 (2010).
20. Gu B, Lou K, Wang HT, and Ji W, "Dynamics of two-photon-induced three-photon absorption in nanosecond, picosecond, and femtosecond regimes", *Opt. Lett.* 35, 417 (2010).
21. Chengliang Yang, Qiang Wu, Jingjun Xu, Keith A. Nelson, and Christopher A. Werley, "Experimental and theoretical analysis of THz-frequency, direction-dependent, phonon polariton modes in a subwavelength, anisotropic slab waveguide", *Opt. Express* 18, 26351-26364 (2010). *
22. Zhe Wang, Qiang Wu,Chengliang Yang, Xinzheng Zhang, Zhigang Chen, Romano A. Rupp, and Jingjun Xu， "Nonlinear spectrum broadening of femtosecond laser pulses in photorefractive waveguide arrays", *Opt. Express* 18, 10112-10119 (2010).
23. Y. Hu, R. Egger, P. Zhang, X. Wang, and Z. Chen, "Interface solitons excited between a simple lattice and a superlattice," *Opt. Express* 18, 14679-14684 (2010).
24. D. Song, C. Lou, K. J. H. Law, L. Tang, Z. Ye, P. G. Kevrekidis, J. Xu, and Z. Chen, "Self-trapping of optical vortices at the surface of an induced semi-infinite photonic lattice," *Opt. Express* 18, 5873-5878 (2010).
25. Yiling Qi and Guoquan Zhang, "Linear discrete diffraction and transverse localization of light in two-dimensional backbone lattices", *Opt. Express* 18, 20170 (2010).
26. Zu-Bin Li, Wen-Yuan Zhou, Xiang-Tian Kong, and Jian-Guo Tian, "Polarization dependence and independence of near-field enhancement through a subwavelength circle hole," *Opt. Express* 18, 5854-5860 (2010).
27. Xiao-Qing Yan, Zhi-Bo Liu, Xiao-Liang Zhang, Wei-Ping Zang, and Jian-Guo Tian, "Modified elliptically polarized light Z-scan method for studying third-order nonlinear susceptibility components," *Opt. Express* 18, 10270-10281 (2010).
28. Xiao-Qing Yan, Zhi-Bo Liu, Shuo Shi, Wen-Yuan Zhou, and Jian-Guo Tian, "Analysis on the origin of the ultrafast optical nonlinearity of carbon disulfide around 800 nm," *Opt. Express* 18, 26169-26174 (2010).
29. Jianxing Li, Weiping Zang, and Jianguo Tian, "Vacuum laser-driven acceleration by Airy beam," *Opt. Express* 18, 7300-7306 (2010).
30. Hua Cheng, Weiping Zang, Wenyuan Zhou, and Jianguo Tian, "Analysis of optical trapping and propulsion of Rayleigh particles using Airy beam," *Opt. Express* 18, 20384-20394 (2010).

31. Lihua Zhao, Yudong Li, Jiwei Qi, Jingjun Xu1 and Qian Sun “Quasi 3-dimensional optical trapping by two counter-propagating beams in nano-fiber”, *Opt. Express* 18, 5724-5729 (2010).
32. Fu-Cai Liu, Yong-Fa Kong, Xin-Yu Ge, Hong-De Liu, Shi-Guo Liu, Shao-Lin Chen, Romano Rupp and Jing-Jun Xu, “Improved sensitivity of nonvolatile holographic storage in triply doped $LiNbO_3$:Zr,Cu,Ce”, *Opt. Express*, 18(6), 6333-6339 (2010).
33. V. Roppo, W. Wang, K. Kalinowski, Y. Kong, C. Cojocaru, J. Trull, R. Vilaseca, M. Scalora,W. Krolikowski and Yu. Kivshar, “The role of ferroelectric domain structure in second harmonic generation in random quadratic media”, *Opt. Express*, 18(5), 4012-4022 (2010).
34. Wen-Bo Yan, Li-Hong Shi, Hong-Jian Chen, Xu-Nan Shen and Yong-Fa Kong, “Light scattering induced by opposite microdomains in $LiNbO_3$:Fe:Hf crystals”, *Opt. Express*, 18(11) 11949-11954 (2010).
35. Ying-jie Zhang, Ruo-yang Zhang, Qing-ru Wang, Zhi-shuai Zhang, Hai-bo Zhu, Jia -dong Liu, Feng Song*, Shan-xin Lin, Edwin Yue Bun Pun, “Fluorescence enhancement of quantum emitters with different energy systems near a sigle spherical metal nanoparticles”, *Opt. Express*, 18, 4316-4328 (2010).
36. Tu CH, Huang ZC, Lou K, Liu HJ, Wang YS, Li YN, Lu FY, Wang HT, “Efficient green-light generation by frequency doubling of a picosecond all-fiber ytterbium-doped fiber amplifier in PPKTP waveguide inscribed by femtosecond laser direct writing”, *Opt. Express* 18, 25183 (2010).
37. Gu B, Lou K, Chen J, Li YN, Wang HT, and Ji W, “Excited-state enhancement of third-order optical nonlinearities: photodynamics and characterization”, *Opt. Express* 18, 26843 (2010).
38. Wang XL, Li YN, Chen J, Guo CS, Ding JP, and Wang HT, “A kind of new vector fields with hybrid states of polarization and spatial-variant spin-angular momentum”, *Opt. Express* 18, 10786 (2010).
39. Bai Q, Chen J, Shen NH, Cheng C, and Wang HT, “Controllable optical black hole in left-handed materials”, *Opt. Express* 18, 2106 (2010).
40. P. Zhang, S. Liu, C. Lou, F. Xiao, X. Wang, J. Zhao, J. Xu, and Z. Chen, "Incomplete Brillouin-zone spectra and controlled Bragg reflection with ionic-type photonic lattices," *Physical Review A* 81, 041801 (2010).
41. Jianbin Liu and Guoquan Zhang, "Unified Interpretation for the Second-order Subwavelength Interference Based on Feynman's path integral theory", *Phys. Rev. A* 82, 013822 (2010).
42. Wei Cai, Lei Wang, Xinzheng Zhang, Jingjun Xu, and F. Javier García de Abajo, "Controllable excitation of gap plasmons by electron beams in metallic nanowire pairs", *Phys. Rev. B* 82, 125454-5 (2010).
43. Zhou XF, Qian GR, Dong X, Zhang L, Tian Y, and Wang HT, “Ab initio study of the formation of transparent carbon under pressure”, *Phys. Rev. B* 82, 134126 (2010).
44. Zhou XF, Dong X, Qian GR, Zhang L, Tian Y, and Wang HT, “Unusual compression behavior of TiO2 polymorphs from first principles”, *Phys. Rev. B* 82, 060102 (R) (2010).
45. Kang M, Li YN, Chen J, Chen J, Bai Q, Wang HT, and Wu PH, “Slow light in a simple metamaterial structure constructed by cut and continuous metal strips”, *Appl. Phys. B* 100, 699 (2010).

46. Bai Q, Liu C, Chen J, Fan YX, and Wang HT, "Actively-controlled polarization independent extraordinary electromagnetic transmission in one-dimensional metal gratings", *Appl. Phys. B* 98, 681 (2010).
47. Meixiu Sun, Chunping Zhang, Shengwen Qi, Yeqing Su, and Jianguo Tian, "Effect of surface roughness on the determination of tissue optical properties," *Optik* 121, 373-377 (2010).
48. Yongliang Liu, Weiping Zang, Zhibo Liu, Shengwen Qi, and Jianguo Tian, "Study on Z-scan characteristics of multilayer nonlinear media using coordinate transformation method," *Optik* 121, 2172-2175 (2010)
49. Xiuqin Yang, Chunping Zhang, Shengwen Qi, Guang Yang, Guiying Chen, and Jianguo Tian, "The dynamic characteristics of self-diffraction efficiency of azo polymer film," *Optik* 121, 506-510 (2010).
50. Xinyuan Qi, Ivan L. Garanovich, Zhiyong Xu, Andrey A. Sukhorukov, Wieslaw Krolikowski, Arnan Mitchell, Guoquan Zhang, Dragomir N. Neshev, and Yuri S. Kivshar, "Nonlinear surface waves in arrays of curved waveguides", *Photonics and Nanostructures* – Fundamentals and Applications 8, 62-66 (2010).
51. Jiajie Liang, Yongsheng Chen, Yanfei Xu, Zhibo Liu, Long Zhang, Xin Zhao, Xiaoliang Zhang, Jianguo Tian, Yi Huang, Yanfeng Ma, and Feifei Li, "Fabrication of Graphene-Based Flexible Electronic Circuits and Memory Cards Using Maskless Laser Direct-Writing," *ACS Appl. Mater. Interfaces* 2, 3310-3317 (2010).
52. Lu KQ, Miao CY, Wei JF, Zhang YP, Xu, JJ, "Sequential formation of incoherent multiple gray solitons in biased photorefractive-photovoltaic crystals", *Optical Materials* 32 (5): 561-565 (2010).
53. Wei Liu, Jian-Guo Tian, Qing He, Feng-Yan Li, Chang-Jian Li, and Yun Sun, "In-situ electrical resistance measurement of the selenization process in the CuInGa-Se system," *Thin Solid Films* 519, 244-250 (2010).
54. X. K. Ren, D. Y. Yang, T. H. Zhang, S. Zhang, L. Zhou, J. G. Tiana, and J. J. Xu, "Polymeric photorefractive surface waves," *Opt. Commun.* 283, 3792-3797 (2010).
55. Wang J, Fan YX, Chen J, Gu B, and Wang HT, "Nonlinear properties of polyurethane-urea/multi-wall carbon nanotube composite films", *Optics & Laser Technology* 42, 956 (2010).
56. Tong-Qing Sun, Xiao-Dong Zhou, Xiao-Qing Wang, Guang-Qiu Shen, Yong-Fa Kong, Jing-Jun Xu and De-Zhong Shen, "Crystal growth and characterization of non-centrosysmmetric polyphosphates, type III KNd(PO3)4 and KGd(PO3)4", *J. Cryst. Growth*, 312(9), 1627-1631 (2010).
57. Uygun V. Valiev, Sharof A. Rakhimov, Nafisa I. Juraeva, Romano A. Rupp, Lijuan Zhao, Zhenhua Wang, ZhaoYang Zhai, John B. Gruber, and Gary W. Burdick, "Optical and magnetooptical properties of Ho3+:YGG"", *Phys. Status Solidi B* 247(1), 163–169 (2010).
58. Wen-Jie Wang, Ksawery Kalinowski, Vito Roppo, Yan Sheng, Kaloian Koynov, Yong-Fa Kong, Crina Cojocaru, Jose Trull, Ramon Vilaseca and Wieslaw Krolikowski, "Second-and third-harmonic parametric scattering in disordered quadratic media", *J. Phys. B: At. Mol. Opt. Phys.*, 43(21), 215404 (2010).

59. Fang Bo, Ze Liu, Feng Gao, Guoquan Zhang, and Jingjun Xu, "Slow and fast light in photorefractive GaAs-AlGaAs multiple quantum wells in transverse geometry", *J. Appl. Phys.* 108, 063101 (2010). *
60. Feifei Xin, Guoquan Zhang, Fang Bo, Haifeng Sun, Yongfa Kong, Jingjun Xu, Tatyana Volk, Natalia M. Rubinina, "Ultraviolet photorefraction at 325 nm in doped lithium niobate crystals", *J. Appl. Phys.* 107, 033113 (2009).
61. Hao Zeng, Yong-Fa Kong, Hong-De Liu, Shao-Lin Chen, Zi-Heng Huang, Xin-Yu Ge and Jing-Jun Xu, "Light-induced super low electric field for domain reversal in near-stoichiometric magnesium-doped lithium niobate", *J. Appl. Phys.*, 107, 063514 (2010).
62. Lanjun Luo, Feng Song, Xiaochen Yu, Wentao Wang, Chengguo Ming, "Intense 1.54μm fluorescence of Er^{3+}/Yb^{3+} codoped phosphate glass and the three-photon phenomenon of near infrared upconversion luminescence", *J. Appl. Phys.*, 107, 033110 (2010).
63. Bai Q, Liu C, Chen J, Cheng C, Kang M, and Wang HT, "Tunable slow light in semiconductor metamaterial in a broad terahertz regime", *J. Appl. Phys.* 107, 093104 (2010).
64. Kang M, Li YN, Lou K, Li SM, Bai Q, Chen J,and Wang HT, "Second-harmonic generation in one-dimensional metal gratings with dual extraordinary transmissions", *J. Appl. Phys.* 107, 053108 (2010).
65. Christopher A. Werley, Qiang Wu, Kung-Hsuan Lin, C. Ryan Tait, August Dorn, Moungi G. Bawendi, and Keith A. Nelson, "A comparison of phase sensitive imaging techniques for studying THz waves in structured $LiNbO_3$", *J. Opt. Soc. Am. B* 27, 2350-2359 (2010).
66. Baogang Zhu, Tianhao Zhang, Huihui Ma, Zheng Yan, Xu Yang, Xiao Li, Weiwei Shao, Cibo Lou, Xiangkui Ren, Jingjun Xu, and Jianguo Tian, "Photorefractive lattice surface waves with diffusion nonlinearity," *J. Opt. Soc. Am. B* 27, 1381-1387 (2010).
67. Gu B, Lou K, Chen J, Wang HT, and Ji W, "Determination of the nonlinear refractive index in multiphoton absorbers by Z-scan measurements", *J. Opt. Soc. Am. B* 27, 2438 (2010).
68. Xiangkui Ren, Tianhao Zhang, Huihui Ma, Weiwei Shao, Jingjun Xu, and Jianguo Tian, "Surface waves in two-photon photorefractive media," *Appl. Opt.* 49, 2215-2219 (2010).
69. J. Milavec, M. Devetak, J. Li, R A Rupp, B. Yao and I. Dreven˘sek-Olenik1, "Effect of structural modifications on the switching voltage of a holographic polymer-dispersed liquid crystal lattice", *J. Opt.* 12, 015106-8 (2010).
70. Cui-Feng Ying, Wen-Yuan Zhou, Qing Ye, Xiao-Liang Zhang, and Jian-Guo Tian, "Band-edge lasing in Rh6G-doped dichromated gelatin at different excitations," *J. Opt.* 12 115101 (2010).
71. X. K. Ren, D. P. Yang, T. H. Zhang, H. H. Ma, W. W. Shao, J. J. Xu, and J. G. Tian, "Photorefractive surface waves in liquid crystal," *J. Opt.* 12, 055201 (2010).
72. Wen-Bo Yan, Li-Hong Shi, Hong-Jian Chen, Xu-Nan Shen and Yong-Fa Kong, "Investigations of the OH^- absorption bands in congruent and near-stoichiometric $LiNbO_3$:Hf crystals", *Euro Phys. Lett.*, 91(3), 36002 (2010).
73. Meixiu Sun, Chunping Zhang, Chai Ying, Shengwen Qi, Yeqing Su, and Jianguo Tian, "Effect of surface roughness on measurement of light distribution in intralipid suspension," *J. Mod. Opt.* 57, 1598-1602 (2010).
74. Xu Zhang , Xiaoli Liu, Leiting Pan, Imshik Lee, "Magnetic fields at extremely low-frequency (50 Hz, 0.8 mT) can induce the uptake of intracellular calcium levels in osteoblasts", *Biochem. Biophys. Res. Commun.* 396(4), 662-666 (2010).

75. Xian Wu, Leiting Pan, Zhenhua Wang, Xiaoli Liu, Dan Zhao, Xinzheng Zhang, Romano A. Rupp, and Jingjun Xu, "Ultraviolet irradiation induces autofluorescence enhancement via production of reactive oxygen species and photodecomposition in erythrocytes", *Biochem. Biophys. Res. Commun.* 396(4), 999-1005 (2010).
76. Wenwu Sun, Leiting Pan, and Zhuang Ma, "Hypo-Osmotic Stress Enhances the Uptake of Polyethylenimine /Oligonucleotide Complexes in A549 Cells via Ca^{2+} Mobilization from Intracellular Stores", *Oligonucleotides* 20(2), 111-115 (2010).
77. Chengguo Ming, Feng Song, Yin Yu, "Calculation on the energy transition coefficient by up-conversion emission intensity ratio", *Journal of Alloys and Compounds*, 506, 33 (2010).
78. Chengguo Ming, Feng Song, Qingru Wang, Gong Zhang, Yin Yu, "Infrared-to-visible upconversion in Er^{3+} and Er^{3+}/Yb^{3+} activated Sb_2O_4 nanopowders prepared by sol-gel route", *Journal of Luminescence*, 131, 271 (2011).
79. Yang Meng, Zhen-Ni He, Jian Yin, Yu Zhang, and Tian-Hao Zhang, "Quantitative Algorithm for Melatonin Suppression by Light at Night," *Prog. Biochem. Biophys.* 37, 686-689 (2010).
80. L. Wu, J.C. Sun, Y. Zhang, S.F. Jin, Y.F. Kong and J.J. Xu, "Structure determination and relative properties of novel chiral orthoborate KMgBO3", *Inorg. Chem.*, 49, 2715-2720 (2010).
81. Yong-Qiang Cao, Tao He, Yong-Mei Chen and Ya-An Cao, "Fabrication of rutile TiO_2−Sn/anatase TiO_2−N heterostructure and its application in visible-light photocatalysis", *J. Phys. Chem. C*, 114(8), 3627-3633 (2010).
82. Meng Chen, Tong-Qing Sun, Hong Chen, Yu Zhang, Li Wu, Yong-Fa Kong and Jing-Jun Xu, "Synthesis and luminescence properties of Yb^{3+} and Er^{3+} doped $KLa(WO_4)_2$ nanoparticles", *J. Solid State Chem.*, 183(9), 2161-2165 (2010).
83. Nan Hu, Hua Yu, Ming Zhang, Pan Zhang, Ya-Zhou Wang and Li-Juan Zhao, "The tetragonal structure of nanocrystals in rare-earth doped oxyfluoride glass ceramics", *Phys. Chem. Chem. Phys.*, DOI: 10.1039/c0cp00903b.
84. Xiao-Liang Zhang, Zhi-Bo Liu, Xin Zhao, Wen-Yuan Zhou, and Jian-Guo Tian, "Nonlinear optical properties of hydroxyl groups modified multi-walled carbon nanotubes," *Chem. Phys. Lett.* 494, 75-79 (2010).
85. L. Wu, Y. Zhang, W.W. Su, Y.F. Kong and J.J. Xu, "Structural study of nonlinear optical borates $K_{1-x}Na_xSr_4(BO_3)_3$ ($x \leq 0.5$)", *Powder Diffr.*, 25, S11-S16 (2010).
86. Wei Li, Xinzheng Zhang, Zhenhua Wang, Qiang Wu, Longchang Liu, Jingjun Xu, and Baiquan Tang, "Observation of modulated spontaneous emission of Rhodamine 6G in low refractive index contrast 1D-periodic gelatin film", *Science China: Physics*, Mechanics, Astronomy 53(1), 54-58 (2010).
87. Gao F, Xu J J, Zhang G Q, et al. "Nonlinear optical properties and superluminal propagation in the ruby." *Chinese Sci Bull*, 55:473-477(2010).
88. Fei Bian, Rui Wang, Huaixin Yang, Xinzheng Zhang, Jianqi Li, Hongxing Xu, Jingjun Xu, Jimin Zhao, "Laser-driven silver nanowire formation: effect of femtosecond laser pulse polarization", *Chin. Phys. Lett.* 27(8), 088101-3 (2010).
89. Hua Cheng, Weiping Zang, Ziyu Zhao, Zubin Li, Wenyuan Zhou, and Jianguo Tian, "Non-paraxial split-step semi-vectorial finite-difference method for three-dimensional wide-angle beam propagation," *Chin. Phys. Lett.* 27, 014201 (2010).

90. Wei Li, Baiquan Tang, Xinzheng Zhang, Feng Gao, Longchang Liu, Qiang Wu, Leiting Pan, Cibo Lou, Shangyu Guo, Romano A. Rupp and Jingjun Xu, “Investigation on the phase shifts of extinction and phase gratings in polymethyl methacrylate”, *Chin. Opt. lett.* 8(1), 18-21 (2010)
91. Xu J, Cheng C, Zheng Z, Chen J, Bai Q, Liu C, and Wang HT, “Electromagnetic transmission in configurations composed of two one-dimensional perfect electric conductor metal gratings”, *Chin. Opt. Lett.* 8, 807 (2010).
92. 唐柏权，向吟啸，张文定，高峰，齐继伟，王振华，张心正，张国权，许京军，“普洱茶的非线性光学效应与光速调控”，科学通报 55(1), 15-19 (2010)。
93. 翟晓辉，龙绘锦，董江舟，曹亚安，“N-TiO2/ZnO 复合纳米管阵列的掺杂机理及其光催化活性”，物理化学学报，26(3)，663-668（2010）。
94. 翟晓辉，赵俊岩，巢晖，曹亚安，“Rup2P 表面敏化 TiO_2 基复合薄膜光致界面电荷转移”，物理化学学报，26(6)，1617-1622（2010）。

专利/Patents

申请专利/ Patents Applied

[1] CN101856611A；一种新型高活性硼酸铟光催化剂；发明；曹亚安、袁继翔、王恩君。

[2] 201210196667.5；一种提高纳米 TiO_2 催化剂光催化效率的有效方法；发明；曹亚安、王海涛、王恩君、高东子。

[3] CN101879443A；一种新型高效率类硼酸锶光催化剂；发明；曹亚安、杨晓丹。

[4] 201010207689.7；掺钒铌酸锂晶体；发明；刘士国、董印锋、孔勇发、张玲、陈绍林、许京军。

[5] CN101776833A；主动式光控可调谐任意波长光延迟器；发明；张国权，徐雷，薄方，高峰，许宁宁，许京军。

授权专利/ Patents Approved

[1] ZL200810053555.7；基于频域 OCT 的生物组织折射率测量方法；发明；叶青，周文远，田建国。

[2] ZL200810053556.1；多波长 OCT 系统；发明；叶青，周文远，田建国。

国际合作与交流/International Cooperation and Exchange

来访人员名单/Visitors List

序号	姓名	国家或地区	单位	职称或职位	来访时间	来访目的
1.	Nikolay I. Zheludev	英国	南安普顿大学	教授	2010.11.5-7	工作访问讲学
2.	Voit Kay Michael	德国	Univ. of Osnabrueck	博士生	2010.1.19-3.21	合作研究
3.	Kruse Annika	德国	Univ. of Osnabrueck	硕士生	2010.1.19-3.21	合作研究
4.	Peter Hertel	德国	Univ. of Osnabrueck	教授	2010.3.15-4.24 2010.9.7-10.30	讲学
5.	Nason Ma'ani-Hessari	英国	Univ. of Ulster	博士	2010.9.19-11.20	合作研究
6.	王晓生	美国	University of Cincinnati	博士	2010.10	学术交流
7.	Ping Yu	美国	密苏里大学	副教授	2010.1.10-11	工作访问学术交流
8.	Yanhua Shih	美国	马里兰大学	教授	2010.8.10	学术交流
9.	Nikolaus Ernsting	德国	Institut für Chemie, Humboldt Universität zu Berlin	Professor	2010.10.17 -28	学术交流
10.	Artem R. Oganov	美国	纽约州立大学石溪分校物理系与地球科学系	教授	2010.5.31	工作访问
11.	Greg SUn	美国	Univ. of Mass. At Boston	教授	2011.07.14	访问

出访人员名单/Personnel exchange Researchers List

序号	姓名	国家或地区	单位	职称或职位	出访时间	出访目的
1.	许京军	德国/奥地利	维也纳大学等	教授	2010.7-2010.9	洪堡基金合作交流
2.	潘雷霆	美国	加州大学洛杉矶分校	讲师	2010.5-2010.8	访问学习
3.	顾 兵	新加坡	新加坡国立大学物理系	副教授	2010.7-2010.8	合作研究

研究生交流情况/Personnel exchange Students List

序号	姓名	国家或地区	单位	博士生/硕士生	出访时间	出访目的
1.	任梦昕	英国	**南安普顿大学**	博士生	2010.4-2011.3	合作研究
2.	张学智	美国	Rice University	博士生	2010.9.1-2011.4	合作研究
3.	向吟啸	德国	Univ. of Osnabrueck	博士生	2010.6-2010.9	合作研究
4.	李辉	斯洛文尼亚	Stefan研究所	硕士生	2010.3.14-4.11	合作研究
5.	胡毅	美国	旧金山州立大学物理天文系	博士	2009.9-2010.1	合作研究
6.	胡毅	美国	旧金山州立大学物理天文系	博士	2010.4-2010.6	合作研究
7.	祁轶舲	美国	罗切斯特大学	博士生	2010.10.24-10.28	参加国际学术会议
8.	翟召辉	美国	罗切斯特大学	博士生	2010.10.24-10.28	参加国际学术会议
9.	刘富才	日本	东北大学	博士生	2009.10	联合培养
10.	张新星	德国	洪堡大学	博士生	2009.7	联合培养
11.	周凯迪	德国	德累斯顿工业大学	博士生	2009.10	联合培养

引进人才情况

序号	姓名	性别	出生年月	职称	研究方向
1	顾 兵	男	1974.10	副教授	非线性光学

国内、国际会议报告/Talks at Conferences

1. Yongfa Kong, Shiguo Liu, Fucai Liu, Shaolin Chen, Jingjun Xu, “Tetravalent ions doped lithium niobate crystals”, Workshop on Optics and New Materials II, Hong Kong, China, April 30-May 3 (2010). (Invited Talk).
2. Feng Song, Qingru Wang, Chengguo Ming, Jianguo Tian, Jingjun Xu, Shangxin Lin, Edwin Y.B.Pun, “The influence of photonic mode density on the luminescence of erbium-doped optical materials”, Proc.of SPIE, Vol.7598 759803 (2010). (Invited talk)
3. Feng Song, Chengguo Ming, Wentao Wang, Lanjun Luo, “Electronic polarizability and optical parameters of Er^{3+}/Yb^{3+} co-doped phosphate glasses”, Proc.of SPIE, Vol.7598 75981P (2010). (Invited talk)
4. Yongfa Kong, Shiguo Liu, Fucai liu, Shaolin Chen, Ziheng Huang, Romano Rupp, Jingjun Xu, “The control of photorefractive effect in lithium niobate by tetravalent dopants”, 11th Europhysical Conference on Defects in Insulating Materials, Pécs, Hungary, July 12-16 (2010).
5. Yongfa Kong, Shiguo Liu, Fucai Liu, Yanjun Zhao, Shengqing Wu, Shaolin Chen, Jingjun Xu, “Recent progress in zirconium doped lithium niobate crystals”, the 16th international conference on crystal growth, Beijing, China, August 8-13 (2010).
6. Tao He, Junyan Zhao, Yaan Cao, “Surface photovoltage spectroscopy - a powerful tool for evaluation of electrodes used in dye-sensitized solar cells”, The 5th Forum On New Materials, Italy, June 13(2010).
7. Chengliang Yang, Qiang Wu, Christopher A. Werley, Jingjun Xu, and Keith A. Nelson, "Measurement of Effective Refractive Index Ellipse of LiNbO3Subwavelength Slab Waveguide for Thz Phonon Polariton Wave," International Conference on Ultrafast Phenomena, Snowmass, USA, July 18-23 (2010).
8. Wei Cai, Lei Wang, Xinzheng Zhang, Jingjun Xu, “Excitation of gap plasmons by electron beams in metallic nanowire pairs”, 11th International Conference on Near-Field Optics, Nanophotonics and Related Techniques, Beijing, China, Aug. 29 – Sep. 3 (2010).
9. Daohong Song，Cibo Lou, Jingjun Xu and Zhigang Chen,”Observation of Higher band gap solitons in photonic lattices” the international conference on Nanophotonics Tsukuba, Japan , May 30-June 3, 2010
10. Yi Hu, Peng Zhang, Simon Huang, Cibo Lou, Jingjun Xu, Zhigang Chen, “Linear and Nonlinear Control of Ballistic Trajectory of Airy Beams”, SPIE Optics Photonics, San Diego, California, USA, August 1-5(2010).
11. Yi Hu, Peng Zhang, Cibo Lou, Weiyu Huang, Jingjun Xu, and Zhigang Chen, “Optimal Control Of The Ballistic Trajectory Of Airy Beams”, Nonlinear Photonics, Karlsruhe, Germany, June 21-24(2010).
12. Yi Hu, Simon Huang, Peng Zhang, Jingjun Xu, Zhigang Chen, “Nonlinearity-Controlled Reshaping and Anomalous Diffraction of Airy Beams”, Conference on Lasers and Electro-Optics (CLEO), San Jose, California, USA, May 16-21(2010).
13. Yiling Qi, and Guoquan Zhang, "Peculiar discrete diffraction characteristic of two-dimensional backbone lattice", LThC5, Frontiers in Optics 2010/Laser Science XXVI,

October 24-28, 2010, Rochester, New York, USA.

14. Zhaohui Zhai, Guoquan Zhang, Yiling Dou, Jingjun Xu, "Phase-matched Generation of Phase Conjugation Wave Based on Atomic Coherence in Solids", FMI4, Frontiers in Optics 2010/Laser Science XXVI, October 24-28, 2010, Rochester, New York State, USA.
15. 孔勇发，刘士国，刘富才，陈绍林，许京军，“四价掺杂铌酸锂晶体的一些进展”，中国物理学会 2010 年秋季学术会议，天津（2010.9.16-19）。（邀请报告）
16. 孙甲明，“兼容 CMOS 技术的硅基发光器件的研究”，中国物理学会 2010 年秋季会议，天津(2010.9.18-19)。（邀请报告）
17. 顾兵，“Z-扫描光学非线性表征技术”，中国物理学会 2010 年秋季会议，天津(2010.9.18-19)。（邀请报告）
18. 吴强，杨程亮，张斌，许京军，Christopher A. Werley, Keith A. Nelson, “太赫兹声子极化激元超快成像及其应用”，中国物理学会 2010 年秋季学术会议，天津（2010.9.16－19）。
19. 杨程亮，吴强，张斌，许京军，Christopher A. Werley, Keith A. Nelson, “太赫兹声子极化激元在亚波长波导中折射率及传播模式的研究”，中国物理学会 2010 年秋季学术会议，天津（2010.9.16－19）。
20. 郭尚雨，吴强，马寅星，杨程亮，杨明，高峰，许京军，“时间分辨超快荧光成像系统”，中国物理学会 2010 年秋季学术会议，天津（2010.9.16－19）。
21. 翟召辉，张国权，窦宜领，许京军，“固体中基于原子自旋相干的位相共轭波的产生”，中国物理学会 2010 年秋季学术会议，天津（2010.9.16－19）。
22. 高峰，张文定，张国权，许京军，“聚焦高斯光束共轴非简并二波耦合的耦合波方程”，中国物理学会 2010 年秋季学术会议，天津（2010.9.16－19）。
23. 孔勇发，刘士国，刘富才，许京军，“四价掺杂铌酸锂晶体的研究进展”，第十五届全国凝聚态光学性质学术会议，宁波（2010.8.16-19）。（邀请报告）
24. 徐燕，王丕东，石凡，张心正，许京军，“非线性对一维无序波导阵列局域化模式影响”，第十五届全国凝聚态光学性质学术会议，宁波(2008.8.16-19)。
25. 石凡 张心正 李俊 王丕东 徐燕 王振华 许京军，“入射光波长对无序介质中光子局域化行为的影响及调控”，第十五届全国凝聚态光学性质学术会议，宁波(2008.8.16-19)。
26. Zhuoyi Ye, Cibo Lou, Liqin Tang, Daohong Song, Zhigang Chen, “Beam steering in defected photonic lattices”, 第十五届全国凝聚态光学性质学术会议，宁波(2008.8.16-19)。
27. 辛非非，张国权，薄方，孙海峰，孔勇发，许京军，Tatyana Volk and Natalia M. Rubinina，“掺杂铌酸锂晶体的 325nm 紫外光折变效应研究”，第十五届全国凝聚态光学性质学术会议，宁波(2008.8.16-19)。
28. 祁轶舲，张国权，“二维脊背型光子晶格中高阶带隙的展开”，第十五届全国凝聚态光学性质学术会议，宁波(2008.8.16-19)。
29. 张文定，高峰，张国权，许京军，“掺 R6G PMMA 中基于类非简并二波耦合效应的光群速调控的实验研究”， 第十五届全国凝聚态光学性质学术会议，宁波(2008.8.16-19)。
30. Xiao-Qing Yan, Zhi-Bo Liu, Shuo Shi, Jian-Guo Tian, “Polarization and thickness dependence of nonlinear absorption and nonlinear scattering in isotropic medium,” 第十五届全国凝聚态光学性质学术会议，宁波(2010.8.16-22)。
31. 张校亮，刘智波，陈旭东，赵欣，田建国，“石墨烯及其杂化材料的光学非线性与光限制效应研究,”第十五届全国凝聚态光学性质学术会议，宁波(2010.8.16-22)。
32. 李亚东，栗建兴，臧维平，田建国，“非傍轴高斯激光束电磁场研究”，中国光学年会 2010 年学术年会，天津（2010.8.23-26）。

33. 程化，臧维平，田建国，“艾里光束对微小颗粒的捕获与输运研究”，中国光学年会 2010 年学术年会，天津（2010.8.23~26）。
34. 翟召辉，张国权，涂燕飞，窦宜领，许京军，“基于电磁感应透明的角度复用光脉冲存储与可选址光缓存”，第十四届全国量子光学学术会议，曲阜 (2008.8.5-7)。
35. 刘建彬，张国权，“单模激光器的亚波长干涉”， 第十四届全国量子光学学术会议，曲阜 (2008.8.5-7)。
36. 孙甲明，“集成硅基发光器件的研究”，第 12 届全国发光学学术会议暨发光学相关产业研讨会，苏州（2010.11.5-8）（邀请报告)。
37. 余华，胡男，张铭，张盼，王亚洲，罗师强，赵丽娟，“Eu^{3+}探针研究制备发光纳米材料过程中晶格场的变化”，第 12 届全国发光学学术会议暨发光学相关产业研讨会，苏州（2010.11.5-8）。
38. 刘海旭，孟繁杰，孙甲明，“Nanosecond field-induced quenching of the luminescence from Er-doped silicon nanocrystals”，第三届全国掺杂纳米材料发光性质学术会议，西安 (2010.8.10-14)（邀请报告） 。
39. J. M. Sun, S. Prucnal, A. Mücklich, W. Skorupa, and M. Helm，“Silicon-based light emission in ultraviolet” 2010 7th IEEE International Conference on Group IV Photonics，Beijing China (GFP 2010).
40. 刘海旭，孙甲明，“富硅氮化硅薄膜及 Si/Si_3N_4 超晶格结构的交流电致发光”，2010 年硅基光电子材料及器件研讨会，南京 (2010.5.23-25)。
41. 王肖珩，孙甲明，“SiO_2 电子加速薄膜电致发光器件中过热电子能量的二次增强现象”，2010 年硅基光电子材料及器件研讨会，南京 (2010.5.23-25)。
42. 刘智波，张校亮，赵欣，陈旭东，田建国，“碳结构材料光学非线性及超快特性研究，”第十四届全国基础光学与光物理学术讨论会，厦门（2010.11.6-10）。

主办国内、国际会议/Conferences Sponsored by the Laboratory

第二届国际先进光子学讲习班（2010.6.30-7.1；天津）

2010 年 6 月 30 日至 7 月 1 日，重点实验室在泰达应用物理学院举办了第二届国际先进光子学讲习班——非线性光学及其奇异现象国际研讨会。本次研讨会吸引了来自美国、意大利、希腊、加拿大、澳大利亚、以色列、法国和中国的百余位代表参会。

研讨会围绕非线性光学及其奇异现象在若干基础研究及其应用领域中的特异优势等主题展开。来自中国北京大学的龚旗煌教授、华东师范大学的曾和平教授和美国科罗拉多大学的 M. Ablowitz 教授、美国麻省理工学院的 T. R. Akylas 教授、美国中央佛罗里达大学的 D. N. Christodoulides 教授、美国斯坦福大学的范汕洄副教授、美国普林斯顿大学的 J. Fleischer 教授、美国南卫理公会大学的 A. Aceves 教授，以色列理工学院的 M. Segev 教授、M. Orenstein 教授、A. Szameit,加拿大魁北克大学的 R. Morandotti 教授，法国尼斯大学的 J. R. Tredicce 教授，意大利拉奎拉大学的 E. DelRe，澳大利亚国立大学的 D. Neshev，希腊的克里特大学的 N. Efremidis 等专家学者应邀作主题报告。在研讨会期间，参会代表展开了热烈的讨论。

本次研讨会提供了国内院校和科研单位研究者与国际知名学者专家的交流平台，在推动国内的非线性光学发展、提高重点实验室科研实力及增强国际合作等方面起到了重要作用。

南开大学弱光非线性光子学教育部重点实验室/ The Key laboratory of Weak Light Nonlinear Photonics (Nankai University, Tianjin 300457), Ministry of Education, China

学术组织与期刊任职/Academic Service

国内学术组织任职/Service to the Domestic Professional Societies

序号	姓名	任职机构	职位	任期
1	许京军	中国高校知识产权研究会	副理事长	2008-
2	许京军	中国光学学会	理事	2006-
3	许京军	天津市光学学会	副理事长	2010-
4	许京军	天津市激光技术学会	副理事长	2010-
5	许京军	应用光学国家重点实验室	主任	2009-
6	孔勇发	中国材料研究学会青年工作委员会	理事	2008－2011
7	孔勇发	天津市硅酸盐学会	晶体生长与材料专业委员会副主任	2006-2010
8	宋　峰	天津市激光学会	副理事长	2009-2014
	孙　骞	天津市光电子学会	常委	2006-
9	张天浩	天津市照明学会	常务理事	2009-2013
10	宋　峰	教育部高等学校物理基础课程教学指导分委员会	委员，高等学校文科类物理课程教学研究协作组成员	2006-2010
11	宋　峰	教育部大学物理基础课程教指委暨医药类基础课程教指委 医药物理协作组	副组长	2008-2010
12	徐章程	中国教育技术协会多元智能专业委员会	主任	2008-2009
13	徐章程	中国电子学会半导体集成分会	委员	2006-2011
14	孙　骞	中国光学学会光电技术委员会	委员	2006-
15	徐晓轩	中国仪器仪表学会分析仪器分会近红外光谱专业委员会	学术委员	2009-2013
16	宋　峰	固体激光技术国防科技重点实验室	第三届学术委员会委员	2007-2010
17	宋　峰	南京师范大学物理系	兼职教授	2006-2010
18	宋　峰	德州学院物理系	兼职教授	2007-2011
19	宋　峰	南通大学	兼职教授	2008-2012

国内期刊任职/Service to the Domestic Journals

序号	姓名	任职机构	职位	任期
1	许京军	Frontiers of Physics in China	编委	2008-2011
2	宋　峰	Applied Optics	编委	2009-2012
3	许京军	《光学学报》	副主编	2008-

4	宋　峰	大学物理	副主编	2009.5-
5	许京军	《红外与毫米波学报》	编委	
6	许京军	《物理》	编委	2007-2011
7	许京军	《物理学进展》	编委	2009-2012
8	许京军	Chinese Physics Letters	编委	2009-
9	许京军	《中国光学与应用光学》	编委	2008-
10	许京军	《激光技术》	编委	2007-2010
11	孔勇发	《激光技术》	编委	2007-2010
12	孔勇发	《人工晶体学报》	编委	2009-2012
13	张国权	《激光技术》	编委	2007-2011
14	张国权	激光与光电子学进展	编委	2010-2013
15	孙　骞	《激光技术》	编委	2006-2010

获奖情况/Awards & Honors

高性能铌酸锂晶体与光电器件产品化的关键技术研究
2010 年全国优秀博士学位论文提名
获得者：孙　军
指导教师：许京军

碳结构杂化材料光学非线性与光限制效应
第七届饶毓泰基础光学奖优秀奖
获奖者：刘智波

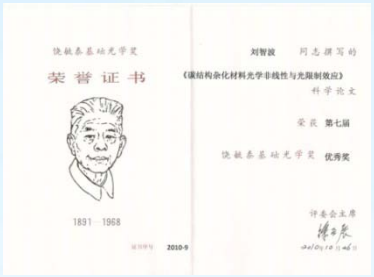

掺锆铌酸锂晶体的光折变性能研究
第七届饶毓泰基础光学奖优秀奖
获奖者：刘富才

获奖教师/Award for excellent teachers

2010 年度捷成教育基金奖教金：
获得者：张心正　刘智波

获奖学生/Award for excellent students

教育部 2010 年度“博士研究生学术新人奖”：汪喜林

《激光与光电子学进展》杂志“2010 中国光学重要成果”：汪喜林

中国物理学会 2010 年秋季学术会议最佳张贴报告奖：杨程亮

南开大学 2009 优秀博士学位论文培育基金资助：汪喜林

南开大学优秀学生干部：　栗建兴　　南开大学优秀毕业生：赵立华

南开大学优秀硕士论文：张文定

泰达学院 2010 年度“泰达之星”——“学习之星”：胡　毅　张文定

南开大学奖学金：
一等奖学金：胡　毅　张文定　栗建兴　刘富才　王文杰
二等奖学金：赵立华　程　化　胡　男　康　明
三等奖学金：吴　限　刘建彬　祁轶舲　辛非非　张校亮　鄢小卿　曾　浩　陈　猛　汪喜林

获奖集体/Award for group
南开大学先进研究生党支部：泰达应用物理学院硕士生支部

学位论文/Dissertations

1. 博士学位论文 Dissertation for Doctoral Degree

[1] 唐柏权，若干弱光非线性光学效应研究；导师：许京军

[2] 王喆，飞秒激光脉冲在一维离散体系中传输特性的研究；导师：许京军

[3] 边飞，飞秒激光液相烧蚀制备银纳米结构及其形成机理研究；导师：许京军

[4] 王俊俏， 表面金属微结构的光学制备及其应用研究；导师：孙骞

[5] 赵立华，纳米尺度光波导及微结构若干性质研究；导师：孙骞

[6] 齐新元，非线性光子学晶格中的光传播性质研究；导师：张国权

[7] 郝召锋，材料的表面特性与有机材料的光学性质研究；导师：田建国

[8] 李建威，高速光电探测器频率响应特性测试研究；导师：田建国

[9] 孟扬，夜间光照对褪黑激素抑制模型与定量化；导师：李宝会，张天浩

[10] 康慧珍，光折变表面波激发及其在二次谐波发生中的应用；导师：刘思敏，张天浩

[11] 邵伟伟，光折变表面波及其在表面等离子体激元长程传播中的应用；导师：张天浩

[12] 任相魁，光折变非线性表面波的研究；导师：宋峰，张天浩

[13] 曹永强，高活性纳米 TiO_2 基催化剂的制备和光催化活性机理研究；导师：曹亚安

[14] 翟晓辉，纳微结构金属氧化物薄膜光电功能性研究；导师：曹亚安

[15] 王恩君，高活性纳米二氧化钛可见光催化剂的制备及其光催化活性研究；导师：曹亚安

2. 硕士学位论文 Dissertation for Master Degree

[1] 李辉，不同液晶体系中的光调控研究；导师：张心正

[2] 金妮娜，紫外光敏聚甲基丙烯酸甲酯光子晶格中飞秒激光离散现象的研究；导师：吴强

[3] 胡金霞，液相外延法生长铌酸锂薄膜中助熔剂对衬底材料的影响；导师：孙骞

[4] 谢楠，光耦合扫描隧道显微镜的研制；导师：孙骞

[5] 高光宇，表面等离子体的时间与空间相干性研究；导师：孙骞

[6] 段长莎，光子晶体薄板中光传输现象的研究；导师：张国权

[7] 许宁宁，单纳米晶体 CdSe/ZnS 光致发光闪烁特性及光子反聚束效应；导师：张国权

[8] 张文定，基于类非简并二波耦合效应的光群速调控；导师：高峰

[9] 梅剑春，嵌入式胶体金免疫层析试纸定量分析仪的研究；导师：田建国

[10] 惠王伟，基于 MOF 的空间分辨免疫传感技术的应用与研究；导师：田建国

[11] 张墨林，一维光波导中的光束传播研究；导师：臧维平

[12] 赵子宇，光波导器件中的有限差分光束传播方法研究；导师：臧维平

[13] 马雅盛，飞秒激光在透明材料中写入微结构的研究；导师：李玉栋

[14] 余璇，有机材料双光子吸收理论和实验研究；导师：刘智波

[15] 张达光，结构光乳房三维测量系统的研究；导师：张天浩

[16] 李晓，扩散漂移机制下的光折变离散表面孤子实验研究；导师：张天浩

[17] 马辉辉，光折变非线性表面波的激发及稳定性研究；导师：张天浩

[18] 张宇，非视觉光感受系统协同作用模型的建立；导师：张天浩

[19] 姚鹏，光折变表面暗孤子的实验研究；导师：张天浩

[20] 戴嘉俊，光敏黄蛋白（PYP）脉冲升温开折叠过程的时间分辨红外光谱研究；导师：张天浩，翁羽翔

[21] 李昕睿，掺钇铌酸锂晶体的生长及其性能研究；导师：孔勇发

[22] 匡元江，高活性纳米二氧化钛基催化剂光催化活性研究；导师：曹亚安

[23] 高东子，纳米结构二氧化钛的制备及其光催化活性研究；导师：曹亚安

[24] 侯春霄，近红外波段红外检测卡原理、设计和制备；导师：赵丽娟

[25] 宋令枝，水溶性 ZnS 纳米晶的合成与结构表征；导师：赵丽娟

[26] 崔磊，铌酸锂晶体热释电性能提高的研究；导师：张玲

[27] 王利忠，掺锡铌酸锂晶体的生长及其光折变性能研究，导师：刘士国

[28] 季鸣元，同基质多色荧光粉的制备与性能研究，导师：武莉

[29] 周晓东，钨酸镧钾晶体生长与性质研究；导师：孙同庆

[30] 张威威，InGaAs/GaAs 应变量子阱不同结构和生长方式对荧光光谱影响的研究；导师：舒永春

[31] 何进密，低维半导体的电学和光学性质研究；导师：姚江宏

[32] 王醉，氧化锌纳米薄膜制备及掺杂性质研究；导师：姚江宏

[33] 朱鸿雁，III-V 族三元化合物半导体材料的光学特性研究；导师：邢晓东

[34] 张俊杰，原子层沉积制备的 HfO_2 高 K 栅介质材料特性研究；导师：孙甲明

[35] 杨阳，可控无序对高迁移率二维电子系统输运性质的影响；导师：孙甲明

[36] 张新霞，Opal 光子晶体的制备及质子辐射和退火对纳米金刚石颗粒的处理；导师：孙甲明

[37] 王文涛，金属氧化物对铒镱共掺磷酸盐玻璃陶瓷发光特性影响的研究；导师：宋峰

[38] 骆兰军，铒镱共掺磷酸盐玻璃与玻璃陶瓷光谱性质的研究；导师：宋峰

[39] 樊学芳，LD 端面泵浦 $Nd:YVO_4$ 固体激光器热效应自适应设计；导师：宋峰

High resistance against ultraviolet photorefraction in zirconium-doped lithium niobate crystals

Fucai Liu,[1] Yongfa Kong,[2,*] Wei Li,[2] Hongde Liu,[1] Shiguo Liu,[1] Shaolin Chen,[2] Xinzheng Zhang,[2] Romano Rupp,[2] and Jingjun Xu[1,2]

[1]*School of Physics, Nankai University, Tianjin 300071, China*
[2]*The MOE Key Laboratory of Weak-Light Nonlinear Photonics and TEDA Applied Physics School, Nankai University, Tianjin 300457, China*
**Corresponding author: kongyf@nankai.edu.cn*

Received August 27, 2009; revised November 4, 2009; accepted November 20, 2009; posted December 3, 2009 (Doc. ID 116337); published December 18, 2009

The UV photorefraction of Zr-doped lithium niobate (LN:Zr) was investigated. The experimental results show that LN:Zr crystals have high resistance against photorefraction in the UV region as well as in the visible range and can withstand a UV light intensity of above 10^5 W/cm^2. According to the fitting results of erasing curves with UV and green light, a two-center $O^{2-/-}$-defect model was suggested. Our results indicate that LN:Zr is an excellent candidate for optical damage resistance from the UV to the visible spectrum.

OCIS codes: 160.3730, 190.5330.

Lithium niobate ($LiNbO_3$, LN) has been described as a decathlon material in nonlinear optics. Since it has good electro-optic, acousto-optic, piezoelectric, and nonlinear properties, LN has been extensively investigated for applications in integrated optics and nonlinear photonics [1–3]. Photorefraction (PR), also called laser-induced optical damage, can be utilized in volume holographic data storage [4–6], but seriously limits the applications of LN at high light intensity, such as in frequency convertors, optical parametric oscillators, and *Q* switches. Therefore the suppression of PR is of prime importance for improving device performance. It has been shown that PR can be greatly suppressed in LN doped with Mg, Zn, or In above threshold [7–9]. However, the so-called PR resistance is not absolute but depends on the incident light wavelength. In fact, PR is effectively resisted in the visible range but is apparently enhanced in the UV region [10,11]. Till now, there has been no report on the resistance of LN against UV PR (UVPR), which seriously hinders its applications in the UV region.

Recently, it was reported that LN doped with tetravalent ions, especially Zr^{4+} [12], exhibited outstanding optical damage resistant performance. In this Letter we investigated the UVPR of Zr-doped LN (LN:Zr). It was found that PR was also significantly reduced.

The LN:Zr crystals were grown along the *c* axis with the conventional Czochralski method. The melt composition was [Li]/[Nb]=48.4/51.6, and 1.0, 2.0, 3.0, and 5.0 mol. % ZrO_2 was added into the melt, labeled as LN:Zr_1, LN:Zr_2, LN:Zr_3, and LN:Zr_5, respectively. After annealing treatment and artificial polarization, 3-mm-thick *y*-cut plates were ground and polished to optical grade. For comparison, normally congruent pure and 5.0 mol. % MgO-doped LN (PLN and LN:Mg_5) crystals were also grown.

The traditional setup for holographic recording was employed to investigate the UVPR property (as shown in [11]). An Ar^+ laser light was split into two equal beams (*e*-polarized, wavelength 351 nm, intensity per beam 0.9 W/cm^2, diameter 1.5 mm) to write gratings. The holographic grating vector was aligned along the *c* axis of the crystal with a grating period of 0.64 μm. The diffraction efficiency η is defined as $\eta = I_d/(I_d+I_t)$, where $I_{d,t}$ are the diffracted and the transmitted beam intensity, respectively. During recording, one of the UV beams is blocked for 0.1 s every 1.0 s, and the second beam is diffracted from the written grating to obtain the diffraction efficiency. After recording for about 80 s, the grating is saturated.

The dependence of UVPR saturated diffraction efficiency on Zr concentration in LN is shown in Fig. 1. We can see that the saturated diffraction efficiency is apparently reduced when Zr is added into LN. The PLN crystal has a saturated diffraction efficiency of 5.06%, while it abruptly decreases to 0.10% in LN:Zr_2. We calculated the saturated refractive index

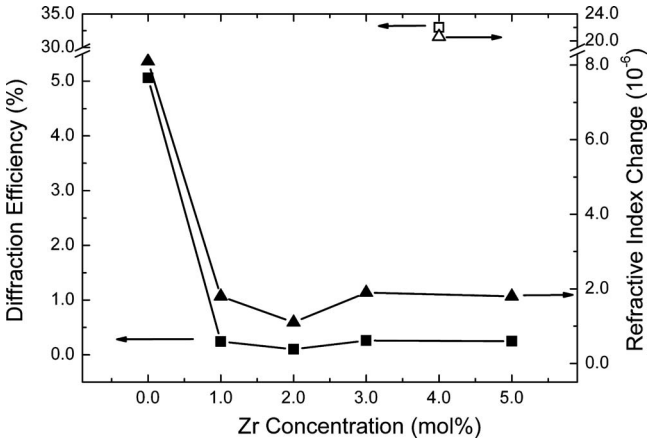

Fig. 1. Dependence of UV photorefractive diffraction efficiency and saturated refractive index change of LN:Zr on the doping concentration of Zr. For comparison, the open symbols show the data for LN:Mg_5. The lines are the guides to the eye.

change from the diffraction efficiency according to $\eta = \sin^2[\pi \Delta n d/(\lambda \cos\theta)]$ (λ is the free-space wavelength and θ the Bragg angle) [13], which is also shown in Fig. 1. The refractive index change of LN:Zr_2 is only 1.1×10^{-6}, which is about eight times smaller than that of PLN, and only one twentieth of that of LN:Mg_5.

To evaluate the intensity threshold of resistance to optical damage, we focused the UV laser beam (*e*-polarized, wavelength 351 nm, intensity 1.6×10^5 W/cm^2), and put the 3 mm *y*-cut plates at the rear focal plane of the lens to observe the distortion of transmitted beams. As shown in Fig. 2, the light spot is distorted seriously for PLN and LN:Zr_1 after 5 min of illumination, while it passes through LN:Zr_2 and LN:Zr_5 almost without distortion. A similar result was also observed in LN:Zr_3, which is omitted in Fig. 2 for simplification. Thus, the intensity threshold of highly doped LN:Zr is above 10^5 W/cm^2, the highest intensity now in our laboratory.

As we know, there are plenty of intrinsic defects in congruent LN (CLN), existing as Li vacancy (V_{Li}) and anti-site Nb^{5+} (Nb_{Li}^{5+}) [14]. The UVPR in CLN is very considerable and is not suppressed but enhanced in LN:Mg. Thus it can be deduced that UVPR has no direct relation to Nb_{Li}^{5+} but is related to V_{Li}. Recently the generally defined UV absorption edge of CLN at $\alpha = 20$ cm^{-1} was attributed to the band tail absorption of V_{Li}, actually of O^{2-} ions near V_{Li} [15]. And O^- holes near V_{Li} have been produced by x-ray and two-photon excitations [16]. The UV-light-induced absorption has been considered to be related to O^- near V_{Li} ($O^- - V_{Li}^-$) [17,18]. Therefore, it is reasonable to consider $O^{2-/-}$ ions near V_{Li} ($O^{2-/-} - V_{Li}$) as the UVPR center. In fact, the amount of V_{Li} in CLN and LN:Mg near the threshold is almost the same; the large UVPR difference between them indicates that other photorefractive centers should exist in LN:Mg. The O^- hole stabilized by Mg^{2+} on the nearest-neighbor Nb site ($O^- - Mg_{Nb}^{3-}$) has been characterized by its electron spin resonance spectrum and attributed to UV-light-induced absorption in LN:Mg [19,20]. Because Mg_{Nb}^{3-} has a different valence with V_{Li}^-, it can be deduced that two kinds of UVPR centers should exist in LN:Mg.

Then we examined the UV light erasing performance of the photorefractive gratings. After the grating is saturated, one of the written beams is blocked, and another beam (wavelength 351 nm, intensity 0.9 W/cm^2) is used to erase the gratings. The normalized typical curves for LN:Mg and LN:Zr are shown in Figs. 3(a) and 3(b) (triangles), respectively. These curves have large deviations when fitted by a monoexponential function but can be perfectly fitted by a double-exponential function: $\eta = \eta_1 \exp(-t/\tau_1) + \eta_2 \exp(-t/\tau_2)$, where $\eta_{1,2}$ are amplitudes of exponents 1 and 2, and $\tau_{1,2}$ are time constants, respectively. The fitting curves (solid curves) are shown in Figs. 3(a) and 3(b), and fit parameters are listed in Table 1. The fitting results also indicate that the one-center model is not suitable for highly doped LN, and there should exist at least two kinds of UVPR center.

The saturated UV gratings were also illuminated by a green beam (*e*-polarized, wavelength 532 nm, intensity 0.9 W/cm^2, diameter 2 mm) incident at the Bragg angle. It was observed that the gratings can be completely erased, just as shown in Figs. 3(c) and 3(d) (triangles). This is quite different from the observation in the visible region, where reading with light of longer wavelength does not erase the photorefractive grating recorded by a shorter one because its photonic energy is not high enough to excite electrons from deep energy levels [6,21]. Therefore, we consider that this erasing process may have relationship with another kind of charge carrier: holes. These green light erasing curves also have large deviations when fitted by a monoexponential function but can be fitted very well with double-exponential functions, as shown in Figs. 3(c) and 3(d) (solid curves), which means that both gratings recorded on two kinds of different photorefractive center can be completely

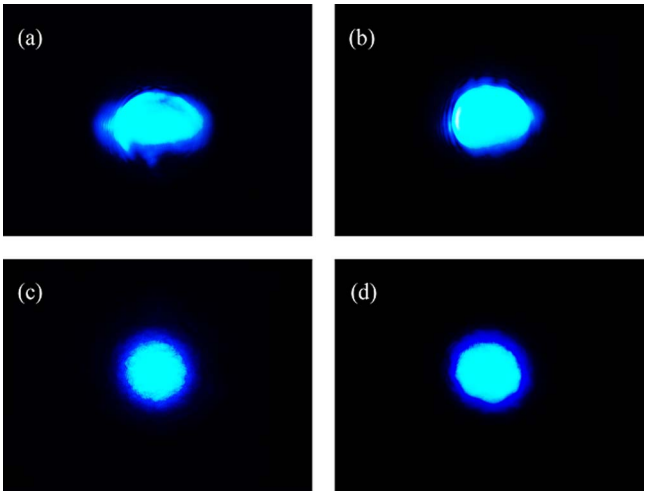

Fig. 2. (Color online) Beam distortion of the transmitted UV lights (wavelength 351 nm, intensity 1.6×10^5 W/cm^2) after passing through LN crystals. (a) PLN, (b) LN:Zr_1, (c) LN:Zr_2, (d) LN:Zr_5.

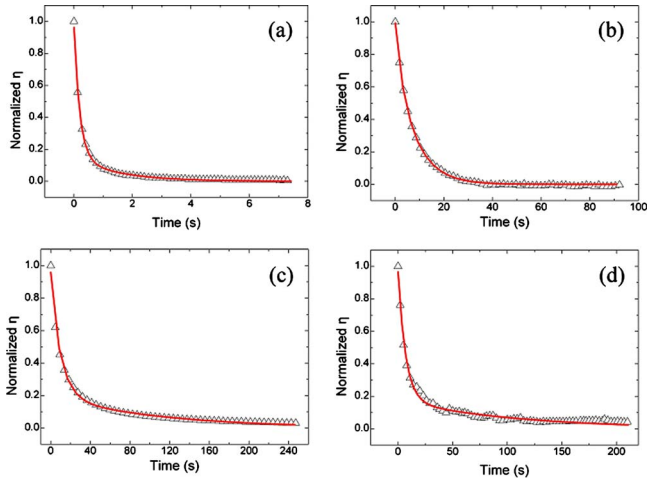

Fig. 3. (Color online) Normalized typical erasing curves for (left) Mg- and (right) Zr-doped LN with (top row) UV and (bottom row) green illumination. The triangles represent experimental data, and the solid curves fits of double-exponential functions.

Table 1. Fit Parameters of the Normalized Typical Erasing Curves (Fig. 3)

	UV				Green			
Crystal	τ_1(s)	η_1	τ_2(s)	η_2	τ_1(s)	η_1	τ_2(s)	η_2
LN:Mg_5	0.19	0.82	1.37	0.18	10.17	0.78	108.89	0.22
LN:Zr_5	8.22	0.81	2.44	0.19	6.93	0.81	106.55	0.19

erased by the green light. The fit parameters are also given in Table 1.

It should be mentioned that similar fit results have been obtained for LN:Zr_2, LN:Zr_3, and LN:Zr_5. For simplification, only the results of LN:Zr_5 are presented in Fig. 3 and Table 1. As can be seen from Table 1, η_2 values for LN:Mg are approximately equal to those for LN:Zr ($\sim$0.2) for both erasing lights. In addition, τ_2 in both samples are nearly the same ($\sim$2.0 and $\sim$100 s for UV and green lights, respectively). Thus we can deduce that the small terms of the double-exponential functions may result from the same kind of photorefractive center: intrinsic defects. While τ_1 is significantly different for LN:Mg and LN:Zr, it indicates the larger terms of the double-exponential functions are induced by different centers, which might be associated with the doping defects of Mg and Zr ions, respectively.

Just as $O^- - Mg_{Nb}^{3-}$ is found in LN:Mg, it can be deduced that the impurity defect of $O^- - Zr_{Nb}^-$ should exist in highly doped LN:Zr. Therefore it would be reasonable to suppose that the two kinds of photorefractive centers are $O^{2-/-} - V_{Li}^-$ and $O^{2-/-} - Mg_{Nb}^{3-}$ in LN:Mg and $O^{2-/-} - V_{Li}^-$ and $O^{2-/-} - Zr_{Nb}^-$ in LN:Zr, respectively. Because Mg_{Nb}^{3-} has a higher negative valence than V_{Li}^-, O^{2-} ions near Mg_{Nb}^{3-} are less stable and lose electrons more easily under the illumination of UV light than near V_{Li}^-, which causes LN:Mg to have stronger UVPR than PLN. Though Zr_{Nb}^- and V_{Li}^- have the same valence, O^{2-} ions near V_{Li}^- may lose electrons more easily than near Zr_{Nb}^- because of the loss of Li^+, which induces the weaker UVPR of LN:Zr compared with PLN. Therefore, the difference in the capacity of $O^{2-} - Mg_{Nb}^{3-}$ and $O^{2-} - Zr_{Nb}^-$ as donors may lead to the UVPR discrepancy between LN:Mg and LN:Zr. However, the UV-light-induced charge carrier process in doped LN is still not so clear, and further investigations are greatly necessary.

In summary, UVPR is highly resisted in Zr-doped LN, which extends the nonlinear optical applications of LN to the UV region. The diffraction efficiency is only 0.10% in LN:Zr_2, and the refractive index change is eight times smaller than that of PLN. The intensity threshold of optical damage resistance in LN:Zr_2 is above 10^5 W/cm^2. In addition, a two-center $O^{2-/-}$-defect model was suggested to explain the micromechanism of the UVPR in doped LN.

This work was financially supported by Chinese National Key Basic Research Special Fund (2006CB921703), National Basic Research Program of China (2007CB307002 and 2010CB934101), and the National Advanced Materials Committee of China (2007AA03Z459). The authors greatly thank the referees for their valuable comments and suggestions.

References

1. M. Soljačié and J. D. Joannopoulos, Nature Mater. **3**, 211 (2004).
2. V. Berger, Phys. Rev. Lett. **81**, 4136 (1998).
3. N. G. R. Broderick, G. W. Ross, H. L. Offerhaus, D. J. Richardson, and D. C. Hanna, Phys. Rev. Lett. **84**, 4345 (2000).
4. Y. S. Bai and R. Kachru, Phys. Rev. Lett. **78**, 2944 (1997).
5. L. Hesselink, S. S. Orlov, A. Liu, A. Akella, D. Lande, and R. R. Neurgaonkar, Science **282**, 1089 (1998).
6. K. Buse, A. Adibi, and D. Psaltis, Nature **393**, 665 (1998).
7. G. Zhong, J. Jian, and Z. Wu, in *Proceedings of the 11th International Quantum Electronics Conference* (IEEE, 1980), p. 631.
8. T. Volk, V. I. Pryalkin, and N. M. Rubinina, Opt. Lett. **15**, 996 (1990).
9. Y. Kong, J. Wen, and H. Wang, Appl. Phys. Lett. **66**, 280 (1995).
10. J. Xu, G. Zhang, F. Li, X. Zhang, Q. Sun, S. Liu, F. Song, Y. Kong, X. Chen, H. Qiao, J. Yao, and L. Zhao, Opt. Lett. **25**, 129 (2000).
11. H. Qiao, J. Xu, G. Zhang, X. Zhang, Q. Sun, and G. Zhang, Phys. Rev. B **70**, 094101 (2004).
12. Y. Kong, S. Liu, Y. Zhao, H. Liu, S. Chen, and J. Xu, Appl. Phys. Lett. **91**, 081908 (2007).
13. H. Kogelnik, Bell Syst. Tech. J. **48**, 2909 (1969).
14. T. Volk and M. Wöhlecke, Ferroelectr. Rev. **1**, 195 (1998).
15. X. Li, Y. Kong, H. Liu, L. Sun, J. Xu, S. Chen, L. Zhang, Z. Huang, S. Liu, and G. Zhang, Solid State Commun. **141**, 113 (2007).
16. O. F. Schirmer and D. von der Linde, Appl. Phys. Lett. **33**, 35 (1978).
17. P. Herth, T. Granzow, D. Schaniel, Th. Woike, M. Imlau, and E. Krätzig, Phys. Rev. Lett. **95**, 067404 (2005).
18. H. Qiao and Y. Tomita, Opt. Express **14**, 5773 (2006).
19. I. Zaritskii, L. Rakitina, G. Corradi, K. Polgár, and A. Bugai, J. Phys. Condens. Matter **3**, 8457 (1991).
20. W. Yan, Y. Kong, L. Shi, L. Sun, H. Liu, X. Li, J. Xu, S. Chen, L. Zhang, Z. Huang, S. Liu, and G. Zhang, Opt. Express **14**, 10898 (2006).
21. H. C. Külich, Opt. Commun. **64**, 407 (1987).

Optical orbital angular momentum from the curl of polarization

Xi-Lin Wang (汪喜林),[1] Jing Chen,[1] Yongnan Li (李勇男),[1] Jianping Ding (丁剑平),[2]
Cheng-Shan Guo (国承山),[1] and Hui-Tian Wang (王慧田)[1,2,*]

[1]School of Physics and Key Laboratory of Weak-Light Nonlinear Photonics, Nankai University, Tianjin 300071, China
[2]Nanjing National Laboratory of Microstructures, Nanjing University, Nanjing 210093, China

(Received 22 June 2010; published 13 December 2010)

We predict a new category of optical orbital angular momentum that is associated with the curl of polarization and a kind of vector field with radial-variant hybrid states of polarization that can carry such novel optical orbital angular momentum. We present a scheme for creating the desired vector fields. Optical trapping experiments validate that the vector fields, which have no additional phase vortex, exert torques to drive the orbital motion of the trapped isotropic microspheres.

DOI: 10.1103/PhysRevLett.105.253602 PACS numbers: 42.50.Tx, 03.50.Kk, 42.25.Ja, 42.50.Wk

A light field can carry spin angular momentum (SAM) or orbital angular momentum (OAM). As an intrinsic part of the nature of a light field, SAM is associated with circular polarization and has two possible quantized values of $\pm\hbar$ [1]. Since the original concept of optical OAM was pioneered by Allen *et al.* in 1992 [2], as a fundamentally new optical degree of freedom [3], OAM has attracted extensive attention and academic interest due to its practical and potential applications in various realms (such as nonlinear optics [4], atom optics [5], quantum optics and information [6], optical communication [7], optical tweezers and micromechanics or microfluidics [8], biosciences [8], and even astronomy [9]). The concept of the optical OAM has now been extended to other natural waves such as a radio wave [10], sonic wave [11], x ray [12], electron beam [13], and a matter wave [14], so that the optical OAM is undoubtedly an extensively interesting issue.

As predicted by Allen *et al.* in 1992 [2], a scalar vortex field with a helicoidal phase front of $\exp(-j\ell\phi)$ could carry an optical OAM of $\ell\hbar$ [1–3,15–21]. Evidently, for scalar fields with homogeneous distribution of states of polarization (SoPs), the space-variant phase is a prerequisite for possibility of producing optical OAM caused by the phase. The question is whether the polarization as a fundamental nature of light can also be used to produce optical OAM. It is imaginable that the light fields with the space-variant distribution of SoPs have the possibility of carrying OAM. Consequently, vector fields with space-variant distribution of SoPs [22–25] offer an opportunity of producing optical OAM associated with the polarization nature.

In this Letter, we predict in theory and validate in experiment a new class of optical OAM associated with the curl of polarization independent of phase. It is quite different from the well-known OAM associated with the phase gradient independent of polarization. The theoretical result reveals that this novel OAM can be carried by a radial-variant vector field with hybrid SoPs. We present a scheme for creating the desired vector fields. An optical trapping experiment confirms that the optical OAM carried by the vector fields we presented drives the motion of trapped isotropic microspheres around the ring focus. The present result is a breakthrough from the limitation that the polarization nature of light field can only influence optically anisotropic materials.

Theoretical Prediction.—A light field at an angular frequency ω has a vector potential $\mathbf{A}$, as $\mathbf{A}(x,y) = A(x,y) \times [\alpha(x,y)\hat{\mathbf{e}}_x + \beta(x,y)\hat{\mathbf{e}}_y]\exp(jkz - j\omega t)$ with $|\alpha|^2 + |\beta|^2 = 1$, where the complex amplitude A can be described by real-valued module u and phase ψ. α and β indicate the distribution of SoPs of a light field. Under the paraxial limit and the Lorenz gauge, the cycle-average momentum flux $\mathbf{P}$ can be written as $\mathbf{P} \propto \langle \mathbf{E} \times \mathbf{H} \rangle$ in terms of the magnetic field $\mathbf{H} = (\nabla \times \mathbf{A})/\mu_0$ and the electric field $\mathbf{E} = j\omega\mathbf{A} + j(\omega/k^2)\nabla(\nabla \cdot \mathbf{A})$. The transversal component of $\mathbf{P}$ is divided into

$$\mathbf{P}_\perp^{(1)} \propto 2u^2\nabla\psi, \tag{1a}$$

$$\mathbf{P}_\perp^{(2)} \propto ju^2(\alpha\nabla\alpha^* - \alpha^*\nabla\alpha + \beta\nabla\beta^* - \beta^*\nabla\beta), \tag{1b}$$

$$\mathbf{P}_\perp^{(3)} \propto j\nabla \times [u^2(\alpha\beta^* - \alpha^*\beta)\hat{\mathbf{e}}_z]. \tag{1c}$$

The cross product of $\mathbf{P}$ with $\mathbf{r}$ (radius vector) gives the angular momentum flux $\mathbf{J} \propto \mathbf{r} \times \mathbf{P}$. Accordingly, the z component of $\mathbf{J}$, J_z, is composed of three parts

$$J_z^{(1)} \propto 2u^2\partial\psi/\partial\phi, \tag{2a}$$

$$J_z^{(2)} \propto ju^2(\alpha\partial\alpha^*/\partial\phi + \beta\partial\beta^*/\partial\phi - \text{c.c.}), \tag{2b}$$

$$J_z^{(3)} \propto jr\partial[u^2(\alpha\beta^* - \alpha^*\beta)]/\partial r. \tag{2c}$$

where $J_z^{(1)}$ is the well-known OAM associated with the azimuthal phase gradient, $J_z^{(2)}$ and $J_z^{(3)}$ are associated with the distribution of SoPs. If α and β are real valued, implying that SoP at any location of the field section is local linearly polarized, both $J_z^{(2)}$ and $J_z^{(3)}$ are zero. If either α or β is at least a complex-valued function, $J_z^{(2)}$ and $J_z^{(3)}$ are possibly nonzero values. $J_z^{(2)}$ arising from the azimuthal

variation of SoPs is the simple superposition of contributions from two orthogonal field components.

We are interested in $J_z^{(3)}$, a new class of optical OAM. We define a parameter σ, describing SoP, as $\sigma = j(\alpha\beta^* - \alpha^*\beta)$. For instance, $\sigma = +1$ or -1 represents the right-handed (RH) or left-handed (LH) circular polarization, whereas $\sigma = 0$ is the linear polarization. Surprisingly, $J_z^{(3)}$ originates from the *curl* of the vector $\sigma u^2 \hat{\mathbf{e}}_z$. As we expected, the optical OAM can be indeed associated with space-variant SoPs independent of phase. To achieve nonzero-valued $J_z^{(3)}$, two prerequisites should be satisfied: (i) $\sigma \neq 0$, i.e., local SoPs at locations in the field section should not be all linearly polarized, and (ii) σ or SoPs should be radial-variant instead of being azimuthal-variant. A nonzero-valued $J_z^{(3)}$ requires the light field to be a vector field with the radial-variant hybrid SoPs. The crucial issue is how to create the desired vector field satisfying the above requirements.

We should emphasize that as a common requirement for light field carrying optical OAM, a certain physical quantity (phase or SoP) of light field must be space-variant. The helically phased scalar fields, which have on-axis phase singularity, carry the known OAM caused by the azimuthal phase gradient independent of polarization [see Eq. (2)]. In contrast, the radial-variant vector fields with hybrid SoPs, which have no polarization singularity, carry the optical OAM associated with the curl of polarization independent of phase [see Eq. (2c)].

Generation of Radial-Variant Vector Fields.—Most reported vector fields [22–32] have a common feature: the distribution of SoPs is a function of ϕ only. However, radial-variant vector fields are rarely involved. Niv *et al.* [33] reported the generation of radial-variant vector fields with space-variant axially symmetric distribution of SoPs with the aid of subwavelength grating for a 10.6 μm CO_2 laser. A crucial issue still remains: how to create the vector fields satisfying the requirements of producing the optical OAM associated with the curl of polarization. Based on the idea of wave-front reconstruction in the scheme presented in Refs. [24,25], the additional phase δ in the transmission function of a spatial light modulator (SLM) is a function of ϕ only, as $\delta = m\phi + \alpha_0$. The generated vector fields have the azimuthal-variant SoPs. In theory, if δ is a function of r only, as $\delta = 2n\pi r/r_0 + \alpha_0$ (where r_0 is the radius of the vector field, n is the radial index, and α_0 determines SoP at $r = 0$), the vector field should have radial-variant SoPs.

Generating the radial-variant vector field with local linear polarization requires a pair of orthogonal base vectors [24]. The scheme similar to Fig. 1 in Ref. [24] is shown by the dashed-line box in Fig. 3 below; in this situation two $\lambda/4$ wave plates are used to generate a pair of orthogonal RH and LH circularly polarized fields, and the additional phase in SLM is set as $\delta = 2n\pi r/r_0 + \alpha_0$. The intensity patterns of all generated vector fields exhibit uniform distribution and are indistinguishable for different values of n and α_0. As shown in Figs. 1(a)–1(d), the intensity patterns of four vector fields passing through a horizontal polarizer exhibit cylindrical symmetry with concentric extinction rings, suggesting that the SoPs of the generated vector fields have radial-variant and local linearly polarized distributions. The linear polarization at the center $r = 0$ is along the direction of $\phi = \alpha_0$.

We now generate the radial-variant vector fields with hybrid SoPs (including linear, elliptical, and circular polarizations). The scheme similar to Fig. 2 in Ref. [25] is shown by the dashed-line box in Fig. 3 below, in this situation two $\lambda/2$ wave plates are used to generate a pair of orthogonal linearly polarized fields, and the additional phase in SLM is still set as $\delta = 2n\pi r/r_0 + \alpha_0$. As shown in the 1st and 2nd columns of Fig. 2, the intensity patterns of two generated radial-variant vector fields exhibit the uniform distribution, although SoPs have hybrid distribution. As an example, in the 1st column, as r increases from $r = 0$ to r_0, SoPs change from $\pi/4$ linear polarization at $r = 0$ to RH elliptical polarization within $r \in (0, r_0/4)$, RH circular polarization at $r = r_0/4$, RH elliptical polarization within $r \in (r_0/4, r_0/2)$, $3\pi/4$ linear polarization at $r = r_0/2$, LH elliptical polarization within $r \in (r_0/2, 3r_0/4)$, LH circular polarization at $r = 3r_0/4$, LH elliptical polarization within $r \in (3r_0/4, r_0)$, and finally, to $-3\pi/4$ linear polarization at $r = r_0$.

To characterize the distribution of SoPs of a vector field, three Stokes parameters, s_1, s_2, and s_3, in the representation of the Poincaré sphere Σ should be specified [25,34]. For the radial-variant vector field with hybrid SoPs, the theoretical Stokes parameters are $s_1 = 0$, $s_2 = \cos(4n\pi r/r_0 + 2\alpha_0)$, and $s_3 = \sin(4n\pi r/r_0 + 2\alpha_0)$. The measured results, as shown in the 2nd to 4th rows of Fig. 2, exhibit cylindrical symmetry, implying that SoPs are indeed radial variant only as predicted in theory, $s_1 = 0$, so SoP at any location of the field section is represented by a point in the $\pi/2$ meridian circle on Σ. For instance, in the 1st column, the SoP at $r = 0$ is $\pi/4$ linearly polarized and is located at point $(s_1, s_2, s_3) = (0, 1, 0)$ in the equator on Σ, whereas the SoP at $r = r_0/4$ is RH circularly polarized and is located at the north pole of (0, 0, 1) on Σ, and so on. For comparison, the measured Stokes parameters of the local linearly polarized vector field are also shown in the 3rd column of Fig. 2. Both theoretical and measured results show that this vector field has $s_3 = 0$, suggesting that the SoP at any location is indeed linearly polarized and is

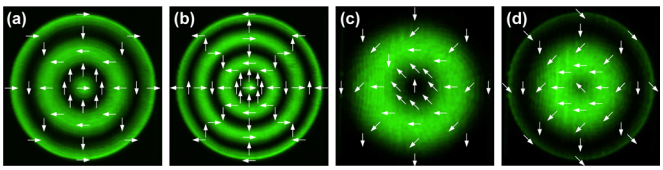

FIG. 1 (color online). Intensity patterns of four radial-variant linearly polarized vector fields passing through a horizontal polarizer and their schematics of SoPs. (a) $n = 1.0$ and $\alpha_0 = 0$, (b) $n = 1.5$ and $\alpha_0 = 0$, (c) $n = 0.5$ and $\alpha_0 = \pi/2$, and (d) $n = 0.5$ and $\alpha_0 = 3\pi/4$.

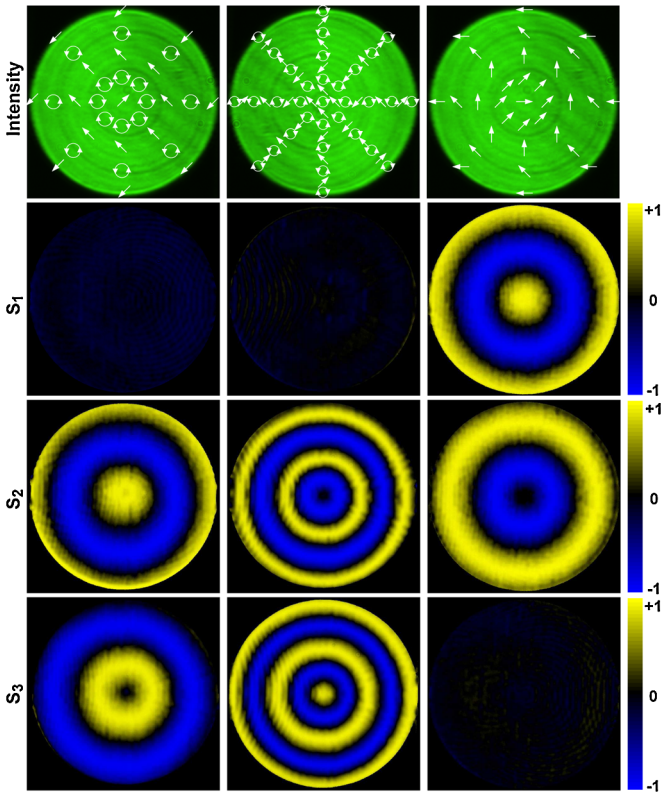

FIG. 2 (color online). Intensity patterns of two radial-variant vector fields with hybrid SoPs, schematics of SoPs, and measured Stokes parameters. The 1st and 2nd columns correspond to ($n = 0.5$, $\alpha_0 = 0$) and ($n = 1.0$, $\alpha_0 = \pi/4$), respectively. For comparison, a local linearly polarized vector field with ($n = 0.5$, $\alpha_0 = 0$) is also depicted in the 3rd column.

located at the equator on Σ. The generated radial-variant vector fields with hybrid SoPs indeed satisfy the two prerequisites previously mentioned for generating OAM associated with the curl of polarization.

Evidence of OAM Associated with the Curl of Polarization.—To confirm the feasibility of OAM associated with the curl of polarization, the focused vector field as an optical tweezer is a useful tool. Figure 3 shows the trapping experimental scheme, wherein the laser source at 532 nm has a power of 20 mW. All the generated vector fields have the same radius of $r_0 = 2.5$ mm, a 60× objective (with NA = 0.7) is used to focus the vector field, and the neutral colloidal microspheres with a diameter of 3.2 μm are dispersed in a layer of sodium dodecyl sulfate solution between a glass coverslip and a microscope slide.

We first implement simulations for the focusing property of radial-variant vector fields. The parameters used in simulations are the same as those used in the experiment. The simulation results indicate that the radial-variant vector fields (not only local linear polarization but also hybrid SoPs) are tightly focused into a ring focus using a high NA objective. As an example, the simulated intensity patten of the ring focus where $n = 10$ is shown in the inset (a) of Fig. 3. The inset (b) of Fig. 3 shows the simulated radial

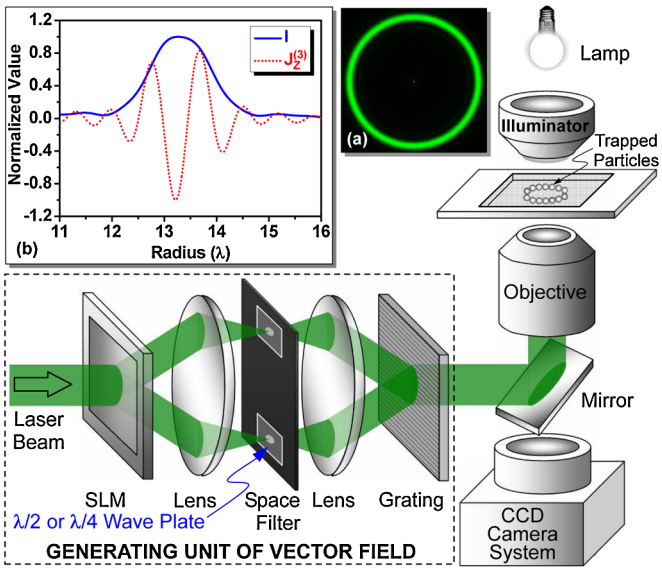

FIG. 3 (color online). Experimental configuration to validate OAM associated with the curl of polarization. The dashed-line box shows the generating unit of radial-variant vector fields. Inset (a) shows an example of simulated ring focus. Inset (b) shows the properties of the ring focus for a radial-variant vector field with hybrid SoPs ($n = 10$), where the solid and dashed lines are the radial dependences of intensity and OAM $J_z^{(3)}$, respectively.

dependences of intensity (solid line) and of OAM $J_z^{(3)}$ associated with the curl of polarization (dashed line) in the focal plane for the radial-variant vector field with hybrid SoPs where $n = 10$. The maximum OAM $J_z^{(3)}$ and the strongest intensity locate at the same radial position, which is of such great importance that trapped particles in the ring focus can acquire the maximum torque when rotating around the ring focus.

The trapping experiments indicate that the ring traps generated by radial-variant vector fields (not only with the local linear polarization but also with hybrid SoPs) can trap an arbitrary number of particles. The reason originates from the fact that the ring focus has a continuously changeable radius because n can be an arbitrary real number, which is quite different from the discrete radius of the ring focus generated by the azimuthal-variant vector field. For the particles trapped in the ring optical tweezers produced by radial-variant vector fields with local linear polarization, no motion is observed around the ring focus, implying that radial-variant vector fields with local linear polarization carry no optical OAM.

We are very interested in the trapping property of the ring traps generated by the radial-variant vector field with hybrid SoPs. As the time-lapse photographs shown in the upper row of Fig. 4, the trapped particles when $n = 10$ move clockwise around the ring focus [35], with an orbital period of ~8.4 s. When n is switched from positive ($n = 10$) to negative ($n = -10$), the motion direction of the trapped particles is synchronously reversed [35], as

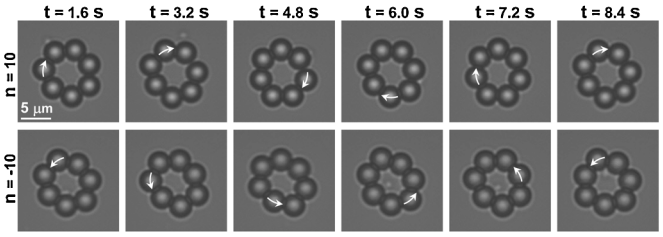

FIG. 4. Snapshots of the motion of trapped particles around the ring focus generated by radial-variant vector fields with hybrid SoPs, caused by polarization-curl-induced OAM (also see Ref. [35]).

shown in the bottom row of Fig. 4. The observed results imply that the ring traps have the capability to exert torque to the trapped isotropic particles. Consequently, the radial-variant vector fields with hybrid SoPs can carry the optical OAM associated with the curl of polarization independent of phase.

For the interaction of light with matter, the polarization can influence anisotropic materials, but not isotropic materials, which is true for scalar fields. As we predicted, the induction of the vector fields breaks this limitation to make the polarization nature of light field influence optically isotropic materials. Since SAM and OAM decouple in the paraxial limit [36] and SAM results in the rotation of an anisotropic particle around its own axis [21], our observed rotation of the trapped isotropic particles should be dominated by OAM.

Summary.—We predict a novel optical OAM associated with the curl of polarization independent of phase. To demonstrate this idea, a scheme is presented for creating the desired radial-variant vector fields and enabling the flexible generation of novel vector fields. Using optical traps, we confirm that the radial-variant vector fields with hybrid SoPs can carry this novel OAM, whereas the radial-variant linearly polarized vector fields cannot. Our results create a link between two important issues on optical OAM and vector field. Our idea may spur further independent insights into the generation of natural waves carrying OAM and the expansion of the functionality of many optical systems, thereby facilitating the development of additional surprising applications.

The authors acknowledge the support of NFSC under Grants No. 10934003 and No. 10874078, and 973 Program of China under Grant No. 2006CB921805.

*htwang@nankai.edu.cn/htwang@nju.edu.cn

[1] M. Padgett, J. Courtial, and L. Allen, Phys. Today **57**, 5, 35 (2004); L. Allen, M. J. Padgett, and M. Babiker, Prog. Opt. **39**, 291 (1999).
[2] L. Allen *et al.*, Phys. Rev. A **45**, 8185 (1992).
[3] G. Molina-Terriza, J. P. Torres, and L. Torner, Nature Phys. **3**, 305 (2007).
[4] See for example: D. N. Neshev *et al.*, Phys. Rev. Lett. **92**, 123903 (2004); N. K. Efremidis *et al.*, Phys. Rev. Lett. **98**, 113901 (2007); S. Feng and P. Kumar, Phys. Rev. Lett. **101**, 163602 (2008).
[5] See for example: S. Barreiro and J. W. R. Tabosa, Phys. Rev. Lett. **90**, 133001 (2003); M. S. Bigelow, P. Zerom, and R. W. Boyd, Phys. Rev. Lett. **92**, 083902 (2004); M. F. Andersen *et al.*, Phys. Rev. Lett. **97**, 170406 (2006).
[6] See for example: A. Mair *et al.*, Nature (London) **412**, 313 (2001); A. R. Altman *et al.*, Phys. Rev. Lett. **94**, 123601 (2005); J. E. Nagali *et al.*, Nat. Photon. **3**, 720 (2009); Leach *et al.*, Science **329**, 662 (2010).
[7] C. Paterson, Phys. Rev. Lett. **94**, 153901 (2005).
[8] D. G. Grier, Nature (London) **424**, 810 (2003).
[9] See for example: G. C. G. Berkhout and M. W. Beijersbergen, Phys. Rev. Lett. **101**, 100801 (2008); M. Harwit, Astrophys. J. **597**, 1266 (2003).
[10] See for example: T. B. Leyser *et al.*, Phys. Rev. Lett. **102**, 065004 (2009); B. Thidé, Phys. Rev. Lett. **99**, 087701 (2007).
[11] See for example: R. Marchiano and J.-L. Thomas, Phys. Rev. Lett. **101**, 064301 (2008); P. Z. Dashti, F. Alhassen, and H. P. Lee, Phys. Rev. Lett. **96**, 043604 (2006).
[12] S. Sasaki and I. McNulty, Phys. Rev. Lett. **100**, 124801 (2008).
[13] M. Uchida and A. Tonomura, Nature (London) **464**, 737 (2010).
[14] See for example: S. Tung, V. Schweikhard, and E. A. Cornell, Phys. Rev. Lett. **97**, 240402 (2006); K. C. Wright *et al.*, Phys. Rev. Lett. **102**, 030405 (2009).
[15] A. T. O'Neil *et al.*, Phys. Rev. Lett. **88**, 053601 (2002).
[16] J. E. Curtis and D. G. Grier, Phys. Rev. Lett. **90**, 133901 (2003).
[17] Y. Roichman *et al.*, Phys. Rev. Lett. **100**, 013602 (2008).
[18] A. Niv *et al.*, Opt. Lett. **33**, 2910 (2008).
[19] K. Miyakawa, H. Adachi, and Y. Inoue, Appl. Phys. Lett. **84**, 5440 (2004).
[20] H. Adachi, S. Akahoshi, and K. Miyakawa, Phys. Rev. A **75**, 063409 (2007).
[21] Y. Zhao *et al.*, Phys. Rev. Lett. **99**, 073901 (2007).
[22] Q. Zhan, Adv. Opt. Photon. **1**, 1 (2009).
[23] C. Maurer *et al.*, New J. Phys. **9**, 78 (2007).
[24] X. L. Wang *et al.*, Opt. Lett. **32**, 3549 (2007).
[25] X. L. Wang *et al.*, Opt. Express **18**, 10786 (2010).
[26] E. Hasman *et al.*, Prog. Opt. **47**, 215 (2005).
[27] K. S. Youngworth and T. G. Brown, Opt. Express **7**, 77 (2000).
[28] Q. Zhan and J. Leges, Opt. Express **10**, 324 (2002).
[29] R. Dorn, S. Quabis, and G. Leuchs, Phys. Rev. Lett. **91**, 233901 (2003).
[30] E. Hasman *et al.*, Appl. Phys. Lett. **82**, 328 (2003).
[31] G. Biener *et al.*, Opt. Lett. **30**, 1096 (2005).
[32] K. Y. Bliokh *et al.*, Opt. Express **16**, 695 (2008).
[33] A. Niv *et al.*, Opt. Lett. **30**, 2933 (2005)
[34] M. Born and E. Wolf, *Principles of Optics* (Cambridge University Press, Cambridge, 1999), 7th ed.
[35] See supplementary material at http://link.aps.org/supplemental/10.1103/PhysRevLett.105.253602 for a movie of the motion of trapped particles around the ring focus. A direct link to this document may be found in the online article's HTML reference section.
[36] M. V. Berry, J. Opt. A **11**, 094001 (2009).

Transcription of domain patterns in near-stoichiometric magnesium-doped lithium niobate

Hao Zeng,[1] Yongfa Kong,[2,a)] Tian Tian,[1] Shaolin Chen,[2] Ling Zhang,[2] Tongqing Sun,[1] Romano Rupp,[2] and Jingjun Xu[1,2]
[1]*School of Physics, Nankai University, Tianjin 300071, People's Republic of China*
[2]*The MOE Key Laboratory of Weak-Light Nonlinear Photonics and TEDA Applied Physics School, Nankai University, Tianjin 300457, People's Republic of China*

(Received 1 August 2010; accepted 29 October 2010; published online 17 November 2010)

Recently, light-induced domain reversal has been developed to a promising method for domain engineering, but the depth of reversed domain is only of several tens of microns, which greatly limits its practical applications. In this Letter, we fabricated domain patterns on the –z face of 1.0 mol % Mg doped near-stoichiometric lithium niobate with the assistance of a focal 532 nm laser, and then succeeded to transcribe these domain patterns from the –z to the +z face by applying external field without laser illumination. The transcribed domains have much larger depths, can sustain more than 100 times of the transcription cycles without large deformation, and can be erased by one transcription cycle with illumination of 532 nm laser. Finally, a light-induced ferroelectric domain transcription model was proposed. © *2010 American Institute of Physics*.
[doi:10.1063/1.3518474]

Lithium niobate ($LiNbO_3$, LN) is a ferroelectric crystal of great interest for material scientists due to its excellent electro-optic, acousto-optic, elasto-optic, piezoelectric, pyroelectric, and nonlinear properties. Ferroelectric domain engineering of LN has received much attention for its wide applications, such as nonlinear frequency conversion devices, optical parametric oscillators, photonic band-gap devices, and electro-optic Bragg modulators.[1–4] Up to now, the most common domain reversal technique for creating domain patterns is electric poling, where a photolithographically patterned electrode provides a spatially modulated electric field across the crystal along z-axis. Because of the complex photolithograph and limited minimal domain widths, some improved poling techniques are proposed to obtain more precise domains.[5–7] Light-induced domain reversal,[8] i.e., reversal by the simultaneous application of an external field and laser illumination, has developed to a promising method for domain engineering in recent years. Because the reverse field is reduced within the illuminated areas, a light pattern can be transformed to a domain pattern without any photolithography.[9,10]

However, a problem of light-induced domain reversal is the limitation of a domain depth. Needle-like domains nucleate first on the –z face within the illuminated area, and then spread outside, but prefer to accomplish reversal at the edge of the laser spot under a much higher external electric field than that for light-induced domain nucleation.[11] In such a high electric field, the domain size will be much larger than that of the laser spot. Usually, the depth of these domains is within several tens of microns without such high external field, which limits their practical applications. In this Letter, we present a method to transcribe domain patterns between the –z and +z faces. The transcribed +z domains have more regular domain walls, smaller sizes, and much larger depths, which is advantageous to some future applications of domain engineering.

The samples used in this study were provided by the R&D Center for Photon-Electro Materials of Nankai University and are 0.3 mm thick z-cut near-stoichiometric LN single crystals doped with 1.0 mol % Mg. The experimental setup mainly involves an insulating holder filled with tap water, which allows simultaneous illumination and application of a uniform electric field along the z-axis of the sample. A beam from a frequency-doubled diode-pumped $Nd:YVO_4$ laser with a wavelength of 532 nm was focused to a spot size of 3.5 μm by using a 10×, 0.25 NA (NA denotes numerical aperture) objective at a depth of less than 50 μm below the –z surface. The power of the laser beam was about 70 mW, and thus the intensity at the focal spot is about 5.2×10^5 W/cm^2. Positioning and exposure were achieved by a computer-controlled two-axis stage system coupled with a mechanical shutter. Arrays of domain spots with selected exposure time and applied field were formed first on the –z face. Then we applied a forward electric field of 2300 V/mm (100 V/mm lower than the reverse electric field) for 10 s. Domains beyond the illuminated regions accomplished reversal normally, while further growths of former light-induced reversed domains were inhibited, leaving +z surface domain islands on a merged background, thus domain patterns were transcribed from –z to +z face. In the back transcribed stage, we used lower electric field of −1200 V/mm with the same duration time to transfer domain patterns back to the –z face. All samples were etched in hydrofluoric acid for 10 min, after then, a microscope was employed to observe the domains on both surfaces.

Figure 1 shows the process of the domain patterns being transcribed between two faces. First, light-induced domain patterns with different domain sizes were fabricated on the –z face by different electric fields (in the range of 600–300 V/mm with a step of 60 V/mm for top to bottom line) and different duration times (1, 2, 4, 6, 8, and 10 s for left to right line) on the –z face. Then an electric field of 2300 V/mm was applied for 2 s to succeed partial forward transcription. Under such a high field, domains first nucleate around the edge

a)Electronic mail: kongyf@nankai.edu.cn.

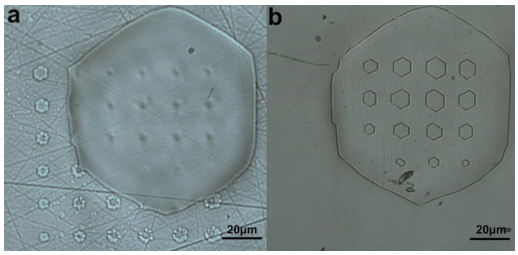

FIG. 1. (Color online) Microscopic images of domain patterns. (a) Light-induced domain patterns on –z face fabricated by different electric fields (600–300 V/mm with a step of 60 V/mm for top to bottom line) and duration time (1, 2, 4, 6, 8, and 10 s for left to right line) under a consequent transcribed electric field of 2300 V/mm for 2 s. (b) Partially transcribed domain patterns on +z face.

of the former light-induced domains, and then become larger and merge with each other, forming a large six-sided polygon of reversed area, which serves as a merged background in the transcribed process [Fig. 1(a)]. The smooth and continuous unetched section shows the newly reversed domain area while the etched area is the nonreversed −z face. Figure 1(b) shows the optical image of partially transcribed domain patterns inside the merged background on the +z face. It is interesting that although the domains on the −z face grow much larger than the laser spot and merge to a big six-sided polygon domain, the transcribed +z domains maintain its original shapes and the size of the minimal transcribed domain is about 3.3 μm, which is almost the same as the size of the laser spot (3.5 μm). It should be pointed out that in Fig. 1(b), there is no transcribed domain corresponding to the lower left domain within the hexagonal region in Fig. 1(a), which indicates that the original –z light-induced domain is unstable and cannot be transcribed as its size is smaller than the laser spot.

In order to compare the domain quality, we observed the etched domain patterns on both surfaces. Figure 2(a) shows the optical image of a two-dimensional light-induced domain pattern on the –z surface fabricated at 600 V/mm and a duration time of 10 s. Figure 2(b) shows the corresponding transcribed domain pattern on the +z face after applying forward transcribed field of 2300 V/mm for 10 s. We can see that the transcribed domains on +z mostly follow the original shapes on the –z face, and importantly, the domain walls appear to be extremely straight while some of them are somewhat irregular on the –z face, origin from the surface pinning effect.[9] Although some transcribed domains seem to be somewhat deformed after transcription, further experiments have shown that such deformations can be overcome

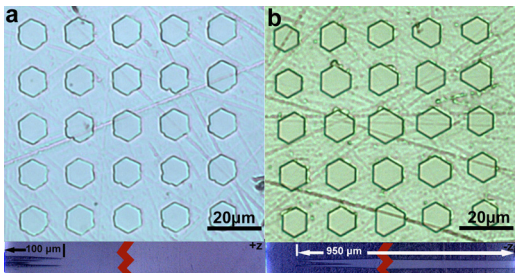

FIG. 2. (Color online) Comparison between light-induced –z patterns and transcribed +z patterns. (a) Two dimensional domain patterns on –z face fabricated by a focal laser beam and electric field of 600 V/mm and a duration time of 10 s. (b) The corresponding transcribed domain patterns on +z face. The imagines beneath are etched y face profiles of domain spots.

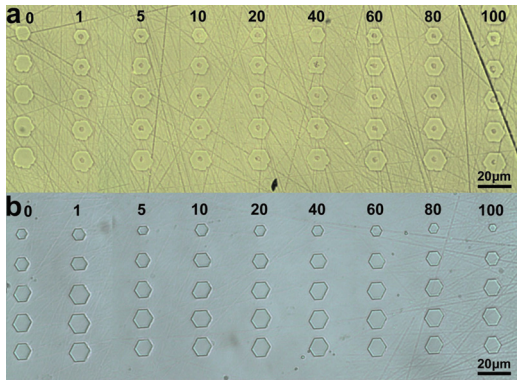

FIG. 3. (Color online) Microscopic images of the domain patterns with varying transcription cycles from 1 to 100. (a) Light-induced and transcribed domain patterns on –z face. (b) Transcribed domain patterns on +z face.

by accurate control of the electric field and the duration time. In order to compare the depths of the domain structures before and after transcription, we duplicated the transcription experiment in another sample of 1 mm thickness and then polished its y face. The pictures at the bottom of Fig. 2 show the light-induced and transcribed domain spot profiles after 3 h of etching of the y face. All light-induced domains on the –z face within the laser spot have limit depths of no more than 60 μm, while domains outside the illuminated region can grow to a deeper depth of about 100 μm. However, the transcribed +z domains have much deeper depths that reach about 950 μm, i.e., they go nearly across the whole thickness of the sample. The domain wall is quite straight inside the crystal, which might be beneficial for future applications of domain engineering.

Another interesting phenomenon is that by applying a back transcribed electric field of somewhat more than 600 V/mm, all the +z face domain patterns disappear and transfer back to the –z face again. Figure 3 shows the optical images of the domain patterns with different transcription cycles on both surfaces. All the domain patterns keep their original shapes quite well even after 100 times of transcription cycle, which means light-induced domain structure holds a high stability during the transcribed process. At the center of each domain on the –z face, it generates a new round area similar to the laser spot after one transcription cycle, the reason of which will be discussed later. Further experiments indicate that while irradiated by 532 nm laser light (intensity of 30 $\mathrm{mW/cm^2}$) with one transcription cycle, the entire domain patterns no matter on –z or +z face will be erased. It means that the polarization of the crystal can be refreshed again by simultaneously applying laser illumination and electric field.

The phase information of the transverse section across the reversed domain has been measured by digital holographic interferometry. It was found that there exists a deformation of the crystal lattice in the area of the focal spot.[12] Besides, y face cross-sectional profiles of light-induced domain in Mg doped congruent LN have shown that many short needle-like domains penetrated into the bulk in the area of the spot with limited depths of no more than 30 μm, while deeper needle-like domains grew outside the area of illumination and kept growing deeper with increasing exposure times.[13] According to former and our results, we proposed a transcribed model as schematically shown in Fig. 4. Strong illumination leads to photoexcitation of charges. A concentration gradient is formed which drives electrons into

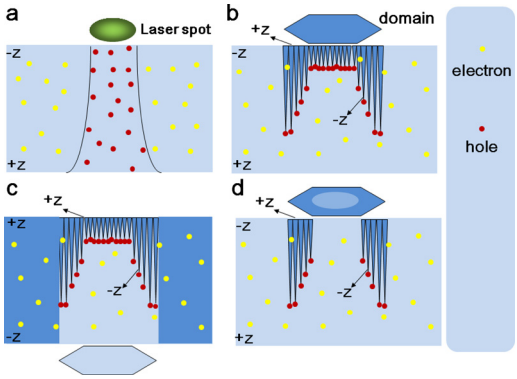

FIG. 4. (Color online) The schematic diagram for domain transcribed process. (a) The distribution of light-induced electrons and holes. (b) The formation of a light-induced domain on –z face. (c) The forward domain transcription. (d) The backward domain transcription.

the dark area and holes with lower mobility remain in the illuminated region, producing a short range extra electric field only near the –z surface, which decreases the coercive field locally [Fig. 4(a)]. The reduction proportion of nucleation field increases exponentially with increasing laser intensity over a threshold value and eventually reaches some saturation value at higher intensities.[12] The intensity used in our experiment was about 5.2×10^5 W/cm^2. We have also tried intensities lower by one order of magnitude and found no difference of the light-induced nucleation field, i.e., with an intensity of 5.2×10^5 W/cm^2 we are far beyond saturation. At such a high intensity, the Gaussian shape of the laser beam, the intensity gradient, and the conductivity of crystal are the most important parameters to determine the light-induced extra field. When a constant electric field and a focal laser beam are applied, domain nucleation occurred within the beam spot; at the same time, domains propagate toward the +z face forming head-to-head boundary beneath the surface[11] [Fig. 4(b)]. In the region of illumination, holes reach a high concentration level, which are easily accumulated by the head-to-head boundary and then screen the depolarization field, stopping these needle-like domains growing any further and leading to a limited depth but large wall energy of domains. After reversing for a longer time, domains spread outside the focal spot, where the laser intensity decreases rapidly, causing a lower concentration of light-induced holes. In this region, the needle-like domains need to grow deeper and larger in order to accumulate enough holes for boundary charge compensation, some of them even cross the whole thickness. Because of merging with each other, domains with lower wall energy in this region become more stable in the consequent poling process, and this is considered to be the precondition of the transcribed process. In the forward transcribed stage, the laser beam is removed and a much higher electric field is applied. Under these conditions, the domains at the edge of the former light-induced reversed domain will grow normally across the whole sample thickness and then spread outside to merge with other domains that spread from other spots. However, the further growth under the illuminated area is inhibited, leaving a +z surface domain island on a merged background [Fig. 4(c)]. In the backward transcribed stage, a negative sign electric field is applied, and domains outside the inhibited area all turn back to their original states. It is proven that there exists a round area in the core of the reversed domain after one transcription cycle, which has a size approximately matching up that of the focal spot [Fig. 3(a)]. That is possibly due to high wall energy of the domains, small domain size, and low density of surface screen charge, and as a result domains in spot region become unstable and turn back to its original state again under backward transcribed operation [Fig. 4(d)]. Because of much low dark mobility of hole and the very strong attractive force from the head-to-head boundary, positive charges can be conserved on the boundary for a long time, compensate the head-to-head boundary charge, and keep the domain pattern sustain 100 cycles in the consequent transcribed poling. This model is proven by further experiments that all the patterns can be erased by laser illumination and simultaneous electric field, because of the increased electron and hole mobility, as a result of an accelerated charge compensation process on the domain boundaries.

In summary, light-induced domain patterns have been fabricated by a focal 532 nm laser and simultaneous electric fields on the –z face of 1.0 mol % Mg doped near-stoichiometric LN. Applying consequently electric poling, we succeed to transcribe domain patterns from –z to +z face. The transcribed +z domains have more regular domain walls and larger depths, which will benefit to future applications. The transcribed domains can keep their original shape for more than 100 cycles, but can be erased by just 1 cycle under illumination of a 532 nm laser. Then, a model for light-induced domain transcription was proposed. This work gives a method to transcribe the surface structures between –z and +z faces without obvious deformation, thus provides an easy alternative method for fabricating useful domain and surface structures.

This work was financially supported by the National Basic Research Program of China (Grant No. 2007CB307002), the Chinese National Key Basic Research Special Fund (Grant No. 2011CB922003), the National Advanced Materials Committee of China (Grant No. 2007AA03Z459), and the National Natural Science Foundation of China (Grant No. 50702026). The authors thank the referee for valuable comments and suggestions.

[1]N. G. Broderick, R. G. W. Ross, H. L. Offerhaus, D. J. Richardson, and D. C. Hanna, Phys. Rev. Lett. **84**, 4345 (2000).
[2]V. Pruneri, J. Webjörn, P. St. J. Russell, and D. C. Hanna, Appl. Phys. Lett. **67**, 2126 (1995).
[3]F. Chen, M. Stepić, C. E. Rüter, D. Runde, D. Kip, V. Shandarov, O. Manela, and M. Segev, Opt. Express **13**, 4314 (2005).
[4]J. A. Abernethy, C. B. E. Gawith, R. W. Eason, and P. G. R. Smith, Appl. Phys. Lett. **81**, 2514 (2002).
[5]V. Ya. Shur, E. L. Rumyantsev, E. V. Nikolaeva, E. I. Shishkin, D. V. Fursov, R. G. Batchko, L. A. Eyres, M. M. Fejer, and R. L. Byer, Appl. Phys. Lett. **76**, 143 (2000).
[6]K. Terabe, M. Nakamura, S. Takekawa, K. Kitamura, S. Higuchi, Y. Gotoh, and Y. Cho, Appl. Phys. Lett. **82**, 433 (2003).
[7]H. Steigerwald, F. Luedtke, and K. Buse, Appl. Phys. Lett. **94**, 032906 (2009).
[8]F. Kahmann, R. Pankrath, and R. A. Rupp, Opt. Commun. **107**, 6 (1994).
[9]H. Zeng, Y. Kong, H. Liu, S. Chen, Z. Huang, X. Ge, and J. Xu, J. Appl. Phys. **107**, 063514 (2010).
[10]V. Dierolf and C. Sandmann, Appl. Phys. Lett. **84**, 3987 (2004).
[11]W. Wang, Y. Kong, H. Liu, Q. Hu, S. Liu, S. Chen, and J. Xu, J. Appl. Phys. **105**, 043105 (2009).
[12]Y. Zhi, D. Liu, W. Qu, Z. Luan, and L. Liu, Appl. Phys. Lett. **90**, 042904 (2007).
[13]C. E. Valdivia, Ph.D. thesis, University of Southampton, 2007.

Electron acceleration in vacuum induced by a tightly focused chirped laser pulse

Jian-Xing Li (栗建兴),[1] Wei-Ping Zang (臧维平),[1,a)] and Jian-Guo Tian (田建国)[1,2,b)]
[1]*The Key Laboratory of Weak Light Nonlinear Photonics, Ministry of Education, Teda Applied Physics School, Nankai University, Tianjin 3000457, People's Republic of China*
[2]*Photonics Center, School of Physics, Nankai University, Tianjin 300071, People's Republic of China*

(Received 25 October 2009; accepted 29 December 2009; published online 19 January 2010)

Electron acceleration in vacuum induced by a tightly focused chirped laser pulse has been studied. For a fixed laser output power, the tightly focused chirped laser pulse can accelerate electrons to much higher energies. Focusing laser down to the order of wavelength requires inclusion of terms of third order at least in the diffraction angle ε in the description of the associated field. Retained electron energy depends strongly on frequency chirp parameter and initial position of the electron. Besides, retained energy increases with laser intensity, pulse duration, and initial velocity of electron, and varies periodically with laser constant phase. © *2010 American Institute of Physics*. [doi:10.1063/1.3294634]

Petawatt lasers[1] with repetition of ultrahigh intensity and ultrashort pulses have been developed based on chirp-pulse-amplification technique. Laser-based accelerators[2] are capable of producing high-energy electrons in much shorter distances than conventional accelerators due to the large electric fields associated with laser, and the problems inherent in laser-plasma interaction, such as instabilities, are absent in vacuum. Consequently, electron acceleration by an intense laser attracts much attention and has been investigated widely.[3–7]

A significant scheme for laser acceleration has been proposed based on chirping in laser frequency.[8–10] In this scheme, due to the contribution of frequency chirp to the phase synchronization of the laser pulse and the electron, the electron can gain considerable energy in the interaction with a focused chirped laser pulse whose electric field can be simulated by low-order Gaussian field. The ultimate goal of electron acceleration is to reach giga-electron-volt or even tera-electron-volt energy, which requires the use of laser with extremely high intensity. Such intensity may be produced in the laboratory by focusing a laser beam to an extremely small spatial dimension, typically a few microns. When a laser beam is focused down to the order of laser wavelength, a Gaussian beam description becomes inaccurate.[3,4] By the use of Lax series approach,[11] some researchers[12–14] analyzed this effect and got the high order correction terms of the diffraction angle ε in the description of the associated fields. For a tightly focused laser, Lax series field is valid near the propagation axis, and its divergence far from the propagation axis can be eliminated by Weniger transformation.[15,16]

In this letter, we present that for a fixed laser power the tightly focused laser pulse is more beneficial to accelerate an electron to high energy. Focusing laser beam down to the order of wavelength requires inclusion of terms of third order in the diffraction angle ε in the description of the associated field. Energy obtained by electron depends strongly on various parameters, such as laser beam waist, chirp parameter, initial position of electron, laser intensity, pulse duration, initial velocity of electron, and laser constant phase.

In comparison with the elliptical and circular polarizations, the linear polarization seems to be more effective for a single electron acceleration using a chirped laser pulse.[10] The chirped laser pulse adopted here polarizes along the x direction and propagates along the z axis, and its electromagnetic field can be described[8–10,14,15]

$$E_x = -iE\left\{1+\varepsilon^2\left[f^2\xi^2-\frac{f^3\rho^4}{4}\right]+\varepsilon^4\left[\frac{f^2}{8}-\frac{f^3\rho^2}{4}-\frac{f^4}{16}(\rho^4-16\xi^2\rho^2)-\frac{f^5}{8}(\rho^6+2\xi^2\rho^4)+\frac{f^6\rho^8}{32}\right]\right\}, \tag{1}$$

$$E_y = -iE\xi\upsilon\left\{\varepsilon^2 f^2+\varepsilon^4\left[f^4\rho^2-\frac{f^5\rho^4}{4}\right]\right\}, \tag{2}$$

$$E_z = E\xi\left\{\varepsilon f+\varepsilon^3\left[-\frac{f^2}{2}+f^3\rho^2-\frac{f^4\rho^4}{4}\right]+\varepsilon^5\left[-\frac{3f^3}{8}-\frac{3f^4\rho^2}{8}+\frac{17f^5\rho^4}{16}-\frac{3f^6\rho^6}{8}+\frac{f^7\rho^8}{32}\right]\right\}, \tag{3}$$

$$B_x = 0, \tag{4}$$

$$B_y = -iE\left\{1+\varepsilon^2\left[\frac{f^2\rho^2}{2}-\frac{f^3\rho^4}{4}\right]+\varepsilon^4\left[-\frac{f^2}{8}+\frac{f^3\rho^2}{4}+\frac{5f^4\rho^4}{16}-\frac{f^5\rho^6}{4}+\frac{f^6\rho^8}{32}\right]\right\}, \tag{5}$$

$$B_z = E\upsilon\left\{\varepsilon f+\varepsilon^3\left[\frac{f^2}{2}+\frac{f^3\rho^2}{2}-\frac{f^4\rho^4}{4}\right]+\varepsilon^5\left[\frac{3f^3}{8}+\frac{3f^4\rho^2}{8}+\frac{3f^5\rho^4}{16}-\frac{f^6\rho^6}{4}+\frac{f^7\rho^8}{32}\right]\right\}, \tag{6}$$

where $x=\xi w_0$, $y=\upsilon w_0$, $\varepsilon=w_0/z_r$, $\rho^2=\xi^2+\upsilon^2$, $f=i/(z/z_r+i)$, Rayleigh length $z_r=kw_0^2/2$, w_0 is the beam waist radius, $E=E_0 f\exp(-f\rho^2)\exp\{i[\omega(\varsigma)t-kz+\varphi_0]-\varsigma^2/\tau^2\}$, the instantaneous frequency $\omega(\varsigma)=\omega_0+b_0\varsigma$, the retarded time $\varsigma=z/c-t$,

a)Electronic mail: wpzang@nankai.edu.cn.
b)Electronic mail: jjtian@nankai.edu.cn.

b_0 is frequency chirp parameter, ω_0 is the frequency at $\varsigma=0$, wave number $k=\omega(\varsigma)/c$, c is the speed of light in vacuum, k_0 is the wave number at $\varsigma=0$, τ is the laser pulse duration, E_0 is field amplitude and φ_0 is constant phase. $b=b_0/\omega_0^2$ is the dimensionless chirp parameter.

Electron acceleration can be simulated by solving the electron dynamics equations

$$\frac{d\mathbf{p}}{dt}=-e(\mathbf{E}+\boldsymbol{\beta}\times\mathbf{B}),\frac{d\chi}{dt}=-ec\boldsymbol{\beta}\cdot\mathbf{E}, \tag{7}$$

where the momentum $\mathbf{p}=\gamma mc\boldsymbol{\beta}$, the energy $\chi=\gamma mc^2$, the Lorentz factor $\gamma=(1-\beta^2)^{-1/2}$, and $\boldsymbol{\beta}$ is the velocity normalized by c. The peak field intensity I_0 can be expressed in terms of $I_0\lambda^2\approx 1.375\times 10^{18}q^2(\mathrm{W/cm^2})(\mu\mathrm{m})^2$, where intensity parameter $q=eE_0/mc\omega$. For the fields given by Eqs. (1)–(6), the laser power P may be calculated by integrating the time-averaged Poynting vector over the entire transverse, preferably through the focus. Dropping terms of order ε^6 and beyond, one gets[4,17]

$$P[TW]=\frac{\pi w_0^2}{2}I_0\left[1+\frac{\varepsilon^2}{4}+\frac{\varepsilon^4}{8}\right]$$
$$\approx 0.0216\left(\frac{qw_0}{\lambda}\right)^2\left[1+\frac{\varepsilon^2}{4}+\frac{\varepsilon^4}{8}\right], \tag{8}$$

where $I_0=I(0,0,0)=cE_0^2/8\pi$ is the on-axis peak intensity at focus. Equation (8) shows clearly that for a fixed laser power, the peak intensity is inversely proportional to the square of beam waist radius, or equivalently q is inversely proportional to w_0.

In simulations, the electron is considered to be accelerated from the initial position (x_0,y_0,z_0) with initial velocity $(\beta_x,\beta_y,\beta_z)$, and the initial position of the laser pulse peak is assumed to be at (0, 0, 0). The interaction of electron-laser locates mainly in the region near laser focus and propagating axis, where electron dynamics simulated by Lax series field keep convergent and valid.[7] Therefore, Lax series field shown above is employed in our simulations. The roles of some parameters such as laser beam waist radius, chirp parameter, laser initial position, laser intensity, pulse duration, initial velocity of electron, and laser constant phase in determining the final energy gain will be discussed below.

Figure 1 gives the curves of retained electron energy versus beam waist radius w_0, which are simulated by the first-order, third-order, and fifth-order correction field, respectively. When the laser power is fixed, its peak intensity is inversely proportional to the square of laser beam waist. Thus, the tightly focused laser pulse is more beneficial to accelerate electrons. But, if the laser beam waist is smaller than $w_{0,\mathrm{peak}}$, the electron will escape quickly the interaction region with a lower energy. For the chosen parameters, retained electron energy peaks at $w_{0,\mathrm{peak}}=3.5$ μm. When an electron is accelerated by an intense field with a suitable frequency chirp, it can remain in acceleration phase for a longer time and gain higher energy. Focusing laser pulse down to the order of wavelength requires inclusion of terms of ε^3 in the description of the associated fields. In the region $w_0>18$ μm, the ε model, the energy gain calculated by using the field accurate to ε, gives accurate results and the relative error is less than 1%. In the region $w_0<18$ μm, the ε model exhibits substantial deviations from the ε^3 model, and the ε^3 model gives the same results with the ε^5 model.

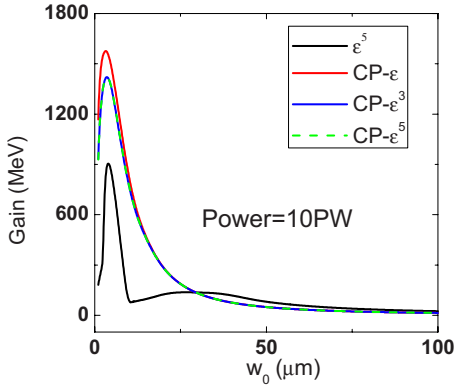

FIG. 1. (Color online) Retained electron energy as a function of beam waist radius w_0. Parameters used in simulations are $\lambda=1$ μm, $\tau=100$ fs, $\varphi_0=0.9\pi$, electron initial coordinate $(x_0,y_0,z_0)=(0,0,120/k_0)$, initial velocity $(\beta_x,\beta_y,\beta_z)=(0,0,0.9)$ and the full interaction time $\omega t=1\times 10^5$. Black curve is simulated by fifth-order correction field with the dimensionless chirp parameter $b=0$, and red, blue, and green (dashed) curves are simulated for $b=0.02$ by first-order, third-order, and fifth-order correction field, respectively. The fixed laser power is 10 PW.

E_z, the longitudinal electric field, always plays a dominate role in accelerating the electron. But the electron final energy is more sensitive to the chirp parameter than that of the longitudinal electric field of the laser pulse. The final energy gain depends strongly on dimensionless frequency chirp parameter b, as shown in Fig. 2. An appropriate linear and negative chirp can prolong effectively the acceleration stage of laser-electron interaction, so that the electron gains high energy. Retained electron energy varies acutely and approximately periodically with the increase in b when $b>0.2$. For the chosen parameters, the peak energy is about 1.86 GeV. Figure 3 gives retained energy as a function of initial position of electron relative to the laser pulse peak for $b=0.2$ and $b=0$, respectively. The laser intensity in the focal region is highest, thus, the electron should be accelerated

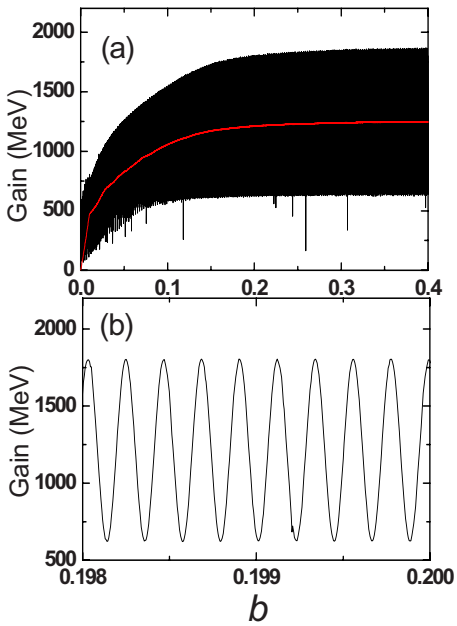

FIG. 2. (Color online) Retained electron energy vs dimensionless chirp parameter b. (b) is a small part of (a). Red curve in Fig. 2(a) is the average value of the oscillations. In the simulations, $w_0=5$ μm, $q=100$, and other parameters are the same as those of Fig. 1.

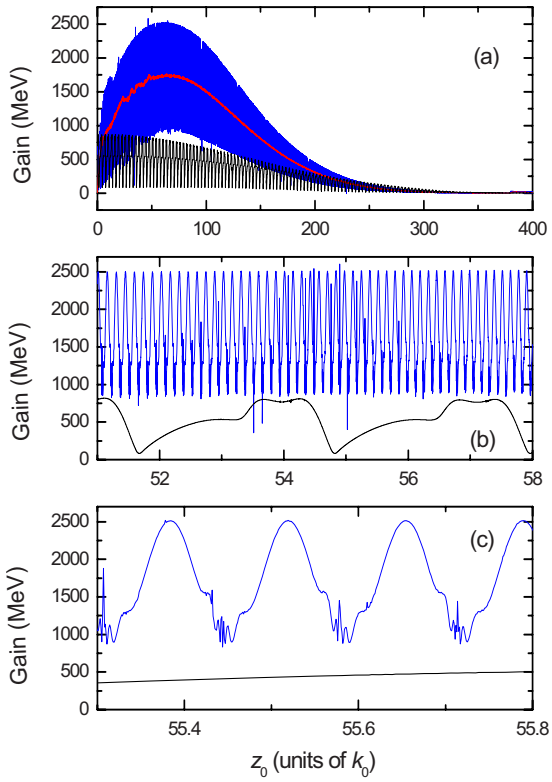

FIG. 3. (Color online) Retained electron energy vs initial coordinate z_0 of electron. Both (b) and (c) are a small part of (a), respectively. Blue and black curves are simulated by fifth-order correction field with dimensionless chirp parameter $b=0.2$ and 0, respectively. The red curve in Fig. 3(a) is the average value of the oscillations (blue curve).

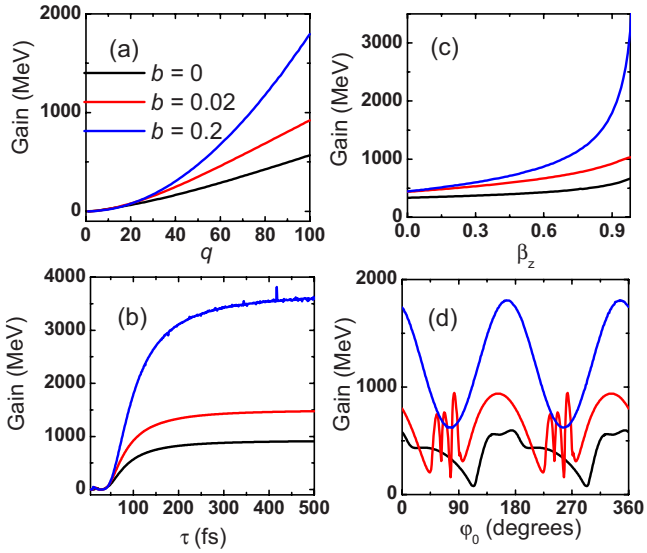

FIG. 4. (Color online) Retained electron energy as a function of (a) laser intensity parameter q, (b) laser pulse duration τ, (c) initial velocity of electron β_z, and (d) laser constant phase φ_0. Black, red and blue curves are obtained by fifth-order correction field with the dimensionless chirp parameter $b=0$, 0.02 and 0.2, respectively. Others parameters used in the simulations are the same as those of Fig. 1.

from a position near the peak of laser pulse. If a suitable frequency chirp is introduced, the electron can gain much higher energy especially in the region $z_0<240/k_0$. For the chosen parameters, the peak energy is about 2.513 GeV at $z_0=55.52/k_0$.

Figure 4 gives the dependences of retained energy on various parameters, such as dimensionless laser intensity q, pulse duration τ, initial velocity of electron β_z and constant phase φ_0 for $b=0$, 0.02, and 0.2, respectively. Results show that retained energy increases with q, τ, and β_z, and changes periodically with φ_0. The phase slippage between faster electron and laser pulse is smaller, thus a fast electron may retain in acceleration stage for a long time. Long pulse duration increases the interaction time of electron-laser. These factors are all beneficial to accelerate electron to high energy. For $b=0.2$, the peak of retained energy as a function of φ_0 is 1.807 GeV at $\varphi_0=166°$ and 346°. Moreover, it is seen that the electron can gain much higher energy with a suitable frequency chirp than that without a frequency chirp, and for the chosen parameters, the model with $b=0.2$ is better than that with $b=0.02$.

In summary, electron acceleration in vacuum by a tightly focused chirped laser pulse has been studied. Focusing laser pulse down to the order of wavelength is more beneficial to acceleration of electron. The final energy gain depends strongly on various parameters and will have a peak value when these parameters are chosen suitably. The energy gain of electron with a suitable frequency chirp is much higher than that without a frequency chirp.

We acknowledge financial supports from the Natural Science Foundation of China (Grant No. 60678025), Chinese National Key Basic Research Special Fund (Grant No. 2006CB921703), Program for New Century Excellent Talents in University, and 111 Project (B07013).

[1]M. D. Perry, D. Pennington, B. C. Stuart, G. Tietbohl, J. A. Britten, C. Brown, S. Herman, B. Golic, M. Kartz, J. Miller, H. T. Powell, M. Vergino, and V. Yanovsky, Opt. Lett. **24**, 160 (1999).
[2]E. Esarey, P. Sprangle, J. Krall, and A. Ting, IEEE Trans. Plasma Sci. **24**, 252 (1996).
[3]Y. I. Salamin and C. H. Keitel, Phys. Rev. Lett. **88**, 095005 (2002).
[4]Y. I. Salamin, G. R. Mocken, and C. H. Keitel, Phys. Rev. ST Accel. Beams **5**, 101301 (2002).
[5]D. N. Gupta and H. Suk, Appl. Phys. Lett. **91**, 211101 (2007).
[6]P. X. Wang and W. Scheid, Appl. Phys. Lett. **90**, 111113 (2007).
[7]J. X. Li, W. P. Zang, and J. G. Tian, Opt. Express **17**, 4959 (2009).
[8]K. P. Singh, Appl. Phys. Lett. **87**, 254102 (2005).
[9]F. Sohbatzadeh, S. Mirzanejhad, and M. Ghasemi, Phys. Plasmas **13**, 123108 (2006).
[10]F. Sohbatzadeh, S. Mirzanejhad, and H. Aku, Phys. Plasmas **16**, 023106 (2009).
[11]M. Lax, W. H. Louisell, and W. B. McKnight, Phys. Rev. A **11**, 1365 (1975).
[12]L. W. Davis, Phys. Rev. A **19**, 1177 (1979).
[13]J. P. Barton and D. R. Alexander, J. Appl. Phys. **66**, 2800 (1989).
[14]Y. I. Salamin, Appl. Phys. B: Lasers Opt. **86**, 319 (2007).
[15]J. X. Li, W. P. Zang, Y. D. Li, and J. G. Tian, Opt. Express **17**, 11850 (2009).
[16]R. Borghi and M. Santarsiero, Opt. Lett. **28**, 774 (2003).
[17]H. Luo, S. Y. Liu, Z. F. Lin, and C. T. Chan, Opt. Lett. **32**, 1692 (2007).

Light-controllable coherent backscattering from water suspension of lithium niobate microcrystalline particles

Xinzheng Zhang, Jun Li, Fan Shi, Yan Xu, Zhenhua Wang, Romano A. Rupp, and Jingjun Xu*

The Ministry of Education Key Laboratory of Weak-Light Nonlinear Photonics, Tianjin Economic-Technological Development Area, Applied Physics School and School of Physics, Nankai University, Tianjin 300457, China
**Corresponding author: jjxu@nankai.edu.cn*

Received January 19, 2010; revised March 23, 2010; accepted April 7, 2010; posted April 26, 2010 (Doc. ID 122906); published May 17, 2010

We experimentally study coherent backscattering of light for a water suspension of lithium niobate microcrystalline particles. Light-controllable weak localization of photons in a suspension is demonstrated for the first time to our knowledge. The effect is attributed to the reorientation of microcrystalline particles in the field of a linearly polarized pump beam. Thus the isotropic suspension becomes partially anisotropic. © 2010 Optical Society of America

OCIS codes: 030.1670, 290.1350, 290.4210, 160.3730.

Anderson localization [1], one of the most interesting phenomena in solid state physics, was first introduced in electron transport as a disorder-induced phase transition from the classical diffusion regime. Realizing that Anderson localization is a wave phenomenon, these concepts were then extended to sound waves, light waves [2], and matter waves [3]. Many phenomena of light localization have been reported, such as random laser, transverse localization of light [4], and coherent backscattering (CBS) [2]. CBS causes an enhancement of intensity in the backscattering direction, which is called the cone of CBS. It has been widely studied theoretically [5] and experimentally in various disordered systems such as suspensions [2], ceramics [6], porous glasses [7], and liquid crystals [8].

In the diffusion regime, light is transported across the diffusive material as a random walk with the average step being the transport mean free path (MFP) l^*. For weak localization, the angular width (full width at half-maximum) W of the CBS cone is proportional to λ/l^*, where λ is the wavelength of light in the scattering medium [2]. In order to effectively control the multiple scattering behavior in a random medium, a relatively large change of the transport MFP has to be achieved. The MFP depends strongly on the concentration [9] and diameter [2] of scatterers in the disordered medium. In particular, an anisotropic CBS cone in nematic liquid crystals has been observed that results from an anisotropic MFP [8]. Here we have chosen a water suspension of congruent lithium niobate (CLN) microcrystalline particles as a disordered medium to investigate CBS, because lithium niobate (LN) possesses exceptional optical, electro-optic, and photorefractive properties.

Localization behavior has been controlled by light in a waveguide [3] or photonic lattices [4] and by temperature in macroporous glass infiltrated with liquid crystal [10]. In this Letter we demonstrate that CBS of green light in a water suspension of CLN microcrystalline particles can be controlled by a red pump beam. It is the first observation of optically controlled weak localization of light in a suspension. The MFP of light inside the water suspension changes with the alteration of the effective refractive index of the particles, due to their reorientation induced by the pump light. The induced anisotropy of the suspension results in a width variation of the CBS cone.

A CLN single crystal was grown by the Czochralski method. Linearly interpolated from data in [11], its refractive indices at 532 nm are $n_{og} = 2.3237$ and $n_{eg} = 2.2346$. Microcrystalline particles were prepared by a planetary ball mill. Their diameter was about 220 nm after membrane filtration, as measured by dynamic light scattering. The suspension, formed by mixing 9.00 wt.% microcrystalline particles with deionized water through ultrasonic dispersion, was filled into cuvettes (10 mm × 10 mm× 45 mm). At higher concentrations, the suspension is not stable for a sufficiently long time because of sedimentation. On the other hand, lower concentrations mean poor signal-to-noise ratio of the backscattering measurements. A diode-pumped CW laser beam at 532 nm with vertical polarization was used as a probe. The beam divergence was less than 0.1 mrad, and the beam diameter was about 4.0 mm. Light at 671 nm from another diode-pumped CW laser passed through a Glan–Taylor prism and provided the pump. Its beam diameter was around 8.0 mm. In order to minimize the possible influence of the probe beam, a probe intensity as low as 37 mW/cm^2 was chosen. The pump intensity was four times larger. Both laser beams were combined through one beam splitter and impinged collinearly onto the sample cuvette. The polarization direction of the pump beam was adjusted by a half-wave plate. The CBS cone of the suspension was monitored by a CCD placed at the rear focal plane of a lens with a focal length of 400 mm. A band-pass filter before the lens blocked scattered red light. The angular resolution of our detection system is about 88 μrad, estimated by the measured Airy disk diameter.

The polarization detection of CBS cones was investigated by putting a polarizer in front of the CCD. As in [8], no enhancement with/without pump light was observed in the polarization reversing channel down to the noise level; i.e., experimental results given in this Letter refer to the polarization-preserving channel. Figure 1(a) shows a CBS image of the green beam without red pump light after 70 s of integration by the CCD. One can see the

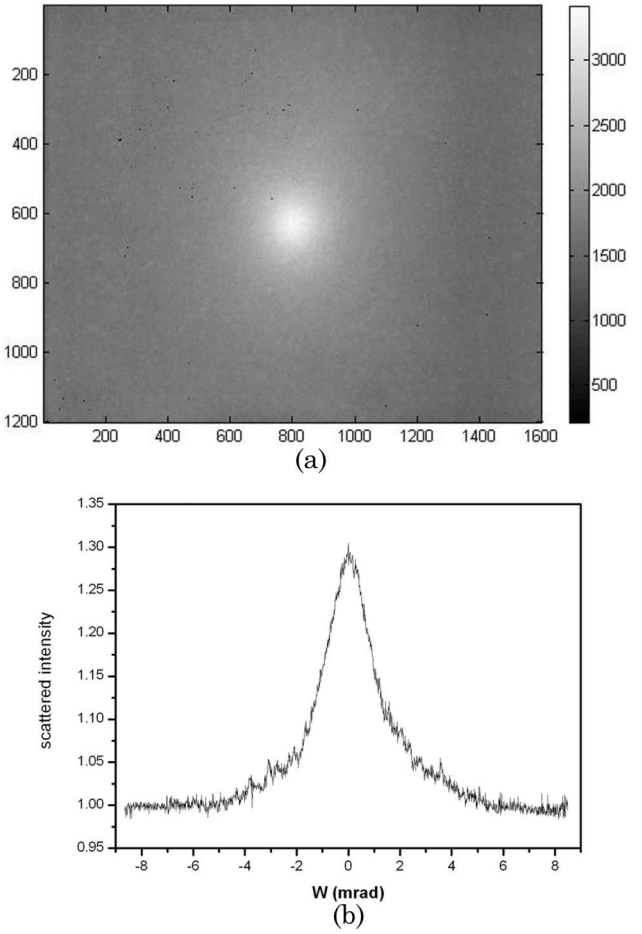

Fig. 1. CBS cone of the suspension: (a) image of backscattered intensity distribution under polarization-preserving detection and (b) intensity profile.

well-known enhanced backscattered cone caused by constructive interference of counterpropagating waves. Configuration averaging happens automatically by the Brownian motion of the scatterers. The profile of the CBS cone shown in Fig. 1(b) is the horizontal cross section of the CBS image through the center of the CBS peak; an angular width W of 2.396 mrad was derived from a Lorentz function fit. There is a slight but apparent asymmetry of the CBS peak that we do not understand, which requires further investigation.

A comparison of the temporal behavior of the angular width of the CBS cone with/without red pump light is shown in Fig. 2. The vertical coordinate α is the ratio W_t/W_o between the width W_t at time t and the initial width W_o. Without pump light, the width of the CBS cone with polarization parallel to the incident light does not have an apparent variation (i.e., $\alpha_{\mathrm{WO}} \approx 1$). This means that the influence of the probe beam itself on the suspension is negligible. However, the angular width changes significantly as soon as the red pump light is switched on. With probe and pump beams both vertically polarized (VV geometry), the cone becomes wider ($\alpha_{\mathrm{VV}} > 1$), while the cone becomes narrower ($\alpha_{\mathrm{VH}} < 1$) with a vertically polarized probe beam and a horizontally polarized pump beam (VH geometry). This demonstrates that it is possible to control weak localization of the green probe beam by a red pump beam.

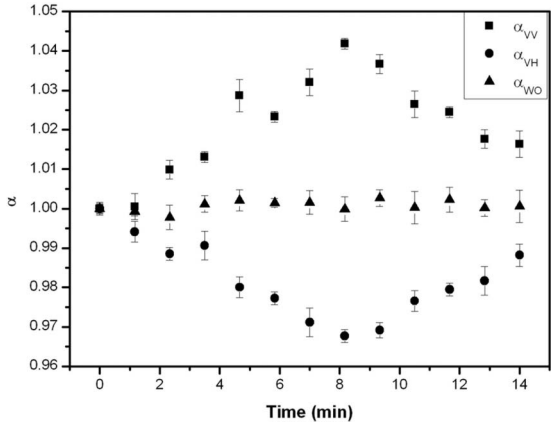

Fig. 2. Temporal evolution of the angular width of CBS cones. The vertical coordinate $\alpha = W_t/W_o$ is the ratio between the width W_t at the time t and the initial width W_o. The quantity α_{WO} is the ratio without pump light, and α_{VV} and α_{VH} are the ratios for VV and VH geometries, respectively.

The experiments were repeated several times. We always found that the angular width reaches its maximum and minimum after about 8 min for VV as well as VH geometry, respectively, as shown in Fig. 2. Thereafter, the change of the angular width becomes small, which might be due to deposition of the particles or to influences of the pump light, such as thermal effects or aggregation. For that reason, we took the ratios at 8 min from five subsequent experimental runs to calculate the average ratios. The average α_{WO} is 1.0009 ± 0.0011, slightly more than 1. The average α_{VV} is 1.0409 ± 0.0014, i.e., about 4.00% wider than α_{WO}. The average α_{VH} is 0.9678 ± 0.0016, i.e., about 3.31% narrower. The induced change for VV geometry is slightly larger than that for VH geometry as W_{VV}:W_{WO}:$W_{\mathrm{VH}} = 1.040$:1:0.9669.

A possible explanation for the change of the width of the CBS cone is reorientation of LN microcrystalline particles under the influence of the pump beam [12]. Though the scatterers in suspension are anisotropic, the suspension is apparently isotropic without pump light due to random orientation of the scatters. However, this isotropic suspension became partially anisotropic under the influence of the pump beam.

The electric polarization induced in a uniaxial microcrystalline particle by linearly polarized light is $\vec{P} = \varepsilon_o(\varepsilon_\perp - 1)\vec{E} + \varepsilon_o \Delta\varepsilon(\hat{n}\cdot\vec{E})\hat{n}$, where $\vec{E}$ is the electric field of the light with an amplitude $\vec{E}_0$, $\hat{n}$ is the unit vector of the optical axis of the microcrystal, ε_o is the dielectric constant of the vacuum, and $\Delta\varepsilon = \varepsilon_\parallel - \varepsilon_\perp$ is the dielectric anisotropy of the crystal for the red pump light. Then one can get the torque $\Gamma^{\mathrm{opt}} = \langle \vec{P} \times \vec{E} \rangle = \varepsilon_o \Delta\varepsilon(\hat{n}\times\vec{E}_0)(\hat{n}\cdot\vec{E}_0)$, and thus the free energy supplied by the light electric field is [13]

$$-\int \vec{D}\cdot \mathrm{d}\vec{E} = -\varepsilon_0[\varepsilon_\perp \vec{E}^2 + \Delta\varepsilon(\hat{n}\cdot\vec{E})^2]/2. \qquad (1)$$

Striving for minimum free energy, the optical axis of positive uniaxial microcrystalline particles tends to be parallel to the light electric field, i.e., $\hat{n} \| E$ for $\Delta\varepsilon > 0$, while $\hat{n} \perp E$ for $\Delta\varepsilon < 0$. LN is a negative uniaxial crystal

with $\Delta\varepsilon < 0$; therefore, the optical axes of the LN microcrystalline particles tend to be perpendicular to the polarization of the pump light. The axes of the microcrystalline particles in VV geometry prefer to orientate horizontally, which results in an effective refractive index close to n_{og} for the particles to the vertically polarized green probe light. In VH geometry, the pump light will lead to an effective refractive index close to n_{eg}.

The width W of the CBS cone can be expressed as $W \approx 0.7\lambda/2\pi l^*$ [8]. The MFP in Fig. 1(b) is 24.7 μm, which is much smaller than the thickness of the sample (10 mm). In the diffusive regime, the MFP of a random medium is expected to be inversely proportional to the concentration ρ and the diffusion cross section σ of the scatterers: $l^* \propto 1/(\rho\sigma)$ [14]. Furthermore, σ is proportional to $(\kappa^2 - 1)^2$ [7], where κ is the relative refractive index of the scattering particles to the surrounding medium at a given wavelength. Therefore, the width of the CBS cone can be expressed by

$$W = k\lambda\rho(\kappa^2 - 1)^2, \tag{2}$$

where the proportionality factor k can be considered constant in our experiments. Supposing that the effective refractive index of the microcrystalline particles in our isotropic sample is $(n_{og} + n_{eg})/2 = 2.2791$ for the green probe light, the relative index $\kappa_{\mathrm{WO}} = n_{\mathrm{LN}}/n_{\mathrm{water}}$ equals 1.708, whereas the refractive index of water n_{water} is 1.334. Illumination of the suspension by linearly polarized pump light leads to reorientation of the microcrystalline particles.

Let us first consider the case that all microcrystalline particles reach their minimum energy, i.e., all particles align perpendicular to the polarization direction of the pump light. Then the relative index $\kappa_{\mathrm{VV}} = n_{og}/n_{\mathrm{water}}$ is 1.742 for VV geometry and the relative index $\kappa_{\mathrm{VH}} = n_{eg}/n_{\mathrm{water}}$ for VH geometry is 1.675; then the ratios among the widths of the CBS cones should be W_{VV}:W_{WO}:$W_{\mathrm{VH}} = 1.124$:1:0.8858. The measured width change of the CBS cone is close to $\pm 3.7\%$, i.e., much smaller than the theoretical value of $\pm 11.9\%$. A reason for this is that the pump light inside the sample is strongly depolarized and no global reorientation can take place. The polarization extinction ratio of the incident pump light was 10^4:1, and the ratio of the reflected pump light fell to 100:1. Behind the sample the ratio decreased close to 1:1, and there is no ballistic contribution to transmitted intensity. Another possible reason may be that most particles do not reach their minimum energy due to perturbation by thermal motion. The CBS cone of the red pump light becomes wider than its initial cone, and its temporal behavior is similar to that of the green light for VV geometry, which is because, in this case, the pump and probe are both red, i.e., have VV geometry. The experiment was also performed in a water suspension of zirconium silicate microcrystalline particles, a kind of positive uniaxial crystal. We observed wider and narrower CBS cones for VV and for VH geometries, respectively, which supports the above analysis.

Angular anisotropy had been observed for weak localization of light from ordered anisotropic scatters [8]. In our experiments both orthogonal angular widths $W_\perp$ and $W_\parallel$ of the CBS cones without pump light are nearly the same, with $W_\perp/W_\parallel$ equal to 1.000 ± 0.020, which suggests that the original suspension is isotropic. For VV geometry, an anisotropy of 1.069 ± 0.021 appears with both angular widths becoming larger. For VH geometry, an anisotropy of 0.951 ± 0.025 arises, with both angular widths becoming smaller.

In conclusion, we realized optical control of CBS based on the reorientation of CLN microcrystalline particles in a suspension by a linearly polarized pump beam. This implies that the apparently isotropic suspension became partially anisotropic under the influence of the pump beam. The effect is, in principle, reversible.

This Letter is supported by the National Natural Science Foundation of China (NSFC) (10874093, 10804055), the National Basic Research Program of China (2007CB307002, 2010CB934101), the 111 Project (B07013), Programme for New Century Excellent Talents in University Science Research Foundation for the Returned Overseas Chinese Scholars (State Education Ministry), and Oesterreichischer Austauschdienst Wissenschaftlich-technische Zusammernarbeit China (OeAd-WTZ CN24/2007).

References

1. P. W. Anderson, Phys. Rev. **109**, 1492 (1958).
2. P. E. Wolf and G. Maret, Phys. Rev. Lett. **55**, 2696 (1985).
3. J. Billy, V. Josse, Z. Zuo, A. Bernard, B. Hambrecht, P. Lugan, D. Clément, L. Sanchez-Palencia, P. Bouyer, and A. Aspect, Nature **453**, 891 (2008).
4. T. Schwartz, G. Bartal, S. Fishman, and M. Segev, Nature **446**, 52 (2007).
5. E. Akkermans, P. E. Wolf, and R. Maynard, Phys. Rev. Lett. **56**, 1471 (1986).
6. H. Kaveh, M. Rosenbluh, I. Edrei, and I. Freund, Phys. Rev. Lett. **57**, 2049 (1986).
7. S. Kawato, T. Hattori, T. Takemori, and H. Nakatsuka, Phys. Rev. B **49**, 90 (1994).
8. R. Sapienza, S. Mujumdar, C. Cheung, A. G. Yodh, and D. Wiersma, Phys. Rev. Lett. **92**, 033903 (2004).
9. B. P. J. Bret, N. J. G. Couto, M. Amaro, E. J. Nunes-Pereira, and M. Belsley, Opt. Express **17**, 6975 (2009).
10. D. S. Wiersma, M. Colocci, and R. Righini, Phys. Rev. B **64**, 144208 (2001).
11. D. F. Nelson and R. M. Mikulyak, J. Appl. Phys. **45**, 3688 (1974).
12. M. E. J. Friese, T. A. Nieminen, N. R. Heckenberg, and H. Rubinsztein-Dunlop, Nature **394**, 348(1998).
13. F. Simoni, *Nonlinear Optical Properties of Liquid Crystal and Polymer Dispersed Liquid Crystal* (World Scientific, 1997).
14. P. Sheng, *Introduction to Wave Scattering, Localization, and Mesoscopic Phenomena* (Academic, 1995).

Persistence and breakdown of Airy beams driven by an initial nonlinearity

Yi Hu,[1,2] Simon Huang,[1] Peng Zhang,[1] Cibo Lou,[2] Jingjun Xu,[2] and Zhigang Chen[1,2,*]

[1]*Department of Physics and Astronomy, San Francisco State University, San Francisco, California 94132, USA*

[2]*The Key Laboratory of Weak-Light Nonlinear Photonics, Ministry of Education and TEDA Applied Physics School, Nankai University, Tianjin 300457, China*

**Corresponding author: zhigang@sfsu.edu*

Received September 8, 2010; revised October 7, 2010; accepted October 19, 2010; posted October 26, 2010 (Doc. ID 134790); published November 23, 2010

We study the behavior of Airy beams propagating from a nonlinear medium to a linear medium. We show that an Airy beam initially driven by a self-defocusing nonlinearity experiences anomalous diffraction and can maintain its shape in subsequent propagation, but its intensity pattern and acceleration cannot persist when driven by a self-focusing nonlinearity. The unusual behavior of Airy beams is examined from their energy flow as well as the Brillouin zone spectrum of self-induced chirped photonic lattices. © 2010 Optical Society of America

OCIS codes: 190.4420, 050.1940, 350.5500.

Airy beams have recently attracted a great deal of interest [1–3] with many proposed applications [4–6]. Generation and control of Airy beams in an effective way is thus desirable. Apart from the linear control of Airy beams' ballistic trajectories [7,8], it has been demonstrated that nonlinearity can play nontrivial roles in both generation and control of Airy beams [9–11]. For example, by changing the phase-matching condition in a second harmonic generation process [9,10], one-dimensional Airy beams can be generated with controllable paths. In a photorefractive material with diffusion-dominated nonlinearity, self-trapping of Airy beams can be realized [11]. In this Letter, we study the transition of Airy beams from a nonlinear to a linear medium driven initially by a self-focusing or self-defocusing nonlinearity. Some unique behaviors of such nonlinearity-controlled Airy beams, including loss or persistence of acceleration and normal or anomalous diffraction are revealed. In particular, we found that an Airy beam under an initial self-defocusing nonlinearity exhibits anomalous diffraction and propagates robustly over a long distance after exiting the nonlinear medium, but it breaks down in both Airy beam pattern and acceleration when driven by a self-focusing nonlinearity. Our numerical results find good agreement with experimental observation.

Our experiments are performed in a biased 1-cm-long photorefractive SBN:60 crystal [Fig. 1(a)]. To create a truncated Airy beam, a spatial light modulator (SLM) is placed at the focal plane of the Fourier transform lens [2,3]. An extraordinarily polarized Airy beam ($\lambda =$ 532 nm) is thus generated, propagating first through the biased crystal under the influence of photorefractive screening nonlinearity and then through air (free space) for another 1 cm. Solely by switching the polarity of the bias field, self-focusing and self-defocusing nonlinearity is achieved for nonlinear control of the Airy beam. The Airy beam patterns, along with **k**-space spectra are monitored by CCD cameras.

Typical experimental results are shown in Figs. 1(b), 1(c), and 1(d). When no bias field is present, the Airy beam undergoes linear propagation inside the crystal. (The photorefractive diffusion effect [11] can be neglected owing to the large size of the Airy beam used here—about 50 μm for the main lobe.) After another 1 cm of propagation in air, its main spot (or "head") is shifted along the vertical direction [Fig. 1(b2)] in comparison with that right at the existing face of the crystal [Fig. 1(b1)] owing to the transverse acceleration [1,2]. When a positive dc field of 4×10^4 V/m is applied, the Airy beam experiences a self-focusing nonlinearity and

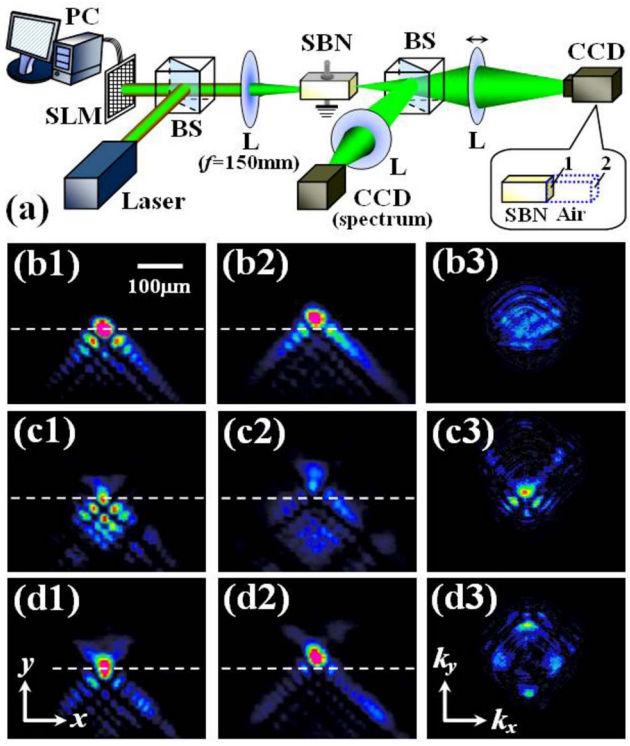

Fig. 1. (Color online) (a) Schematic of experimental setup. SLM, spatial light modulator; SBN, strontium–barium–niobate crystal; PC, personal computer; BS, beam splitter; L, Fourier transform lens. (b)–(d) Output intensity patterns of an Airy beam after 1 cm through crystal (first column) plus another 1 cm through air (second column) when (b) no nonlinearity, (c) self-focusing nonlinearity, and (d) self-defocusing nonlinearity are present. White dashed line marks the "head" position of the Airy beam at crystal output. The third column shows Fourier spectra of the Airy beam corresponding to the first column.

reduces its overall size with most of its energy distributed to the four spots close to the Airy "head" [Fig. 1(c1)]. In this case, the nonlinearity seems to cause stagnation of the Airy beam's acceleration, and the subsequent free-space propagation shows that the Airy beam is strongly deformed by the nonlinearity [Fig. 1(c2)]. In addition, its **k**-space spectrum is "focused" toward the center [Fig. 1(c3)] as compared to the case without initial nonlinearity [Fig. 1(b3)], suggesting that the Airy beam exhibits normal diffraction. By reversing the polarity of the bias field (to -4×10^4 V/m) so the Airy beam experiences a self-defocusing nonlinearity, its nonlinear output [Fig. 1(d1)] and subsequent linear propagation [Fig. 1(d2)] behaves dramatically differently. The intensity profile of the Airy beam is less affected by the self-defocusing nonlinearity, and the peak intensity of the Airy beam after subsequent linear propagation in air is not decreased but rather increased while persistent in its acceleration [Fig. 1(d2)]. Furthermore, the Fourier spectrum reshapes into four major spots in **k**-space, as shown in Fig. 1(d3), resembling the Brillouin zone (BZ) spectrum and associated anomalous diffraction behavior in photonic lattices [12–14].

The above experimental observations can be corroborated with numerical simulations. Propagation of an Airy beam in a biased photorefractive crystal is described by the following nonlinear Schrödinger equation:

$$\frac{\partial U}{\partial z}=\frac{i}{2k_0n_0}\left(\frac{\partial^2U}{\partial x^2}+\frac{\partial^2U}{\partial y^2}\right)+ik_0\Delta nU, \qquad (1)$$

where U is the wave function, k_0 is the vacuum wave vector, and $n_0=2.3$ is the unperturbed refractive index. In the biased crystal, the nonlinearity for an e-polarized beam can be determined by $\Delta n=-0.5n_0^3\gamma_{33}E_0/(1+|U|^2)$, in which $\gamma_{33}=280$ pm/V and E_0 is the amplitude of the bias field. The wave function of an input Airy beam can be expressed as $U(x,y,z=0)=U_0\mathrm{Ai}(X/x_0)\exp(\alpha X/x_0)\mathrm{Ai}(Y/y_0)\exp(\alpha Y/y_0)$, where U_0 is the amplitude; Ai denotes the Airy function; X and Y are equivalent to $(x+y)/\sqrt{2}$ and $(-x+y)/\sqrt{2}$, respectively; x_0 and y_0 are two scaling constants; and α is the decay factor for the truncated beam profile.

Numerical simulations are performed by solving Eq. (1) with the split-step beam propagation method. (Parameters U_0, x_0, and α are chosen as 7.3, 13.5×10^{-6}, and 0.11, respectively.) Without the nonlinearity, i.e., $E_0=0$, the Airy beam is nearly unchanged after 2 cm linear propagation, and its output Fourier spectrum has a Gaussian-like shape. When $E_0=+4\times10^4$ V/m is applied, it experiences a self-focusing nonlinearity, and its intensity concentrates mainly onto the four spots close to the Airy "head" while the "tails" get shorter [Fig. 2(a)], diverging even more in subsequent linear propagation [Fig. 2(b)]. The **k**-space spectrum reshapes asymmetrically into a bowtielike pattern, more localized toward the center [Fig. 2(c)]. The propagation can be better visualized from the side view evolution, as shown in Fig. 2(d), where the dashed curve marks the path of the same Airy beam without initial nonlinearity. The acceleration is reduced or lost as compared to the case without the nonlinear control. In Figs. 2(e) and 2(f), we plotted the transverse energy flow of the output beam corresponding to the areas marked in Figs. 2(a) and 2(b). Apparently, after initial nonlinear propagation, the direction of the energy flow goes toward all directions, suggesting that the phase of the Airy beam is destroyed by the self-focusing nonlinearity. Once the Airy beam is released into free space, it behaves more like a confined Gaussian beam, showing normal diffraction without evident acceleration.

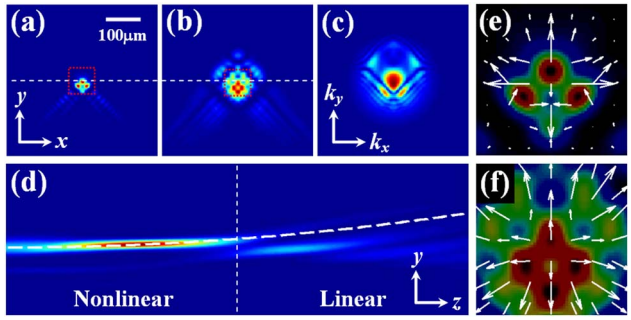

Fig. 2. (Color online) Numerical simulation of an Airy beam propagating under initial self-focusing nonlinearity. (a), (b) Transverse intensity patterns after (a) 1 cm through crystal plus (b) another 1 cm through air. (c) Fourier spectrum of the output Airy beam. (d) Side view of 2 cm propagation, where the dashed curve represents the trajectory of the Airy beam without initial nonlinearity. (e), (f) Calculated transverse energy flow around the main lobe corresponding to the square area shown in (a) and (b), respectively.

Now with a reversed bias field of $E_0=-4\times10^4$ V/m, numerical results (Fig. 3) show that the Airy beam is somewhat expanded at the beginning owing to the self-defocusing nonlinearity, but its shape is nearly unchanged [Fig. 3(a)]. In contrast to the self-focusing case, the Airy beam persists in its intensity pattern and transverse acceleration during subsequent free-space propagation [Figs. 3(b) and 3(d)]. Furthermore, its power spectrum reshapes into a diamondlike pattern [Fig. 3(c)], resembling the first BZ [14] of an asymmetric square lattice. The energy flow of the Airy beam is also quite different from that in the self-focusing case, since the Poynting vectors of the Airy beam line up toward the same direction around the Airy "head" [Figs. 3(e) and 3(f)]. Counterintuitively, the peak intensity of the main lobe gets even stronger after subsequent linear propagation, as seen from the side view evolution [Fig. 3(d)]. This phenomenon suggests that the Airy beam might experience anomalous diffraction after initial self-defocusing nonlinearity, akin to that observed in photonic lattices [12,13].

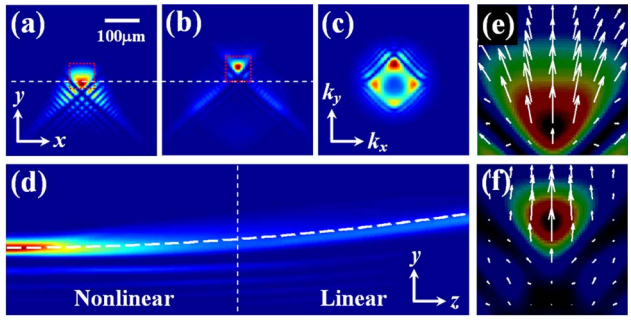

Fig. 3. (Color online) Numerical simulation of an Airy beam propagating under initial self-defocusing nonlinearity. Other description is the same as that for Fig. 2.

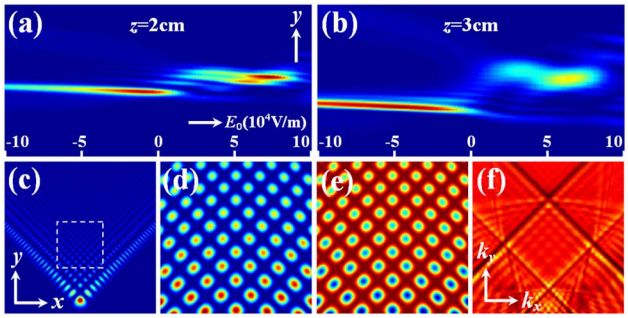

Fig. 4. (Color online) (a), (b) Plots of output intensity profiles along the y axis of an Airy beam as a function of the bias field after (a) 2 cm and (b) 3 cm of propagation, while the nonlinearity is on only for the first 1 cm. Positive (negative) values of E_0 correspond to self-focusing (self-defocusing) nonlinearity. (c) Transverse intensity pattern of a perfect Airy beam. (d) Zoom-in of nonuniform intensity pattern in the region marked by dashed square in (c). (e) Index lattice self-induced by the intensity pattern of (d) at $E_0 = -4 \times 10^4$ V/m. (f) Brillouin zone spectrum of the induced lattice of (e).

To get an idea of how much nonlinearity an Airy beam can withstand before it becomes deformed, we performed a series of simulations at different levels of nonlinearity as controlled by the bias field. The results are shown in Figs. 4(a) and 4(b), where the output transverse profiles along the y axis are plotted as a function of the bias field after 2 cm and 3 cm of propagation (only the first 1 cm with nonlinearity). Clearly, the Airy beam cannot maintain its shape after 2 cm of propagation even at a weak self-focusing nonlinearity (say, $E_0 = +10^4$ V/m), and it gets strongly deformed at higher bias fields. On the other hand, the Airy beam's main lobe withstands after 3 cm of propagation even at a strong self-defocusing nonlinearity (say, $E_0 = -10 \times 10^4$ V/m). In addition, from Fig. 4(b), it is evident that, under self-defocusing nonlinearity, the peak intensity of the Airy beam becomes much stronger than that in the linear case (i.e., $E_0 = 0$) after the same distance of propagation.

To better understand the "anomalous" behavior, let us take a close look at the diamondlike Fourier spectrum, as shown in Fig. 3(c). This spectrum is very similar to that of a gap soliton generated by balancing anomalous diffraction with a self-defocusing nonlinearity [14], for which the **k**-space spectrum populates mainly the four corners of the first BZ, indicating that the anomalous diffraction of the Airy beam might originate from the self-induced lattice structures. In Figs. 4(c) and 4(d), we zoom in the Airy beam intensity pattern not far from the "head," and it indeed exhibits a squarelike structure with nonuniform intensity distribution and lattice spacing. Under a self-defocusing nonlinearity, the Airy beam induces an index distribution akin to a nonuniform or chirped "backbone" lattice, as shown in Fig. 4(e). This self-induced lattice could exhibit properties similar to those of uniformed lattices [15] and thereby change the diffraction of the Airy beam. To visualize the BZ of the self-induced lattice, the BZ spectroscopy method is used to calculate the BZ spectrum of the induced lattice [16]; the result is displayed in Fig. 4(f). Clearly, the self-induced lattice of the Airy beam shows a BZ structure. Thus, the principle for anomalous diffraction observed here could be similar to that reported in [12,14,17].

In summary, we have studied nonlinearity-controlled persistence and breakdown of Airy beams. Our results bring about another possibility for control of Airy beams.

This work was supported by the National Science Foundation (NSF) and the Air Force Office of Scientific Research (USAFOSR) and by the 973 Program (2007CB613203), the 111 Project, the National Natural Science Foundation of China (NSFC), and the Program for Changjiang Scholars and Innovation Research Team (PCSIRT) in China. We thank D. N. Christodoulides for discussion.

References

1. G. A. Siviloglou and D. N. Christodoulides, Opt. Lett. **32**, 979 (2007).
2. G. A. Siviloglou, J. Broky, A. Dogariu, and D. N. Christodoulides, Phys. Rev. Lett. **99**, 213901 (2007).
3. J. Broky, G. A. Siviloglou, A. Dogariu, and D. N. Christodoulides, Opt. Express **16**, 12880 (2008).
4. J. Baumgartl, M. Mazilu, and K. Dholakia, Nat. Photon. **2**, 675 (2008).
5. P. Polynkin, M. Kolesik, J. V. Moloney, G. A. Siviloglou, and D. N. Christodoulides, Science **324**, 229 (2009).
6. A. Chong, W. Renninger, D. N. Christodoulides, and F. W. Wise, Nat. Photon. **4**, 103 (2010).
7. G. A. Siviloglou, J. Broky, A. Dogariu, and D. N. Christodoulides, Opt. Lett. **33**, 207 (2008).
8. Y. Hu, P. Zhang, C. Lou, S. Huang, J. Xu, and Z. Chen, Opt. Lett. **35**, 2260 (2010).
9. T. Ellenbogen, N. Voloch, A. Ganany-Padowicz, and A. Arie, Nat. Photon. **3**, 395 (2009).
10. I. Dolev, T. Ellenbogen, and A. Arie, Opt. Lett. **35**, 1581 (2010).
11. S. Jia, J. Lee, G. A. Siviloglou, D. N. Christodoulides, and J. W. Fleischer, Phys. Rev. Lett. **104**, 253904 (2010).
12. T. Pertsch, T. Zentgraf, U. Peschel, A. Bräuer, and F. Lederer, Phys. Rev. Lett. **88**, 093901 (2002).
13. P. Zhang, C. Lou, S. Liu, J. Zhao, J. Xu, and Z. Chen, Opt. Lett. **35**, 892 (2010).
14. X. Wang, A. Bezryadina, Z. Chen, K. G. Makris, D. N. Christodoulides, and G. I. Stegeman, Phys. Rev. Lett. **98**, 123903 (2007).
15. M. I. Molina, Y. V. Kartashov, L. Torner, and Y. S. Kivshar, Opt. Lett. **32**, 2668 (2007).
16. S. Liu, P. Zhang, X. Gan, F. Xiao, and J. Zhao, Appl. Phys. B **99**, 727 (2010).
17. C. Lou, X. Wang, J. Xu, Z. Chen, and J. Yang, Phys. Rev. Lett. **98**, 213903 (2007).

Analysis of electron capture acceleration channel in an Airy beam

Jian-Xing Li,[1] Wei-Ping Zang,[1,2,*] and Jian-Guo Tian[1,2,3]

[1]*Photonics Center, School of Physics, Nankai University, Tianjin 300071, China*

[2]*The Key Laboratory of Weak Light Nonlinear Photonics, Ministry of Education, Teda Applied Physics School, Nankai University, Tianjin 3000457, China*

[3]*e-mail: jjtian@nankai.edu.cn*

**Corresponding author: wpzang@nankai.edu.cn*

Received June 1, 2010; revised August 27, 2010; accepted September 5, 2010; posted September 10, 2010 (Doc. ID 129387); published September 24, 2010

Using numerical simulation, we have studied in detail vacuum electron acceleration induced by an Airy beam. The phase of the field varies slowly, and the intensity of the field is independent of the decaying parameter of the beam in the asymmetric field channel [(AFC) Opt. Express **18**, 7300 (2010)] formed by the Airy beam. Results show that an electron entering into the AFC may be captured and gain high energy. Meanwhile, the decaying parameter, injection energy, and injection angle of the electron play important roles in the electron energy gain.

OCIS codes: 260.1960, 260.2110, 350.5500.

Advances in the technology of intense laser fields [1–3] continue to motivate the research of vacuum laser acceleration in recent years [4–7]. The drawback of laser-driven acceleration by Gaussian beams is that the interaction length over which the high intensity can be sustained is relatively short due to transverse spreading. Therefore, laser-driven electron acceleration by quasi-diffraction-free beams has attracted widespread attention [8–10]. Recently, optical Airy beams, first predicted and realized by Siviloglou *et al.* [11,12], have attracted intense attention [13–15].

The behavior of transverse accelerating and nondiffraction of the one-dimensional (1D) Airy beam led to the formation of a long "asymmetric field channel" (AFC) along the propagation axis [15]. In this Letter, the propagation dynamics of the field inside the AFC are studied in detail. Inside the AFC, the phase of the field varies slowly, and the intensity of the field is independent of the decaying parameter. The electron entering into the AFC may be captured and retained in the accelerating stage continuously. The longitudinal electric field makes a significant contribution to the energy gain of the captured electron. The decaying parameter, injection energy, and angle of electron play important roles in determining the energy gain.

The 1D Airy laser beam polarizes along the x direction and propagates along the z axis. Its electromagnetic field can be expressed as [15]

$$E_x = -iE\{(2a^2 + 2ia\xi - \xi^2/4 + 2s + 2k^2x_0^2)Ai(A) + (4a + i\xi)Ai'(A)\}/(2k^2x_0^2), \quad (1)$$

$$E_z = E\{[2a^3 + 9ia^2\xi/2 + a(-3\xi^2/2 + 6s - 4k^2x_0^2) - i(2i + \xi^3/8 - 3s\xi/2 + \xi k^2x_0^2)]Ai(A) + (6a^2 + 4ia\xi + 2s - \xi^2/2 - 4k^2x_0^2)Ai'(A)\}/(4k^3x_0^3), \quad (2)$$

$$B_y = iE\{(2a^2 + 2ia\xi - \xi^2/4 + 2s - 4k^2x_0^2)Ai(A) + (4a + i\xi)Ai'(A)\}/(4k^2x_0^2), \quad (3)$$

$E_y = 0$, $B_x = 0$, and $B_z = 0$. Ai represents the Airy function, and $Ai'(A)$ denotes the derivative of $Ai(A)$. $A = s - (\xi/4)^2 + ia\xi/2$, $B = as - a\xi^2/8 - i\xi^3/96 + ia^2\xi/4 + is\xi/4$, and $E = E_0 \exp[i(\omega t - kz + \varphi_0) + B]$, where E_0 is the field amplitude, φ_0 is the constant phase, $s = x/x_0$, x_0 is an arbitrary transverse scale, $\xi = z/z_r$, $z_r = kx_0^2/2$, k is the wavenumber, and a is the decaying parameter.

To facilitate analysis, we define $f_x(s,\xi) = E_x(s,\xi)\exp(ikz_r\xi)$ as the slowly varying envelope of the transverse electric field. Figure 1 gives the spatial variations of f_x and E_x. f_x is quasi-diffraction free and varies with parabolic trajectory. The transverse accelerating property deflects the main lobe toward the positive x direction and forms a "channel" along the propagation axis, as shown in Figs. 1(a) and 1(b). The propagation dynamics of E_x are shown in Figs. 1(c)–1(f). The field is asymmetric along the propagation axis and forms a "channel," namely, AFC. Also, the boundary of AFC is determined by that of the axis wave channel of f_x. The phases of f_x and E_x are given in Fig. 2. The phase inside the AFC varies more slowly than that outside the AFC. And the AFC mainly locates in the region of $z > 15z_r$ in the longitudinal direction. Figure 3 gives the cross sections of E_x for different decaying parameters a. The field outside the AFC decreases with the increasing of a, and the field inside the AFC is nearly independent of a.

Electron dynamics in a laser beam in vacuum is governed by the relativistic equations of motion $d\mathbf{p}/dt = -e(\mathbf{E} + \boldsymbol{\beta} \times \mathbf{B})$ and $d\Xi/dt = -ec\boldsymbol{\beta} \cdot \mathbf{E}$, where the momentum $\mathbf{p} = \gamma mc\boldsymbol{\beta}$, energy $\Xi = \gamma mc^2$, Lorentz factor $\gamma = (1 - \boldsymbol{\beta}^2)^{-1/2}$, and $\boldsymbol{\beta}$ is the velocity scaled by c. The peak field intensity I_0 will be given in terms of the dimensionless parameter $q = eE_0/mc\omega$, where $I_0\lambda^2 \approx 1.375 \times 10^{18} q^2$ (W/cm^2)(μm)^2. Electrons with different initial energies are injected and interact with an intense 1D Airy beam. The simulated results are given in Fig. 4. The initial fast electron quickly passes through the intense field region (IFR), and then it is captured by the asymmetric field in the AFC. In the IFR, the phases of the field vary rapidly and the electron senses the accelerating and decelerating phases alternately. So the

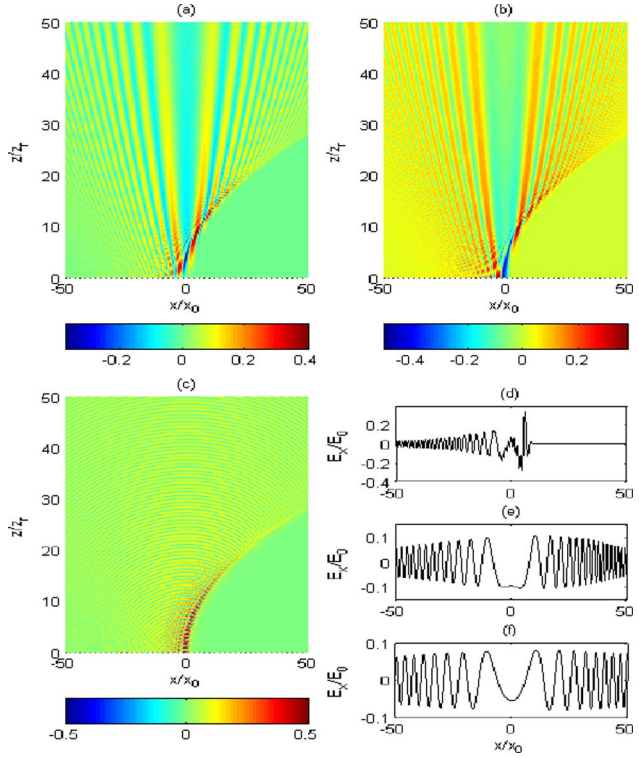

Fig. 1. (Color online) (a)–(c) Propagation dynamics of real component and imaginary component of f_x and the real component of E_x, respectively. (d)–(f) Cross section of E_x at $10z_r$, $30z_r$, and $50z_r$, respectively. Parameters used here are $t = 0$, $\lambda = 1\ \mu$m, $x_0 = 5\lambda$, $a = 0.05$, and $\varphi_0 = 0$.

electron gains little energy. In the AFC, the phase of the field varies slowly. Therefore, the captured electron can remain in the accelerating phase continuously and gain much higher energy. For this case, the final energy gain is about 655.72 MeV. Energies obtained from the transverse and longitudinal fields are 297.96 and 357.76 MeV, respectively. The initial slow electron is strongly influenced by the transverse field and reflected outside the AFC. It gains a majority of its energy in IFR, which is mainly afforded by the transverse field. Outside the AFC, the electron senses the accelerating and decelerating phases alternately and cannot gain energy any longer. The final energy gain is about 238.47 MeV.

Variations of the electron energy with the decaying parameter, injection energy, and injection angle are given

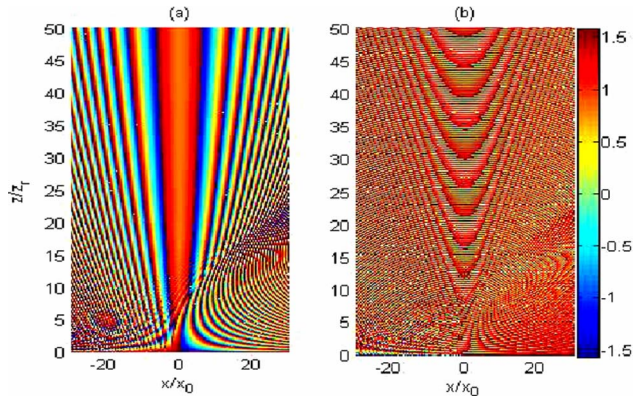

Fig. 2. (Color online) (a), (b) Phases of f_x and E_x.

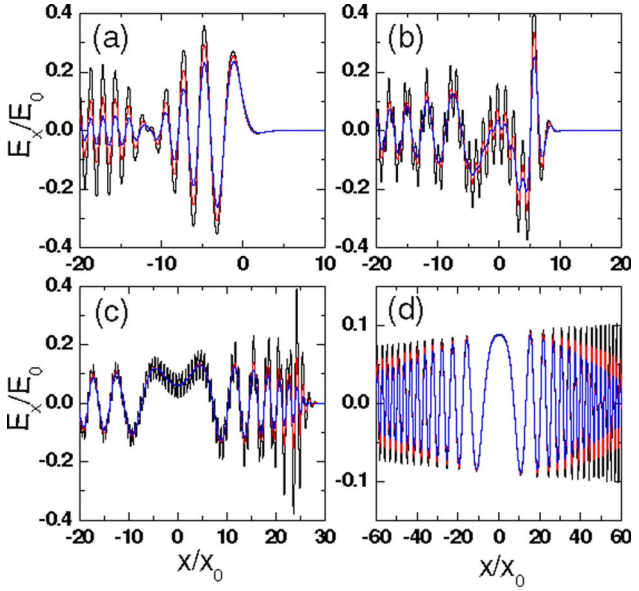

Fig. 3. (Color online) (a)–(d) Cross sections of E_x at z_r, $10z_r$, $20z_r$, and $40z_r$, respectively. The black, light gray (red online), and dark gray (blue online) curves are calculated with $a = 0.01$, 0.05, and 0.1, respectively.

in Fig. 5. There are three regions in every figure, which are symbolized with α, β, and χ. In region α, the trajectories of the electron are indeterminate and the electron may be captured or reflected. In region β, the electron is always reflected and gains little energy. And in region χ, the electron is captured and gains high energy. Specifically, for the given parameters, the electron is captured in the region $0.0455 < a < 0.1$, as shown in Fig. 5(a). The electron, whose scaled injection energy is $\gamma_0 > 18.84$ or

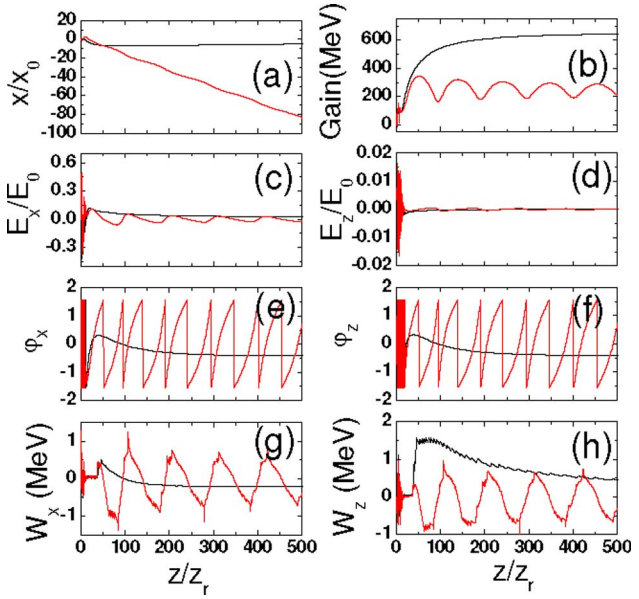

Fig. 4. (Color online) (a) Trajectory and (b) energy gain. (c)–(h) E_x, E_z, phases of E_x and E_z, and the works done by E_x and E_z, sensed by the electron along its trajectory, respectively. Parameters used here are $a = 0.05$, $\lambda = 1\ \mu$m, $x_0 = 5\lambda$, $q = 20$, and $\varphi_0 = 0$, initial location of the electron $(x, z) = (0.1x_0, 0)$, injection angle of the electron $\theta = 0$, and black and light gray (red online) curves are calculated with the initial injection energy of $\gamma_0 = 40$ and 16, respectively.

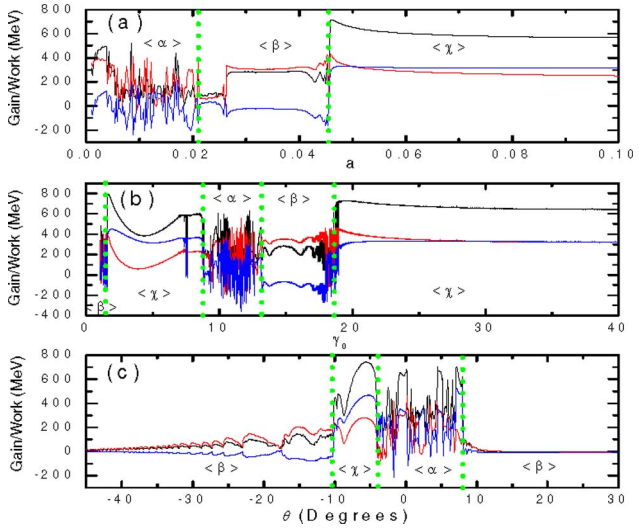

Fig. 5. (Color online) (a)–(c) Variation of the energy gain with a, γ_0, and θ. The black, light gray (red online), and dark gray (blue online) curves represent the energy gains and the total work done by E_x and E_z, respectively. (a) $\gamma_0 = 30$ and $\theta = 0$, (b) $a = 0.05$ and $\theta = 0$, and (c) $\gamma_0 = 30$ and $a = 0.05$.

$1.63 < \gamma_0 < 8.75$, can enter into the AFC and be continuously accelerated, as shown in Fig. 5(b). Moreover, the electron injecting at a small angle, $-10.1° < \theta < -4.1°$, is more likely to enter into the AFC and be captured, because the phase varies relative slowly in these directions in the IFR, as shown in Fig. 5(c).

In summary, electron acceleration in vacuum by an Airy beam has been studied in detail. An electron entering into the AFC may be captured and remain in the accelerating stage continuously. The decaying parameter, injection energy, and injection angle of the electron play important roles in determining the electron energy gain. The adjustable injection parameters have been discussed and optimized to gain high-energy electrons.

We acknowledge financial support from the National Natural Science Foundation of China (NSFC) (60678025), the Chinese National Key Basic Research Special Fund (2006CB921703), the Program for New Century Excellent Talents in University, and the 111 Project (B07013).

References

1. M. D. Perry, D. Pennington, B. C. Stuart, G. Tietbohl, J. A. Britten, C. Brown, S. Herman, B. Golick, M. Kartz, J. Miller, H. T. Powell, M. Vergino, and V. Yanovsky, Opt. Lett. **24**, 160 (1999).
2. P. G. O'Shea and H. P. Freund, Science **292**, 1853 (2001).
3. R. Kienberger, M. Hentschel, M. Uiberacker, Ch. Spielmann, M. Kitzler, A. Scrinzi, M. Wieland, Th. Westerwalbesloh, U. Kleineberg, U. Heinzmann, M. Drescher, and F. Krausz, Science **297**, 1144 (2002).
4. Y. Cheng and Z. Xu, Appl. Phys. Lett. **74**, 2116 (1999).
5. G. V. Stupakov and M. S. Zolotorev, Phys. Rev. Lett. **86**, 5274 (2001).
6. Y. I. Salamin and C. H. Kertel, Phys. Rev. Lett. **88**, 095005 (2002).
7. J. X. Li, W. P. Zang, and J. G. Tian, Appl. Phys. Lett. **96**, 031103 (2010).
8. B. Hafizi, E. Esarey, and P. Sprangle, Phys. Rev. E **55**, 3539 (1997).
9. S. Liu, H. Guo, H. Tang, and M. Liu, Phys. Lett. A **324**, 104 (2004).
10. D. Li and K. Imasaki, Appl. Phys. Lett. **86**, 031110 (2005).
11. G. A. Siviloglou and D. N. Christodoulides, Opt. Lett. **32**, 979 (2007).
12. G. A. Siviloglou, J. Broky, A. Dogariu, and D. N. Christodoulides, Phys. Rev. Lett. **99**, 213901 (2007).
13. J. Baumgartl, M. Mazilu, and K. Dholakia, Nat. Photon. **2**, 675 (2008).
14. J. Baumgartl, G. M. Hannappel, D. J. Stevenson, D. Day, M. Gu, and K. Dholakia, Lab Chip **9**, 1334 (2009).
15. J. X. Li, W. P. Zang, and J. G. Tian, Opt. Express **18**, 7300 (2010).

Giant enhancement of surface second-harmonic generation using photorefractive surface waves with diffusion and drift nonlinearities

H. Z. Kang, T. H. Zhang,* H. H. Ma, C. B. Lou, S. M. Liu, J. G. Tian, and J. J. Xu

Photonics Research Center, the MOE Key Lab of Weak-Light Nonlinear Photonics, and Tianjin Key Lab of Photonics Materials and Technology for Information Science, Nankai University, Tianjin, China, 300071
**Corresponding author: zhangth@nankai.edu.cn*

Received January 7, 2010; revised March 1, 2010; accepted March 26, 2010;
posted April 15, 2010 (Doc. ID 122366); published May 6, 2010

Giant enhancement of second-harmonic generation (SHG) with 83.4%/W coversion efficiency is obtained, taking advantage of photorefractive surface waves with diffusion and drift nonlinearity. In this method, the self-bending induced by diffusion nonlinearity can be utilized at the surface and can solve the phase-mismatch problem in bulk due to beam self-bending. With drift nonlinearity, an applied external electric filed and background illumination can further constringe surface waves to the surface and consequently enhance SHG, which provides the possibility and flexibility of control. © 2010 Optical Society of America

OCIS codes: 240.4350, 190.2620, 190.5330.

In particular, one of the fundamental issues in second-harmonic generation (SHG) is the realization of phase matching (PM) between the fundamental and second-harmonic (SH) waves, which traditionally are achieved using birefringence [1]. However, the involved light waves are required to have different polarizations, and thus only those off-diagonal elements of the nonlinear coefficient whose values are relatively small can be utilized. Moreover, in many crystals the birefringence cannot compensate the dispersion. A quasi-phase-matching (QPM) scheme was proposed by Armstrong *et al.* and has been applied in various practical nonlinear optical crystals [2]. Conventionally, QPM is realized by using the vector of the periodical inversed domain grating as an additional vector to compensate the phase mismatching [3]. However, complicated structures had to be prefabricated [4].

Spatial solitons provide a promising method for SHG, which can overcome the above mentioned disadvantage. In 1999 Song *et al.* reported the observation of 0.996%/W SHG in $Fe:KNbO_3$ taking advantage of the photorefractive (PR) soliton with local drift nonlinearity, where PM occurs among propagation constants of the fundamental light and SH light, rather than wave vectors in a bulk [5]. However, as we demonstrate in this Letter, nonlocal diffusion nonlinearity induced self-bending may result in the phase mismatching and the consequent depressing of SHG in bulk. The conversion efficiency η of SHG is proportional to the intensity of the light energy and second-order nonlinear coefficient $\chi^{(2)}$, which can also depend on the electro-optic coefficient r_{eff}. On the one hand, high r_{eff} is favorable to SHG, but on the other hand, high r_{eff} is also favorable to decreasing the size of the soliton and consequently increasing the intensity of the light energy, as a result of increasing the conversion efficiency η of SHG. However, at the same time, the larger the r_{eff}, the more drastic the self-bending is and the more difficult the PM is to be satisfied, and even no SHG can be observed.

Fortunately, the surface provides a natural line-path and shows excellent efficacy to take advantage of diffusion nonlinearity-induced self-bending to solve the above problem very well, where a laser beam can be confined and propagate straight along a line. In this case, so-called surface waves (SWs) may be excited [6,7]. Taking advantage of photorefractive surface waves (PR SWs), all nonlinear optical phenomena may be expected to be strongly enhanced near the surface. In 1999, Smolyaninov *et al.* reported a 1% strong enhanced SHG in $BaTiO_3$ with diffusion nonlinearity [8]. In 2006, we also realized 1%/W SHG in $Sr_{0.6}Ba_{0.4}NbO_3$ with diffusion nonlinearity [9].

It is well-known that self-focusing local drift nonlinearity can concentrate the intensity of light energy, so stronger enhancement of SHG may be expected. In this Letter, taking advantage of the PR SWs with photorefractive diffusion and drift nonlinearity, a η=83.4%/W 532 nm SHG is successfully achieved using a 73.6 mW, 1064 nm cw laser. On the one hand, with drift nonlinearity, applied external electric field E_0 and background illumination I_b can concentrate the light energy of PR SWs; on the other hand, high intensity of light energy can enhance the diffusion nonlinearity induced self-bending and further constringe PR SWs to the surface.

First, a Gaussian laser beam (λ=1064 nm and P=73.6 mw) was focused into the bulk of strontium barium niobate crystal, with its minimum waist about 30 μm at the input face. Both c surfaces of the crystal are polished to ensure an ideal interface and provide the circumstances for the straight propagation of solitons. Two copper sheets glued on the c surfaces by conductive adhesives are used as electrodes. Figure 1 shows the setup for the generation and observation of SH waves. Figure 2(a_1) shows the image of the expanding of transmitted laser beam at output face without SHG detected, as shown in Fig. 2(a_2). When an external electric field E_0=413 V/mm (1900 V, 4.6 mm) and an uniform incoherent back-

0146-9592/10/101605-3/$15.00

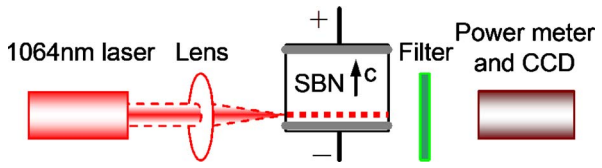

Fig. 1. (Color online) Setup for the generation and observation of SH waves.

ground illumination of $I_b=43.5$ mW/cm^2 (15.6 mW, 0.46×0.78 cm^2) were applied, the light spot at the output face is constrained to a size similar to that at the input face, and it deflects towards the direction of $-c$. A soliton formed and reached its steady state at 95 s; however, there was also no SHG detected, as shown in Figs. 2(b_1) and 2(b_2), just due to the phase mismatching caused by self-bending of the soliton. The dashed lines in Figs. 2(a) and 2(b) show the center of the light beam.

Then we shift the crystal parallel to the c axis to make the incident center close to the $-c$ surface of the crystal. The distance between the incident beam center and the edge of the $-c$ surface is about 40 μm, and the incident angle is 0°. Without an applied external electric field, interference between the incident beam and the reflected beam occurred, and PR SWs with diffusion nonlinearity formed, as shown in Fig. 2(c_1). At the same time, bight green SH waves emitted from the $-c$ edge at the output face, as shown in Fig. 2(c_2). The dashed lines in Figs. 2(c) and 2(d) show the crystal edge in the output surface. When an external electric field $E_0=413$ V/mm and an uniform incoherent background illumination of $I_b=43.5$ mW/cm^2 are applied, the interference stripes at the output face converge toward the $-c$ surface and reach steady state at 95 s. Simultaneously, the intensities of interference stripes and SH waves are greatly increased, as shown in Figs. 2(d_1) and 2(d_2), respectively. In the experiment a 532 nm bandpass filter and a heat absorbing glass (with the transmissivity less than 0.1% for wavelengths over 1000 nm) are used in front of the CCD or powermeter to image the distribution or measure the power of the SHG, respectively. The power of SH wave in Figs. 2(c_2) and 2(d_2) are 1.12 and 4.52 mW, respectively, and the conversion efficiencies are 20.7%/W and 57.1%/W, respectively.

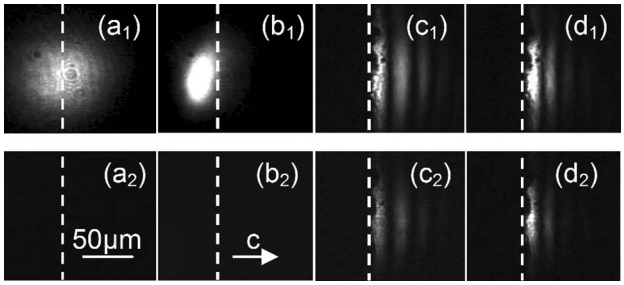

Fig. 2. Images of solitons, SWs, and the corresponding SH waves at the output face: (a_1) diffraction of incident beam; (b_1) PR soliton with $E_0=413$ V/mm and $I_b=43.5$ mW/cm^2; (c_1) PR SW with diffusion nonlinearity; (d_1) PR SW with diffusion and drift nonlinearities, $E_0=413$ V/mm and $I_b=43.5$ mW/cm^2; (a_2)–(d_2) corresponding SH waves of (a_1)–(d_1) at the output face.

To understand the principle and rule of the SHG in this configuration, an e-polarized fundamental laser beam propagating along the interface of a PRC and metal is considered, taking into account the diffusion and drift components of PR nonlinearity; the complex amplitude $E(x,z)$ of the light field satisfies the nonlinear scalar wave equation

$$\nabla^2E(x,z)+k^2E(x,z)=0, \tag{1}$$

where $k=k_0[n+\Delta n]$, $k_0=2\pi/\lambda_0$, λ_0 is the wavelength in vacuum, n is the refractive index of e-polarized beam in PRC, Δn is the nonlinear refractive index change in PRC, $[n+\Delta n]^2=n^2-n^4r_{\rm eff}E_{\rm sc}$, $r_{\rm eff}$ is the effective electro-optical coefficient, and $E_{\rm sc}$ is the space-charge field, which can be can be written as:

$$E_{\rm sc}(x,z)=\frac{k_BT}{e}\nabla\ \ln[I(x,z)+I_b{}']+\frac{E_0I_b{}'}{I(x,z)+I_b{}'}, \tag{2}$$

where k_B is Boltzman constant, T is the temperature, e is the charge of electron, E_0 is the applied external electric field, $I(x,z)$ is the light intensity of the surface waves, and $I_b{}'=I_b+I_d$, where I_b and I_d are the intensity of background illumination and equivalent dark irradiance, respectively. The first and the second terms on the right-hand side of Eq. (2) describe the effect of diffusion and drift nonlinearities, respectively. Rewrite $E(x,z)$ as $A(x,z)\exp(ik_0nz)$, where $A(x,z)$ is the complex amplitude normalized by $I_b{}'^{-1/2}$ and $I(x,z)=A^2(x,z)$. Substituting Eq. (2) into Eq. (1) produces

$$\frac{\partial^2A}{\partial x^2}+\frac{\partial^2A}{\partial z^2}+\gamma\frac{A^2}{A^2+1}\frac{\partial A}{\partial x}-a\frac{E_0A}{A^2+1}=-i2k_0n\frac{\partial A}{\partial z}, \tag{3}$$

where $\gamma=2k_0{}^2n^4r_{\rm eff}k_BT/q$ and $a=k_0{}^2n^4r_{\rm eff}$. The intensity distributions of the fundamental beam can be calculated by the beam propagation method (BPM) and are shown in Fig. 3. Figure 3(a) shows the profile of incident beam at the input face, and the FWHM of light beam is about 30 μm and incident at $x=40$ μm; Figs. 3(b)–3(i) shows the profiles at the output face at $z=7.8$ mm. Figure 3(b) shows the linear case; Fig. 3(c) shows the case with diffusion nonlinearity only; and Figs. 3(d)–3(f) show the cases with diffusion and drift nonlinearity when $E_0=50$, 150, and 435 V/mm, respectively, without background illumination. The beam gradually is drawn toward the boundary, and the intensity increases with the increasing of E_0. Figures 3(g)–3(i) show the cases with diffusion and drift nonlinearity when $I_b=10$, 100, 160 mW/cm^2, respectively, with $E_0=435$ V/mm. The beam also continually is drawn toward the boundary, and the intensity increases with the increasing background illumination.

The conversion efficiency η from the fundamental beam to the SH wave can be expressed as

$$\eta=\frac{P_{2\omega}}{P_\omega}\propto\frac{(\chi^{(2)})^2P_\omega L^2}{A}\frac{\sin^2(\Delta kL/2)}{(\Delta kL/2)^2}, \tag{4}$$

where P_ω and $P_{2\omega}$ are the power of the fundamental wave and the SH wave, respectively; L is the length

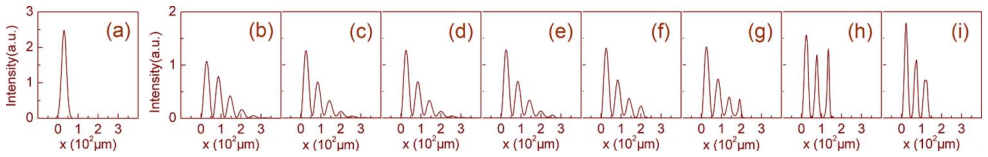

Fig. 3. (Color online) Intensity distribution profiles of the surface wave. (a) Input face; (b)–(i) output face at $z=7.8$ mm: (b) linear; (c) with diffusion nonlinearity; (d)–(f) with diffusion and drift nonlinearity, $I_b=0$ mW/cm^2, $E_0=50$, 150, 435 V/mm, respectively; (g)–(i) with diffusion and drift nonlinearity, $E_0=435$ V/mm, $I_b=10$, 100, 160 mW/cm^2, respectively.

the of medium; A is the cross-sectional area of the beam; and Δk is the PM factor of the SHG. In the experimental configuration, the SHG conversion efficiency is mainly determined by intensity of light energy P_ω/A and PM factor Δk. The above theoretical analysis indicates that intensity of light energy P_ω/A and consequently the conversion efficiency η could be effectively improved by increasing the applied electric field and the background illumination.

In the experiments, first the applied electric field E_0 varied from 0 V/mm to 435 V/mm. The conversion efficiency η increased along with the increasing of E_0, as shown in Fig. 4(a). Second, the uniform incoherent background illumination I_b varied from 0 to 164 mw/cm^2. The conversion efficiency also increased with the increasing of I_b, as shown in Fig. 4(b). One can find from Fig. 4(b) that the increasing of η becomes slow when high enough background illumination is applied. From Eq. (2) one can know that with the increasing of I_b, the effect of drift nonlinearity saturates gradually. So the increasing of η gradually reaches saturation. The theoretical analyses of the evolution of the fundamental beam are in good agreement with the experimental results. In the experiment, the conversion efficiency is improved almost four times with applied E_0 and I_b.

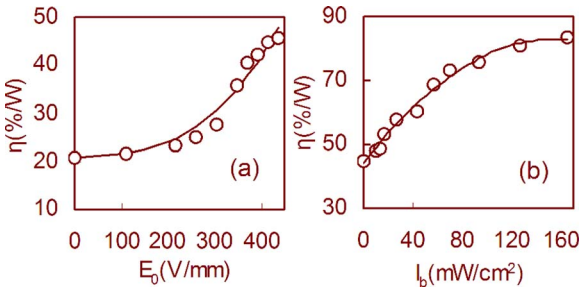

Fig. 4. (Color online) Conversion efficiency η of SHG versus (a) applied external electric field E_0 and (b) background illumination I_b.

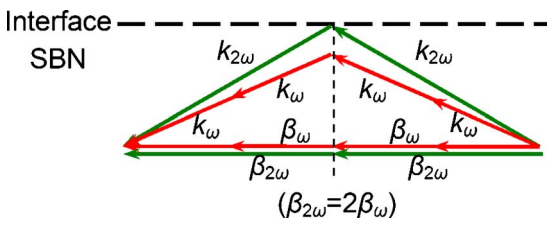

Fig. 5. (Color online) Scheme of PM for SHG in the surface waveguide induced by PR SWs.

The scheme of PM for SHG using PR SWs is shown in Fig. 5. k_ω and $k_{2\omega}$ are the wave vectors of the fundamental wave and the SH wave, respectively. β_ω and $\beta_{2\omega}$ are the propagation constants of the fundamental wave and the SH wave, respectively. Let us consider fundamental light and SH waves propagating along the surface waveguide induced by PR SWs. In such a surface waveguide, the wave vectors $k_{2\omega}$ and k_ω are in a wide angular range. So always the SH waves with propagation constant $\beta_{2\omega}=\beta_\omega$ can be resonant excited, as shown in Fig. 5. That is to say, the momentum conservation is satisfied by propagation constant. At the same time, such a waveguide is highly multimode with many optical modes corresponding to geometrical optics rays propagating in a zigzag manner parallel to the surface. Thus there is multimode SHG with various $\beta_{2\omega}$ that couple together and compose a pattern similar to that of the fundamental beam, as shown in Figs. 2(c) and 2(d).

To summarize, giant enhancement of SHG conversion efficiency can be obtained by taking advantage of the surface. This study also indicates a way to enhance the nonlinear phenomena, and a series of surface related applications may be expected.

This work is supported by the National Natural Science Foundation of China (NSFC) under grants 60678026 and 10874094, the Program for Changjiang Scholars and Innovative Research Team, the 111 Project (B07013), and the Chinese National Key Basic Research Special Fund (2006CB921703).

References

1. M. Scalora, M. J. Bloemer, C. M. Bowden, G. D' Aguanno, M. Centini, C. Sibilia, M. Bertolotti, Y. Dumeige, I. Sagnes, P. Vidakovic, and A. Levenson, Opt. Photonics News **12** (4), 39 (2001).
2. J. A. Armstrong, N. Bloembergen, J. Duelling, and P. S. Pershan, Phys. Rev. **127**, 1918 (1962).
3. M. M. Fejer, G. A. Magel, D. H. Jundt, and R. L. Byer, IEEE J. Quantum Electron. **28**, 2631 (1992).
4. Y. Y. Zhu, R. F. Xiao, J. S. Fu, G. K. L. Wong, and N. B. Ming, Opt. Lett. **22**, 1382 (1997).
5. S. Lan, M. F. Shih, G. Mizell, J. A. Giordmaine, Z. G. Chen, C. Anastassiou, J. Martin, and M. Segev, Opt. Lett. **24**, 1145 (1999).
6. G. S. Garcia Quirino, J. J. Sanchez-Mondragon, and S. Stepanov, Phys. Rev. A **51**, 1571 (1995).
7. M. Cronin-Golomb, Opt. Lett. **20**, 2075 (1995).
8. I. I. Smolyaninov, C. H. Lee, and C. C. Davis, Phys. Rev. Lett. **83**, 2429 (1999).
9. T. H. Zhang, J. Yang, H. Z. Kang, L. Feng, J. J. Xu, C. P. Zhang, X. K. Ren, B. H. Wang, Y. Z. Lu, F. Jia, and W. W. Shao, Phys. Rev. B **73**, 153402 (2006).

Experimental and theoretical analysis of THz-frequency, direction-dependent, phonon polariton modes in a subwavelength, anisotropic slab waveguide

Chengliang Yang,[1,3,4] Qiang Wu,[1,*] Jingjun Xu,[1,3] Keith A. Nelson,[2] and Christopher A. Werley[2,4]

[1]*The Key Laboratory of Weak Light Nonlinear Photonics, Ministry of Education, School of Physics, and TEDA Applied Physics School, Nankai University, Tianjin 300457, P. R. China*
[2]*Department of Chemistry, Massachusetts Institute of Technology, Cambridge, Massachusetts 02139, USA*
[3]*Changchun Institute of Optics, Fine Mechanics and Physics, Chinese Academy of Sciences, Changchun 130033, P. R. China*
[4]*These authors have contributed equally to the work in this article.*
**wuqiang@nankai.edu.cn*

Abstract: Femtosecond optical pulses were used to generate THz-frequency phonon polariton waves in a 50 micrometer lithium niobate slab, which acts as a subwavelength, anisotropic planar waveguide. The spatial and temporal electric field profiles of the THz waves were recorded for different propagation directions using a polarization gating imaging system, and experimental dispersion curves were determined via a two-dimensional Fourier transform. Dispersion relations for an anisotropic slab waveguide were derived via analytical analysis and found to be in excellent agreement with all observed experimental modes. From the dispersion relations, we analyze the propagation-direction-dependent behavior, effective refractive index values, and generation efficiencies for THz-frequency modes in the subwavelength, anisotropic slab waveguide.

OCIS codes: (040.2235) Far infrared or terahertz; (100.0118) Imaging ultrafast phenomena; (320.7110) Ultrafast nonlinear optics; (240.5420) Polaritons; (130.3730) Lithium niobate.

References and links

1. Y.-S. Lee, *Principles of Terahertz Science and Technology* (Springer, New York, 2009).
2. R. M. Koehl, S. Adachi, and K. A. Nelson, "Real-Space Polariton Wave Packet Imaging," J. Chem. Phys. **110**(3), 1317–1320 (1999).
3. N. S. Stoyanov, D. W. Ward, T. Feurer, and K. A. Nelson, "Terahertz polariton propagation in patterned materials," Nat. Mater. **1**(2), 95–98 (2002).
4. T. Feurer, J. C. Vaughan, and K. A. Nelson, "Spatiotemporal coherent control of lattice vibrational waves," Science **299**(5605), 374–377 (2003).
5. T. Feurer, N. S. Stoyanov, D. W. Ward, J. C. Vaughan, E. R. Statz, and K. A. Nelson, "Terahertz Polaritonics," Annu. Rev. Mater. Res. **37**(1), 317–350 (2007).
6. T. P. Dougherty, G. P. Wiederrecht, and K. A. Nelson, "Impulsive Stimulated Raman Scattering Experiments in The Polariton Regime," J. Opt. Soc. Am. **9**(12), 2179–2189 (1992).
7. Y. X. Yan, E. B. Gamble, and K. A. Nelson, "Impulsive Stimulated Scattering: General Importance in Femtosecond Laser Pulse Interactions with Matter, and Spectroscopic Applications," J. Chem. Phys. **83**(11), 5391–5399 (1985).
8. D. Auston, and M. Nuss, "Electrooptic Generation and Detection of Femtosecond Electrical Transients," IEEE J. Quantum Electron. **24**(2), 184–197 (1988).
9. Y. S. Lee, T. Meade, V. Perlin, H. Winful, T. B. Norris, and A. Galvanauskas, "Generation of narrow-band terahertz radiation via optical rectification of femtosecond pulses in periodically poled lithium niobate," Appl. Phys. Lett. **76**(18), 2505–2507 (2000).
10. J. Hebling, A. G. Stepanov, G. Almási, B. Bartal, and J. Kuhl, "Tunable THz pulse generation by optical rectification of ultrashort laser pulses with tilted pulse fronts," Appl. Phys. B **78**, 593–599 (2004).
11. K. L. Yeh, M. C. Hoffmann, J. Hebling, and A. Keith, "Generation of 10 μJ ultrashort terahertz pulses by optical rectification," Appl. Phys. Lett. **90**(17), 171121 (2007).

#136308 - $15.00 USD Received 8 Oct 2010; revised 18 Nov 2010; accepted 19 Nov 2010; published 1 Dec 2010

12. K.-H. Lin, C. A. Werley, and K. A. Nelson, "Generation of multicycle THz phonon-polariton waves in a planar waveguide by tilted optical pulse fronts," Appl. Phys. Lett. **95**(10), 103304 (2009).
13. D. H. Auston, K. P. Cheung, J. A. Valdmains, and D. A. Kleinman, "Cherenkov Radiation from Femtosecond Optical Pulses in Electro-Optic Media," Phys. Rev. Lett. **53**(16), 1555–1558 (1984).
14. J. K. Wahlstrand, and R. Merlin, "Cherenkov radiation emitted by ultrafast laser pulses and the generation of coherent polaritons," Phys. Rev. B **68**(5), 054301 (2003).
15. N. S. Stoyanov, T. Feurer, D. W. Ward, and K. A. Nelson, "Integrated diffractive terahertz elements," Appl. Phys. Lett. **82**(5), 674–676 (2003).
16. P. Peier, S. Pilz, F. Müller, K. A. Nelson, and T. Feurer, "Analysis of phase contrast imaging of terahertz phonon-polaritons," J. Opt. Soc. Am. B **25**(7), B70–B75 (2008).
17. Q. Wu, C. A. Werley, K. H. Lin, A. Dorn, M. G. Bawendi, and K. A. Nelson, "Quantitative phase contrast imaging of THz electric fields in a dielectric waveguide," Opt. Express **17**(11), 9219–9225 (2009).
18. C. A. Werley, Q. Wu, K. H. Lin, C. R. Tait, A. Dorn, and K. A. Nelson, "A comparison of phase sensitive imaging techniques for studying THz waves in structured $LiNbO_3$," J. Opt. Soc. Am. B **27**(11) 2350-2359 (2010).
19. E. A. Bahaa, B. Saleh and M. C. Teich, *Fundamentals of photonics* (JOHN WILEY&SONS, 1991)
20. M. Born and E. Wolf, *Principles of Optics (Cambridge University Press, Cambridge, 1999).*
21. D. H. Auston, and M. C. Nuss, "Electrooptic generation and detection of femtosecond electrical transients," IEEE J. Quantum Electron. **24**(2), 184–197 (1988).
22. A. S. Barker, Jr., and R. Loudon, "Dielectric properties and optical phonons in $LiNbO_3$," Phys. Rev. **158**(2), 433–445 (1967).
23. N. S. Stoyanov, T. Feurer, D. Ward, E. Statz, and K. Nelson, "Direct visualization of a polariton resonator in the THz regime," Opt. Express **12**(11), 2387–2396 (2004).
24. S. Wang, M. L. Shah, and J. D. Crow, "Wave propagation in thin film optical waveguides using gyrotropic and anisotropic materials as substrates," IEEE J. Quantum Electron. **8**(2), 212–216 (1972).
25. D. P. G. Russo, and J. H. Harris, "Wave propagation in anisotropic thin-film optical waveguides," J. Opt. Soc. Am. **63**(2), 138–145 (1973).
26. W. K. Burns, and J. Warner, "Mode dispersion in uniaxial optical waveguides," J. Opt. Soc. Am. **64**(4), 441–446 (1974).
27. V. Ramaswamy, "Propagation in asymmetrical anisotropic film waveguides," Appl. Opt. **13**(6), 1363–1371 (1974).
28. S. Nemoto, and T. Makimoto, "Further discussion of the relationship between phase and group indices in anisotropic inhomogeneous guiding media," J. Opt. Soc. Am. **67**(9), 1281–1283 (1977).
29. D. Marcuse, "Modes of a symmetric slab optical waveguide in birefringent media-Part I: Optical axis not in plane of slab," IEEE J. Quantum Electron. **14**(10), 736–741 (1978).
30. D. Marcuse, and I. P. Kaminow, "Modes of a Symmetric Slab Optical Waveguide in Birefringent Media Part II: Slab with Coplanar Optical Axis," IEEE J. Quantum Electron. **15**(2), 92–101 (1979).

1. Introduction

Terahertz-frequency phonon polariton generation, control and detection have received extensive attention in recent years due to their outstanding capabilities in terahertz (THz) spectroscopy, imaging and advanced signal processing [1–5]. Phonon polariton waves result from the coupling of lattice vibrational waves and electromagnetic waves, and can be generated in ferroelectric crystals such as $LiNbO_3$ (LN) via impulsive stimulated Raman scattering (ISRS) using femtosecond optical pulses [6,7]. The electromagnetic component of the phonon polariton wave can be coupled into free space and is a source for intense THz pulses [8–12]. THz waves generated in the sample do not propagate collinearly with the pump beam due to the large index-mismatch between optical and THz frequencies. Instead they generate a Cherenkov radiation pattern and propagate primarily in the lateral direction [13, 14]. This lateral propagation facilitates coherent control of the THz wave, which can easily be made to interact with subsequent optical pulses, other THz waves, or patterned structures all in the same small crystal of LN. As a result, a LN slab can serve as a platform for THz processing because generation, propagation, detection, and control can be fully integrated in one sample [5, 15]. Furthermore, when the sample thickness becomes comparable to or less than the THz wavelength, the strong evanescent field of the THz wave can interact with material deposited on the crystal surface. This opens the door for spectroscopic analysis and interfacing the LN slab with other optical or photoelectric devices.

Because the THz wave propagates almost perpendicular to the optical pump beam, it is possible to obtain time-resolved images of the electric field in the LN slab. As the THz wave propagates through the crystal, its electric field changes the refractive index through the electro-optic effect. The time-delayed probe pulses, which can be expanded to illuminate the

#136308 - $15.00 USD Received 8 Oct 2010; revised 18 Nov 2010; accepted 19 Nov 2010; published 1 Dec 2010

whole crystal, experience a spatially dependant phase shift proportional to the refractive index change. Four methods have been introduced to convert this phase pattern to an amplitude image: Talbot imaging [2], Sagnac interferometry [16], polarization gating [16,18], and phase contrast imaging [17]. In a recent comparison [18], an improved geometry for polarization gating was found to offer the best sensitivity and most reliable field quantification, while phase contrast imaging was best in situations requiring high spatial resolution. In this paper, we used the polarization gating system similar to that shown in [18] to record a sequence of images. The full spatio-temporal evolution was extracted from the image sequence and double Fourier transformed to obtain the wave vector vs. frequency dispersion curves [e.g 17.]. The data collection and analysis were performed as a function of wave propagation direction to study the complex mode structure present in an anisotropic slab waveguide, which was found to be in excellent agreement with theory. From the dispersion relations we extract the mode and propagation-angle dependent effective refractive index (ERI) and discuss pumping efficiencies for THz phonon polariton waves in a LN waveguide.

2. Experimental section

The experiments were performed with a Ti:sapphire regenerative amplifier whose pulse duration was 120 fs, central wavelength was 800 nm, and repetition rate was 1 KHz. The laser pulses were divided into a pump beam (370 μJ per pulse) and probe beam (35 μJ per pulse). The vertically polarized pump beam was routed through a mechanical delay stage and then focused to a line on the sample by a 200 mm focal length cylindrical lens (about 1 TW/cm^2). The probe was frequency-doubled to 400 nm in a BBO crystal and expanded to be larger than the sample. The probe beam is nearly collinear with the pump by using a dichroic mirror, so the second harmonic wave of the pump on the sample, whose wavelength is the same as probe, can be blocked with a razor blade on the focal plane of the imaging lens. Figure 1(a) shows a sketch of the experimental setup and the coordinate system. A quarter-wave plate (QW1) and a retroreflective mirror were used in a 4-f system. The mirror and lenses imaged the sample precisely back onto itself without magnification or inversion. The axis of QW1, which was the same as the first Glan-Taylor polarizer (GTP1), was at + 45° so it exchanged the ordinary and the extraordinary polarization components of the probe. In this way the spatially varying phase shift between the vertical and horizontal polarization components accumulated from the probe's first pass through the sample was compensated after the second pass. The phase shift after the first pass resulted from the intrinsic birefringence of the LN slab, and self-compensation was necessary to correct for spatial inhomogeneities in the phase shift due to thickness variation, strain, or other imperfections in the slab. The phase shift electro-optically induced by the THz wave, however, was not compensated because the THz wave was launched only after the probe pulse had passed through the sample the first time. The THz-induced phase information was converted to amplitude information prior to detection with the camera by QW2 (oriented vertically) and GTP2 (oriented at −45°). In this geometry a positive field results in a positive amplitude change and vice versa [18].

#136308 - $15.00 USD Received 8 Oct 2010; revised 18 Nov 2010; accepted 19 Nov 2010; published 1 Dec 2010

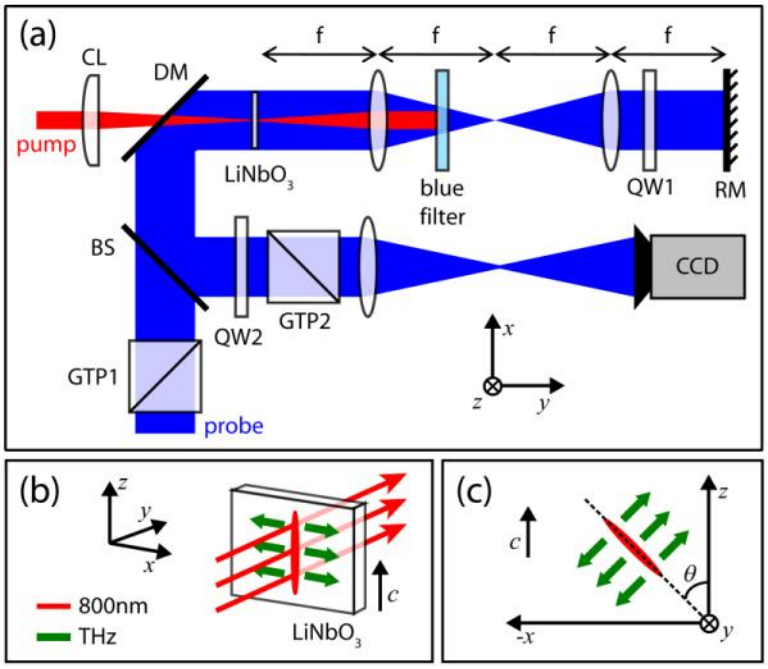

Fig. 1. (a) Overview diagram of the experimental setup. GTP1 and GTP2 are Glan-Taylor prisms, whose polarizations are at + 45° and –45° to *z*-axis respectively. BS: 400 nm beam splitter; CL: cylindrical lens; DM: dichroic mirror; RM: retroreflective mirror. QW1 and QW2 are zero order 400 nm quarter-wave plates with optic axes at + 45 ° and parallel to z-axis respectively. The 800 nm pump (red) and 400 nm probe (blue) are nearly collinear when they arrive at the sample, a 50 μm thick $LiNbO_3$ slab. (b) The pump geometry and coordinate system. The 800 nm pump beam (red) propagates through the crystal, orthogonal to the crystal surface, while the THz (green) is guided down the slab. (c) The cylindrical lens can be rotated by θ relative to the *z*-axis (the *c* crystallographic axis of the LN sample) in order to launch the THz wave in a 90°-θ direction.

The pump geometry is shown in Fig. 1(b). Red lines represent the 800 nm pump beam and green the broadband THz waves generated when the pump is focused into the 50 μm thick $LiNbO_3$ crystal slab. Because the center wavelength of the THz phonon polariton wave is about 100 μm, the slab acts as a sub-wavelength waveguide. As Fig. 1(c) shows, the THz wave propagation direction was changed by rotating the cylindrical lens. Because of the strong anisotropy of LN at THz frequencies, the nature and behavior of the waveguide modes change drastically as the propagation direction rotates relative to the optic axis.

3. Results

By changing the delay between the pump and probe pulses, a series of images can be obtained. The image sequence can be compiled to form a movie showing THz propagation [2–5, 17, 18]. Because the line focus launches plane-wave THz transients that propagate laterally away from the focal region (i.e. the origin), in each image recorded at a different probe time delay the signal was uniform along the direction of the line focus. Therefore at each propagation distance from the origin, we averaged the signal over this direction, collapsing each 2D matrix of values and the corresponding image to 1D. We then displayed each 1D image corresponding to a selected time delay as a horizontal line, and we displayed the 1D images one above the other in time order, showing the full temporal and spatial information in a single graphic (Fig. 2(a)). From Fig. 2(a) we can see dispersion, reflection, and different waveguide modes clearly and the THz electric field E(t) also can be acquired using the same method as [18]. A 2-dimensional Fourier transformation of Fig. 2(a) yields the THz dispersion curves (Fig. 2(b)). Along the vertical axis, time is transformed to frequency,

#136308 - $15.00 USD Received 8 Oct 2010; revised 18 Nov 2010; accepted 19 Nov 2010; published 1 Dec 2010

and along the horizontal axis, space is transformed to the wave vector, k_x, which is often called the waveguide propagation constant, β. In Fig. 2, $\theta = 0$, so the crystal's *c*-axis is parallel to the 800 nm pump polarization. In this geometry, which has been most used in previous work [2–5,15–18], only *z*-polarized THz is generated, and true transverse electric (TE) modes are launched in the slab. Overlaid on the experimental data are the dispersion curves for air (white line), bulk LN (magenta line), and the calculated TE mode dispersion curves (see e. g [19].) up to a frequency of 2 THz for an isotropic slab waveguide with $n = n_e$ (dotted blue lines). The curves show four TE waveguide modes, which propagate at different group velocities, $v_g = d\omega / dk$, and phase velocities, $v_p = \omega / k$. Cutoff frequencies can be seen for the all but the first mode as expected. Although the isotropic waveguide analysis is predictive in this simple geometry, a more complete analysis is required when $\theta \neq 0$, as will be shown below.

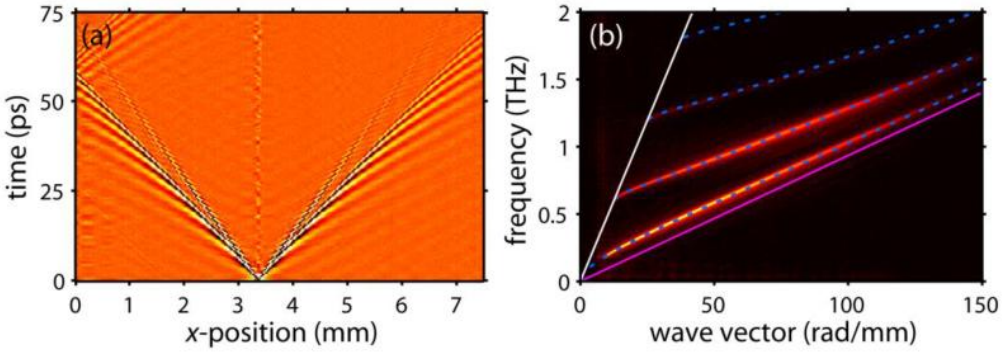

Fig. 2. (a) Space-time plot of a propagating THz wave. We can see waveguide dispersion (the frequencies separate as time progresses), reflection from the crystal edge, and the first two waveguide modes (the second mode has a higher frequency and a steeper slope because of its lower group velocity) in this picture. The horizontal axis is the *x*-axis of the coordinate system in Fig. 1 and vertical axis is the delay time between the probe and pump. (b) Dispersion curves of the THz wave in the LN slab waveguide computed by taking 2D Fourier transformation of (a). The horizontal axis is the wave vector, k_x (also called the propagation constant, β), and the vertical axis is frequency of THz wave in the sample. Theoretical dispersion curves in air (white), bulk LN (magenta) and in a 50 μm slab waveguide (dotted blue) are overlaid on the experimental data where the first three modes are visible.

In an anisotropic waveguide, constraints relating to propagation in bulk anisotropic material and constraints relating to propagation in a waveguide both come into play. In bulk anisotropic material waves are divided into two normal modes, ordinary waves and extraordinary waves, which propagate through the material at different velocities [20]. In an isotropic waveguide there are also two uncoupled eigenmodes, the transverse electric (TE) and transverse magnetic (TM) modes, which propagate through the waveguide at different velocities [19]. When $\theta = 0$ or 90°, these modes map directly onto one another. For $\theta = 0°$ the TE mode is an extraordinary wave and the TM mode is an ordinary wave while for $\theta = 90°$ the opposite pairing holds. When $\theta \neq 0$, however, the high-symmetry configuration is broken and all the modes couple together. The new eigenmodes of the system are neither purely TE nor TM and also not purely ordinary or extraordinary. The coupling effects the mode profiles, dispersion curves, and effective refractive indices in a fundamental and significant way, as will be demonstrated experimentally (presented immediately below) and theoretically (the full analysis can be found in the appendix) in the remainder of this paper.

With the experimental system mentioned above, we measured the dispersion curves for different propagation directions by rotating the cylindrical lens and CCD camera together, which kept the THz wavefront aligned vertically in the images. In this manner the THz wave propagation direction was varied from 0 to 90 degrees relative to the *c*-axis as shown in Fig. 1(c). The polarization of the 800 nm pump light was not rotated and thus was parallel to the *c*-axis in all measurements. Because of the strong r_{33} electro-optic coefficient in LN, this

#136308 - $15.00 USD Received 8 Oct 2010; revised 18 Nov 2010; accepted 19 Nov 2010; published 1 Dec 2010

ensured efficient pumping of THz waves with a large component polarized along the optic axis [21–23]. Using the same data collection and analysis procedure as was used to generate Fig. 2(b), the dispersion curves were measured for different angles θ, some examples of which are shown in Fig. 3. Overlaid on the experimental data are the theoretical solutions for a bound mode propagating in an anisotropic, dielectric slab waveguide with a thickness of 50 μm, an extraordinary index of 5.11, and an ordinary index of 6.8. The full derivation is presented in appendix A. For all modes and all angles, the data agree very well with theoretical predictions.

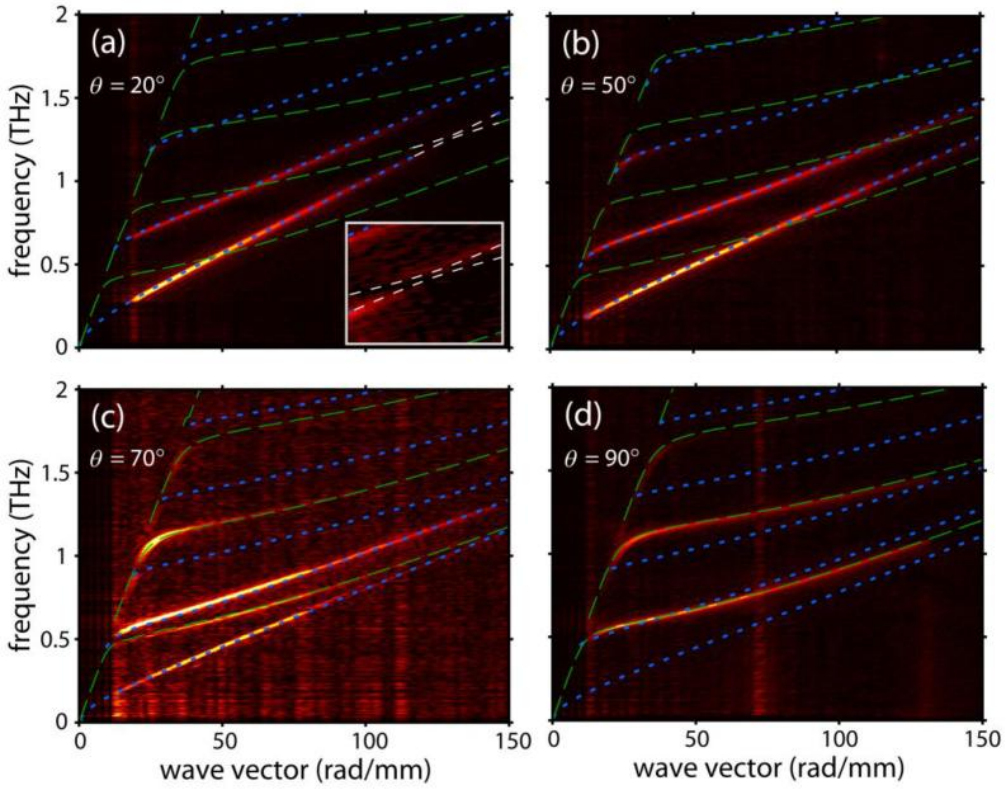

Fig. 3. (a) Dispersion curves for θ = 20°. Blue dotted lines are calculated TE-like mode dispersion curves and green dashed lines are TM-like modes. Experimentally we see three TE-like modes and no TM-like modes. The white box in the lower right shows a blow-up of the region around an avoided crossing between the two lowest symmetrical modes. (b) Dispersion curves for θ = 50°. In this case, TE-like modes still predominate and TM-like modes are too weak to be observed. (c) Dispersion curves for θ = 70°. We can see both TE- and TM-like modes, and all of the first 7 modes are observed experimentally. (d) Dispersion curves for θ = 90°, in which only the TM modes are excited. All the experimental data agree well with the calculated curves.

In Fig. 3(a) where θ = 20°, one set of modes is very TE-like, and one is strongly TM-like. Because the TE-like modes have their primary polarization component along the *c*-axis, they were pumped much more strongly than the TM-like modes, which were too weak to be observed clearly. Blue dotted lines are calculated TE-like modes and green dashed lines are TM-like modes. An interesting effect resulting from propagation in the anisotropic waveguide when $\theta \neq 0$ or 90° is visible in the region containing the white lines, a magnified view of which is shown in the lower right corner. Although the TM-like modes are not visible, we still see an avoided crossing when two modes with the same symmetry (symmetric or antisymmetric) cross. The avoided crossing, visible in experiment and predicted by theory, results from coupling between TE- and TM-like modes in the anisotropic waveguide. Here

#136308 - $15.00 USD Received 8 Oct 2010; revised 18 Nov 2010; accepted 19 Nov 2010; published 1 Dec 2010

the two lowest symmetric modes, the lowest TE-like mode and the second TM-like mode, avoid each other.

Figure 3(b) shows dispersion curves for the case of θ = 50°. The three TE-like modes predominate, although their strength is reduced, and TM modes still cannot be observed. No avoided crossings occur between modes of the same symmetry within the bandwidth of the experiment. As θ increases, the velocity of the extraordinary wave approaches that of the ordinary wave [30], which means that the slopes of TE-like and TM-like modes tend to be more similar at higher frequencies. Figure 3(c) shows the results for θ = 70°, where both TM-like and TE-like modes can be seen clearly. The strength of the TE-like modes continues to decrease with increased θ and TM-like modes are finally pumped strongly enough to detect. Although some of the modes are weak, the first seven modes can be observed in the experiment, all of which agree with theoretical predictions. Continuing the trend, at high frequencies the slopes of the TM-like and TE-like modes become even more similar. Finally, Fig. 3(d) shows results for θ = 90°, where only TM modes can be observed.

Using the derivation in appendix A, we can calculate the E-field profile of THz waves as shown in Fig. 4. Figures 4(a) and (b) show field profiles for TE and TM modes respectively at θ = 0°. The coordinate system in Fig. 4 is the same as in the appendix (see Fig. 8), where the axes are defined by the propagation direction of the wave and not by the lab frame as in Fig. 1. Blue, green and red lines represent electric field along *x*-axis, *y*-axis and *z*-axis respectively. The electric field along the *y*-axis, whose polarization is perpendicular to the surface of the slab, changes drastically at the slab surface (± 25 μm). As mentioned above, pure TE and TM modes only exist at 0 and 90 degrees. At any other angle the eigenmodes are superpositions of TE and TM modes and contain all three polarization components, as shown in Fig. 4 (c) and (d) where θ = 50°.

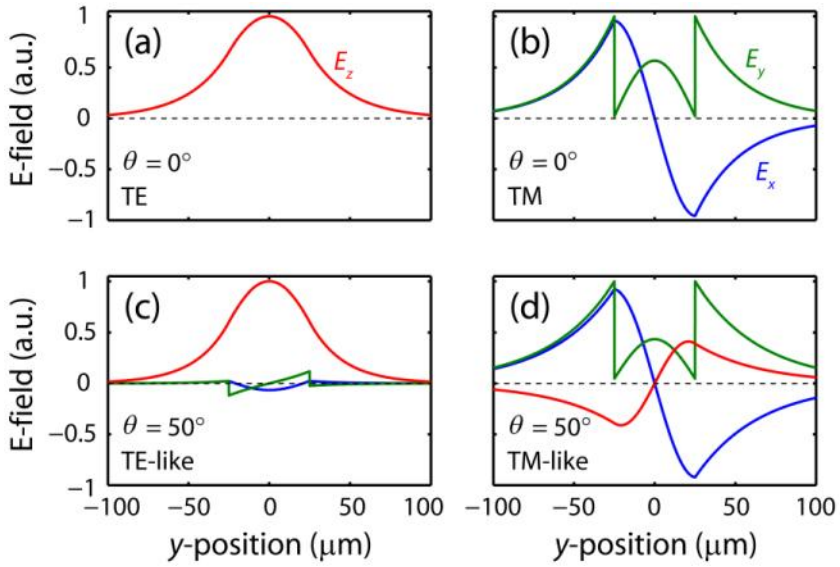

Fig. 4. Electric field profiles for the lowest symmetric and antisymmetric modes at 0.5 THz. E_x, E_y and E_z are represented by blue, green and red lines respectively. The discontinuities in E_y located at ± 25 μm occur because of the slab surfaces. (a)-(b) TE and TM profiles when θ is 0°. (c) and (d) The electric field profile when θ is 50°.

One can extract the group and phase effective refractive index (ERI) from dispersion curves like those shown in Fig. 3. The phase ERI can be retrieved directly from the dispersion curve, $n_p = c/v_p = ck/(2\pi f)$, and the group ERI can be retrieved from the slope of the dispersion curve, $n_g = c/v_g = c\Delta k/(2\pi\Delta f)$. Here v_p and v_g are the phase and group velocities, and the wave vector, *k*, and frequency, *f*, correspond to the axes in Fig. 3. From the

#136308 - $15.00 USD Received 8 Oct 2010; revised 18 Nov 2010; accepted 19 Nov 2010; published 1 Dec 2010

derivation in the appendix, we can calculate both phase and group ERI for all propagation directions of TE-like and TM-like modes in the LN slab waveguide. Based on the agreement between experimental data and theoretical predictions shown in Fig. 3, Fig. 5 gives the theoretically calculated phase and group ERI for different angles, modes and frequencies. The ERI values are important for phase-matching in THz generation and for many nonlinear as well as linear optical processes.

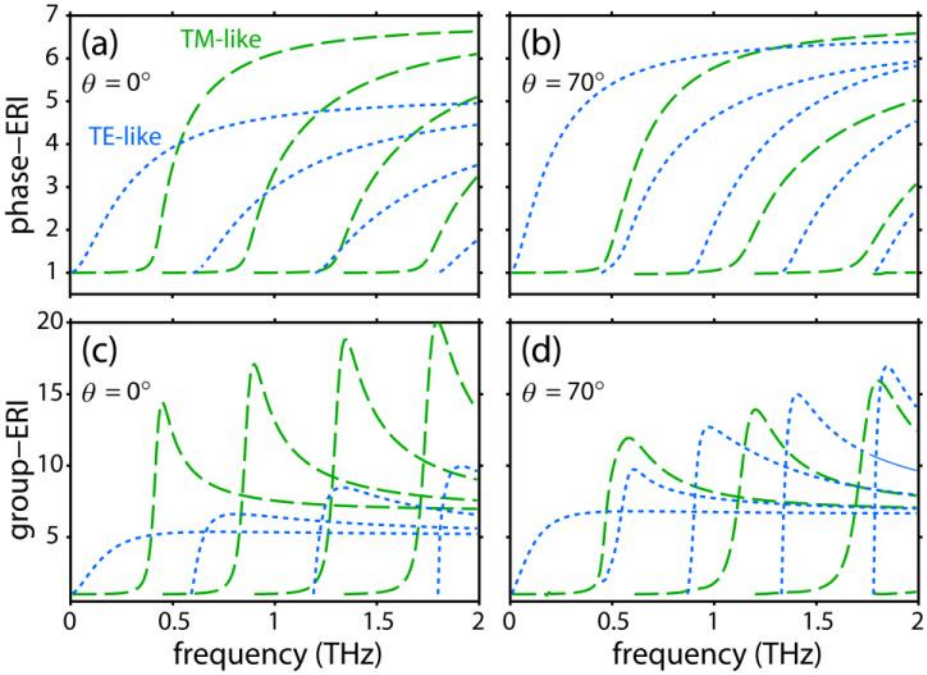

Fig. 5. (a) The frequency- and mode- dependent phase ERI for TE-like (dotted blue) and TM-like (dashed green) modes when $\theta = 0°$. (b) The phase ERI when $\theta = 70°$. (c) and (d) are the same as (a) and (b), but for the group ERI.

In Fig. 5 dotted blue lines are the calculated ERI for TE-like modes and dashed green lines are the ERI for TM-like modes. From Fig. 5(a) and (b), we can see that the phase ERI for both TE-like and TM-like modes transitions from 1 (the index of air) to the bulk effective index. For the TM-like waves the bulk index is always the ordinary index of refraction, $n_o \approx$ 6.8, while for the TE-like waves the bulk index is that for the extraordinary wave in the anisotropic material, and changes from ~5.1 at 0° to ~6.8 at 90°. At all angles, the low-frequency TM-like modes have most of their energy in the evanescent field in the air and have ERI values near unity. The ERI then transitions rapidly to bulk-like values at higher frequencies. Much like the phase ERI, the group ERI transitions from 1 to the bulk effective index (see Fig. 5 (c) and (d)). In contrast to the phase ERI, however, the group ERI rises well above the bulk values before approaching them asymptotically at high frequencies. In contrast to the phase index, where higher modes always have lower ERIs, the group ERI is usually higher for higher modes. Another difference is that the peak group index changes drastically with θ for both TE-like and TM-like modes, while the peak phase ERI for the TM-like modes is just the bulk value and insensitive to angle.

A useful way to display the ERI is with an index ellipse, which highlights the angle-dependant behavior. Figure 6 follows the phase ERI for the first three TE-like modes at wave vector magnitude $\beta = 50$ rad/mm as a function of angle, tracing out the phase ERI ellipse. We measured data in the first quadrant, and because of the symmetry these results can also be used for 90° to 360°. Values over 70° were not recorded because the TE-like modes were too weak to be observed. Figure 6 shows the measured values for the first three TE-like modes as

#136308 - $15.00 USD Received 8 Oct 2010; revised 18 Nov 2010; accepted 19 Nov 2010; published 1 Dec 2010

open symbols and the calculated values predicted by the derivation in the appendix as solid lines. The experimental data can be fit to an ellipse, where the long and short axes are 5.44 and 4.18 for the first mode, 3.36 and 2.59 for the second mode and 2.01 and 1.74 for the third mode. The value of the long axis represents the ERI for an ordinary wave (the TE mode is purely ordinary at 90°) and the short axis represents the ERI for an extraordinary wave (the TE mode is purely extraordinary at 0°).

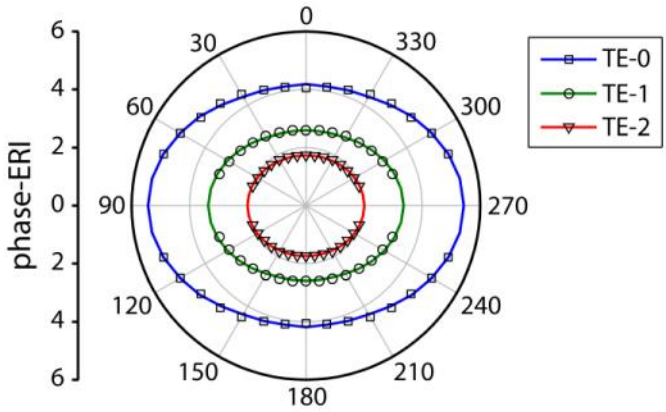

Fig. 6. Effective refractive index (phase ERI) ellipse for three TE modes at a wave vector β = 50 rad/mm in a 50 μm LN slab waveguide. The open symbols are experimental data and the solid lines are calculated results. The scale along the *x*-axis is the same as that along *y*.

Because the 800 nm light was always polarized along the *c*-axis, we only pumped through the r_{33} electro-optic coefficient, which generated THz polarized along the optic axis [5]. The THz generated by the pump can be represented by a linear combination of waveguide modes, and the magnitude of the contribution from a given mode is related to the projection of its polarization along the *c*-axis. Thus, for a given mode and frequency, one can make a rough estimate of the relative pumping efficiency $\eta(\theta)$ by looking at the fraction of the mode energy corresponding to a field inside the crystal oriented along the optic axis:

$$\eta(\theta) = \frac{\int_{-\ell}^{\ell} \left[E_x^2(y) \sin^2\theta + E_z^2(y) \cos^2\theta \right] dy}{\int_{-\infty}^{\infty} \left[E_x^2(y) + E_y^2(y) + E_z^2(y) \right] dy} \qquad (1)$$

Through the integration limits, the expression also takes into account the degree to which the mode is localized within the slab, which improves the efficiency since generation only occurs in the crystal, or is extended into the (air) cladding where no generation occurs.

Figure 7 shows η as a function of θ. When θ = 0°, the TE mode is polarized purely along the optic axis and is pumped most efficiently. As θ increases, the component of the TE wave along the optic axis slowly decreases. In contrast, the component of the TM wave along the optic axis increases, especially after 60°, and at 90°only the TM mode is pumped. At 70°, both modes are pumped with similar efficiencies. The qualitative trends in η explain the mode amplitudes observed in Fig. 3. For θ less than about 60°, TM-like modes are too weak to be observed, while for θ more than about 85°, the TE-like modes are not visible. As predicted, both kinds of modes are visible at 70° as shown in Fig. 3(c). Using different pump polarizations and reflective elements integrated into the waveguides, it will be possible to generate modes not observed in this study.

#136308 - $15.00 USD Received 8 Oct 2010; revised 18 Nov 2010; accepted 19 Nov 2010; published 1 Dec 2010

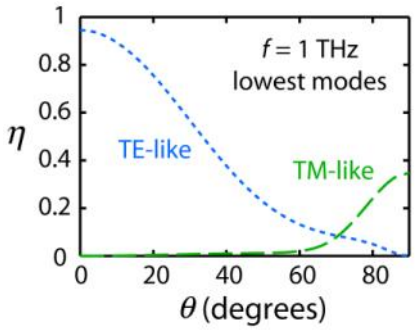

Fig. 7. The fraction of total mode energy corresponding to a field inside the crystal polarized along the optic axis, η, which gives a rough prediction for pumping efficiency. The dotted blue line corresponds to the first symmetric, TE-like mode at 1 THz and the dashed green dashed line corresponds to the first antisymmetric, TM-like mode at the same frequency. As the angle increases, the TE-like mode becomes weaker while the TM-like mode grows in.

4. Conclusions

We have measured the propagation properties of THz waves in a 50 μm $LiNbO_3$ anisotropic slab waveguide using a self-compensating polarization gating imaging system. This system can detect the THz electric fields both temporally and spatially over a wide wavelength range. Using the system, we studied the propagation-direction-dependent behavior of waveguide modes and determined the dispersion curves and effective refractive index for THz waves. A general solution for waveguide modes in a uniaxial slab waveguide was derived and found to agree with the experimental data.

Dispersion is integral to many processes in THz science and generally in linear and nonlinear optics, including broadening of ultrashort pulses, walk-off between pump and probe pulses, phase-matching of parametric processes, and generation of optical solitons. Because dispersion in a waveguide is determined by both the intrinsic material dispersion and geometric dispersion, it is essential to understand waveguiding effects. The results presented here will facilitate the design of functional devices with new capabilities in the $LiNbO_3$ platform for integrated THz experiments and processing.

Appendix A: **The general solution to a uniaxial slab waveguide with isotropic cladding**

Anisotropic slab waveguides were extensively studied in the 1970's [24–30]. In many cases, attention was focused on anisotropic films deposited on a substrate that was itself anisotropic because mode converters, polarization mode filters, and other devices of that time had such a geometry [26]. The case in this paper is somewhat simpler because the geometry is symmetric (see Fig. 8). An additional simplification is that the anisotropic core (the slab) is embedded within an isotropic cladding (air in our experiment). In the derivation of the waveguide dispersion curves and mode profiles presented below, we assume the experimentally relevant conditions that the crystal is uniaxial (like $LiNbO_3$) and its optic axis is parallel to the slab surface. The slab is assumed to extend infinitely along x and z and both core and cladding have no magnetic response. The wave is assumed to propagate along the x-direction and extend infinitely along the z-direction. In the experiment the cylindrical lens generating the wave was rotated instead of the sample, so the derivation here is performed in the coordinate frame of the lens. Finally, to simplify the analysis we assume that the waves are harmonic in space and along the propagation direction: $\vec{E}(x,y,z,t) = \vec{E}(y)\exp[i(\beta x - \omega t)]$, where $\beta = k_x$ is the propagation constant.

#136308 - $15.00 USD Received 8 Oct 2010; revised 18 Nov 2010; accepted 19 Nov 2010; published 1 Dec 2010

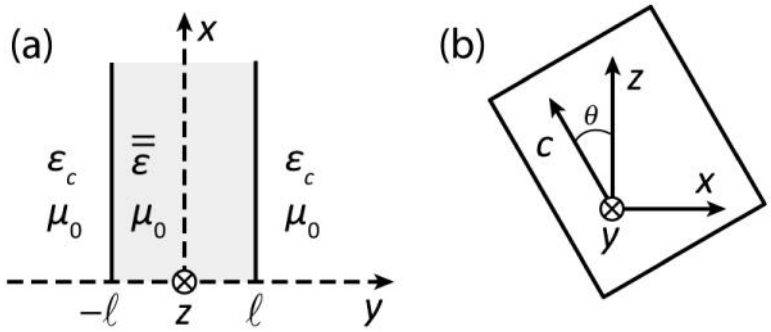

Fig. 8. The geometry for the waveguide mode derivation. (a) An anisotropic slab of width 2ℓ centered at $y = 0$ embedded in an isotropic cladding which extends to infinity. The bound wave propagates along x and extends infinitely along z. ε and μ are the permittivity and permeability in the different regions. (b) The coordinate system for the derivation is defined by the slab surface normal and the propagation direction, which differs from Fig. 1 where the coordinates are defined in the lab frame. θ is the angle between the z-axis and the optic axis of the crystal.

The derivation presented below will loosely follow the analysis of Marcuse and Kaminow [30] where the more complicated symmetric geometry of an anisotropic slab with anisotropic cladding is studied. For the sake of brevity our analysis will skip some intermediate steps, many of which can be found in [30]. The first step in the derivation is to determine the characteristics of waves in bulk material, i.e. the dispersion curves and polarizations, in both core and cladding. Linear combinations of these bulk waves, constrained by system symmetry, are used to build the waveguide modes and lay out the general functional form of the solution. The boundary conditions at the waveguide surface generate a homogeneous system of equations which can be used to solve for the coefficients in the linear combination. Solutions exist for this system of equations, i.e. the determinant of the corresponding matrix is zero, only for certain pairs of frequency and propagation constant. These allowed solutions correspond to the waveguide dispersion curves.

To simplify notation we define several important variables. The propagation constant, $\beta \equiv k_x$, was defined above, and the wave vector orthogonal to the slab surface is defined both outside the crystal, $i\alpha \equiv k_y^{\text{out}}$, and for the ordinary and extraordinary waves inside the crystal, $\kappa_o, \kappa_e \equiv k_{yo}^{\text{in}}, k_{ye}^{\text{in}}$. α is defined as imaginary because bound modes will have evanescent, decaying fields in the cladding. There are three relevant bulk dispersion curves which define the relationships between wave vector, frequency, and index, one for the cladding and one each for the ordinary and extraordinary waves in the uniaxial core. They are:

$$\text{cladding: } \alpha^2 = \beta^2 - k^2 n_c^2 \tag{2a}$$

$$\text{ordinary: } \kappa_o^2 = k^2 n_o^2 - \beta^2 \tag{2b}$$

$$\text{extraordinary: } \kappa_e^2 = k^2 n_e^2 - \beta^2 \left(\cos^2\theta + \frac{n_e^2}{n_o^2} \sin^2\theta \right) \tag{2c}$$

where $k = \omega / c$ is the wave vector in free space and $n_c, n_o, \text{and } n_e$ are the cladding index, ordinary index in the slab, and extraordinary index in the slab respectively. These relations are used to eliminate $\alpha, \kappa_o, \text{and } \kappa_e$ from the equations which follow, so everything is expressed in terms of β and k.

For a specific pair of β and k, there are four possible plane waves in each region, two signs for k_y and two polarizations. In the anisotropic medium, the polarizations correspond to the ordinary (later represented by $\vec{o}$) and extraordinary (later represented by $\vec{e}$) waves. In the

#136308 - $15.00 USD Received 8 Oct 2010; revised 18 Nov 2010; accepted 19 Nov 2010; published 1 Dec 2010

cladding, any pair of orthogonal polarizations can be chosen, so for convenience we choose the TE polarization (represented below by $\vec{v}$ for vertical polarization) and the TM polarization (represented later by $\vec{h}$ for horizontal polarization). We can write out the most general form of the waveguide mode solution as:

$$\text{cladding: } \vec{E}(y) = A_1\vec{v}^{-}\exp[\alpha y] + A_2\vec{h}^{-}\exp[\alpha y] + A_3\vec{v}^{+}\exp[-\alpha y] + A_4\vec{h}^{+}\exp[-\alpha y] \quad (3a)$$

$$\text{core: } \vec{E}(y) = B_1\vec{e}^{+}\exp[i\kappa_e y] + B_2\vec{o}^{+}\exp[i\kappa_o y] + B_3\vec{e}^{-}\exp[-i\kappa_e y] + B_4\vec{o}^{-}\exp[-i\kappa_o y] \quad (3b)$$

$$\text{cladding,: } \vec{E}(y) = C_1\vec{v}^{-}\exp[\alpha y] + C_2\vec{h}^{-}\exp[\alpha y] + C_3\vec{v}^{+}\exp[-\alpha y] + C_4\vec{h}^{+}\exp[-\alpha y] \quad (3c)$$

where A_i, B_i, and C_i are scalar constants and the +/– superscripts correspond to the sign of k_y.

The polarizations in the expression above can be determined from the appropriate vector constraints. In the cladding:

$$\vec{v}^{\pm} = \vec{v} = \begin{bmatrix} 0 \\ 0 \\ 1 \end{bmatrix}, \qquad \vec{k}^{\pm} \times \vec{v} \propto \vec{h}^{\pm} \equiv \begin{bmatrix} \pm i h_x \\ -h_y \\ 0 \end{bmatrix} \propto \begin{bmatrix} \pm i\alpha \\ -\beta \\ 0 \end{bmatrix} \quad (4)$$

where h_x and h_y are the magnitudes of the components of the normalized polarization vector. In contrast to the isotropic cladding, where any orthogonal polarizations could be chosen, in the slab the polarizations are uniquely determined as the ordinary and extraordinary wave polarizations in bulk material. The ordinary wave will be orthogonal to the plane containing the crystal axis and the wave vector: $\vec{o} \propto \vec{k} \times \vec{c}$. The extraordinary wave will be located in the plane of $\vec{k}$ and $\vec{c}$. The displacement field will be given by $\vec{D} \propto \vec{k} \times (\vec{k} \times \vec{c})$, and the electric field is given through the constitutive relation: $\vec{E} = \overline{\overline{R}}(-\theta)\overline{\overline{\varepsilon}}^{-1}\overline{\overline{R}}(\theta)\vec{D}$ where $\overline{\overline{R}}$ is the rotation matrix for rotation around the *y*-axis. This yields:

$$\vec{o}^{\pm} \equiv \begin{bmatrix} \pm o_x \\ -o_y \\ \mp o_z \end{bmatrix} \propto \begin{bmatrix} \pm\kappa_o \cos\theta \\ -\beta\cos\theta \\ \mp\kappa_o \sin\theta \end{bmatrix} \quad (5a)$$

$$\vec{e}^{\pm} \equiv \begin{bmatrix} e_x \\ \mp e_y \\ e_z \end{bmatrix} \propto \begin{bmatrix} \left[\frac{1}{\varepsilon_o} - \frac{1}{\varepsilon_e}\right]\left(\beta^2 + \kappa_e^2\right)\cos^2\theta\sin\theta + \kappa_e^2\sin\theta\left[\frac{\cos^2\theta}{\varepsilon_o} + \frac{\sin^2\theta}{\varepsilon_e}\right] \\ \mp\frac{\beta\kappa_e\sin\theta}{\varepsilon_o} \\ \left[\frac{1}{\varepsilon_o} - \frac{1}{\varepsilon_e}\right]\kappa_e^2\sin^2\theta\cos\theta + \left(\beta^2 + \kappa_e^2\right)\cos\theta\left[\frac{\sin^2\theta}{\varepsilon_o} + \frac{\cos^2\theta}{\varepsilon_e}\right] \end{bmatrix} \quad (5b)$$

where $o_x, o_y, o_z, e_x, e_y,$ and e_z are the magnitudes of the components of the normalized polarization vectors.

With the dispersion curves (Eq. 2) and polarizations (Eqs. 4 & 5) of waves in the bulk material in hand, we can simplify the expressions in Eq. 3 for $\vec{E}(y)$. For bound solutions, we require that the electric field decays to zero as $y \to \pm\infty$, so the terms in the cladding that are exponentially growing can be discarded. We now apply the symmetry condition that there is a reflection plane down the center of the sample, which eliminates half of the coefficients. In

#136308 - $15.00 USD Received 8 Oct 2010; revised 18 Nov 2010; accepted 19 Nov 2010; published 1 Dec 2010

this situation, the solution must be made of symmetric and antisymmetric modes. Absorbing some constant factors into the coefficients, we have:

Symmetric:

$$\text{cladding, } y<-\ell:\ \vec{E}(y)=\begin{bmatrix} h_x A_2 \\ -ih_y A_2 \\ A_1 \end{bmatrix}\exp[\alpha(y+\ell)] \tag{6a}$$

$$\text{core: } \vec{E}(y)=B_1\begin{bmatrix} e_x\cos(\kappa_e y) \\ -ie_y\sin(\kappa_e y) \\ e_z\cos(\kappa_e y) \end{bmatrix}+B_2\begin{bmatrix} -o_x\cos(\kappa_o y) \\ io_y\sin(\kappa_o y) \\ o_z\cos(\kappa_o y) \end{bmatrix} \tag{6b}$$

$$\text{cladding, } y>\ell:\ \vec{E}(y)=\begin{bmatrix} h_x A_2 \\ ih_y A_2 \\ A_1 \end{bmatrix}\exp[-\alpha(y-\ell)] \tag{6c}$$

Antisymmetric:

$$\text{cladding, } y<-\ell:\ \vec{E}(y)=\begin{bmatrix} h_x A_2 \\ -ih_y A_2 \\ A_1 \end{bmatrix}\exp[\alpha(y+\ell)] \tag{7a}$$

$$\text{core: } \vec{E}(y)=B_1\begin{bmatrix} e_x\sin(\kappa_e y) \\ ie_y\cos(\kappa_e y) \\ e_z\sin(\kappa_e y) \end{bmatrix}+B_2\begin{bmatrix} o_x\sin(\kappa_o y) \\ io_y\cos(\kappa_o y) \\ -o_z\sin(\kappa_o y) \end{bmatrix} \tag{7b}$$

$$\text{cladding, } y>\ell:\ \vec{E}(y)=\begin{bmatrix} -h_x A_2 \\ -ih_y A_2 \\ -A_1 \end{bmatrix}\exp[-\alpha(y-\ell)] \tag{7c}$$

Applying the symmetry conditions eliminated half the unknowns, so now we need only apply boundary conditions at one interface to solve for the coefficients. The boundary condition is that the tangential *E* and *H* fields must be continuous across the boundary [20]. Using Faraday's law and the fact that $\partial/\partial z=0$, $\partial/\partial x=i\beta$, and $\partial/\partial t=-i\omega$ for our functional form, $\vec{E}(x,y,z,t)=\vec{E}(y)\exp[i(\beta x-\omega t)]$, we can express all the boundary conditions in terms of the electric field components:

$$E_{z,\text{clad}}=E_{z,\text{core}} \tag{8a}$$

$$\frac{\partial E_{z,\text{clad}}}{\partial y}=\frac{\partial E_{z,\text{core}}}{\partial y} \tag{8b}$$

$$E_{x,\text{clad}}=E_{x,\text{core}} \tag{8c}$$

$$i\beta E_{y,\text{clad}}-\frac{\partial E_{x,\text{clad}}}{\partial y}=i\beta E_{y,\text{core}}-\frac{\partial E_{x,\text{core}}}{\partial y} \tag{8d}$$

The constant coefficients in functional form of the solutions (Eqs. 6 & 7) must be chosen so the above boundary conditions are satisfied at the interface ($y=\ell$). They must be solved

#136308 - $15.00 USD Received 8 Oct 2010; revised 18 Nov 2010; accepted 19 Nov 2010; published 1 Dec 2010

independently for the symmetric and antisymmetric modes. The four expressions above yield a set of homogeneous equations which can be recast in matrix notation.

Symmetric:

$$\begin{bmatrix} -1 & 0 & e_z\cos(\kappa_e\ell) & o_z\cos(\kappa_o\ell) \\ -\alpha & 0 & e_z\kappa_e\sin(\kappa_e\ell) & o_z\kappa_o\sin(\kappa_o\ell) \\ 0 & h_x & -e_x\cos(\kappa_e\ell) & o_x\cos(\kappa_o\ell) \\ 0 & h_y\beta - h_x\alpha & (e_y\beta + e_x\kappa_e)\sin(\kappa_e\ell) & -(o_y\beta + o_x\kappa_o)\sin(\kappa_o\ell) \end{bmatrix} \begin{bmatrix} A_1 \\ A_2 \\ B_1 \\ B_2 \end{bmatrix} = \begin{bmatrix} 0 \\ 0 \\ 0 \\ 0 \end{bmatrix} \quad (9)$$

Antisymmetric:

$$\begin{bmatrix} 1 & 0 & e_z\sin(\kappa_e\ell) & -o_z\sin(\kappa_o\ell) \\ \alpha & 0 & -e_z\kappa_e\cos(\kappa_e\ell) & o_z\kappa_o\cos(\kappa_o\ell) \\ 0 & h_x & e_x\sin(\kappa_e\ell) & o_x\sin(\kappa_o\ell) \\ 0 & h_y\beta - h_x\alpha & (e_y\beta + e_x\kappa_e)\cos(\kappa_e\ell) & (o_y\beta + o_x\kappa_o)\cos(\kappa_o\ell) \end{bmatrix} \begin{bmatrix} A_1 \\ A_2 \\ B_1 \\ B_2 \end{bmatrix} = \begin{bmatrix} 0 \\ 0 \\ 0 \\ 0 \end{bmatrix} \quad (10)$$

The polarizations (Eqs. 4 & 5) and bulk dispersion curves (Eq. 2) can be used to remove all dependence on $\alpha, \kappa_o,$ and κ_e, so for a given angle θ, the only variables are β and k. The determinant will be zero, i.e. the set of equations has a solution, only for β and k pairs that are on the waveguide dispersion curve, and finding all allowed pairs traces out these curves. Using the allowed pairs, the bulk dispersion curves, and one additional "normalization condition" such as $B_1 + B_2 = 1$, all wave vectors and coefficients can be completely determined. The theoretical dispersion curves for several angles are plotted along with the experimental data in Fig. 3, selected electric field profiles are shown in Fig. 4, and the effective indices of refraction for two angles are shown in Fig. 5.

Acknowledgements

The authors would like to thank Alexei Maznev for his invaluable insights regarding anisotropic waveguide behavior and solutions. This work was supported by the National Basic Research Program of China (2010CB933801), the 111 Project (B07013), the National Natural Science Foundation of China (10604033), the Tianjin Natural Science Foundation (09JCYBJC15100), U.S. National Science Foundation Grant No. ECCS-0824185, and a National Science Foundation Graduate Research Fellowship (C.A.W.).

#136308 - $15.00 USD Received 8 Oct 2010; revised 18 Nov 2010; accepted 19 Nov 2010; published 1 Dec 2010

Slow and fast light in photorefractive GaAs–AlGaAs multiple quantum wells in transverse geometry

Fang Bo,[1,2] Ze Liu,[1,2] Feng Gao,[1,2] Guoquan Zhang,[2,3,a)] and Jingjun Xu[2,3]
[1]*TEDA Applied Physics School, Nankai University, Tianjin 300457, China*
[2]*The MOE Key Laboratory of Weak Light Nonlinear Photonics, Nankai University, Tianjin 300457, China*
[3]*Photonics Center, School of Physics, Nankai University, Tianjin 300071, China*

(Received 9 June 2010; accepted 1 August 2010; published online 16 September 2010)

We show theoretically that, based on the dispersive phase coupling effect during the wave mixing process, both slow and fast light can be achieved in GaAs–AlGaAs photorefractive multiple quantum wells (PRMQWs) films applied with a transverse direct-current electric field. The general formula for the group velocity of the diffracted beams in the Raman–Nath regime during the wave mixing process in a nonlinear thin film is derived and is then applied to the case of the PRMQWs films in the transverse geometry. The simulation results in the transverse-geometry PRMQWs films show that the group velocity and bandwidth of slow light can be on the order of centimeter per second and 100 kHz, respectively. The extremely low group velocity and the relatively broad bandwidth are mainly originated from the strong quadratic electro-optic effect and the fast response rate of the PRMQWs films, respectively. Our results show that the delay-bandwidth product of slow light can be significantly improved in PRMQWs films as compared to the reported results in other photorefractive materials. © *2010 American Institute of Physics*.
[doi:10.1063/1.3485829]

I. INTRODUCTION

Recently precise control on the group velocity of light pulses has attracted much attention from both fundamental and practical view points. Many resonant effects, such as electromagnetically induced transparency,[1] coherent population oscillation,[2] stimulated Brillouin/Raman scattering,[3,4] and nonlinear wave mixing process,[5–8] have been developed to generate strong dispersion in a relatively narrow spectral range, thereby tuning the light group velocity to a value very different from the light speed in vacuum. Various potential applications based on light group velocity control, including quantum computing,[9] optical delay lines and buffer memories,[10] sensitive measurements,[11–13] and so on, have also been proposed or demonstrated.

It is well known that the nonlinear two-wave mixing (TWM) process in photorefractive and Kerr media is dramatically dispersive with respect to the frequency difference between the coupling beams. Both the energy and the phase coupling coefficients of the TWM process are dependent on the frequency difference between the two coupling beams. The case for a multiple wave mixing process is similar. The light group velocity control via the dispersive phase coupling effect during nonlinear wave mixing process was experimentally demonstrated in a variety of nonlinear materials such as barium titanate ($BaTiO_3$),[5] tin hypothiodiphosphate ($Sn_2P_2S_6$),[5,6] cadmium telluride (CdTe),[6] bithium silicon oxide ($Bi_{12}SiO_{20}$),[7] and liquid crystals.[8] Using this technique, ultraslow light with a group velocity less than 1 mm/s can be easily achieved at room temperature with a relatively simple experimental setup similar to that used in the traditional TWM experiments. Fast light can also be produced in some nonlinear materials listed above. One advantage of this technique is that a common laser at almost any wavelength can be used in the slow/fast light experiment, as long as the material is nonlinearly sensitive at the operating wavelength, so it is a promising technique to manipulate the group velocity of signal pulses in a wide spectral range. On the other hand, the spectral bandwidth of the slow- or fast-light window, within which the group velocity of the signal pulse can be tuned to a large extent with a negligible wave profile distortion, is quite narrow because of the relatively slow response rate of the wave-mixing processes in these nonlinear materials. The typical spectral bandwidth of the slow- or fast-light window was reported to be of the order of or less than kilohertz.[5–8]

The narrow bandwidth puts a serious limitation on the cut-off modulation frequency of the signal beam in practical applications of slow and fast light. Due to the same reason, the delay-bandwidth product per unit propagation distance, which indicates the capacity to delay a light pulse, is very small as well. To overcome this obstacle, several methods were proposed to expand the spectral bandwidth of the dispersive phase-coupling-induced slow or fast light. These methods include the increase in the coupling beam intensities,[7] the use of fast response materials,[7] and the employment of multiple pump beams with each pump beam responsible for a portion of the frequency components of the signal pulses.[14] It is worthy noting that one can easily extend the spectral bandwidth of slow/fast light by use of the former two methods, while one can improve both the spectral bandwidth and the relative time delay/advance simultaneously, and therefore, the delay-bandwidth product, by use of the third method. This method is similar to the technique used in the slow light induced by the stimulated Brillouin scattering,

a)Electronic mail: zhanggq@nankai.edu.cn.

where two adjacent Lorentzian gain lines were generated to expand the slow-light bandwidth and therefore to improve the delay-bandwidth product.[15]

It is well known that the photorefractive multiple quantum wells (PRMQWs) is one of the photorefractive materials with the fastest response rate, and its response time is of the order of ms in general even under the illumination of weak light beams with a total intensity on the order of milliwatt per square centimeter.[16–18] So it is a promising candidate to expand the spectral bandwidth of slow light, and thereby to manipulate the group velocity of light pulses with a relatively high modulation frequency. More importantly, both the quantum-confined exciton and the quadratic electro-optic effect will contribute to the energy and phase coupling, and the photorefractive coupling effects will be extremely strong when the PRMQWs applied with a strong direct-current (dc) electric field is illuminated by the photons with their energy near to the band gap of the PRMQWs.[16–18] As a result, it is possible to improve both the bandwidth and the delay-bandwidth product per unit propagation distance, and shorter signal pulses with higher modulation frequency can be delayed effectively. So it is attractive to explore the control of light group velocity in PRMQWs during the wave mixing process.

In this paper, we discuss theoretically the dispersive properties of the energy and the phase coupling coefficients during the wave mixing process and the corresponding group velocity in a PRMQWs film applied with a transverse dc electric filed in the plane of the quantum wells (the transverse geometry). Compared with the reported results in other photorefractive materials, the bandwidth of slow and fast light in PRMQWs is broadened to ~100 kHz with group velocities on the order of centimeter per second. In Sec. II, a general theoretical model for the derivation of the group velocity of light pulses propagating in a nonlinear thin film in the presence of a pump beam is given. In Sec. III, the light-induced space-charge field and refractive index grating in PRMQWs are given, and the theoretical model described in Sec. II is applied to a PRMQWs film in the transverse geometry. In Sec. IV, we numerically simulate the dispersive properties of the energy and the phase coupling effects as well as the group velocity of multiple diffraction beams in a PRMQWs film in transverse geometry. Furthermore, the dependence of the group velocity and the bandwidth of slow/fast light on the wave-mixing parameters for the zeroth-order diffraction beam are discussed in detail. A brief conclusion is given in Sec. V.

II. GENERAL THEORETICAL MODEL IN A NONLINEAR THIN FILM

Suppose that two plane waves, s wave for the signal and p wave for the pump, are incident symmetrically into an optically nonlinear thin film from the same side with a crossing angle 2θ and interfere with each other (see Fig. 1), when the two waves have slightly different angular frequencies (i.e., $\omega_s \neq \omega_p$) and wave vectors (i.e., $\vec{k}_s \neq \vec{k}_p$), the electric fields for the signal and pump beams can be written as

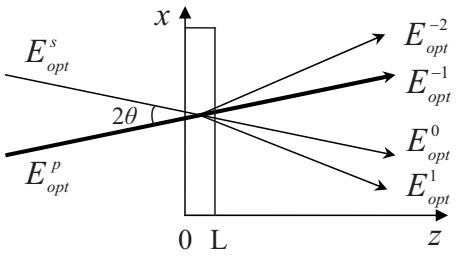

FIG. 1. The schematic diagram of the two-wave coupling in a nonlinear thin film with a thickness L.

$$\vec{E}^{j}_{opt} = \vec{A}_j e^{i(\vec{k}_j \cdot \vec{r} - \omega_j t)}, j = s, p, \tag{1}$$

where $\vec{A}_s$ and $\vec{A}_p$ are the wave amplitude for the signal and the pump beams, respectively. Since the incident angle θ is usually small, we can assume that the two coupling beams propagate paraxially (approximately along z-axis) and have the same polarization for simplicity, and thus the electric fields of the two waves can be treated as scalars. The total light intensity distribution in the superposition region of two coupling beams can be written as

$$I = |E^{s}_{opt} + E^{p}_{opt}|^2 = I_0 + \mathrm{Re}[I_1 e^{i(Kx - \Omega t)}], \tag{2}$$

where $I_0 = |A_s|^2 + |A_p|^2$ is the average intensity of the superposed beams, $I_1 = 2A_s A_p^*$ is the amplitude of the interference pattern, $\Omega = \omega_s - \omega_p$ represents the angular frequency difference between two beams, $\vec{K} = \vec{k}_s - \vec{k}_p$ is the grating vector with a magnitude of $2\pi/\Lambda$, where $\Lambda = \lambda/2 \sin\theta$ is the period of the fringe pattern and λ is the wavelength of the incident beams in vacuum.

If the angular frequency difference Ω is so small that the nonlinear optical thin film can response linearly to the interference pattern, a modulated traveling electric field will be formed via photorefractive effect. The total electric field in the nonlinear thin film is along the x-axis and given by

$$E = E_0 + \mathrm{Re}[E_1 e^{i(Kx - \Omega t)}], \tag{3}$$

where E_0 is the externally applied dc electric field with its positive polarity along the positive x-axis in Fig. 1, E_1 is the light-induced space-charge field. Both the amplitude and the spatial phase shift ϕ (with respect to the light interference pattern) of the space-charge field E_1 depend on the properties of the nonlinear medium and the experimental conditions such as the angular frequency difference Ω, the total light intensity I_0, the externally applied electric field E_0, and the period of the fringe pattern Λ.

The generation of the space-charge field in the nonlinear optical thin film will give rise to a refractive index grating via the electro-optic effect. The index grating, including the fundamental component only, is

$$n = n_b + \Delta n = n_b + n_0 + n_1 e^{i(Kx - \Omega t + \psi)}, \tag{4}$$

where n_b is the background refractive index of the nonlinear medium when no light is present, n_0 is the refractive index change induced by the spatially homogeneous screening electric field, n_1 is the amplitude of the index grating, and ψ is the spatial phase shift in the light-induced index grating with respect to the original light interference fringe pattern.

Note that both the amplitude and the phase shift ϕ of the space-charge field E_1 are influenced by the angular frequency difference Ω. Thus, the amplitude n_1 and the phase shift ψ of the refractive index grating arising from the space-charge field are also sensitive to the change in the angular frequency difference Ω.

To investigate the wave mixing process in the nonlinear thin film, we substitute Eq. (4) for the refractive index into the wave propagation equation

$$\nabla^2 E_{opt} + \frac{\omega^2}{c^2} n^2 E_{opt} = 0, \tag{5}$$

where c is the light speed in vacuum. If the typical effective thickness of the optical medium L is much less than the period of the refractive index grating, the dimensionless Q factor ($Q = 2\pi\lambda L/(n\Lambda)^2$) is much less than unity, the scatterings of the incident beams will be governed by the Raman–Nath diffraction. Otherwise, it is governed by the Bragg diffraction. In this paper, we focus on the wave mixing process in a nonlinear thin film where the Raman–Nath diffraction dominates, therefore high order scatterings must be taken into account. In this case, the total light field at the output face of the sample is given by

$$E_{opt} = \sum_{m=-\infty}^{\infty} A_m e^{i[(n_b+n_0)k_m L - \omega_m t]}, \tag{6}$$

where the term in the summation represents the mth-order outgoing field, $\vec{k}_m = \vec{k}_s + m\vec{K}$, $\omega_m = \omega_s + m\Omega = \omega_p + (m+1)\Omega$, and

$$A_m = [A_s J_m(\delta) + iA_p J_{m+1}(\delta) e^{i\psi}] e^{im(\pi/2+\psi)}, \tag{7}$$

with $J_m(\delta)$ being the mth-order Bessel function of the first kind, $\delta = 2n_1 k_m L$, and ψ is the phase shift in the index grating with respect to the interference fringe pattern as noted above. Note that paraxial approximation is also applied to the case for the diffracted beams here.

It is evident that the presence of a phase-shifted refractive index grating in a nonlinear thin film allows for nonreciprocal energy transfer and phase coupling. We can define γ_m and β_m as the energy and the phase coupling coefficients related to the mth-order diffraction beam during the wave mixing process in a nonlinear thin film, respectively, and therefore the amplitude A_m can be rewritten as

$$A_m = A_s e^{(\gamma_m L + i\beta_m L)}. \tag{8}$$

On the other hand, the dispersive phase coupling during the wave mixing process allows for the control on the group velocity of light. Following the derivation process in Ref. 19, one can get the group velocity of the mth-order diffraction beam

$$v_g = \left(\frac{\partial \beta_m}{\partial \omega_m}\right)^{-1} = \left(\frac{\partial \beta_m}{\partial (m+1)\Omega}\right)^{-1}. \tag{9}$$

Note that the dispersion of the refractive index of the material is out of consideration because it is usually negligibly small in comparison with that of the phase coupling coefficient during the wave-mixing process in any kind of optical nonlinear materials when the angular frequency difference between the two coupling beams fall into or near to the slow- or fast-light window.

III. PHOTOREFRACTIVE GRATINGS IN PRMQWS FILM IN TRANSVERSE GEOMETRY

The formation of photorefractive gratings and the wave mixing properties, especially the energy coupling effect, in PRMQWs thin films and the related physical mechanisms were extensively investigated.[16–18] In order to get significant photorefractive effect, a strong electric field is always applied across the sample in two different experimental geometries: the transverse geometry with the external electric field applied in the plane of the quantum wells and the longitudinal geometry with an electric field perpendicular to the PRMQWs thin films. In this work, we will focus on the transverse geometry.

In the transverse geometry, both the external electric field and the light-induced grating vector are set to be in the plane of PRMQWs, and most of the photocarriers will transport in the plane of PRMQWs due to drift and diffusion. The photocarriers transporting perpendicular to the plane of the quantum wells through ways such as quantum tunneling or thermal emission over the quantum barriers is negligible. Therefore, one-dimensional transport equations governing the generation and distribution of the photocarriers in bulk materials is a good approximation to describe the general photorefractive properties of the PRMQWs film. The set of the transport equations for the photocarriers, including the generation-recombination equations, the current equations, the charge conservation equation, and the Gauss's law, are as follow

$$\frac{\partial n}{\partial t} - \frac{\nabla \cdot \vec{j}_e}{e} = I\alpha + Is_e N_D^0 - \sigma_e n v_e N_D^+ - \gamma_{eh} np, \tag{10}$$

$$\frac{\partial p}{\partial t} + \frac{\nabla \cdot \vec{j}_h}{e} = I\alpha + Is_h N_D^+ - \sigma_h p v_h N_D^0 - \gamma_{eh} np, \tag{11}$$

$$\vec{j}_e = e\mu_e n\vec{E} + k_B T_e \mu_e \nabla n, \tag{12}$$

$$\vec{j}_h = e\mu_h p\vec{E} - k_B T \mu_h \nabla p, \tag{13}$$

$$\frac{\partial}{\partial t}(n + N_A - p - N_D^+) = \frac{\nabla \cdot (\vec{j}_e + \vec{j}_h)}{e}, \tag{14}$$

$$\nabla \cdot (\epsilon_r \epsilon_0 \vec{E}) = -e(n + N_A - p - N_D^+), \tag{15}$$

where n, p, N_D^0, N_D^+, and N_A are the number densities of electrons, holes, deep donors, ionized deep donors and shallow acceptors, respectively, I is the incident intensity, α is the absorption coefficient for the generation of electron-hole pairs, $\vec{j}_{e,h}$, $s_{e,h}$, $\sigma_{e,h}$, $v_{e,h}$, and $\mu_{e,h}$ are the current density, the photoionization cross-section, the defect capture cross section, the drift velocity, and the mobility for electrons and holes, respectively, γ_{eh} is the direct combination rate of electron-hole pair, k_B, T, T_e, ϵ_r, and ϵ_0 are the Boltzmann constant, the absolute temperature of the circumstance, the absolute temperature of electrons, the relative dielectric con-

TABLE I. Various rates related to electrons and holes.

Transition rate	$\Gamma_{lh}=s_h I_0+\gamma_h p_0$	$\Gamma_{le}=s_e I_0+\gamma_e p_0$
Ion recombination rate	$\Gamma_{Rh}=\gamma_h(N_A+n_0-p_0)$	$\Gamma_{Re}=\gamma_e(N_A-N_D^+ +n_0-p_0)$
Drift rate	$\Gamma_{Eh}=K\mu_h E_0$	$\Gamma_{Ee}=Kv_e$
Diffusion rate	$\Gamma_{Dh}=K^2 k_B T\mu_h/e$	$\Gamma_{De}=K^2 k_B T_e\mu_e/e$
Direct recombination rate	$\Gamma_{ehh}=\gamma_{eh}n_0$	$\Gamma_{eeh}=\gamma_{eh}p_0$
Dielectric relaxation rate	$\Gamma_{dih}=e\mu_h p_0/\epsilon\epsilon_0$	$\Gamma_{die}=\frac{en_0}{\epsilon_r\epsilon_0}\left[\frac{dv_e}{dE}+\frac{iKk_BT_e}{e}\left(\frac{d\mu_e}{dE}+\frac{\mu_e d\ln T_e}{dE}\right)\right]$

stant, and the permittivity of vacuum, respectively. The thermal excitation of the carriers is neglected here because its rate is much smaller than the light excitation rate.

Note that the hot electron effect[18] must be considered in the PRMQWs film in transverse geometry, because a strong external electric filed was always applied across the PRMQWs film. In this regime, the electrons gain kinetic energy through acceleration by the strong electric field, then the electron temperature can be significantly higher than the circumstance temperature, and it can be high enough to promote a significant fraction of electrons into the indirect valleys. Since the mobility of the electrons in the upper valleys is smaller than that in the lower valley, the intervalley transfer of electrons between the upper and the lower valleys will affect the statistical mobility of electrons significantly. For simplicity, we assume a two-valley system and the dependence of the mobility of the electrons on the electric field is primarily determined by the intervalley transfer. Under this circumstance, the electric-field-dependent T_e, v_e, and μ_e are given by

$$T_e = T + \frac{2e\tau_r v_e}{3k_B}E, \tag{16}$$

$$v_e = \mu_e E, \tag{17}$$

$$\mu_e = \frac{[\mu_l + \mu_u R\exp(-\Delta U/k_B T_e)]}{1+E\exp(-\Delta U/k_B T_e)}, \tag{18}$$

where τ_r represents the energy relaxation time with a typical value ~ 1 ps, μ_l and μ_u are the mobilities of electrons in the lower and upper valleys, respectively, R and ΔU are the density-of-state ratio and the energy difference between the upper and the lower valleys, respectively.

By solving the transport equations under the small modulation depth approximation, we can obtain the concentrations of the photocarriers and the space-charge field in the illuminated region of the PRMQWs film. In the linear response approximation, the quantities such as E, p, and n can be expressed as

$$E = E_0 + \mathrm{Re}(E_1 e^{i(Kx-\Omega t)}), \tag{19}$$

$$p = p_0 + \mathrm{Re}(p_1 e^{i(Kx-\Omega t)}), \tag{20}$$

$$n = n_0 + \mathrm{Re}(n_1 e^{i(Kx-\Omega t)}), \tag{21}$$

respectively, where E_0 is the external dc electric field across the sample, $n_0=I_0\alpha/\sigma_e v_e N_A$ and $p_0=I_0\alpha/\sigma_h v_h(N_D-N_A)$ are the zeroth-order solutions of the transport equations under homogeneous illumination. Here we neglect the relatively small terms, such as the photoionization from the deep defects, the thermal excitations and the direct recombination. By defining various rates related to electrons and holes listed in Table I,[18] the transport equations in the linear response regime become

$$(i\Omega - i\Gamma_{Ee}+\Gamma_{Re}+\Gamma_{De}+\Gamma_{le}+\Gamma_{eeh})n_1+(\Gamma_{ehh}-\Gamma_{le})p_1 + (\Gamma_{le}-\Gamma_{die})N_1 = I_1[\alpha+s_e(N_D-N_A-n_0+p_0)], \tag{22}$$

$$(\Gamma_{eeh}-\Gamma_{lh})n_1+(-i\Omega+i\Gamma_{Eh}-\Gamma_{Dh}+\Gamma_{Rh}+\Gamma_{lh}+\Gamma_{ehh})p_1 + (-\Gamma_{lh}+\Gamma_{dih})N_1 = I_1[\alpha+s_h(N_A+n_0-p_0)], \tag{23}$$

$$(i\Gamma_{Ee}-\Gamma_{De})n_1+(i\Gamma_{Eh}-\Gamma_{Dh})p_1+(-i\Omega+\Gamma_{die}+\Gamma_{dih})N_1=0, \tag{24}$$

where $N_1=i\epsilon_r\epsilon_0 KE_1/e$ stands for the total number density of the space charges. In these equations, some rates are negligibly small, such as the transition rates Γ_{le}, Γ_{lh}, the dielectric relaxation rates Γ_{die}, Γ_{dih}, and the direct recombination rates Γ_{eeh}, Γ_{ehh}. By keeping only the large terms and the terms related to the angular frequency difference Ω, the solution for the space-charge field is

$$E_1 = \frac{e}{\epsilon\epsilon_0}\frac{mI_0\alpha}{iK}\frac{A+iB}{C+iD}, \tag{25}$$

where

$$A = (\Gamma_{Rh}\Gamma_{De}-\Gamma_{Re}\Gamma_{Dh})+\Omega(\Gamma_{Rh}\Gamma_{Ee}/\Gamma_{Re}+\Gamma_{Ee}+2\Gamma_{Eh}), \tag{26}$$

$$B = -\Gamma_{Re}\Gamma_{Eh}-\Gamma_{Rh}\Gamma_{Ee}+\Omega(\Gamma_{Rh}\Gamma_{De}/\Gamma_{Re}+\Gamma_{De}-2\Gamma_{Dh}), \tag{27}$$

$$C = \Gamma_{Rh}\Gamma_{dih}(\Gamma_{De}+\Gamma_{Re})+\Gamma_{Re}\Gamma_{die}(\Gamma_{Dh}+\Gamma_{Rh}) + \Omega[\Gamma_{Ee}(\Gamma_{Dh}+\Gamma_{Rh})-\Gamma_{Eh}(\Gamma_{De}+\Gamma_{Re})], \tag{28}$$

$$D = \Gamma_{Re}\Gamma_{die}\Gamma_{Eh}-\Gamma_{Rh}\Gamma_{dih}\Gamma_{Ee}+\Omega[\Gamma_{Eh}\Gamma_{Ee}+(\Gamma_{Dh}+\Gamma_{Rh}) \times(\Gamma_{De}+\Gamma_{Re})]. \tag{29}$$

From the obtained total electric field E, including the contributions from the external dc electric field E_0 and the space-charge field E_1, we can get the index grating in the PRMQWs film during the wave mixing process. Note that the physical mechanism governing the generation of index grating due to the space-charge field in PRMQWs film is the quadratic electro-optic effect. In this regime, the relation between the index grating and the space-charge field is given by

TABLE II. The material parameters for a typical PRMQWs film (Ref. 18) used in the numerical simulations.

N_A (m^{-3})	N_D (m^{-3})	ϵ_r	n_b	α (m^{-1})	S_1 (m^2/V^2)	S_2 (m^2/V^2)	μ_h (m^2/Vs)
1×10^{24}	1×10^{22}	16	3.5	1×10^{6}	1.5×10^{-16}	-3.1×10^{-16}	0.04
μ_l (m^2/Vs)	μ_u (m^2/Vs)	R	ΔU (eV)	s_e (m^2)	s_h (m^2)	σ_e (m^2)	σ_h (m^2)
0.6	0.03	96	0.3	1×10^{-21}	1×10^{-20}	1×10^{-18}	1×10^{-18}

$$n = n_b + \Delta n = n_b + \tfrac{1}{2}n_b^3 S E^2, \tag{30}$$

where n_b is the background refraction index of PRMQWs when no light is present, $S=S_1+iS_2$ stands for the complex quadratic electro-optic coefficient with S_1 corresponding to the electrorefraction and S_2 related to the index change induced by electroabsorption, and

$$E^2 = (E_0^2 + 0.5E_1^2) + \mathrm{Re}(2E_0E_1 \exp[i(Kx - \Omega t)]), \tag{31}$$

is the square of the total electric field where high-order components are ignored. The first term on the right-hand side of Eq. (31) is the screening field, which will result in a homogeneous refractive index change n_0, and the second term represents the field grating that allows for the generation of the index grating.

It is worthy noting that the amplitude of the refractive index grating in the PRMQWs film is proportional to the product of the external field E_0 and the space-charge field E_1. Therefore, even if the space-charge field is relatively weak, a strong index grating can be generated when a large external dc electric field is applied across the sample. As a result, strong energy and phase coupling can be realized in PRMQWs film with a large E_0. In previously reported experimental results, the energy coupling coefficient with contribution only from the electrorefraction grating can be on the order of 1000 cm^{-1},[17] which is much higher than that observed in typical ferroelectric crystals. The large energy coupling coefficient indicates the possibility to achieve a phase coupling coefficient with a large amplitude, therefore, a steep dispersion slope of the dispersion curve of the phase coupling coefficient. Combining the fast response rate of PRMQWs films, it means that one can achieve extremely slow light with relatively broad spectral bandwidth, i.e., the delay bandwidth product per unit propagation distance can be significantly improved.

Since exact and explicit expressions for the space-charge field and the group velocity related to the mth-order diffraction beam cannot be given in a simple analytic form, we will study numerically the dispersion properties of the diffracted beams during the wave mixing process in PRMQWs film in Sec. IV.

IV. NUMERICAL SIMULATIONS AND DISCUSSIONS

In this section, we will show the dispersion properties of the energy and the phase coupling coefficients, and the corresponding group velocities of the mth-order diffraction beam during the wave mixing process in a PRMQWs film in transverse geometry. The operating wavelength of the incident beams are set at 836 nm, the corresponding material parameters used in the numerical simulations for a typical PRMQWs film are list in Table II, and the sample temperature is set to be 300 K.

The effective thickness of the PRMQWs sample is in general of the order of micrometer and it is usually much less than the grating spacing, therefore, the diffraction of the two coupling beams is governed by the Raman–Nath diffraction other than the Bragg diffraction. High order diffractions will appear together with the zeroth order. In the Raman–Nath regime, the energy of high-order diffraction beam is generally much less than that of the zeroth order beam and it becomes weaker as the diffraction order increases, therefore, only the −2nd, zeroth, and 1st order cases will be representatively discussed in the following. The property of the −1st order is not discussed here because it copropagates with the pump beam.

Figure 2 shows the energy (a) and the phase (b) coupling coefficients and the absolute values of the corresponding group velocities (c) for the −2nd order (dotted curves), the zeroth order (solid curves), and the 1st order (dashed curves) diffraction beams, respectively, during the wave mixing process. From Figs. 2(a) and 2(b), we can see that the magnitudes of the energy and the phase coupling coefficients are on the order of 10^6 m^{-1} because of the strong external electric field through the quadratic electro-optic effect. Thus, the magnitudes of the energy and the phase coupling of the diffraction beams after propagation through the sample, i.e., $\gamma_m L$ and $\beta_m L$, are on the order of unity provided that the thickness of the PRMQWs sample is of the order of 1 μm. This means that the signal beam (the zeroth order beam) can be amplified under appropriate conditions. On the other hand, the slope of the phase coupling coefficient dispersion curves can be very steep even with a relatively broad dispersion bandwidth due to the fast response rate of the sample. The steep slope of the phase coupling coefficient dispersion curve allows for the generation of extremely slow light. From dispersion curves of the phase coupling coefficient shown in Fig. 2(b), we can derive the group velocities of the diffraction beams according to Eq. (9). The absolute values of the group velocity are shown in Fig. 2(c) with bold and thin curves for the absolute value of positive and negative group velocity, respectively. It is easy to see from Fig. 2(c) that ultraslow light with group velocity of the order of centimeter per second is achievable. The spectral bandwidth of the slow- or fast-light window is on the order of 10^5 Hz, which is much broader than the results reported in other photorefractive materials.[5–8] For the −2nd order diffraction

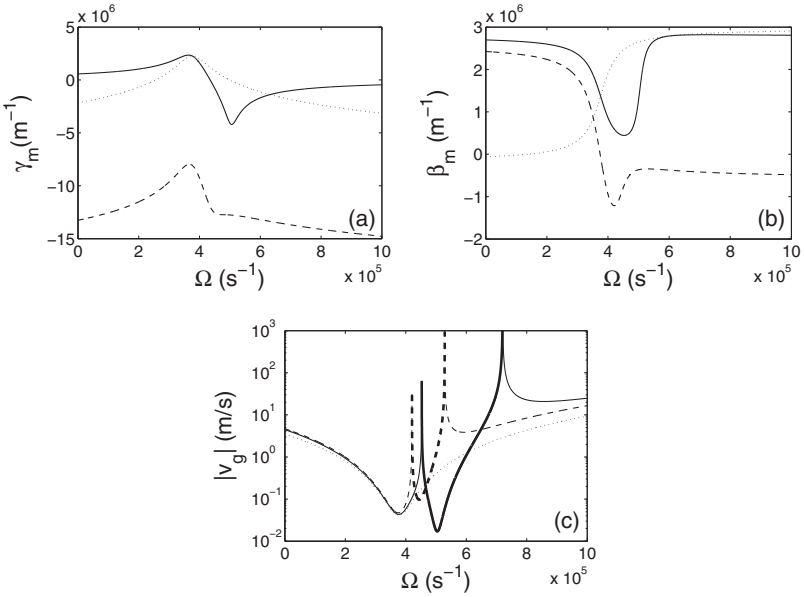

FIG. 2. The dispersion curves of γ_m (a), β_m (b), and v_g (c) with respect to Ω for the -2nd (dotted), the zeroth (solid), and the 1st order (dashed) diffraction beams during the wave mixing process in PRMQWs film. The simulation parameters are $E_0=-6$ kV/cm, $\Lambda=30$ μm, $I_0=1$ mW/cm^2, and $\beta=300$. Other parameters are listed in Table II.

beam only fast light can be realized, which seems to be a general property for all negative orders. On the other hand, both slow and fast light can be observed in the zeroth order and other positive orders. It is worthy noting that, for the -2nd order diffraction beam, it seems that fast light shown by the dotted thin curve in Fig. 2(c) corresponds to the normal-dispersion region of the phase coupling coefficient with respect to the angular frequency difference Ω [see the dotted curve in Fig. 2(b)]. This is because the group velocity is inversely proportional to the first-order partial differential of the phase coupling coefficient β_m to the angular frequency ω_m of the signal beam instead of the angular frequency difference Ω.

Note that the peak energy coupling coefficients for the zeroth and the -2nd order diffraction beams are greater than the typical absorption coefficient of the PRMQWs film (in the range of $5\sim9\times10^5$ m^{-1}).[17] Therefore the zeroth order diffraction beam, which is actually the signal beam and, therefore, is of great interests, can be amplified with appropriate parameters. The simulated energy coupling coefficient in Fig. 2(a) is one order of magnitude larger than the energy coupling coefficient ($\sim10^5$ m^{-1}) observed in experiments in Ref. 17. There are two major factors allowing for such extremely strong energy coupling: (1) we include contributions from both the electrorefraction grating and the electroabsorption grating, but the energy coupling coefficient reported in Ref. 17 only originates from the electrorefraction grating; (2) the intensity ratio between the pump and the signal is set to be 300 in our simulation instead of unity as in the experiments in Ref. 17, which can also result in a larger energy coupling coefficient. We confirm numerically that the energy coupling coefficient is on the same order as that observed in experiments when the intensity ratio is set to be unity in the simulation.

In order to get significant coupling effect, a strong external electric field is always applied in the plane of the PRMQWs film. Therefore, the drift governs the transportation of the photocarriers during the buildup processes of the space-charge field and the index grating. If the polarity of the external electric field is reversed, the drift direction of the photocarriers will also be reversed. It is known that strong energy and phase couplings occur only when the index grating is well established and keeping in step with the movement of the light interference grating during the nondegenerate wave mixing process. In other words, the sign of the angular frequency difference Ω between the two incident beams, which determines the moving direction of the interference pattern, must be reversed when the polarity of the external electric field is reversed. Figure 3 shows the dispersion properties of the phase coupling coefficient and the corresponding group velocity of the -2nd, zeroth, and 1st order diffraction beam with an external electric field $E_0=6$ kV/cm. Note that the polarity of the external electric field here is opposite to that used to simulate the results shown in Fig. 2. It is easy to see that the sign of the dispersion slope of the phase coupling coefficients for the positive

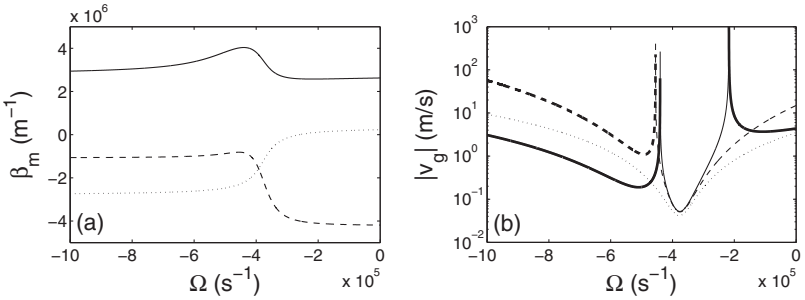

FIG. 3. The dispersion curves of β_m (a) and the corresponding v_g (b) with respect to Ω for the -2nd (dotted), the zeroth (solid), and the 1st (dashed) diffraction orders with $E_0=6$ kV/cm. Other parameters are the same as those of Fig. 2.

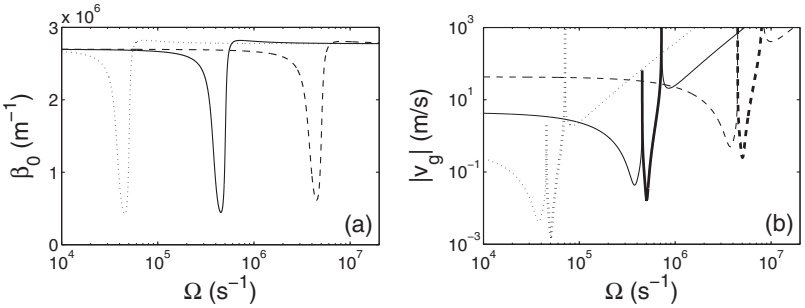

FIG. 4. The dispersion curves of β_0 (a) and the corresponding v_g (b) with respect to Ω during the wave mixing process in PRMQWs sample. The dotted, solid, and dashed curves indicate the results for I_0=0.1, 1, and 10 mW/cm^2, respectively. Other parameters are the same as those of Fig. 2.

orders is also reversed, which induces a switch between the slow and fast light windows. However, the situation for the negative diffraction orders is quite different, the slope sign of the phase coupling coefficient dispersion curves is kept to be negative, indicating that only fast light is possible for the negative diffraction orders.

The construction process of the index grating in the PRMQWs film during wave mixing process is influenced by the experimental conditions such as the incident intensity of the coupling beams, the grating spacing (the crossing angle between the coupling beams), and the external electric field. All these parameters will influence the magnitude and phase of the index grating, therefore, dispersion properties of the diffracted beams during the wave mixing process. As a typical example, we will discuss the impacts of these parameters on the dispersion properties of the zeroth order diffraction beam in the following.

Figure 4 is the dispersion curves of the phase coupling coefficient (a) and those of the corresponding group velocity (b) of the zeroth order diffraction beam with different pump intensities. The dotted, solid, and dashed curves are the results for the pump intensities of 0.1, 1, and 10 mW/cm^2, respectively. Here, the pump intensity is approximately equal to the total intensity of the two coupling beams because the intensity ratio of the pump to the signal is 300. It is easy to see that the bandwidth of the phase coupling coefficient dispersion curve of the zeroth order diffraction beam becomes broader with the increase in the pump intensity, but the peak magnitude of the phase coupling coefficient keeps nearly to be the same. Thus both the bandwidth of slow- or fast-light window and the achievable minimal group velocity increase gradually with the increment of the pump intensity, which obeys the same rule as that in other photorefractive materials.[7,19] Due to the dramatic spectral shift in the slow or fast light window with the variation in pump intensity, as shown in Fig. 4, the group velocity of light varies rapidly in a complicated way for a fixed frequency shift Ω. A switch from slow light to fast light, or vice versa, is achievable by simply tuning the pump intensity. For example, when the pump intensity is changed from 0.1 to 1 mW/cm^2, a switch from slow light to fast light is observed for $\Omega=5\times10^4$ s^{-1}, and vice versa for $\Omega=5\times10^5$ s^{-1} [see the dips of the dotted and solid curves in Fig. 4(b)].

The dispersion properties of the phase coupling coefficient (a) and the corresponding group velocity (b) with different grating spacing are shown in Fig. 5. The dotted, solid, dashed, and dashed-dotted curves are the results for the grating spacing to be 20 μm, 30 μm, 40 μm, and 50 μm, respectively. The bandwidth of slow or fast light increases with the increase in the grating spacing as expected. The spectral variation in the phase coupling coefficient peaks at a certain grating spacing, and the minimal group velocity is achieved near this optimal grating spacing ($\sim$40 μm in our case, see Fig. 5).

As mentioned above, the transport velocity of free electrons in the PRMQWs film is influenced by the external electric field through hot electron effect.[18] If there is a strong dc field applied across the PRMQWs film, the electrons with high energy will migrate into the indirect band of the medium where the mobility μ_u of the electrons is much smaller, this reduces the response rate of the PRMQWs film even electrons are not the dominated carriers. Thus, the achievable minimal group velocity and the slow-light bandwidth decrease with the increase in the externally applied dc field E_0. In addition, the slow- or fast-light window will be redshifted when E_0 becomes stronger. These phenomena can be clearly seen from the dispersion curves of β_0 and the corresponding v_g with E_0 set to be -5, -6, and -7 kV/cm in Fig. 6.

V. CONCLUSIONS

In conclusion, slow and fast light in PRMQWs film based on the dispersive phase coupling effect during the

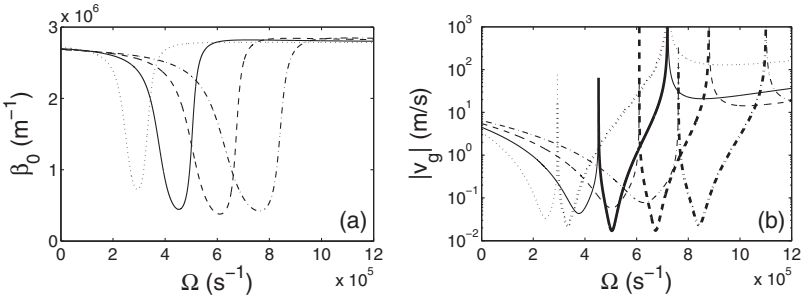

FIG. 5. The dispersion curves of β_0 (a) and the corresponding v_g (b) with respect to Ω during the wave mixing process in PRMQWs sample. The dotted, solid, dashed, and dashed-dotted curves correspond to the results for Λ=20 μm, 30 μm, 40 μm, and 50 μm, respectively. Other parameters are the same as those of Fig. 2.

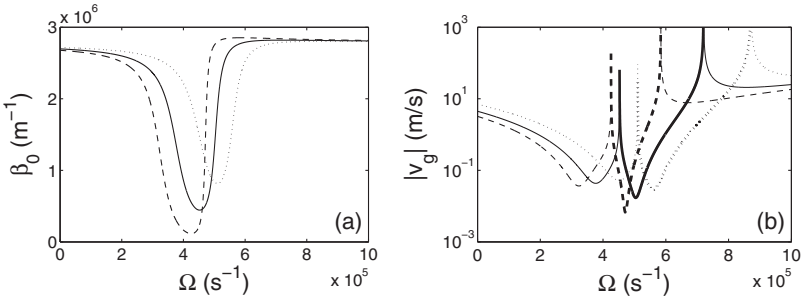

FIG. 6. The dispersion curves of β_0 (a) and the corresponding v_g (b) with respect to Ω during the wave mixing process in PRMQWs sample. The dotted, solid, and dashed curves are the results for $E_0=-5$ kV/cm, -6 kV/cm, and -7 kV/cm, respectively. Other parameters are the same as those of Fig. 2.

wave mixing process are studied and discussed. The dependence of the group velocity and the bandwidth of slow- and fast-light windows on various simulation parameters such as the incident intensity, the grating spacing, and the externally applied dc field are presented. Due to the fast response rate and the strong phase coupling effect originated from the quadratic electro-optic effect in the PRMQWs film in the transverse geometry, ultraslow light with group velocity of the order of centimeter per second and a bandwidth of the order of 100 kHz is achievable, which improves the delay-bandwidth product per unit distance significantly as compared to other photorefractive materials reported up to now. The results indicate that the PRMQWs film is a promising candidate for manipulation of the group velocity of light in various practical applications.

ACKNOWLEDGMENTS

The authors wish to thank Professor D. D. Nolte for his helpful discussions and suggestions. This research is financially supported by the NSFC (Grant Nos. 10904077, 10804054, and 90922030), the RFDP (Grant No. 200800551034), the MOE Cultivation Fund of the Key Scientific and Technical Innovation Project (Grant No. 708022), the 111 Project (Grant No. B07013), the 973 Program (Grant No. 2007CB307002), and the CNKBRSF (Grant No. 2006CB921703), and the Fundamental Research Funds for the Central Universities.

[1] L. V. Hau, S. E. Harris, Z. Dutton, and C. H. Behroozi, Nature (London) **397**, 594 (1999).
[2] M. S. Bigelow, N. N. Lepeshkin, and R. W. Boyd, Phys. Rev. Lett. **90**, 113903 (2003).
[3] Y. Okawachi, M. S. Bigelow, J. E. Sharping, Z. Zhu, A. Schweinsberg, D. J. Gauthier, R. W. Boyd, and A. L. Gaeta, Phys. Rev. Lett. **94**, 153902 (2005).
[4] J. E. Sharping, Y. Okawachi, and A. L. Gaeta, Opt. Express **13**, 6092 (2005).
[5] E. Podivilov, B. Sturman, A. Shumelyuk, and S. Odoulov, Phys. Rev. Lett. **91**, 083902 (2003).
[6] A. Shumelyuk, K. Shcherbin, S. Odoulov, B. Sturman, E. Podivilov, and K. Buse, Phys. Rev. Lett. **93**, 243604 (2004).
[7] G. Zhang, F. Bo, R. Dong, and J. Xu, Phys. Rev. Lett. **93**, 133903 (2004).
[8] S. Residori, U. Bortolozzo, and J. P. Huignard, Phys. Rev. Lett. **100**, 203603 (2008).
[9] L. V. Hau, Nat. Photonics **2**, 451 (2008).
[10] R. S. Tucker, P.-C. Ku, and C. J. Chang-Hasnain, J. Lightwave Technol. **23**, 4046 (2005).
[11] Z. Shi, R. W. Boyd, D. J. Gauthier, and C. C. Dudley, Opt. Lett. **32**, 915 (2007).
[12] U. Bortolozzo, S. Residori, and J. P. Huignard, Opt. Lett. **34**, 2006 (2009).
[13] Y. Zhang, H. Tian, X. Zhang, N. Wang, J. Zhang, H. Wu, and P. Yuan, Opt. Lett. **35**, 691 (2010).
[14] Z. Deng, D.-K. Qing, P. Hemmer, C. H. R. Ooi, M. S. Zubairy, and M. O. Scully, Phys. Rev. Lett. **96**, 023602 (2006).
[15] M. D. Stenner, M. A. Neifeld, Z. Zhu, A. M. C. Dawes, and D. J. Gauthier, Opt. Express **13**, 9995 (2005).
[16] Q. N. Wang, D. D. Nolte, and M. R. Melloch, Appl. Phys. Lett. **59**, 256 (1991).
[17] Q. Wang, R. M. Brubaker, D. D. Nolte, and M. R. Melloch, J. Opt. Soc. Am. B **9**, 1626 (1992).
[18] Q. N. Wang, R. M. Brubaker, and D. D. Nolte, J. Opt. Soc. Am. B **11**, 1773 (1994).
[19] G. Zhang, R. Dong, F. Bo, and J. Xu, Appl. Opt. **43**, 1167 (2004).